Investigation of the (p,α) Reaction on Isotopes of Titanium at 40.35 Mev

Ossama A. Abouzeid

Department of Physics
University of Manitoba
Winnipeg, Man., Canada.

A thesis submitted to the Faculty of Graduate Studies of the University of Manitoba in partial fulfillment of the requirements for the Ph.D. Degree.

INVESTIGATION OF THE (P,α) REACTION ON ISOTOPES OF TITANIUM AT 40.35 Mev

BY

OSSAMA AHMED MOSTAFA ABOU-ZEID

A thesis submitted to the Faculty of Graduate Studies of the University of Manitoba in partial fulfillment of the requirements of the degree of

DOCTOR OF PHILOSOPHY

To my wife, Edith

Acknowledgments

I would like to express my gratitude and thanks to my advisor Prof. W.R. Falk for the help and guidance he provided me.

I would like also to thank the high resolution beam line research group for helping in the experimental stages of this work.

Special thanks go to the target preparation division of Chalk River Nuclear Laboratories for preparing the targets.

The financial assistance of the National Research Council of Canada, the Cyclotron laboratory and Physics Department of The University of Manitoba is also appreciated.

Abstract

The $^{46,48,50}Ti(p,\alpha)^{43,45,47}Sc$ reactions were studied at a proton energy of 40.35 Mev and with an overall energy resolution of about 80 kev FWHM.

Angular distributions for states with excitation energies up to about 7 Mev in ^{43}Sc and ^{45}Sc and up to 8.4 Mev in ^{47}Sc are presented. The J^{π} assignments were in agreement with those available in literature. For some states where more than one J^{π} value was given, the measured angular distributions were used to determine a J^{π} value.

Both positive parity and negative parity states were observed. The positive parity states are excited mainly by pickup of two (fp) shell neutrons and an (sd) shell proton while the negative parity states are excited mainly by pickup of all the nucleons from the (fp) shell.

In an attempt to establish the (p,α) reaction as a useful spectroscopic tool, the microscopic form factor (MFF) formalism of the three nucleon transfer reaction developed by Falk was applied. This form factor was calculated using single-particle states calculated in a Woods-Saxon potential, then expanded in a harmonic oscillator basis. To account for the truncation in this expansion a cluster form factor (CFF) tail was attached to the MFF.

First order calculations were performed assuming the simplest possible configuration for the transferred nucleons. Subsequently, the $(1f_{7/2})^n$ shell model wave functions of Kutschera were also used in a more detailed test. All components with different neutron angular momentum couplings were considered. Reasonable agreement was obtained for most

of the states considered. However, the calculations point to the need for Ti and Sc shell model wave functions calculated in a broader basis that include both the sd and fp shells.

Shell model expressions for calculating the spectroscopic amplitudes needed for this microscopic analysis are given.

The effect of including different configurations for each transition on the calculated analyzing power was also investigated to see to what extent there is sensitivity to the details of the nuclear structures.

Contents

LIST OF TABLES

LIST OF FIGURES

Chapter 1

Introduction

During the last two decades many direct transfer reactions have been utilized to extract nuclear structure information.

Single-nucleon pick-up and stripping reactions have been studied extensively and have yielded important information about spins and parities of energy levels. The differential cross section for these reactions is incoherent in the orbital (ℓ) and total angular momenta (j) of the transferred nucleon [1],[2] but coherent in the principal quantum number (n). The measured spectroscopic factors for each transition can be directly compared with the calculated ones.

The more complicated two-nucleon transfer reactions have two interesting advantages. First, as few other reactions, they can produce states in the final nucleus for which $T > |T_z|$. Second, the differential cross section is coherent in the configuration of the transferred nucleons and incoherent in the transferred total angular momentum. The second property makes the cross section sensitive to the signs of the components of the nuclear wave functions. This has the advantage that data can be used to test not only the magnitudes of various components of the calculated wave functions but also the relative signs, this information being inaccessible from single-nucleon reactions.

In the case of three-nucleon transfer reactions - or specifically for the (p,α) reaction of interest in the present study - the situation is considerably more complicated than for two-nucleon transfer reactions due to the presence of a third nucleon. The differential cross section

is coherent not only in n,ℓ,j of the individual nucleons but also in the total angular momentum (J') of the two neutrons.

In spite of this complexity the (p,α) reaction has many interesting features that could yield a wealth of information on nuclei and wave functions. These features have been documented by a number of authors [3],[4],[5] and will be summarized briefly here.

1. The (p,α) reaction can populate single proton hole states in nuclei with two neutrons away from the stability line. An example is the reaction $^{58}Ni(p,\alpha)^{55}Co$. Single proton pick-up reactions cannot be employed to study ^{55}Co due to lack of a suitable target.

2. The j-dependence [6],[7],[8]. The angular distributions observed in the (p,α) reaction are dependent on the total angular momentum transfer J, as well as on L, the orbital angular momentum. This is due to the spin-orbit potential term in the proton channel. Fig. (1.1) shows L=1 angular distributions for the two cases J=L+S=1+1/2=3/2 and J=L-S=1-1/2=1/2 for the reaction $^{116}Sn(p,\alpha)^{113}In$ at 22 Mev [4]. This property is used quite often in spin assignments although, unfortunately, the J-dependence of the angular distributions decreases as the orbital angular momentum transfer L increases [7]. However, from the measurement of the analyzing power in the $(\vec{p},\alpha)$ reaction [9], the strong J-dependence noted for L=1 angular distribution appears again in the analyzing power for the $^{116}Sn(\vec{p},\alpha)^{113}In$ reaction at 22 Mev as shown in Fig. (1.2). In Fig. (1.3), the J-dependence of the analyzing powers for the cases where L=3 and L=4 are shown together with the angular distributions. While the angular distributions show little difference between J=L+S and J=L-S, the analyzing powers show strong J-dependence. This

Fig. (1.1) Angular distributions of cross sections for L=1 for J=L+S=3/2 and J=L-S=1/2 for the reaction $^{116}Sn(p,\alpha)^{113}In$ at 22 Mev [4].

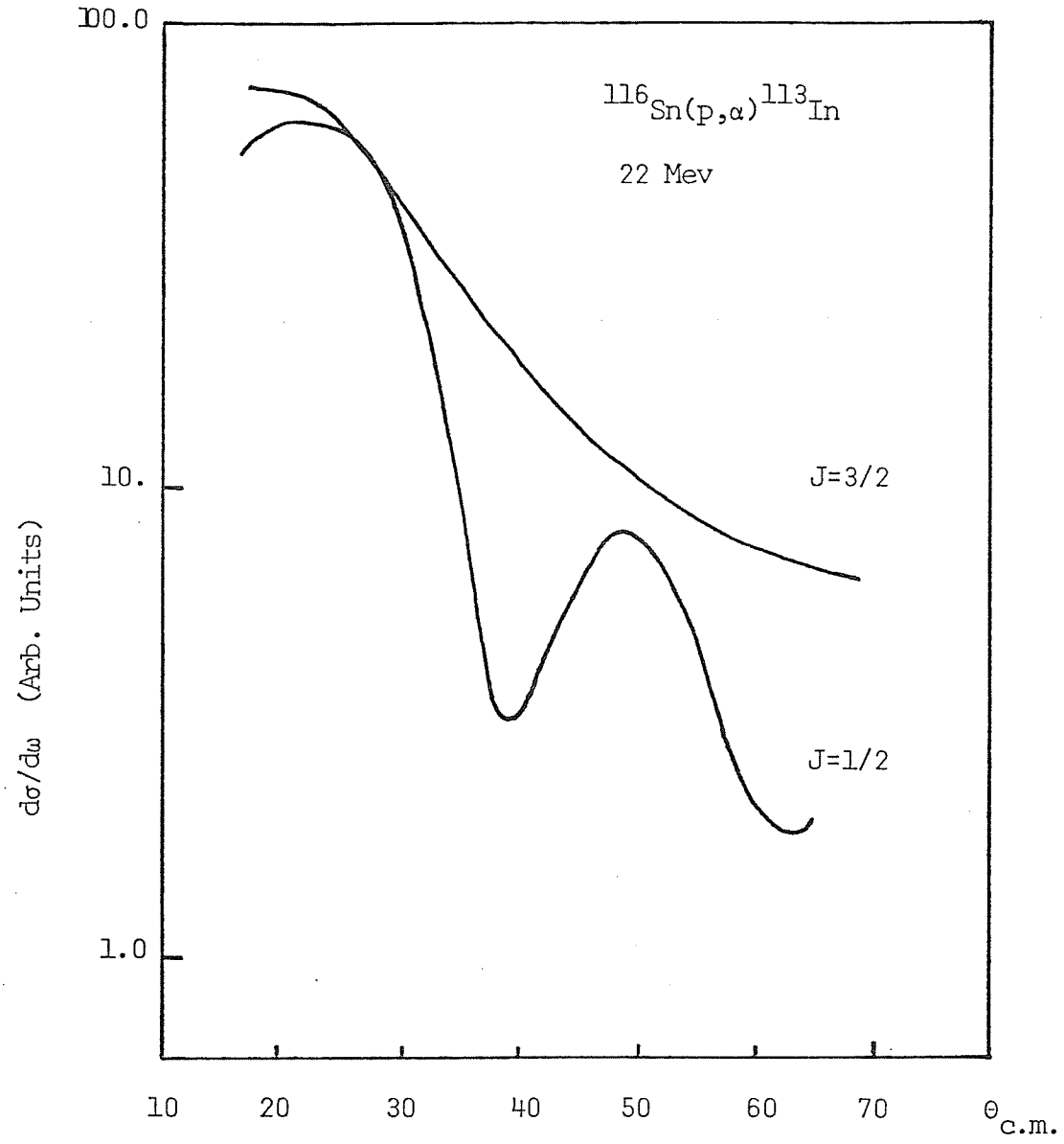
100.0
10.
1.0
$^{116}Sn(p,\alpha)^{113}In$
22 Mev
J=3/2
J=1/2
dσ/dω (Arb. Units)
10
20
30
40
50
60
70
$\theta_{c.m.}$

Fig.(1.2) Angular distributions of cross sections and analysing powers for the $^{116}Sn(\vec{p},\alpha)^{113}In$ at 22 Mev (9).

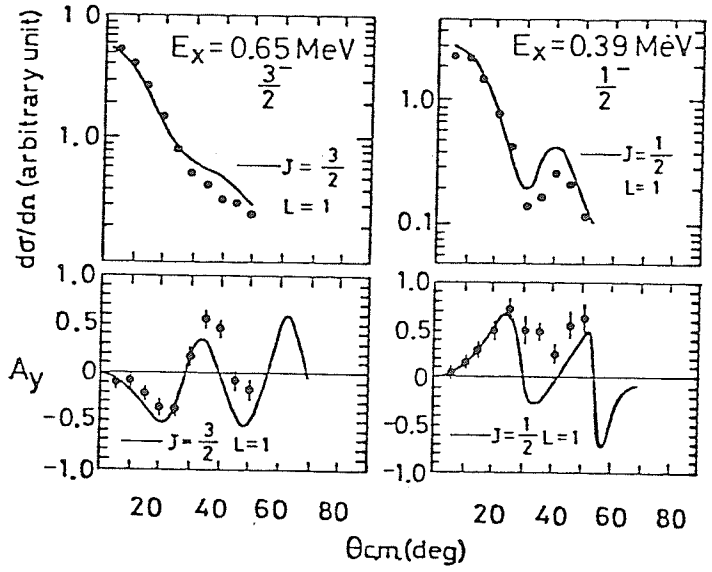
dσ/dΩ (arbitrary unit)
Ex = 0.65 MeV
3/2⁻
J = 3/2
L = 1
Ex = 0.39 MeV
1/2⁻
J = 1/2
L = 1
Ay
J = 3/2 L = 1
J = 1/2 L = 1
θc.m.(deg)

Fig.(1.3) Angular distributions of cross sections and analysing powers for the $^{116}Sn(\vec{p},\alpha)^{113}In$ reaction at 22 Mev.

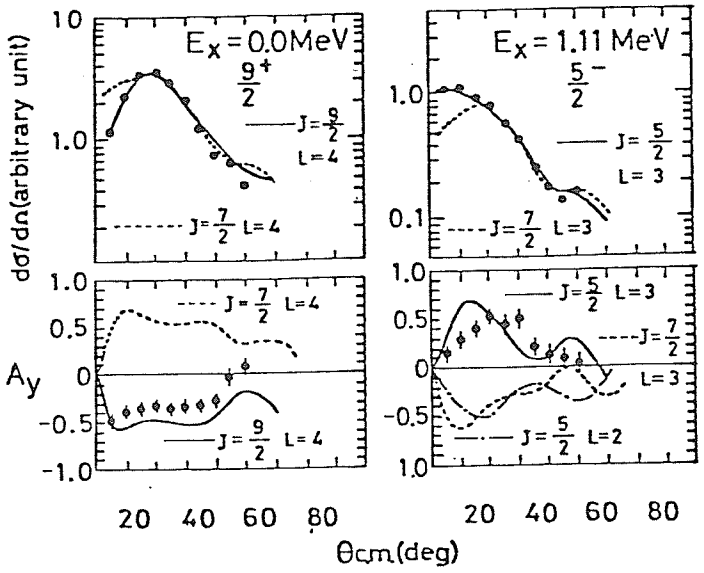
Ex = 0.0MeV
9+/2
J=9/2 L=4
J=7/2 L=4
Ex = 1.11 MeV
5−/2
J= 5/2 L= 3
J=7/2 L=3
dσ/dΩ(arbitrary unit)
Ay
J=7/2 L=4
J=9/2 L=4
J=5/2 L=3
J=7/2 L=3
J=5/2 L=2
θcm(deg)

property can be used for unambiguous J assignment.

3. The (p,α) reaction on target nuclei with seniority ν=0 can reach states in the final nuclei with seniority ν=3. Examples of such a case is $^{46}Ti(p,\alpha)^{43}Sc$ $(19/2^-)$.

4. Another useful property of the (p,α) reaction is its ability to excite states with both $T_<=T_3=\frac{N-Z}{2}$ and $T_>=T_3+1$. This is not allowed for example in the reaction $(d,^3He)$.

Until five years ago quantitative microscopic calculations employing the (p,α) reaction had been performed on relatively few nuclei[3], [10],[11], unlike the two nucleon transfer reaction which was formulated and tested[12],[13] in many instances as long as fifteen years ago.

Nevertheless, over the last two decades or so several investigators have studied the (p,α) and (α,p) reactions[14]. However, generally these were of qualitative nature; only in few cases was a quantitative analysis attempted. One of the earliest efforts to obtain quantitative information from the (p,α) reaction was conducted by Sherr and Bayman[15]. The measurements and calculations were for selected cases of $(1f_{7/2})^3$ transfer to the ground states. Expressions for transition strengths between ground states were derived and reproduced the experimental trends. Ground state wave functions were assumed to have a simple seniority (zero for even A nuclei and one for odd A nuclei). Bayman[1] has analysed the (p,α) data on ^{48}Ti, ^{51}V, ^{45}Sc and ^{54}Fe and was able to predict correctly the experimental cross sections using the wave functions of McCullen, Bayman and Zamick (M.B.Z.)[16].

Nolen[17] has presented a fully microscopic description of the (p,α) reaction. However, he did not apply it in analysing the (p,α) reaction

on Cu isotopes. Instead he introduced a simple spectator model where the two neutrons were coupled to angular momentum J'=0.

Falk[3],[10] introduced a fully microscopic form factor by starting with single particle wave functions calculated in a Woods-Saxon well, which were then expanded in an harmonic oscillator basis. This improved form factor was applied successfully to $^{12}C(\alpha,p)^{15}N$[7] , $^{130}Te(p,\alpha)^{127}Sb$[18] and recently to $^{40,42}Ca(p,\alpha)^{37,39}K$[19] where it was demonstrated that in cases where the transferred neutrons come from two major shells, details of the nuclear wave functions become increasingly important.

Smits[4] introduced a semi-microscopic description of the (p,α) reaction. He chose as a natural degrees of freedom for the three-nucleon transfer reaction the following:

(a) a single-particle degree of freedom, describing the transfer of the odd particle (the proton).

(b) a collective degree of freedom, describing the (collective) transfer of the remaining pair (the neutrons).

Thus he was able to separate the structure and dynamic parts. The model was used successfully to predict transition strengths of the (p,α) reaction on Sn isotopes.

Smith[20] presented a theory for the (p,α) and (α,p) reactions which is derived from a generalization of the Bayman and Kallio[21] method for calculating two nucleon form factors. Starting with single particle wave functions generated in a Woods-Saxon potential, he first calculated the two neutron wave function. Then the di-neutron is treated as a mass-two particle and coupled to the proton to make a triton in a OS internal state. The form factor of the latter part was

calculated as a two nucleon form factor but with unequal mass. This method was restricted to those reactions where the transferred particles are in 0S state of internal motion. This form factor is similar to that used by Falk. The difference is in the method of evaluation. Both form factors start with single-particle states calculated in a Woods-Saxon potential. However, in Falk's form factor these single-particle states are expanded in harmonic oscillator basis to permit analytical evaluation, while in Bayman's approach the integration is done numerically. A comparison between the two form factors gave agreement between the two methods as mentioned in Ref. (24).

Smith[20] also presented calculations of the form factor where the single-particle states were taken to be harmonic oscillator wave functions. A hankel tail was matched to the oscillator form factor to give the correct asymptotic behaviour. These two form factors were found to be essentially the same, although they differed a bit in the surface region.

Pellegrini[22] has studied the $^{34}S\ (p,\alpha)^{31}P$ reaction and compared it with the reaction $^{32}S\ (d,^{3}He)^{31}P$. This comparison ruled out the spectator model in describing the (p,α) reaction where the two neutrons were coupled to angular momentum $J'=0$.

Recently Oberhummer[23] studied the low-lying states in ^{53}Mn using the $^{56}Fe(p,\alpha)^{53}Mn$ reaction. DWBA calculations using a fully microscopic form factor resulted in good fits. However, the relative transition strength could not be reproduced. It was pointed out that the inclusion of small admixtures of additional proton shell configurations could account for the observed strengths.

In the present work the objective is to study the Sc isotopes 43, 45, and 47 through the (p,α) reaction. Additional structure information can be obtained that cannot be obtained through other reactions. Also this study will allow us to investigate the applicability of the microscopic formalism for the (p,α) reaction on a series of isotopes.

The choice of these particular reactions was motivated by several factors, among them:

1. The availability of shell model wave functions for both the target and the residual nuclei[16],[25]. These wave functions were calculated in the truncated space $(1f_{7/2})^n$. Although shell model calculations with a broader basis are needed to describe adequately the Ti and Sc isotopes, the available ones provide a useful testing ground for microscopic calculations.

2. The Ti(p,α)Sc reaction has been studied before on a few occasions[26],[27],[28]. However, to the best of our knowledge, the investigations did not exceed the qualitative stage. Moreover, only states with excitation energies up to about 3 Mev were identified. In the present work a quantitative analysis will be presented for states with excitation energies up to 8.4 Mev.

3. The single hole structure of ^{45}Sc and ^{47}Sc have been studied using the (d,^{3}He) reactions by Ohnuma[29] and Mairle[30] and more recently by Doll[31]. The study of Sc isotopes through the (p,α) reaction will provide additional information about the structure of some of these states. ^{43}Sc has not been studied by the (d,^{3}He) reaction due to the lack of a suitable target.

The bombarding energy was chosen to be in the neighborhood of 40 Mev. This was governed by the desire to avoid compound nucleus contribution[6],[32] and good cyclotron behaviour and transmission at this energy.

Chapter 2 contains the details of the microscopic form factor. This form factor is calculated using single-particle wave functions calculated in Woods-Saxon potential and expanded in harmonic oscillator basis. Also contained in chapter 2 are the shell model spectroscopic amplitudes connecting the initial and final states for the three-nucleon transfer reactions. These spectroscopic amplitudes are needed for the microscopic calculations.

The experimental procedure and setup, a description of the beam facility, the electronic circuitry and other experimental details are given in chapter 3.

Chapter 4 contains a brief theoretical discussion about the nuclear structure of Sc and Ti isotopes summarized from the existing literature.

Chapter 5 contains the experimental data together with the microscopic calculations. The microscopic calculations have been performed in two stages. In the first, simple configurations for the transferred nucleons have been assumed, in order to investigate to what extent such configurations can account for the observed transition strengths. In the second stage the microscopic calculations have employed the shell model wave functions of Kutschera[25] where the Ti and Sc nuclei were assumed to have the structure of closed ^{40}Ca core coupled to $(f_{7/2})^n$. The residual interaction between nucleons in the unfilled shell was estimated from the experimental data on three different two-body systems

in $1f_{7/2}$ nuclei: ^{42}Sc, ^{48}Sc and ^{54}Co. The wave functions of the first and second excited state of each spin were calculated.

Chapter 2

Microscopic Description for the (p,α) Reaction

2.1 The DWBA Formalism of the (p,α) Reaction

Fig. (2.1) shows a diagrammatic representation of the pickup reaction A(p,α)B.

The DWBA expression for the differential cross section can be written analogous to single-nucleon[33] and two-nucleon transfer reactions[12] as follows:

$$\frac{d\sigma}{d\Omega} = \frac{\mu_p \mu_\alpha}{(2\pi\hbar^2)^2} \cdot \frac{K_\alpha}{K_p} \cdot \frac{1}{(2J_A+1)(2S_p+1)} \sum_{\substack{M_A M_B \\ m_\alpha m_p}} |T_{DW}|^2 \qquad (2.1)$$

where

μ_p and μ_α are the reduced masses of the proton-target and alpha-residual nucleus, respectively. K_p and K_α are the magnitudes of the wave numbers in the proton and α channels, respectively.

T_{DW} is the distorted wave transition amplitude.

J_A is the target nucleus spin.

The transition amplitude T_{DW} is given by:[34],[35]

$$T_{DW} = J \int \underline{dr}_{PA} \int \underline{dr}_{\alpha B} \; \chi^{(-)}_{\alpha B}(\underline{K}_{\alpha B}, \underline{r}_{\alpha B}) \cdot$$

$$< \psi_{B\alpha} | V_{PA} - \bar{V}_{PA} | \psi_{PA} > \cdot \chi^{(+)}_{PA}(\underline{K}_{PA}, \underline{r}_{PA}) \qquad (2.2)$$

where

J is the Jacobian of transformation to the relative coordinates $\underline{r}_{PA}$ and $\underline{r}_{\alpha B}$. J is given by[4]: $\left| \begin{matrix} 1 & B/A \\ 1_4 & 1 \end{matrix} \right|^{-3}$

Fig.(2.1) A diagramatic representation of the A(p,α)B reaction.

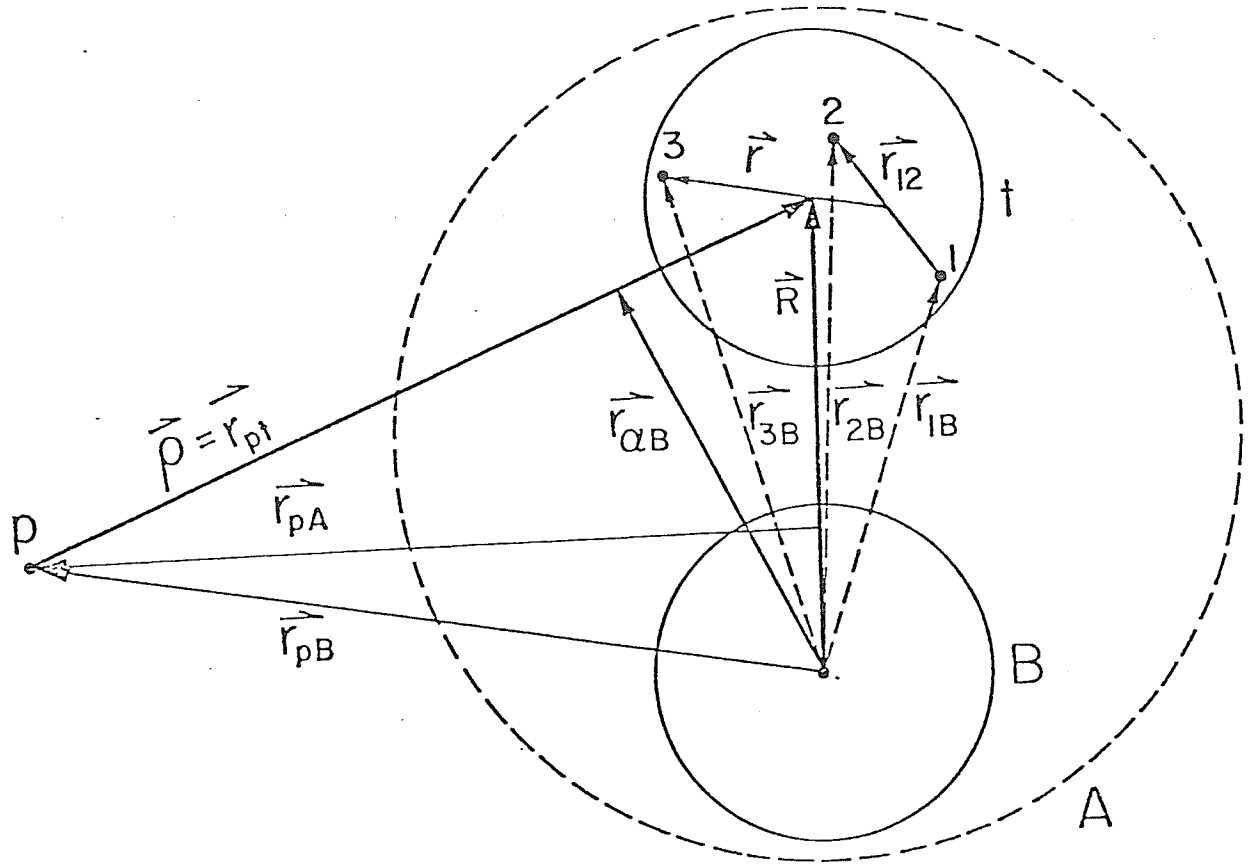
2
3
$\vec{r}$
$\vec{r}_{12}$
t
1
$\vec{R}$
$\vec{\rho} = \vec{r}_{pt}$
$\vec{r}_{\alpha B}$
$\vec{r}_{3B}$
$\vec{r}_{2B}$
$\vec{r}_{1B}$
p
$\vec{r}_{pA}$
$\vec{r}_{pB}$
B
A

V_{PA} is the sum of all two-body interaction potentials between the proton and each nucleon in the target nucleus A.

$\bar{V}_{PA}$ is the optical potential describing elastic scattering in the incident channel.

$\chi^{(-)}_{\alpha B}$ is the α distorted wave.

$\chi^{(+)}_{PA}$ is the proton distorted wave.

All nuclear structure details are contained in the nuclear matrix element $< \psi_{B\alpha} |V_{PA} - \bar{V}_{PA}| \psi_{PA} >$. The main problem in applying this matrix element is in the construction of the form factor which is more complicated than that of two-nucleon transfer reactions. Besides, the evaluation of spectroscopic amplitudes (or equivalently, the overlap integral) is needed for each possible transition. Falk[24] has described in detail the calculation of the form factor for describing the (p,α) reaction. Appendix A contains a copy of the paper by Falk[24] and the reader is referred to it at this point, since no details will be given here about the lengthy procedure of evaluating the nuclear matrix element. Symbols and notations used in Appendix A are adopted here.

Of particular interest to us is section 2.7 of Appendix A where expressions of the nuclear matrix element and the microscopic form factor are given. For completeness these expressions will be given here.

The nuclear matrix element is given by:[24]

$$< B\alpha|V|AP > \alpha \sum_{LJM_B M\lambda\mu_t} (J_B\ M_B\ J\ M\ |\ J_A\ M_A)\ (L\lambda\tfrac{1}{2}\mu_t\ |\ JM)$$

$$(\tfrac{1}{2}\ \mu_t\ \tfrac{1}{2}\ \mu_p\ |\ o\ o)\ \sum_{\gamma J'} I_{AB}(\gamma,J',J) \cdot \begin{bmatrix} \ell_1 & \ell_2 & J' \\ \tfrac{1}{2} & \tfrac{1}{2} & o \\ j_1 & j_2 & J' \end{bmatrix} \begin{bmatrix} J' & \ell_3 & L \\ o & \tfrac{1}{2} & \tfrac{1}{2} \\ J' & j_3 & J \end{bmatrix} \cdot$$

$$F^{\gamma}_{J'L}(\rho,R)\ Y^{\lambda}_{L}(\hat{R}) \ . \qquad (2.3)$$

The function $F^{\gamma}_{J'L}(\rho,R)$ is the form factor for transfer of the configuration (γ,J',J) and is given by:

$$F^{\gamma}_{J'L}(\rho,R) = g(\gamma) \sum_{P_1P_2P_3} \sum_{N'n'Nn} a_{P_1} a_{P_2} a_{P_3} \left(\frac{A}{A-1}\right)^{P_1+P_2+P_2+(\ell_1+\ell_2+\ell_3)/2}$$

$$x < P_1\ell_1P_2\ell_2,\ J'|\mu,\mu|N'J'n'\ o,\ J' > < N'J'\ P_3\ell_3,L|2\mu,\mu|NLno,L >$$

$$x \left(\frac{A-3}{A}\right)^{N+L/2} I_{nn'}(\nu,\nu_\alpha,\beta,\rho) R_{NL}\left[\frac{3(A-3)}{A}\ \nu R^2\right] \qquad (2.4)$$

The proportionality constant in Equ. (2.3) is the same for all (p,α) reactions and remains as an overall (unspecified) normalization constant.

2.2 Spectroscopic Amplitudes

The spectroscopic amplitudes $S^{1/2}_{AB}$ are related to the expansion coefficients $I_{AB}(\gamma,J',J)$ as shown in Equ. (2.7) of Appendix A.

The spectroscopic amplitudes for pure shell model configurations were calculated in Ref. (12) for two-nucleon transfer reactions in the neutron-proton formalism. The same procedure will be extended to the case of three-nucleon transfer reactions.

The coefficients $I_{AB}(\gamma,J',J)$ have to be calculated for each

configuration γ,J',J, as may be noted from Equ. (2.3). The following will illustrate how $I_{AB}(\gamma,J',J)$ has been calculated.

Consider a nucleus A with the outermost proton shell w having m protons coupled to angular momentum β_p. Let the outermost neutron shell be ρ having n neutrons coupled to angular momentum β_n. The wave function of this nucleus can be symbolized by:(37)

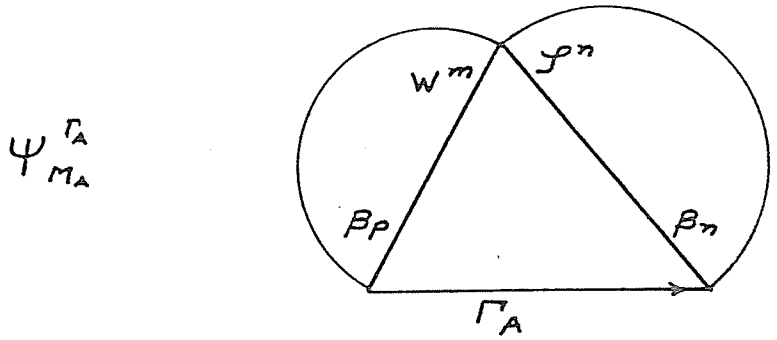

The circular arc indicates that the wave functions has been antisymmetrized in the m protons and separately in the n neutrons. The arrow in Γ_A indicates the order of coupling, i.e.:

$$\bar{\beta}_p + \bar{\beta}_n = \bar{\Gamma}_A$$

Consider a simple transition involving pickup of a proton from shell w and pickup of two neutrons from the ρ shell coupled to angular momentum J'. Such a transition would be represented by:

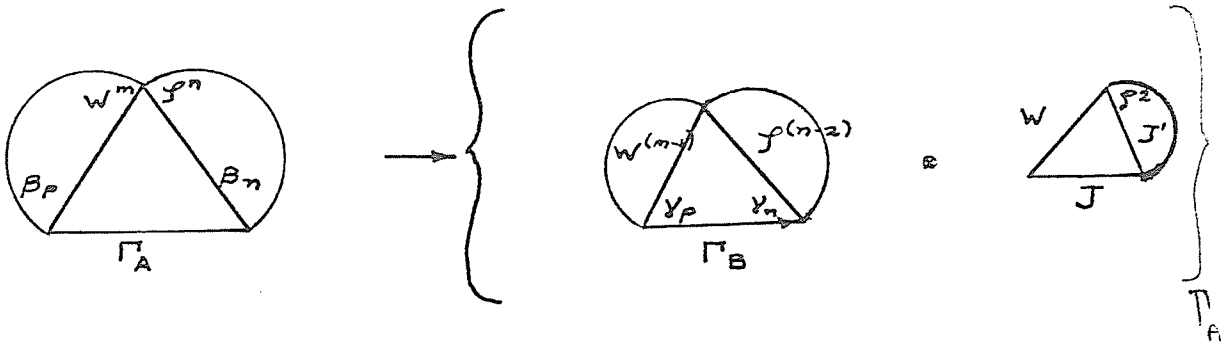

where $\otimes$ indicates vector coupling to a resultant Γ_A. γ_p and γ_n are the angular momenta of protons and neutrons in the residual nucleus, respectively. J is the total angular momentum of the transferred group, and Γ_B the residual nucleus angular momentum.

The expansion coefficients $I_{AB}(\gamma,J',J)$ are represented by the overlap integral symbolized by:

$I_{AB} =$ 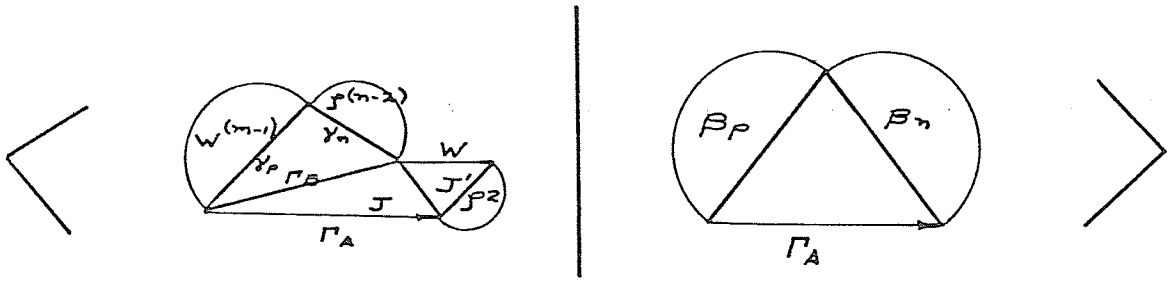

(2.5)

To evaluate the right-hand side, fractional parentage expansions are made as follows:

Consider first a proton removed from the w shell:

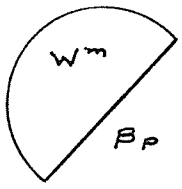

$= \sum^{v'\gamma_p'} < w^m(\alpha\beta_p) \{| w^{m-1}(v'\gamma_p'); W > .$

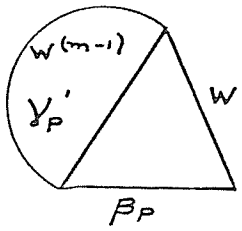

(2.6)

where $< \{| >$ is one-particle coefficient of fractional parentage (cfp).[38]

u and v' are additional quantum numbers required to completely specify a state (usually seniority).

Now, consider the neutron shell. For two neutrons picked up from the ρ shell coupled to angular momentum J' we can write:

$$\left(\rho^n\right)_{\beta_n} = \sum^{\gamma_n' y'} \langle \rho^n (x\, \beta_n) \{ | \rho^{n-2} (y'\, \gamma_n') ; J' \rangle \quad .$$

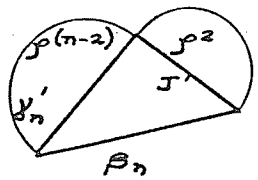

(2.7)

Here $\langle \{ | \rangle$ is a two-particle cfp.

Again x and y' are two additional quantum numbers required to completely specify the state.

Also we can write:

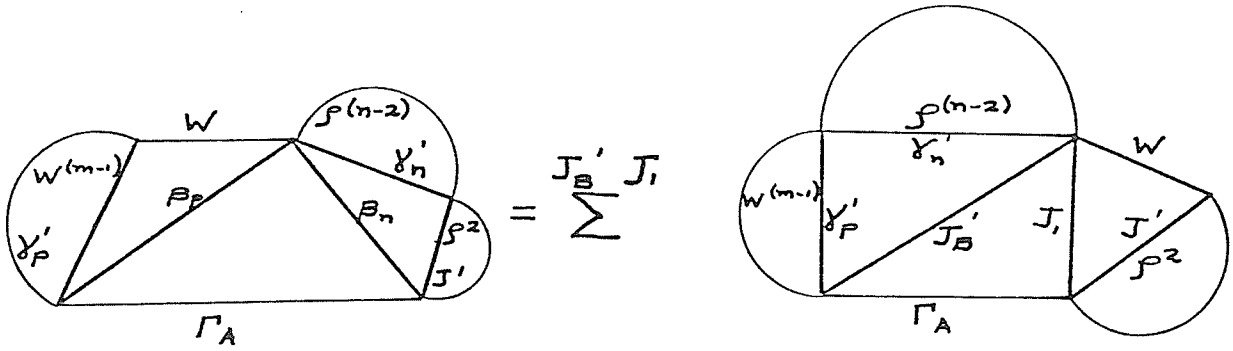

$$\begin{bmatrix} \gamma_\rho' & \gamma_n' & J_B' \\ W & J' & J_1 \\ \beta_\rho & \beta_n & \Gamma_A \end{bmatrix} \qquad (2.8)$$

where [ ] is the normalized 9-j symbol.

Combining the above result together with Equs. (2.6) and (2.7), the overlap integral I_{AB} in Equ. (2.5) will be given by:

$$I_{AB} = \sum_{\upsilon'\gamma_p'}^{} < w^m (u\ \beta_p) \{| w^{(m-1)} (\upsilon'\gamma_p'); w > .$$

$$\sum_{y'\gamma_n'}^{} < \rho^n (\chi\ \beta_n) \{| \rho^{(n-2)} (y'\gamma_n'); \rho^2(J') > .$$

$$\sum_{J_B'J_1} \begin{vmatrix} \gamma p' & \gamma n' & J_B' \\ w & J' & J_1 \\ \beta_p & \beta_n & \Gamma_A \end{vmatrix} .$$

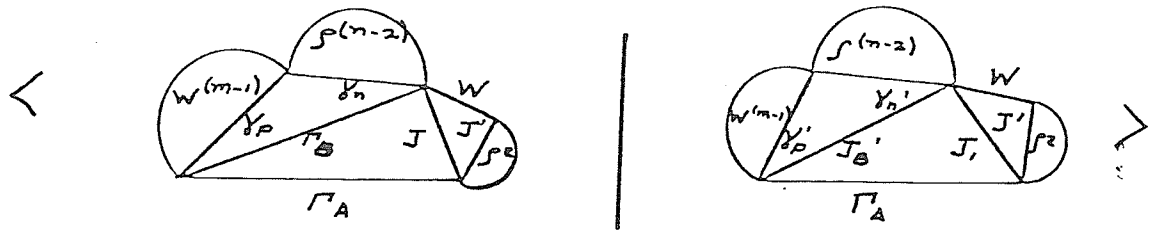

(2.9)

The spectroscopic amplitude in this case is related to I_{AB} as follows:

$$S_{AB}^{1/2} (w\ \rho^2\ J'\ J) = \binom{m}{1}^{1/2} \binom{n}{2}^{1/2} I_{AB} \qquad (2.10)$$

From Equs. (2.9) and (2.10), the spectroscopic amplitude for a given transition will be given by:

$$S_{AB}^{1/2} (w\ \rho^2\ J',\ J) = \binom{m}{1}^{1/2} \binom{n}{2}^{1/2} < w^m (u\ \beta_p) \{| w^{(m-1)} (\upsilon\ \gamma_p)\ ;\ w >$$

$$< \rho^n (\chi\ \beta_n) \{| \rho^{(n-2)} (y\ \gamma_n)\ ;\ \rho^2\ (J') >$$

$$\begin{bmatrix} \gamma_p & \gamma_n & \Gamma_B \\ w & J' & J \\ \beta_p & \beta_n & \Gamma_A \end{bmatrix} \qquad (2.11)$$

Equ. (2.11) gives the spectroscopic amplitude for a transition which involves picking up three nucleons from the outermost neutron and proton shells, all the other shells being closed. In the case of two or more active shells, spectroscopic amplitudes can be derived following the same method illustrated above. A numerical example for a sample transition is given in Appendix B to illustrate the work involved in calculating each amplitude.

Superposition of basic states

So far, spectroscopic amplitudes have been evaluated assuming pure (basic) shell model configurations for the nuclear wave functions. For the cases where the wave functions are linear combinations of basic states the above results can be easily generalized.

Let the target A wave function be

$$\psi^{J_A}_{A\,M_A} = \sum_p A_p \, \psi^{J_A}_{p\,M_A} \tag{2.12}$$

and that of the residual nucleus B be

$$\psi^{J_B}_{B\,M_B} = \sum_q B_q \, \psi^{J_B}_{q\,M_B} \tag{2.13}$$

where the wave functions ψ_p and ψ_q form some basic set, and A_p and B_q are coefficients determined from shell model calculations. Then $S^{1/2}_{AB}$ must be replaced by

$$\sum_{pq} A_p \, B_q \, S^{1/2}_{pq} \, (\gamma, J', J) \tag{2.14}$$

and Equ. (2.3) can be written as:

$$\langle B \alpha | V | A p \rangle \propto \sum_{L J M_B M \lambda \mu_t} (J_B M_B J M | J_A M_A) \cdot (L \lambda \tfrac{1}{2} \mu_t | J M)(\tfrac{1}{2} \mu_t \tfrac{1}{2} \mu_p | 0 0) \cdot \sum_{\gamma J'} \sum_{pq} I_{pq}(\gamma, J', J) \cdot A_p \cdot B_q \cdot \begin{bmatrix} \ell_1 & \ell_2 & J' \\ \tfrac{1}{2} & \tfrac{1}{2} & 0 \\ j_1 & j_2 & J' \end{bmatrix} \begin{bmatrix} J' & \ell_3 & L \\ 0 & \tfrac{1}{2} & \tfrac{1}{2} \\ J & j_3 & J \end{bmatrix} \cdot F^{\gamma}_{J'L}(\rho, R)\, Y_L^{\lambda}(\hat{R}) \qquad (2.15)$$

It is important to note that the signs of A_p and B_q and $S^{1/2}_{pq}$ are dependent upon the choice of the signs for the fractional parentage coefficients used in their calculation. Hence consistency of sign convention is of prime concern in the use of the above in calculations. In addition, the nuclear structure calculations of A_p and B_q involve other conventions as well. These are discussed in section (2.3).

Zero Range Approximation

Finite range effectshave been studied for the (p,α) reaction (e.g. see Ref. 39, 4) and it was concluded that such effects are not very important. On this basis and due to the fact that the DWBA finite range code available[40] does not allow a spin-orbit potential in the distorted waves the analysis in the present work will be limited to the zero range calculations. The zero range microscopic form factor is given by Equ. (2.4) with $I_{nn'}$, evaluated using a delta function interaction, is a func. of ν and ν_α only.

2.3 Implementation of Formalism

The DWBA code DWUCK 2[36] has been modified to calculate angular distributions using the nuclear matrix element given by Equation (2.15). The 3 Clebsch Gordon coefficients appearing in this equation are already included in the DWBA code in a standard calculation of cluster transfer. Hence, only summation over the terms γ, J', P, q need to be implemented.

The expansion coefficients $I_{pq}(\gamma,J',J)$, calculated separately as illustrated in Appendix B for each γ, J' and J, are fed, together with the wave function's amplitudes A_p and B_q, as input to the code DWUCK 2. The microscopic form factor $F^{\gamma}_{J'L}(\rho,R)$ is calculated for each γ, J' and L according to Equ. (2.4) using the computer code FF3FR[41]. The normalized 9-j symbols are calculated externally too, then fed as input together with the form factor into the DWBA code.

The single particle states are generated in a Woods-Saxon potential and then expanded in a harmonic oscillator (H.O.) series using the computer code of Nelson-Macefield[42]. The H.O. expansion coefficients a_{pi} are fed into FF3FR as input. The choice of Woods-Saxon parameters and binding energies used will be described in the following section.

The angular distributions calculated by the modified DWUCK as described above using the microscopic form factor and the nuclear structure information, should differ from the experimentally measured cross sections only by a normalization factor. This normalization factor should be the same for all states. In other words, the ratio $\sigma_{exp}/\sigma_{theory}$ should be consistent for all states under investigation. This will represent a severe test for all wave functions calculated in the framework of the shell model for both the target and the residual nuclei.

Sign Conventions

As mentioned in the last section, for calculations that involve wave functions which are superposition of basic states it is important that the same sign conventions be used throughout for the cfp's involved. Thus, the sign choices used in the shell-model wave function calculations should be known. In other words, the same cfp's should be used in calculating the expansion coefficients in order to be able to use the wave function amplitudes directly.

Furthermore, some other sign choices were made in evaluating the microscopic formalism implemented above. These choices are summarized below and they should be consistent with the DWBA code and the shell model calculations.

1. The order of coupling is given by $\bar{\ell} + \bar{s} = \bar{j}$.

2. The sign of the radial wave function is positive as $r \to o$.

The sign conventions of Kutschera wave functions are the same as those mentioned above.

2.4 Discussion of the microscopic form factor

The microscopic form factor given by Equ. (2.4) has been calculated using single particle wave functions generated in a Woods-Saxon well, and then expanded in a harmonic oscillator series. This procedure has been used by Falk[10],[19],[18] in studying the reactions $^{12}C(\alpha,p)^{15}N$, $^{40,42}Ca(p,\alpha)^{37,39}K$ and $^{130}Te(p,\alpha)^{127}Sb$. Only components in the target wave functions where the protons and the neutrons were each coupled to zero were considered. A reasonable agreement between theory and experiment was obtained for most states.

Fig. (2.2) shows a plot of this microscopic form factor for the reaction $^{46}Ti(p,\alpha)^{43}Sc$ for a representative state L=3, $J^{\pi} = 7/2^-$. The single-particle states required for the generation of the form factor were calculated in a Woods-Saxon potential well with parameters[44] shown in table (2.1). The triton experimental binding energy of 22.89 Mev was divided among the three transferred nucleons in proportion to the actual separation energies of both proton and neutron from the target. The binding energies (B.E.) used are shown in table (2.2). The same values of B.E. of the nucleons were used for other excited states since in all cases the form factor tail was replaced by a cluster tail.

The expansion of the single-particle states in harmonic-oscillator functions was limited to 3 terms only because of the greatly increased computational time involved as the number of terms in the expansion was increased (see Equ. 2.10 of Appendix A). The computer code of Nelson-Macefield[41] was used to perform the above expansion. The harmonic-oscillator expansion coefficients together with the overlap of this expansion with the single-particle wave functions are given in table (2.2). The shell model oscillator parameter was calculated from the formula[43]:

$$\nu = 0.02411 \left(\frac{45}{A^{1/3}} - \frac{25}{A^{2/3}} \right) \qquad (2.16)$$

Also shown in Fig. (2.2) is a plot of the cluster form factor for the same transition. The cluster wave function was calculated with parameters r = 1.17 fm and a_o = 0.65 fm.

The triton cluster was assumed to be bound by its experimental separation energy. The MFF differs considerably from the CFF in the nuclear

Fig. (2.2) Comparison between MFF and CFF for L=3

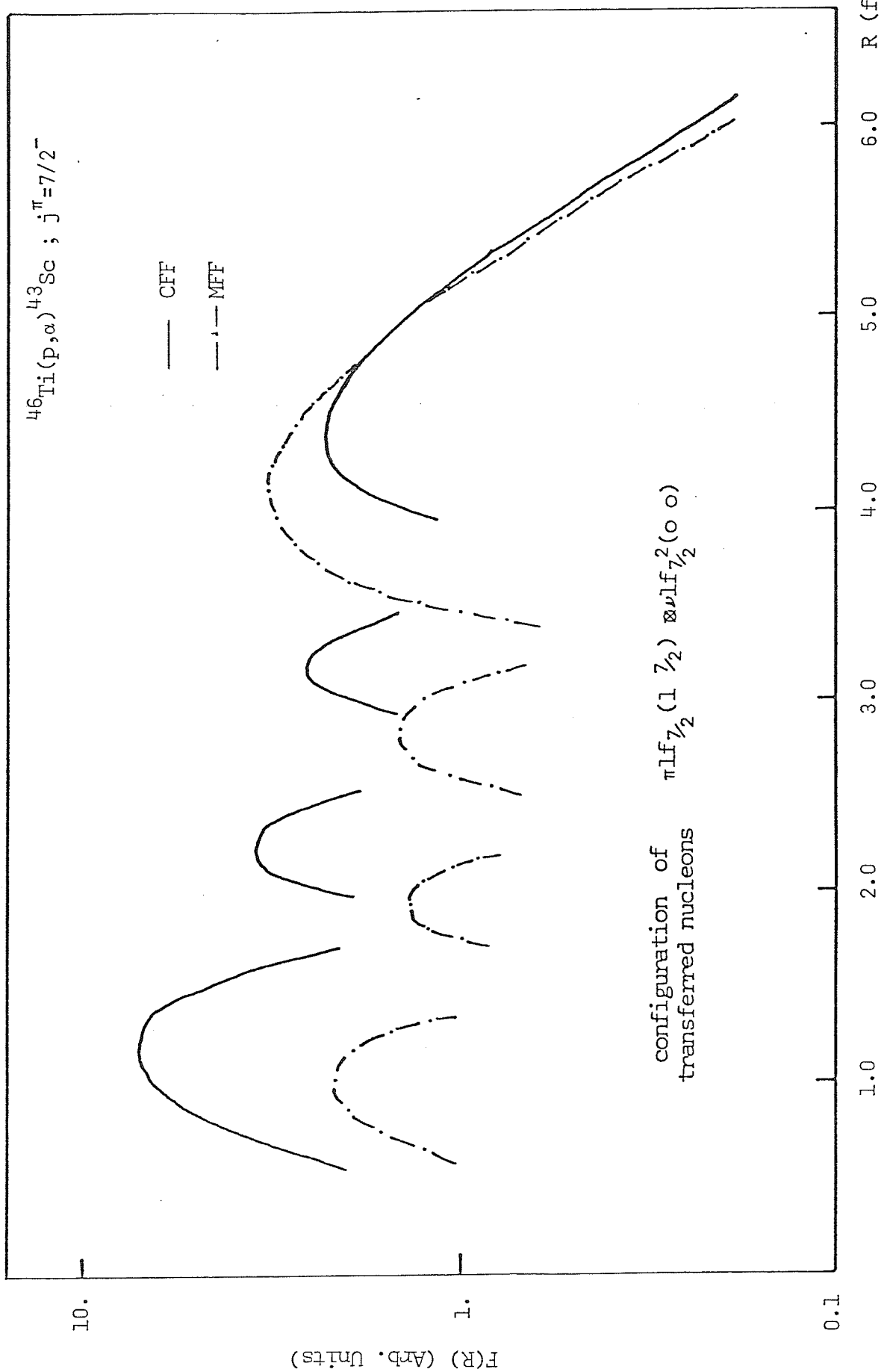
$^{46}Ti(p,\alpha)^{43}Sc$; $j^{\pi}=7/2^-$
CFF
MFF
configuration of transferred nucleons
$\pi lf_{7/2}(1\ 7/2)\ \otimes\nu lf_{7/2}^2(o\ o)$
F(R) (Arb. Units)
10.
1.
0.1
1.0
2.0
3.0
4.0
5.0
6.0
R (fm)

Table (2.1) Optical-Model parameters used in the calculations of the single-particle states

V (Mev)	r (fm)	a (fm)	$V_{s.o.}$ Mev	$r_{s.o.}$ (fm)	$a_{s.o.}$ (fm)	Rc (fm)
Varied	1.25	0.62	6.42	1.25	0.62	1.25

Table (2.2) Calculated single-particle binding energies and wave-function expansions in harmonic-oscillator functions

Single-particle state	Binding Energy (Mev)	H.O. Expansion(1) a_o	a_1	a_2	Overlap(2)
$1f_{7/2}$ neutron $(\nu f_{7/2})$	8.22	.9952	.0734	.0441	.9998
$1f_{7/2}$ proton $(\pi f_{7/2})$	6.45	.9906	.122	.0416	.9990

(1) $\nu_{S.P.} = .248\ fm^{-2}$

(2) Overlap = $\int u_\ell(r) \sum_p a_p H_{p\ell} (\nu r^2) dr$ = overlap of the expansion on the original wave function.

interior. The MFF falls rapidly compared to the CFF. This is due to the truncation in the number of terms in the harmonic-oscillator expansion. In order to correct this behaviour we replaced the MFF in the asymptotic region by the CFF wave function. The point of matching is taken at the radius where the logarithmic derivatives of the two functions are equal.

The MFF calculated as described above may actually be of a limited usefullness towards establishing the (p,α) reaction as a useful spectroscopic tool. The reason for this is that with such a complicated dependence of the form factor on the detailed structure of each state, one needs to know the wave functions in all their detail. Moreover, the single-particles states have to be calculated for each transition to reflect the appropriate triton separation energy, and then expanded in an H.O. series. The latter involves a great deal of effort.

A simplification to this procedure results if the single-particle states are taken to be oscillator functions. The obvious deficiency of the resulting form factor in the nuclear surface region must be corrected by attaching the CFF tail. All other details of the nuclear structure are incorporated as before. In other words, all possible configurations γ and values of J' leading to a particular J value will be considered.

Fig. (2.3) shows a comparison between the MFF calculated with 3 terms in the H.O. expansion with that calculated using the dominant term only. As may be noticed, both form factors are similar in the nuclear interior but, not unexpectedly, differ considerably in the asymptotic region. This is expected to have a minimal effect on the calculated cross sections since a CFF tail will be matched in the exterior

Fig. (2.3) Comparison between CFF and MFF with different number of terms in the H.O. expansion

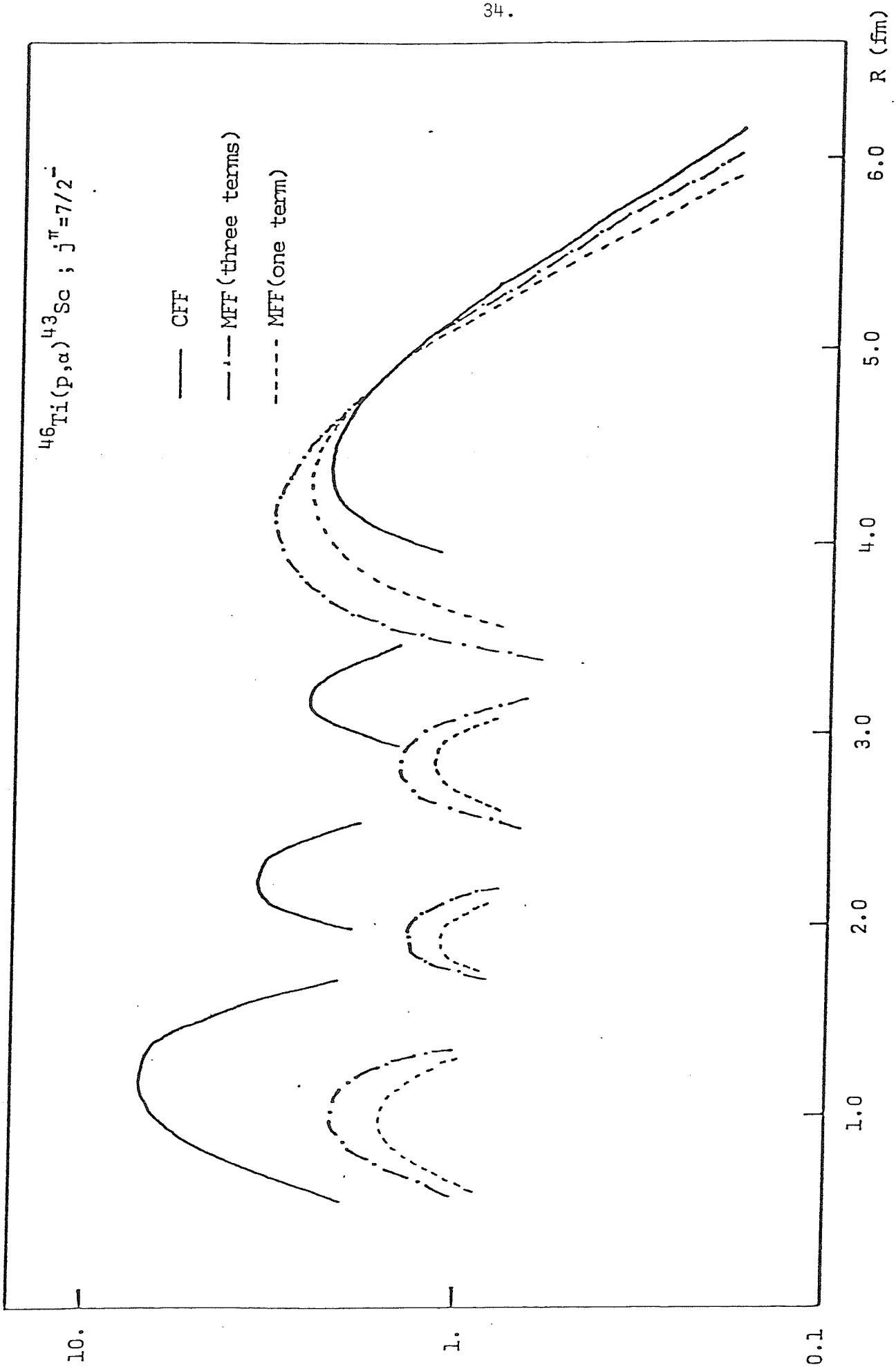
$^{46}Ti(p,\alpha)^{43}Sc$; $j^{\pi}=7/2^-$
CFF
MFF (three terms)
MFF (one term)
F(R) (Arb. Units)
10.
1.
0.1
1.0
2.0
3.0
4.0
5.0
6.0
R (fm)

region in all cases.

The angular distributions calculated using these three form factors are shown in Fig. (2.4). Table (2.3) shows the relative DWBA cross sections calculated with the two MFF. Each microscopic form factor had a cluster tail attached to it. Both MFF were normalized as shown in table (2.3). As may be noticed, all values are consistent with each other within $\sim$ 20%. Further, a comparison between the relative magnitude squared of both microscopic form factors at the outer maxima is shown in Table (2.4). With the exception of the $\frac{1}{2}^+$ state, one expects the error introduced into the ratio σ_{exp}/σ_{th} due to using only a single H.O. term will be about 24%. The error in the $\frac{1}{2}^+$ state will be larger (a factor of $\sim$ 2).

Fig. (2.5) shows another comparison of the MFF for L=4, $J^\pi=\frac{7}{2}^+$ for both cases where one and 3 terms in the H.O. expansion were considered. Fig. (2.6) shows the corresponding angular distributions. Once more the main differences between the two form factors are evident in the asymptotic region where the one-term F.F. tends to fall faster than the three-terms F.F. However, the process of matching the tail with a Woods-Saxon wave function will eliminate much of the error introduced by the truncation process.

Finally, it should be noted that a further consequence of using only the dominant term in the harmonic oscillator expansion (i.e. assuming oscillator functions for the single particle states), is that the form factor shape generated this way depends only on the shells involved but not on the coupling J' of the two neutrons. In other words, the form factor for the transferred configurations $\left|(\pi f_{7/2}) \otimes (\nu f_{7/2})^2_0\right|_{7/2}$ has the

Fig. (2.4) Comparison of angular distributions calculated with different number of terms in the H.O. expansion

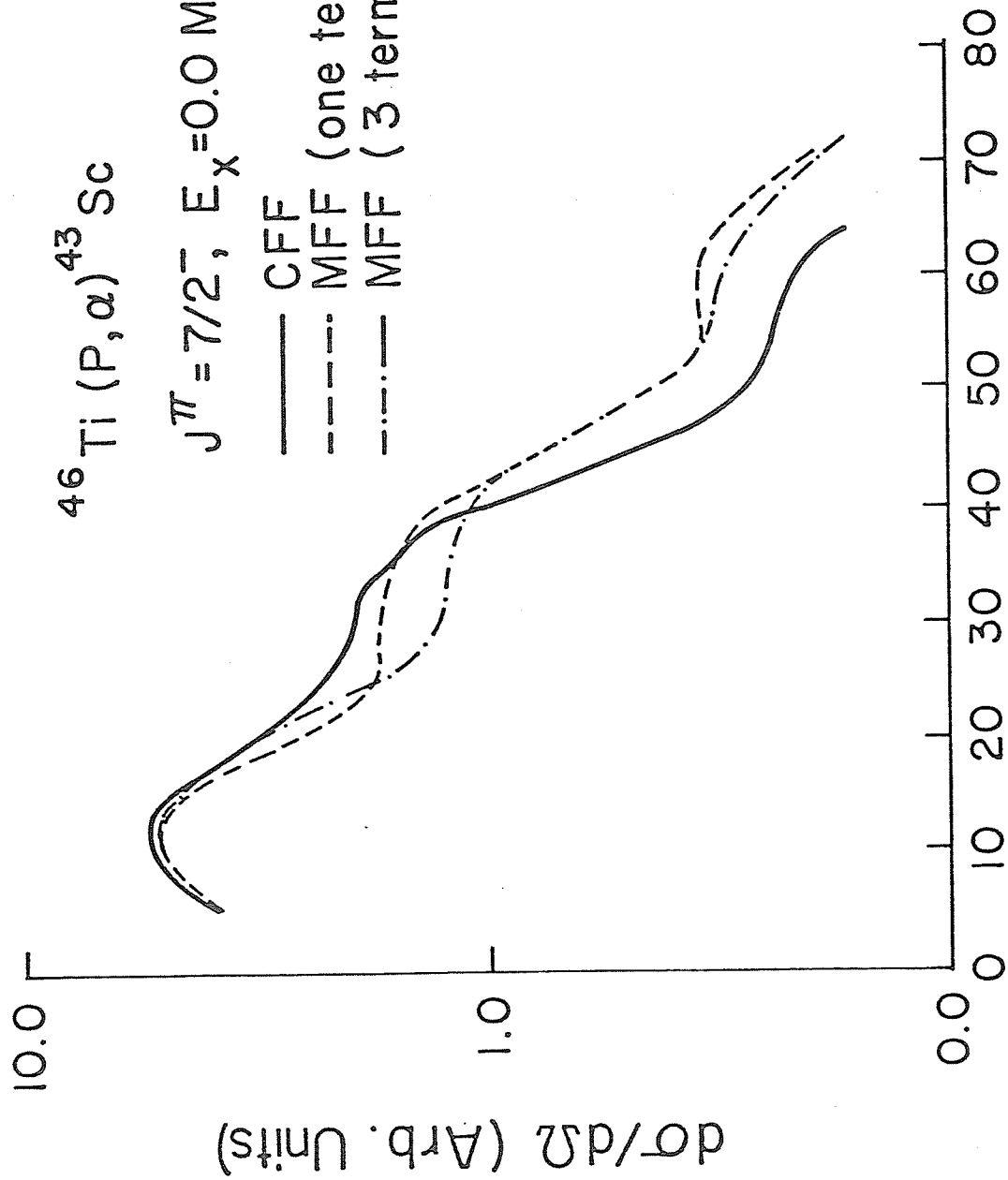
^{46}Ti (P,α)^{43}Sc
$J^{\pi}=7/2^-$, E_x=0.0 MeV
CFF
MFF (one term)
MFF (3 terms)
dσ/dΩ (Arb. Units)
10.0
1.0
0.0
0
10
20
30
40
50
60
70
80
θcm (degrees)

Table (2.3) Comparison between relative DWBA cross sections calculated using different form factors for the reaction $^{46}Ti(p,\alpha)^{43}Sc$

$\frac{\sigma(\text{one term})}{\sigma(\text{full expansion})}$	$J^\pi=1\frac{+}{2}(18°)$	$J^\pi=3\frac{+}{2}(24°)$	$J^\pi=7\frac{-}{2}(32°)$	$J^\pi=7\frac{+}{2}(22°)$
(a)	1.1	1.2	0.85	1.2
(b)	1.8	5.1	4.2	4.1

(a) Both F.F.'s are normalized to unity

(b) Using the normalization of the F.F.'s given by the computer code FF3FR.

Table (2.4) Comparison between the relative magnitudes squared of MFF at the outer maxima

Form Factor	$1\frac{+}{2}$	$3\frac{+}{2}$	$7\frac{+}{2}$	$7\frac{-}{2}$	$11\frac{-}{2}$
MFF (full expansion)	1.0	1.0	1.0	1.0	1.0
MFF (one term only)	1.4	3.3	2.8	3.2	3.0

Fig (2.5) Comparison between MFF and CFF for L=4. The configuration of the transferred nucleons is :

$\pi 1d_{3/2}\,(1\ 3/2) \otimes \nu 1f_{7/2}\,(2\ 2)$

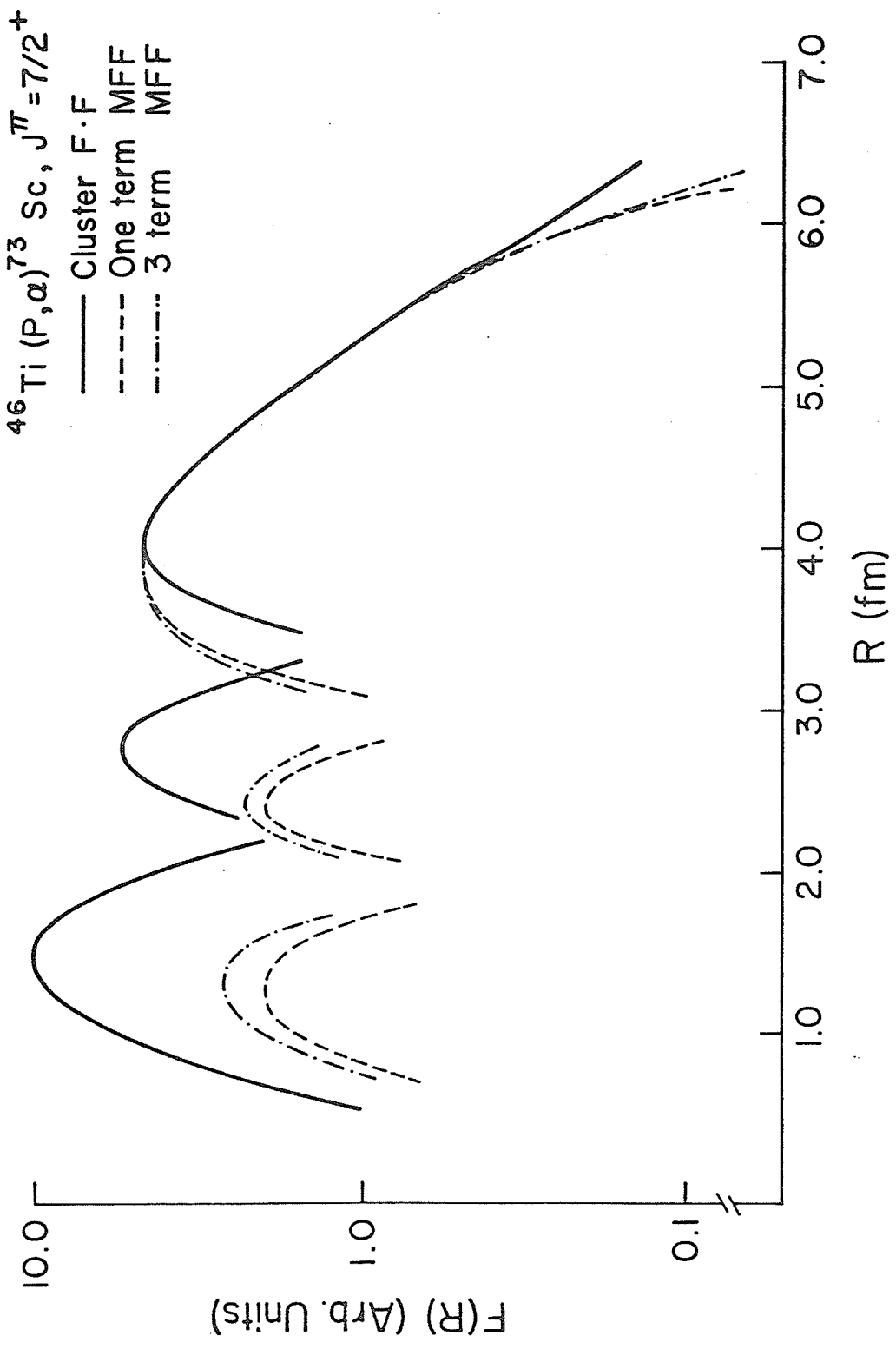
^{46}Ti (P,α)^{73} Sc, $J^{\pi}=7/2^{+}$
Cluster F·F
One term MFF
3 term MFF
10.0
1.0
0.1
F(R) (Arb. Units)
1.0
2.0
3.0
4.0
5.0
6.0
7.0
R (fm)

Fig. (2.6) Angular distributions for $J^{\pi} = 7/2^{+}$ using MFF with different number of terms in the H.O. expansion

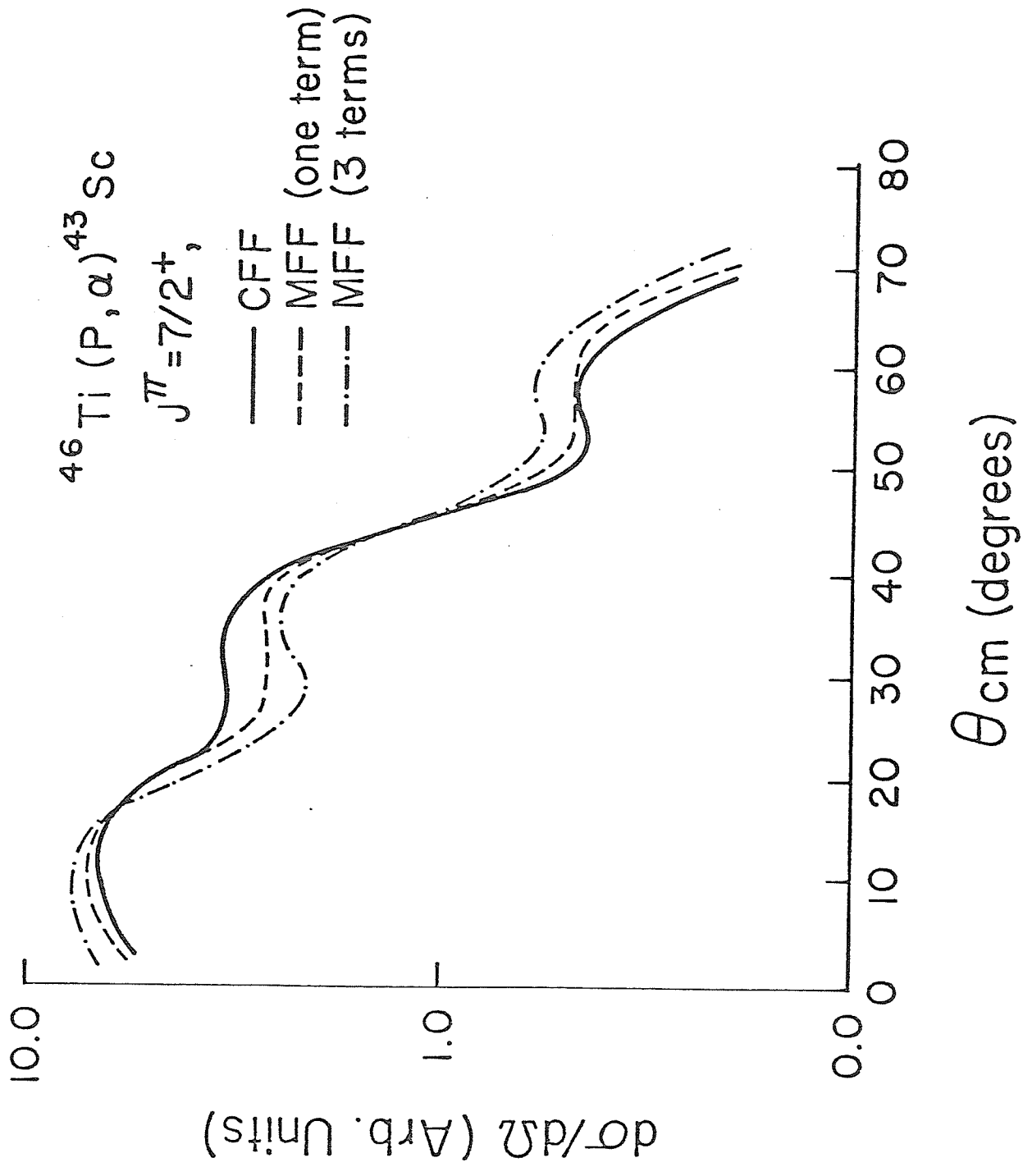

same shape as the form factor for the configuration $\left|(\pi f_{7/2}) \otimes (\nu f_{7/2})^2_2\right|_{7/2}$. The only difference is in the magnitude, and this will appear as an overall normalization factor dependent on J'. This empirical result has the advantage of allowing us to write the form factor as a part dependent on the configuration γ and the transferred angular momentum L, and a part (normalization factor) dependent on the intermediate coupling J'. Hence we can write:

$$F^{\gamma}_{J'L}(R) = N^{\gamma}_{J'} \; F^{\gamma}_{L}(R)$$

In this way only one form factor shape is required for the DWBA calculation for each transition. A tabulation of $N^{\gamma}_{J'}$ values can be prepared and used.

Chapter 3

Experimental Procedure

3.1 Cyclotron and External Beam Facility

The high resolution beam line shown in Fig. (3.1) together with the 56 cm scattering chamber was used in these experiments. The proton beam used was produced by the University of Manitoba 42" sector focussed cyclotron[45]. The axial injection system injects a beam of negative hydrogen ions vertically into the centre of the cyclotron at 11 Kev[46]. The ions are deflected into the median plane by an electrostatic mirror and accelerated by a 28 keV RF voltage. Extraction is achieved by stripping the two electrons from the negative hydrogen ion using a thin aluminum foil causing the magnetic force to reverse and sweep the beam out of the cyclotron field.

The high resolution beam analysis system was built on the 15° right beam line. For economic reasons, space limitations, and the requirement to handle a beam with large emittance, the system was chosen to consist of two 90° single focussing analyzing magnets of 30 inches bending radius. The two magnets bend in opposite directions to each other, in a manner makes the dispersions additive[47]. The system accepts as input a beam of horizontal emittance as high as 15 mm·mrad and provides at target position a beam of intensity 1% that of the intensity on slits S1 shown in Fig. (3.1), and a final intrinsic energy resolution $\Delta E/E = 5 \times 10^{-4}$[48].

3.2 Scattering Chamber

The 56 cm scattering chamber of the high resolution beam line has

Fig. (3.1) High Resolution beam line

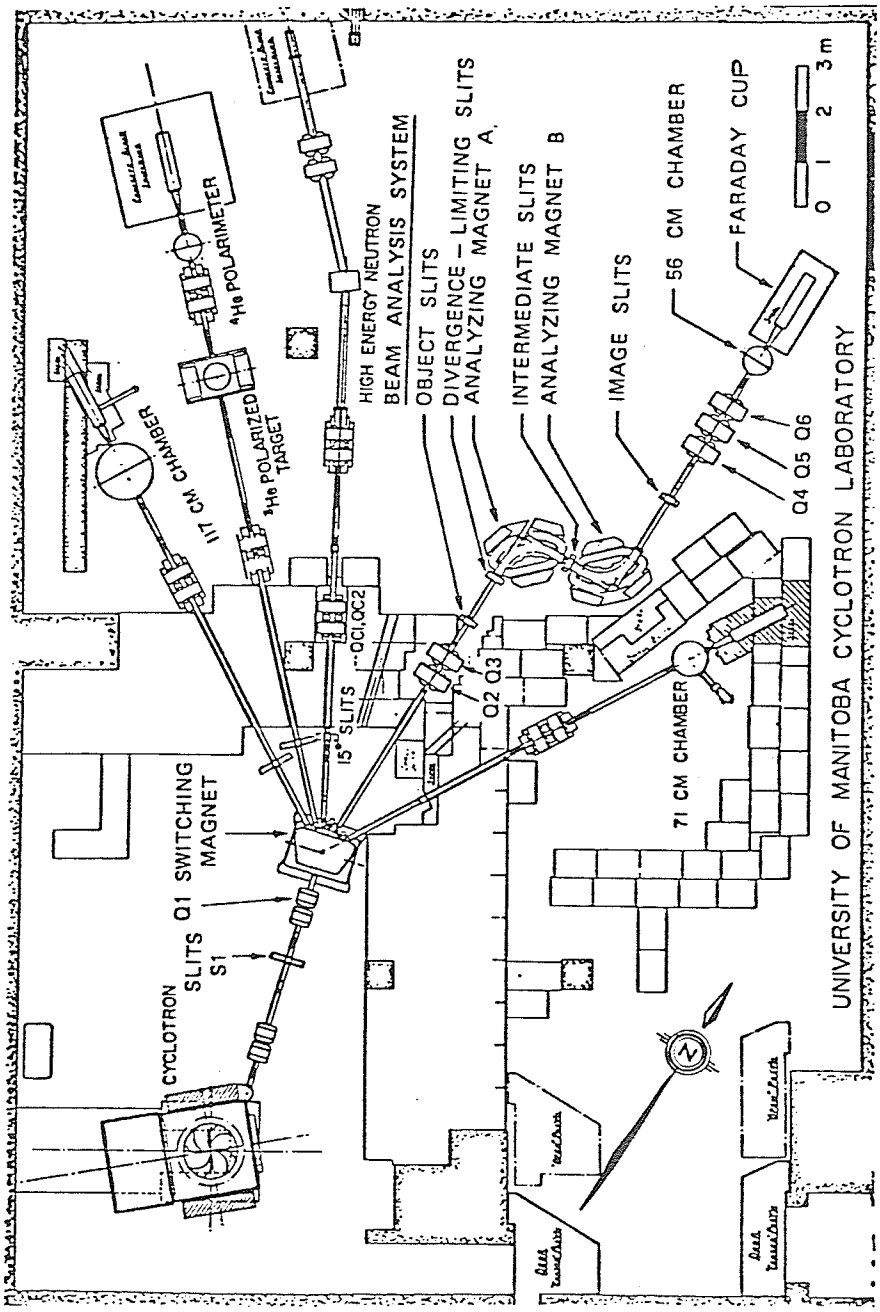
CYCLOTRON
SLITS S1
Q1 SWITCHING MAGNET
15° SLITS
QC1, QC2
Q2 Q3
71 CM CHAMBER
117 CM CHAMBER
^{3}He POLARIZED TARGET
^{4}He POLARIMETER
HIGH ENERGY NEUTRON
BEAM ANALYSIS SYSTEM
OBJECT SLITS
DIVERGENCE – LIMITING SLITS
ANALYZING MAGNET A
INTERMEDIATE SLITS
ANALYZING MAGNET B
IMAGE SLITS
56 CM CHAMBER
FARADAY CUP
Q4 Q5 Q6
0 1 2 3m
UNIVERSITY OF MANITOBA CYCLOTRON LABORATORY

a single rotating table with milled grooves 10° apart for mounting detectors. There are 12 vacuum sealed connectors for detector connections. The top of the chamber carries a vacuum lock and the target ladder slides through this lock into the chamber. The target ladder can hold up to 3 targets at the same time, although one place is normally occupied by a BeO screen used for viewing the beam. The vacuum was about 4×10^{-6} Torr.

In order to improve energy resolution, the kinematic matching technique prescribed in Ref. (49) was used. For a typical beam with characteristic length[49] of 30 mm/mrad and a focussing point 150 mm beyond the target the detectors should be placed at distances shown in Table (3.1). Also shown in Table (3.1) are the solid angles subtended by each detector. A small solid angle was used for the forward detector in order to reduce pile-up.

3.3 Electronics

In the scattering chamber the α-particles were detected using counters at angular intervals of 10°. The most forward two counters were telescopes consisting of ΔE-E silicon surface barrier detectors while the other counters consisted of single E silicon detectors. The reason for the ΔE-E telescopes was to eliminate protons elastically scattered from target depositing their full energy in the E-detector after being deflected 90° inside the detector. These protons appear as a broad peak at a position close to the α-particle peaks, and thus their presence might complicate the spectrum[17].

The ΔE detectors were 100 μm in thickness, while the E detectors were 1000 μm, which is more than sufficient to stop the $\sim$ 40 Mev α-particle from the (p,α) reactions. The Q-value for the (p,^{3}He) reaction is about 12 Mev more negative, thus ^{3}He spectrum will not complicate α-spectrum.

Table (3.1) Detectors Distances and Solid Angles

Dectector	Distance (cm)	Solid Angle Steradian x 10^{-3}
#1 (most forward)	17.0	0.5226
#2	17.9	0.6428
#3	18.0	0.6688
#4	17.9	0.6907
#5	17.0	0.6078
#6	15.7	0.8582

Fig. (3.2a) shows the electronics diagram used for the ΔE-E telescopes. An ^{241}Am α-source and a research pulser were used for the gain matching process.

Fig. (3.2b) shows the circuit diagram used for the single E counters. Pairs of the single E detectors were routed through separate ADC's.

3.4 Targets and Determination of Absolute Cross Sections

The targets used for the present work were prepared by the target division of the Chalk River Nuclear Laboratories. ^{46}Ti and ^{50}Ti targets were prepared by rolling Ti isotopes down to a thickness of 333 μg/cm^2 and 269 μg/cm^2, respectively. The ^{48}Ti target was prepared by reducing and evaporating TiO as a self-supporting ^{48}Ti target of thickness 60 μg/cm^2. The isotopic composition of these targets is shown in Table (3.2a).

The target thicknesses were measured initially by the energy loss technique using an ^{241}Am α-source. Another measurement was performed using a proton monitor fixed at an angle of 20°. The proton optical model parameters given in Ref. (44) were used to calculate proton elastic cross section. Thus, the target thickness can be calculated. The uncertainty in target thickness measured by this method is mainly due to angular uncertainty of 0.2°. Table (3.2b) shows the results of both measurements. The adopted values for target thicknesses were taken to be the weighted average.

The absolute cross section scale is accurate within ∿ 8%.

Proton monitor measurements at a fixed scattering angle of 20° were taken at all times during the (p,α) runs in order to detect any change in

Fig. (3.2) Electronics diagram

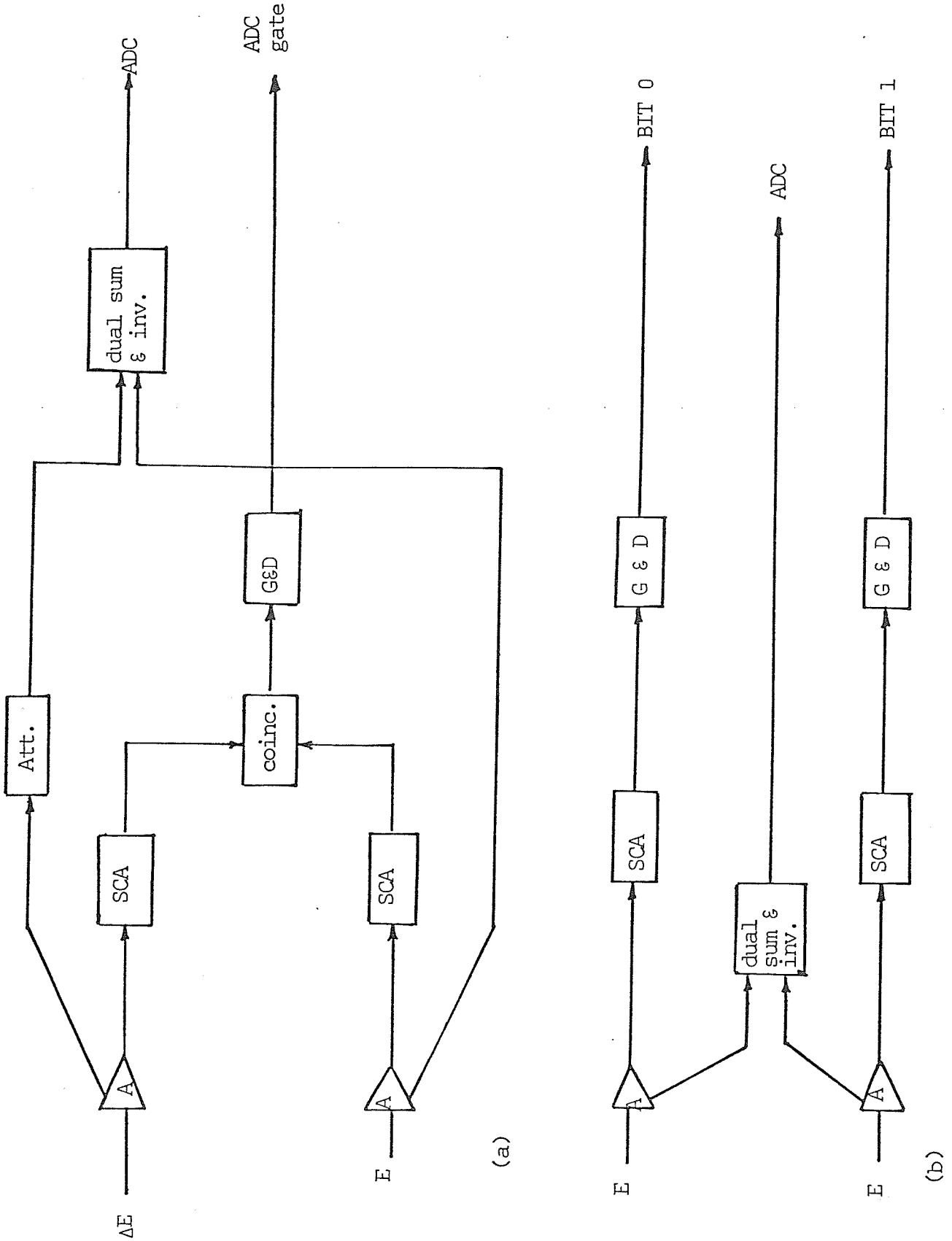
ADC
ADC gate
dual sum & inv.
G&D
Att.
coinc.
SCA
SCA
A
A
ΔE
E
(a)
BIT 0
ADC
BIT 1
G & D
G & D
SCA
SCA
dual sum & inv.
A
A
E
E
(b)

Table (3.2)a Isotopic Composition of $^{46,48,50}Ti$ Targets(*)

Target	^{46}Ti	^{47}Ti	^{48}Ti	^{49}Ti	^{50}Ti
^{46}Ti	81.2%	2.1%	14.1%	1.5%	1.1%
^{48}Ti	.25%	.26%	99.13%	0.19%	.17%
^{50}Ti	2.0%	1.8%	17.8%	2.0%	76.4%

(*)As per supplier's analysis.

Table (3.2)b Targets Thickness Measurements Results

Target	Energy loss method $\mu g/cm^2$	Proton elastic scattering $\mu g/cm^2$	Adopted value $\mu g/cm^2$
^{46}Ti	335 ± 10	327 ± 20	333 ± 9
^{48}Ti	61 ± 6	58 ± 6	60 ± 4
^{50}Ti	270 ± 9	267 ± 16	269 ± 8

beam position on target.

3.5 Data Reduction and Analysis

The on-line PDP15/20 computer was used for data acquisition. Spectrum analysis and fitting were done using the computer code Autofit[50] on the IBM 370/168 computer. However, preparing the input data required by Autofit - initial peak guesses, reference peak,... - was done on the off-line cyclotron PDP 15/40 computer. The quality of the fits produced by Autofit is shown by a sample spectrum in Fig. (3.3).

An energy calibration for each detector was made by performing a linear least-squares fit. The states used were the g.s., $\frac{1}{2}^+$, $\frac{3}{2}^+$ from the (p,α) spectrum and the g.s. from the (p,^{3}He) spectrum. Channel zero represented E=o. The excitation energy of each peak was determined by averaging the values obtained from at least four different scattering angles. Only peaks whose calculated excitation energies were consistent within 15 kev over the whole angular range were considered here.

The uncertainties in the excitation energies reported in the present work vary between 10-15 kev. The excitation energies obtained here will be used to identify all states throughout the present work.

3.6 Optical Model Parameters

The optical model potential used is given by the expression:

$$V = V_c(r_c) - Vf\,(r_o,r_o) - i\,Wf\,(r_w,a_w) + i\,W_D a_w \frac{d}{dr} f\,(r_w,a_w)$$

$$+ \left(\frac{\hbar}{m_\pi c^2}\right)^2 V_{s.o.} \frac{1}{r}\frac{d}{dr} f(r_{so},a_{so})\;\bar{\ell}\cdot\bar{\sigma} \qquad (3.1)$$

where

Fig. (3.3) Sample spectrum

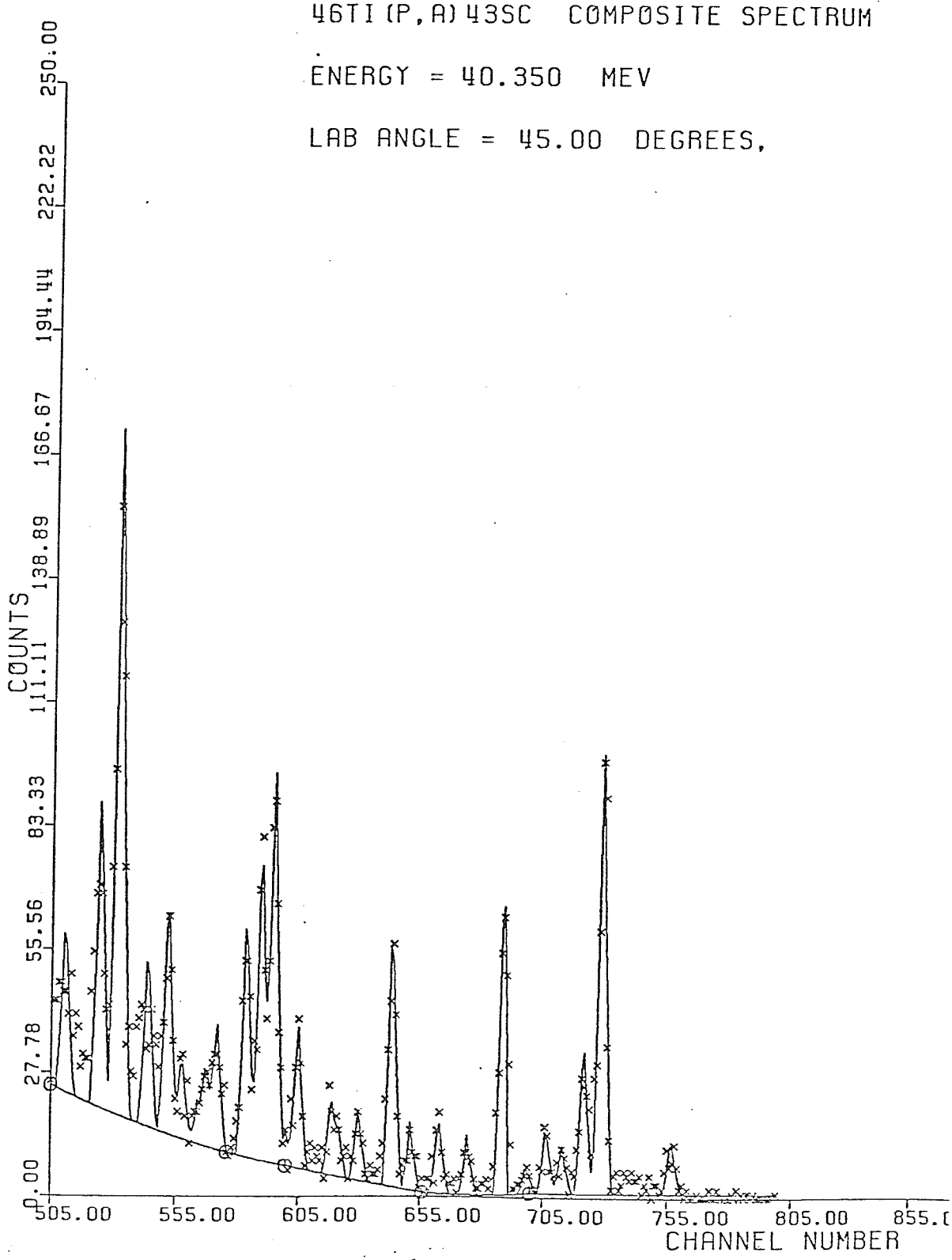
46TI(P,A)43SC COMPOSITE SPECTRUM
ENERGY = 40.350 MEV
LAB ANGLE = 45.00 DEGREES,
COUNTS
0.00
27.78
55.56
83.33
111.11
138.89
166.67
194.44
222.22
250.00
505.00
555.00
605.00
655.00
705.00
755.00
805.00
CHANNEL NUMBER

$$f(r_i,a_i) = \left[1 + \exp\left[(r - r_i A^{1/3})/a_i\right]\right]^{-1} \qquad (3.2)$$

V_c is the columb potential

W and W_D are the volume and surface absorption potentials and $V_{s.o.}$ is the spin-orbit potential.

For the $^{46}Ti(p,\alpha)^{43}Sc$ reaction it was found that the global optical potential parameters for the proton channel of Becchetti and Greenlees[51] gave better fits to the experimental data than the parameters given in the Perey compilation. This is in contrast to the case of ^{48}Ti and ^{50}Ti where the Perey compilation parameters gave better fits. The potential parameters for the α-channels for the three reactions were taken from Ref. (44). The triton cluster was assumed to be bound by its separation energy and the geometrical dimensions of the well were chosen such that the experimental angular distributions are closely reproduced. Details of the optical-model potential parameters are given in Table (3.3).

Fig. (3.4) shows the results of zero-range DWBA calculations for some representative states using the parameters in Table (3.3) in order to show the quality of the fits obtained by these parameters. It should be mentioned here that changing the bound states parameters improves the fits for some states and worsens them for a few others. The final choice of the parameters given here is a result of a compromise reached after fitting and examining a large number of states for many different values of J.

The "well matching" procedure for choosing the optical potentials for poorly L-matched reactions, suggested by Dodd and Greider[52] and

Table (3.3)

Optical Model Parameters used for $^{46,48,50}Ti(p,\alpha)^{43}Sc, ^{45}Sc, ^{47}Sc$ Reactions

	V (Mev)	r (fm)	a (fm)	W (Mev)	W_D (Mev)	r_w (fm)	a_w (fm)	$V_{s.o.}$ (Mev)	$r_{s.o.}$ (fm)	$a_{s.o.}$ (fm)	r_c (fm)
	I. $^{46}Ti(p,\alpha)^{43}Sc$										
P	44.64	1.17	0.75	6.14	9.08	1.35	.54	24.8	1.01	.75	1.25
α	202.2	1.395	.565	26.4		1.395	.565				1.39
t	(1)	1.17	0.75								
	II. $^{48}Ti(p,\alpha)^{45}Sc$, $^{50}Ti(p,\alpha)^{47}Sc$										
P	44.85	1.16	.75	7.82	4.56	1.37	.63	24.16	1.064	.738	1.25
α	The same as in ^{46}Ti										
t	r=1.17, a=0.65 for ^{48}Ti, a=0.75 for ^{50}Ti										

(1) Allowed to vary to reproduce triton separation energy. (∿ 140 Mev).

Fig. (3.4) Angular distributions for representative states in ^{47}Sc. The solid lines represent the result of CFF zero-range DWBA calculations using the optical model parameters given in Table (3.3)

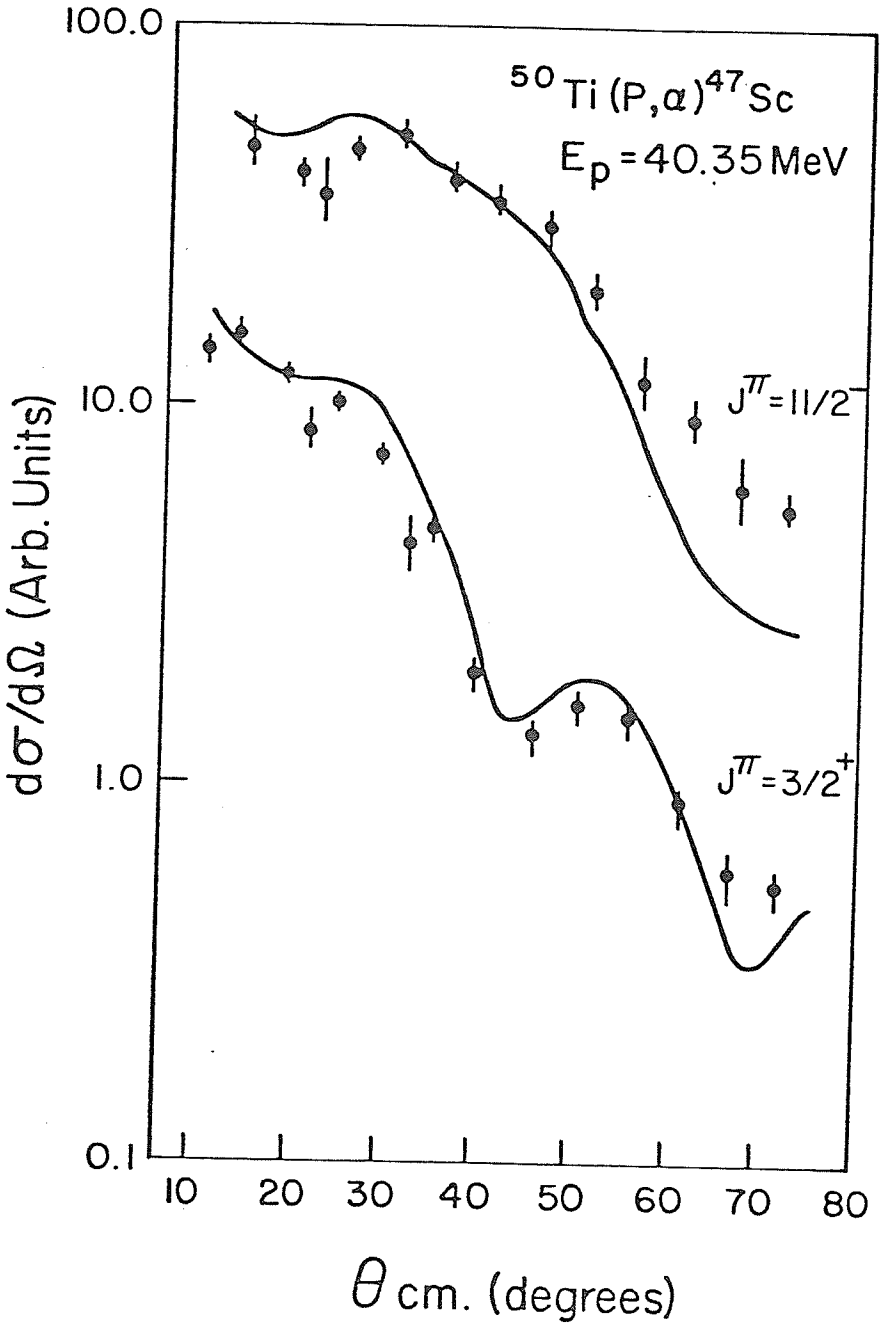
100.0
10.0
1.0
0.1
^{50}Ti (P,α)^{47}Sc
E_p = 40.35 MeV
$J^\pi = 11/2^-$
$J^\pi = 3/2^+$
dσ/dΩ (Arb. Units)
10
20
30
40
50
60
70
80
θ cm. (degrees)

applied successfully to the (d,α) reaction[53] and the (p,α) reaction[20], was tried in the present work. The proton parameters given in Table (3.3) for the ^{48,50}Ti(p,α) reactions were kept fixed. The α-scattering data of Priest[54] were fitted using the code Seek[55] to find another set of optical potential parameters with real radius and diffuseness equal to those of the proton (r = 1.16 and a = .75). The search for the new parameters involved only search for the real potential depth V. It was found that a value of V = 234 Mev was required to reproduce the experimental α-scattering data with a χ^2/N value comparable to that of Priest.

However, as may be noticed from Fig. (3.5), the DWBA fits obtained using the well matching parameters were in general less satisfactory than those obtained previously using Table (3.3). Thus this procedure was not pursued further.

Finally, it should be mentioned that the choice of the optical model potential parameters introduces an uncertainty in the ratio σ_{exp}/σ_{th}. It was found that different optical parameters might produce comparable fits while yielding different relative values of σ_{theory} for different J values. It is estimated that the uncertainty in σ_{exp}/σ_{th} is about 10% for L values of 3-7. This uncertainty increases to about 15% for $J = \frac{1}{2}$ mainly because of the oscillatory character of the angular distribution for this J value.

Fig. (3.6) shows angular distributions for a large range of J^π values. These distributions were calculated using the optical model parameters given in Table (3.3). These distributions will serve the purpose of being a "yard stick" for J^π assignment in chapter 5. The

Fig. (3.5) Comparison between DWBA fits using Perey parameters and "well matching" parameters.

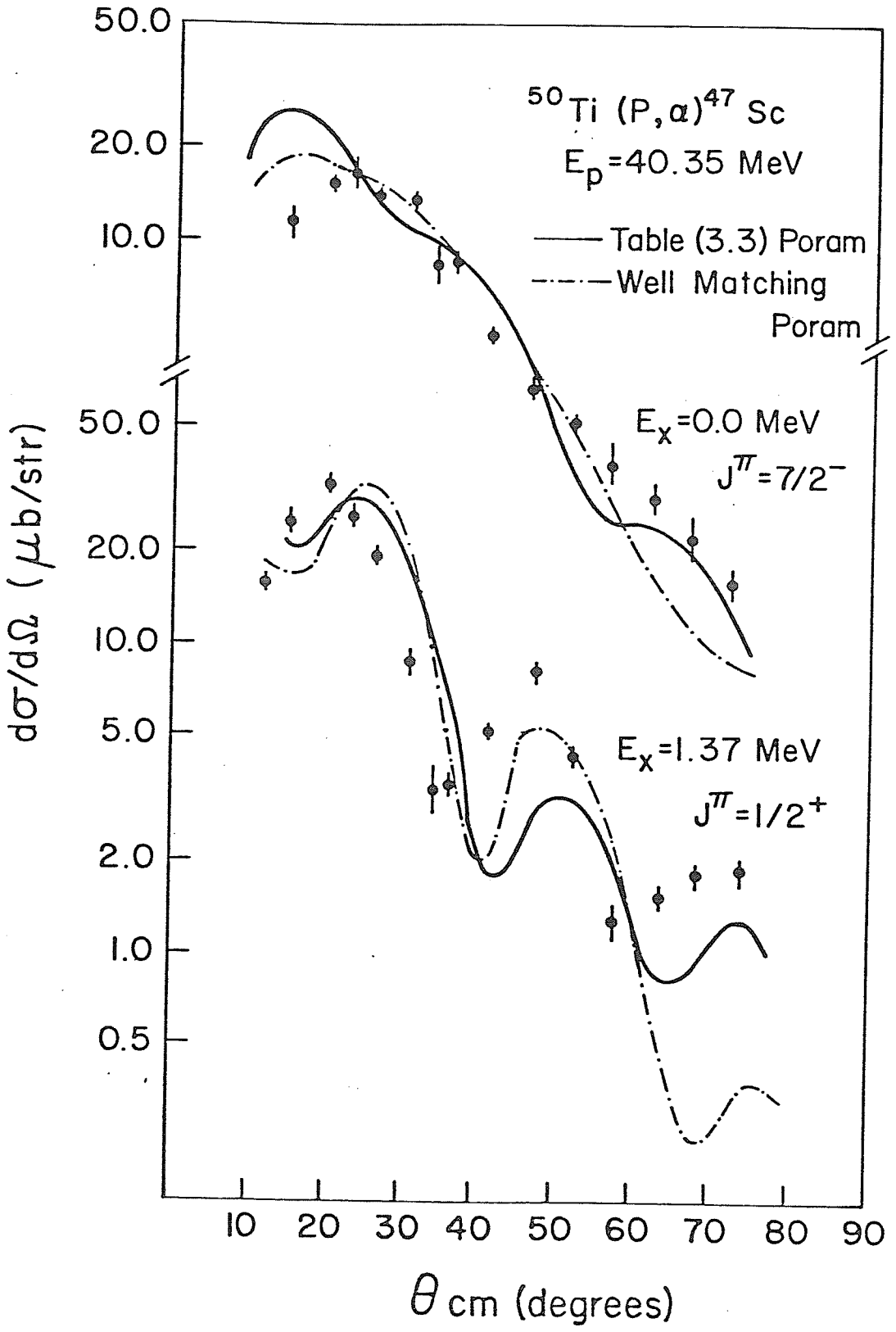
^{50}Ti (P,α)^{47} Sc
E_p=40.35 MeV
Table (3.3) Poram
Well Matching Poram
E_x=0.0 MeV
J^π=7/2$^-$
E_x=1.37 MeV
J^π=1/2$^+$
dσ/dΩ (μb/str)
θ cm (degrees)
50.0
20.0
10.0
5.0
2.0
1.0
0.5
10
20
30
40
50
60
70
80
90

Fig. (3.6) Calculated angular distributions for different j^{π} values.

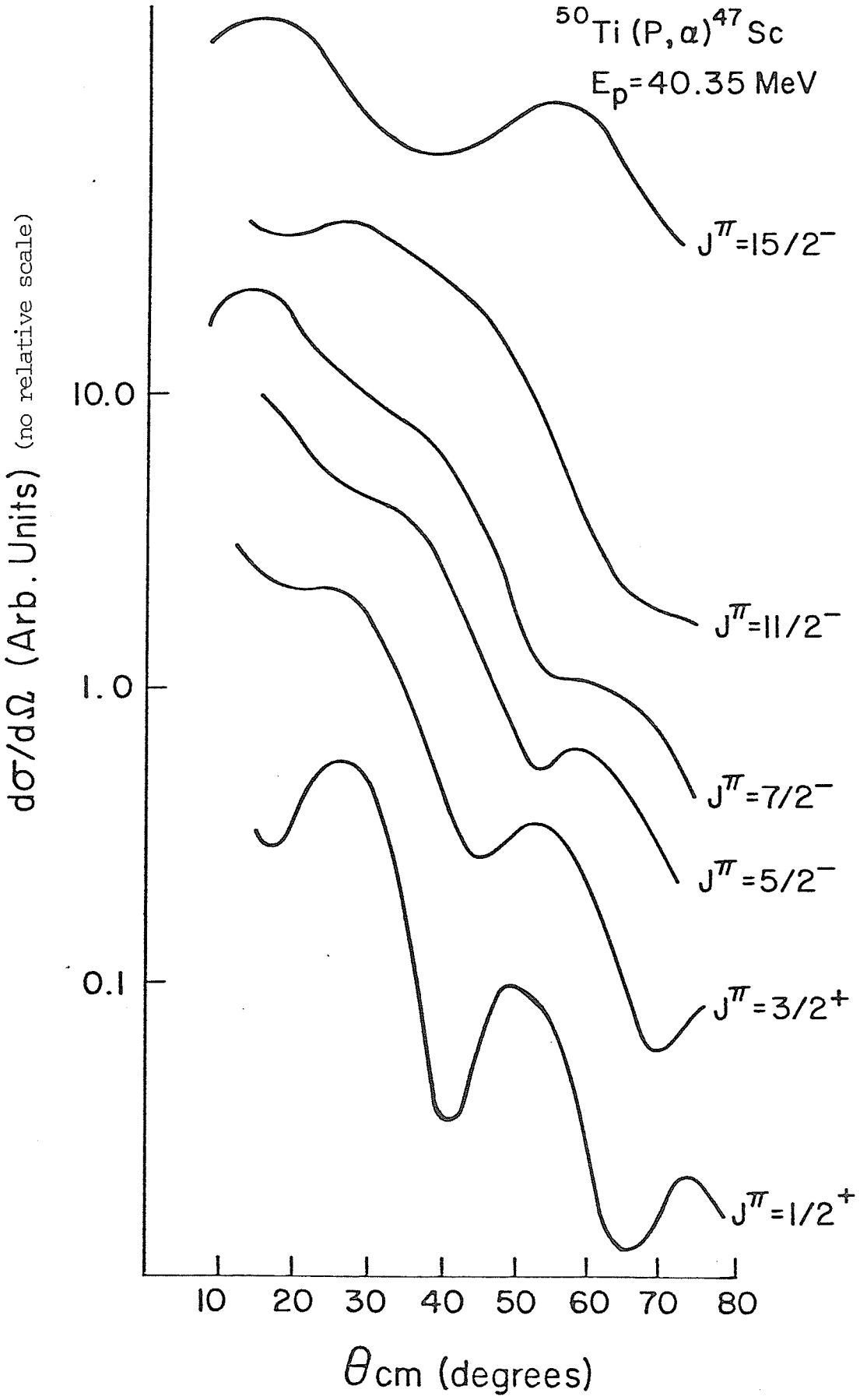
^{50}Ti (P, α)^{47}Sc
E_p=40.35 MeV
J^π=15/2$^-$
J^π=11/2$^-$
J^π=7/2$^-$
J^π=5/2$^-$
J^π=3/2$^+$
J^π=1/2$^+$
dσ/dΩ (Arb. Units) (no relative scale)
10.0
1.0
0.1
10
20
30
40
50
60
70
80
θcm (degrees)

dependence of these angular distributions on excitation energies is very weak in this energy range.

Chapter 4

Theoretical Interpretation of the nuclear structure of Sc and Ti isotopes

4.1 Shell Model Studies

The early theoretical investigations on the structure of the fp-shell nuclei were carried out in the framework of the spherical shell model by McCullen, Bayman and Zamick (M.B.Z.)[16],[56]. The wave functions and spectra for nuclei in the fp shell up to ^{56}Ni were calculated with effective interactions deduced from the ^{42}Sc spectrum as it was known in 1964. All valence nucleons were restricted to the $1f_{7/2}$ shell. The calculated spectra of M.B.Z. agreed well for even-even nuclei. Figs. (4.1) and (4.2) show respectively, the ^{46}Ti and ^{48}Ti observed spectra and their comparison with M.B.Z. calculations. Whereas the calculation agrees well for the case of ^{46}Ti the chief failure of the theory in even-even isotopes is the predicted 3^+ level at 3.01 Mev in ^{48}Ti for which there is no experimental evidence.

The theoretical predictions are less successful in the odd-even nuclei than in either the odd-odd or even-even. This is partly due to the configuration mixing from the higher configurations, the effects of which are more pronounced in the odd-even isotopes.

Fig. (4.3) shows in the first column the ^{43}Sc spectrum of negative parity states as calculated by the M.B.Z. model. The experimental spectrum is spread over 3 columns. One notices immediately that the $(1f_{7/2})^n$ calculation is quite inadequate from the point of view of the number of levels that are present. In addition, the lowest-spin state

Fig. (4.1) ^{46}Ti spectrum compared with M.B.Z. calculation

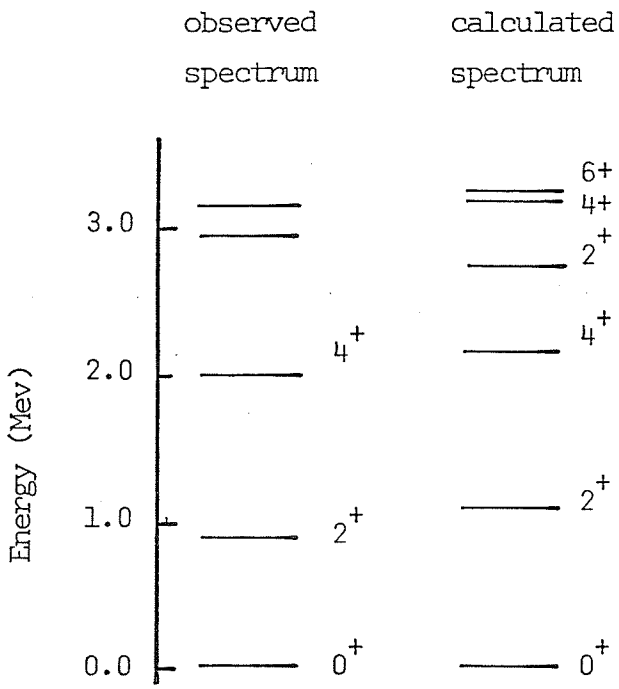
observed
spectrum
calculated
spectrum
Energy (Mev)
3.0
2.0
1.0
0.0
4+
2+
0+
6+
4+
2+
4+
2+
0+

Fig.(4.2) ^{48}Ti spectrum compared with M.B.Z. caculation

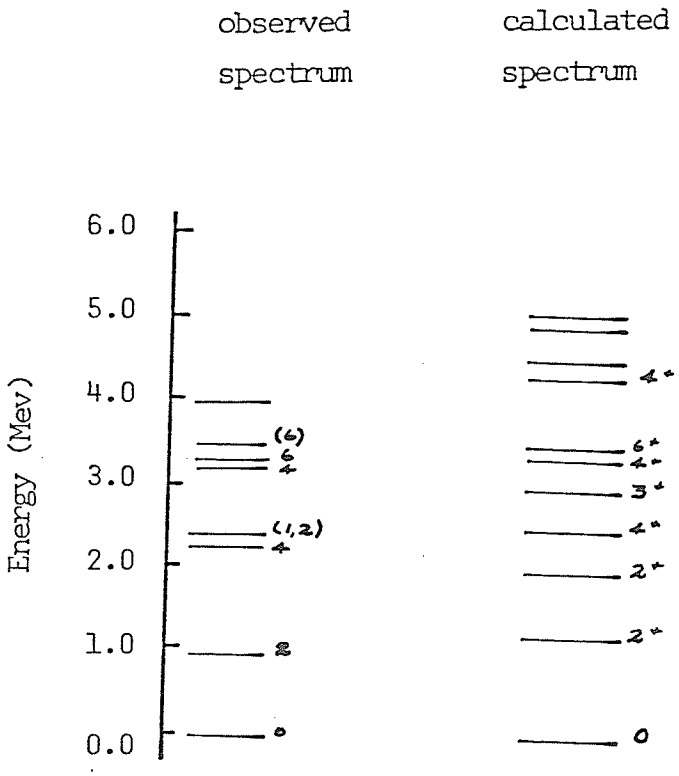
observed
spectrum
calculated
spectrum
Energy (Mev)
6.0
5.0
4.0
3.0
2.0
1.0
0.0
(6)
6
4
(1,2)
4
2
0
4+
6+
4+
3+
4+
2+
2+
0

Fig.(4.3) The ^{43}Sc spectrum of negative-parity states compared with the M.B.Z. theory.

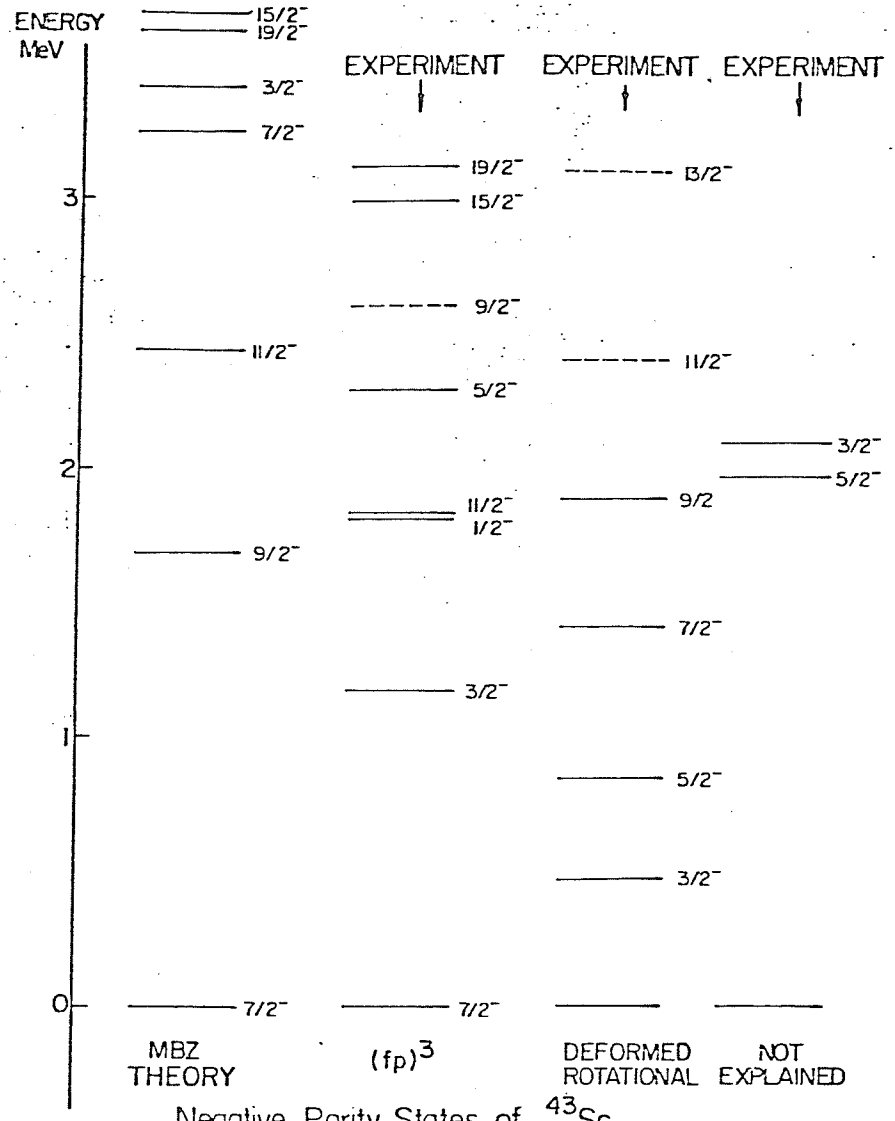

Negative Parity States of ^{43}Sc

in the M.B.Z. calculations is a $J^{\pi} = 3/2^{-}$ state at 3.4 Mev, but experimentally the lowest $3/2^{-}$ state is at 400 Kev. There is another $3/2^{-}$ state at 1.1 Mev.

Figs. (4.4) and (4.5) show a comparison between the calculated and observed spectra for ^{45}Sc and ^{47}Sc respectively. The same remarks mentioned above about the ^{43}Sc spectrum are applicable here. The experimental energy levels for ^{43}Sc, ^{45}Sc and ^{47}Sc are given in Appendix D.

Flowers[59] introduced the next stage of sophistication in the study of ^{43}Sc. The ^{40}Ca core was still regarded as inert, but the three extra-core nucleons were allowed to occupy the complete 1f-2p shell. Appropriate single-particle energies were deduced from the ^{41}Ca spectrum. The second column of Fig. (4.3) shows the experimental levels that can be described by this model. The same conclusion has been reached also by Ripka and Zamick[58].

The third column of Fig. (4.3) lists the levels of those states which are associated[60] with the $K = 3/2$, 5p-2h rotational band. The last column lists states which do not yet have any theoretical interpretation.

The shell model calculation of M.B.Z. was also extended by Lips[61] for the nuclei $N = 28$, $20 < Z \leq 28$ to include $1f_{7/2}^{n-1}\ 2p_{3/2}$ and $1f_{7/2}^{n-1}\ 1f_{5/2}$ proton configurations. They found that the lowest state of each J^{π} is mainly of $(1f_{7/2})^n$ structure for all the nuclei studied. Although the spectra predicted improved, nevertheless, the predicted M1 transion rates were too small.

Recently Kutschera[25] performed a new $(1f_{7/2})^n$-type shell model calculation using more recent experimental information to deduce the

Fig. (4.4) ^{45}Sc negative parity spectrum compared with M.B.Z. calculation.

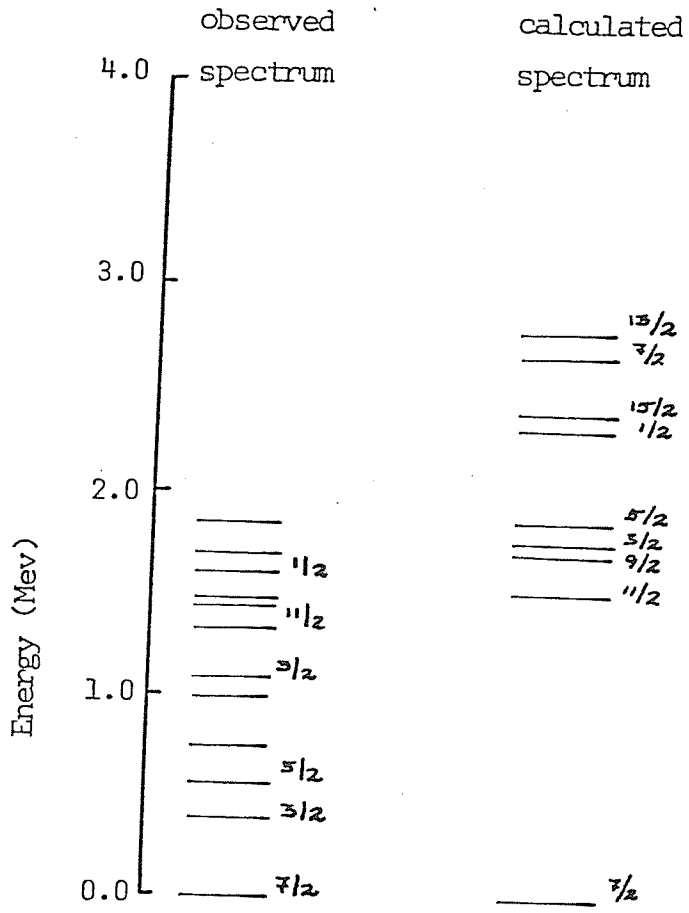
observed
spectrum
calculated
spectrum
4.0
3.0
2.0
1.0
0.0
Energy (Mev)
13/2
7/2
15/2
1/2
5/2
3/2
9/2
11/2
11/2
11/2
3/2
5/2
3/2
7/2
7/2

Fig.(4.5) ^{47}Sc negative parity spectrum compared with M.B.Z. calculation.

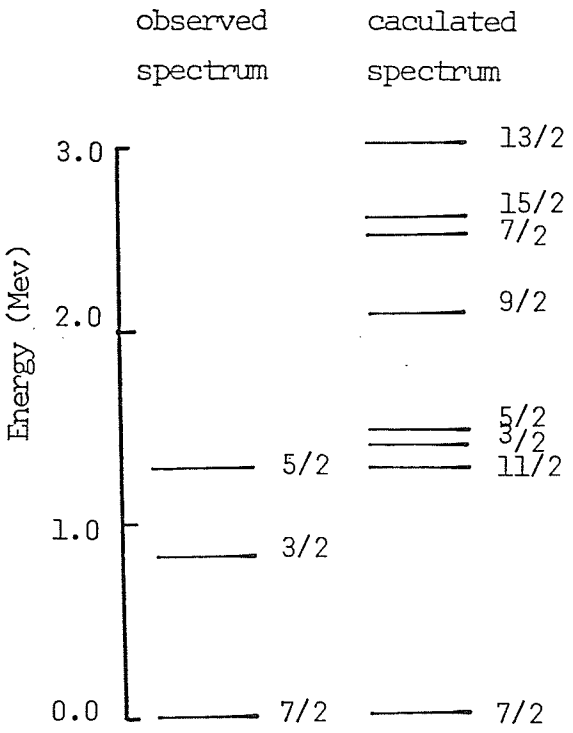
observed
spectrum
caculated
spectrum
Energy (Mev)
3.0
2.0
1.0
0.0
13/2
15/2
7/2
9/2
5/2
3/2
11/2
5/2
3/2
7/2
7/2

empirical two-body interactions. The calculated spectrum for ^{43}Sc is shown in Fig. (4.6). These wave functions will be tested in the present work.

4.2 Cluster Interpretation for Sc-isotopes spectra

The cluster representation offers[27] a method for predicting a qualitative level scheme for Sc-isotopes. Both positive and negative parity spectra of ^{19}F have been accounted for with the aid of this method[62]. The low-lying negative parity states of ^{43}Sc are pictured to arise from the interaction of an unexcited ^{40}Ca core with a ^{3}H cluster. The lowest oscillation permitted by the Pauli principle are of the 9th order, resulting in motions with possible angular momentum 1^-, 3^-, 5^-, 7^- . Coupling with the spin of ^{3}H cluster gives rise to $\frac{3}{2}^-$, $\frac{1}{2}^-$, $\frac{7}{2}^-$, $\frac{5}{2}^-$ ... states.

The positive parity states are pictured to arise from the interaction of an unexcited ^{39}K and ^{4}He cluster. The lowest permitted oscillations are of the 12th order, with angular momentum 0^+, 2^+, 4^+.. . Coupling with $\frac{3}{2}^+$ spin of the ^{39}K cluster results in $\frac{3}{2}^+$, $\frac{1}{2}^+$, $\frac{3}{2}^+$, $\frac{5}{2}^+$, $\frac{7}{2}^+$, ... states. The predicted spectrum is shown in Fig. (4.7). The cluster representation is still qualitatively applicable for the case of ^{45}Sc, but it is complicated for ^{47}Sc.

4.3 The Collective Model Approach

An alternate way to describe some of the states of the odd-mass Sc nuclei is to use the collective model to which single-particle effects have been coupled. Fig. (4.8) shows the Nilsson diagram[76]. From this figure, positive deformations of $1f_{7/2}$ nuclei are expected to result in a negative-parity level sequence $\frac{1}{2}^-$, $\frac{3}{2}^-$, $\frac{5}{2}^-$, $\frac{7}{2}^-$, with a rotational band

Fig.(4.6) ^{43}Sc spectrum as predicted by Kutschera [25].

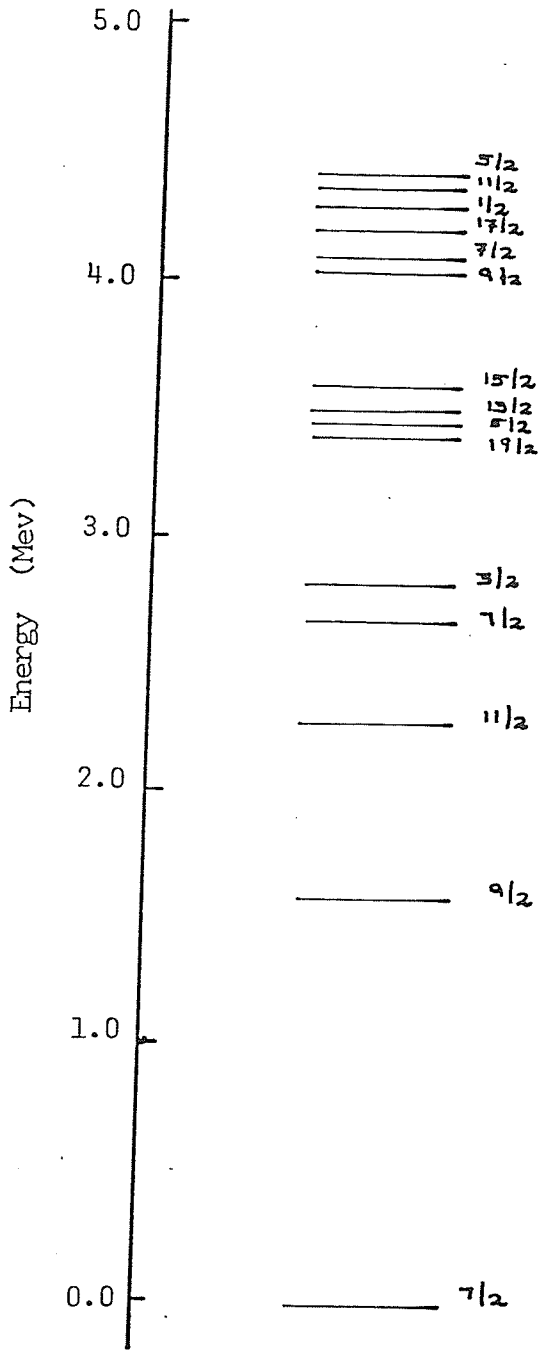
5.0
4.0
3.0
2.0
1.0
0.0
Energy (Mev)
5/2
11/2
1/2
17/2
7/2
9/2
15/2
13/2
5/2
19/2
3/2
7/2
11/2
9/2
7/2

Fig(4.7) ^{43}Sc energy levels :

(a) qualitative cluster-representation levels

(b) calculated shell model levels [16].

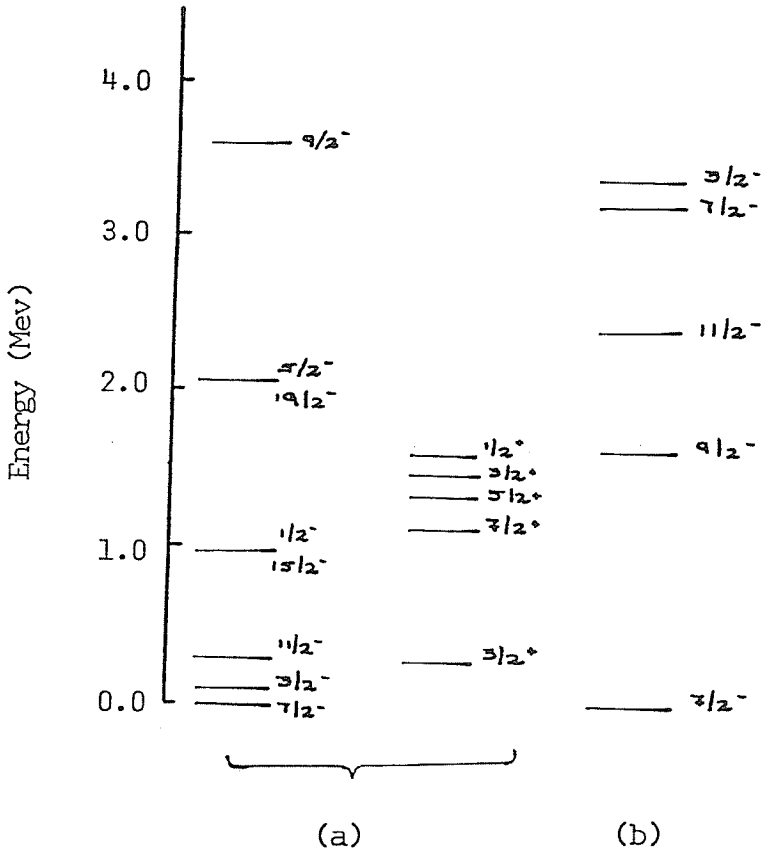
Energy (Mev)
4.0
3.0
2.0
1.0
0.0
9/2⁻
5/2⁻
19/2⁻
1/2⁻
15/2⁻
11/2⁻
3/2⁻
7/2⁻
1/2⁺
3/2⁺
5/2⁺
7/2⁺
3/2⁺
3/2⁻
7/2⁻
11/2⁻
9/2⁻
7/2⁻
(a)
(b)

superimposed on each of these intrinsic states. That the Sc isotopes with odd mass numbers have $J^{\pi} = 7/2^-$ rather than $1/2^-$ can be accounted for by noting that the band built on the $1/2^-$ intrinsic state has a highly negative decoupling parameter for the deformation range $0 \leq \delta \leq .27$ as shown in Fig. (4.9) and that this causes a depression of the $7/2^-$ member of that band relative to its $1/2^-$ member.

Positive parity levels starting with $3/2^+$ are expected to occur at excitation energies that vary with the amount of deformation. The smallest deformation (represented qualitatively by line a in Fig. (4.8)) is expected for ^{41}Sc and ^{49}Sc, with one nucleon outside closed shells. The ^{45}Sc nucleus, with 5 particles (or 1 particle and 4 holes) outside closed shells, is expected to have the largest deformation (line d in Fig. (4.8)). The deformation of ^{43}Sc (3 particles) is expected to be somewhat larger than that of ^{47}Sc (1 particle, 2 holes), because such a particle-hole asymmetry has been observed in other deformed regions (lines c and b in Fig. (4.8)). The length of lines a - c can be taken as an indication of the excitation energy at which the lowest positive parity state is expected to occur.

4.4 Core-plus-particle Model Interpretation

The low-lying odd-parity states of ^{45}Sc are pictured[26] to arise from intermediate coupling of a single proton in the 1f-2p major shell to the ^{44}Ca core in either its 0^+ ground state or 2^+ first excited state at 1.156 Mev.

As shown in Fig. (4.10) a good agreement is obtained between fitted levels and their experimental counterpart. All the energy levels below 2 Mev are well accounted for and a model space truncation allowing only for

Fig.(4.8) Single-particle energy level positions as a function of deformation (Nilsson diagram).

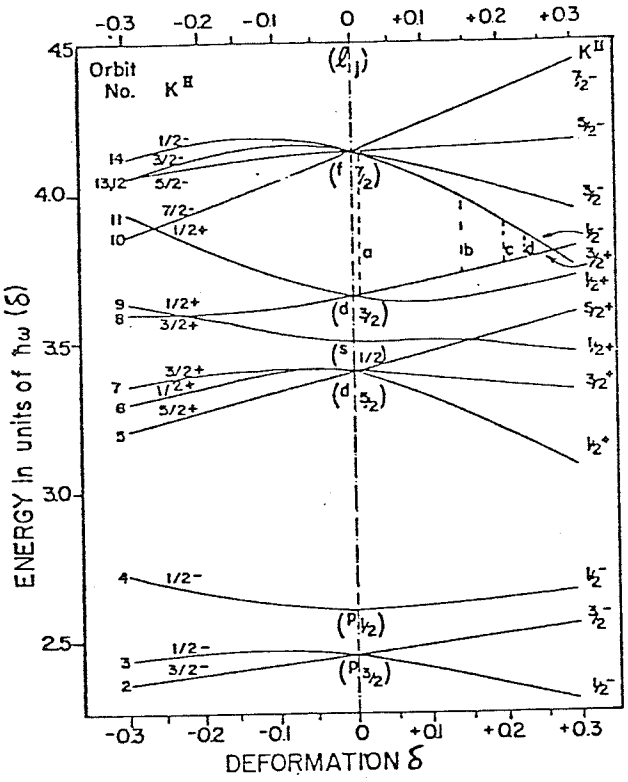
Orbit No. K^π
ENERGY in units of ħω (δ)
DEFORMATION δ
-0.3
-0.2
-0.1
0
+0.1
+0.2
+0.3
4.5
4.0
3.5
3.0
2.5
1/2-
3/2-
5/2-
7/2-
1/2+
3/2+
5/2+
a
1b
c
d

Fig.(4.9) Decoupling parameter versus deformation for Nilsson orbit no. 14 of Fig.(4.8).

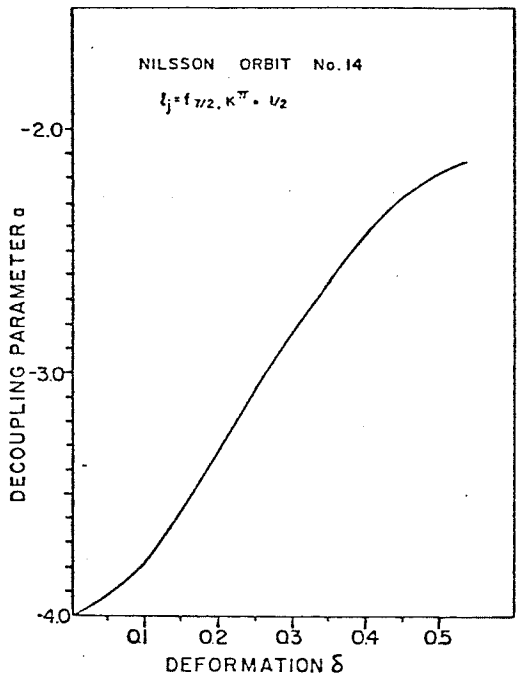
NILSSON ORBIT No. 14
$\ell_j = f_{7/2}, K^{\pi} = 1/2$
-2.0
-3.0
-4.0
DECOUPLING PARAMETER a
0.1
0.2
0.3
0.4
0.5
DEFORMATION δ

the coupling between $1f_{7/2}$ and $1p_{3/2}$ proton states and the 0^+ and 2^+ core states, is justified since the inclusion of further single particle orbitals does not alter the predicted structure of levels.

As for the positive parity states it was found that[26] they are predominantly a $1d_{3/2}$ proton hole with $|0^+ \; 1d_{3/2}^{-1}>$ for the 0.012 Mev state and $|2^+, \; 1d_{3/2}^{-1}>$ for all other levels obtained.

Seth [73] presented a similar interpretation for the 1.40 Mev, $7/2^-$ state in ^{43}Sc only. This will be discussed in chapter 5.

Fig. (4.10) The results of core-plus-particle coupling calculations as compared with the experimental level scheme of ^{45}Sc.

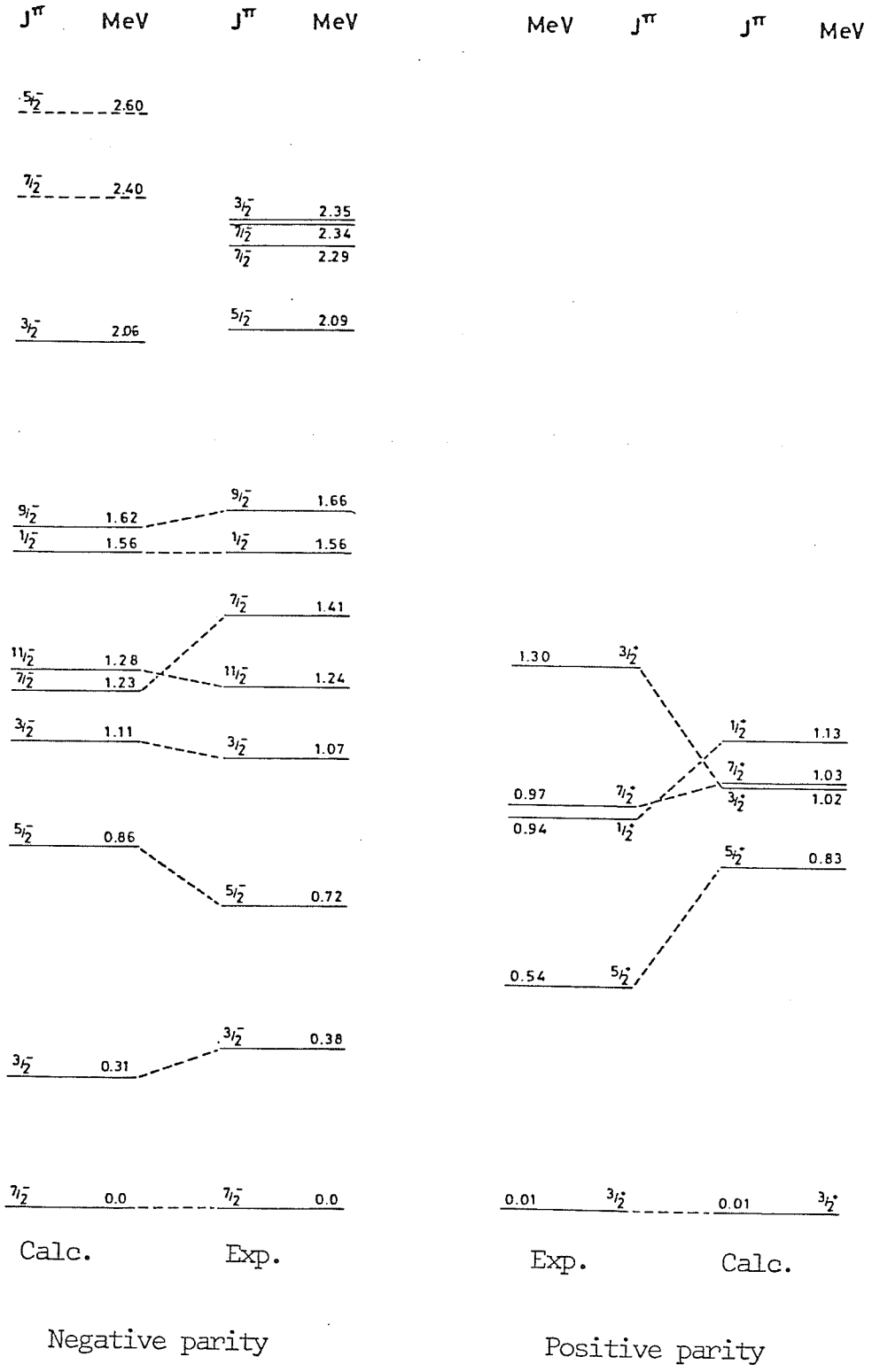
Jπ MeV Jπ MeV
5/2⁻ 2.60
7/2⁻ 2.40
3/2⁻ 2.06
3/2⁻ 2.35
7/2⁻ 2.34
7/2⁻ 2.29
5/2⁻ 2.09
9/2⁻ 1.62
1/2⁻ 1.56
9/2⁻ 1.66
1/2⁻ 1.56
11/2⁻ 1.28
7/2⁻ 1.23
7/2⁻ 1.41
11/2⁻ 1.24
3/2⁻ 1.11
3/2⁻ 1.07
5/2⁻ 0.86
5/2⁻ 0.72
3/2⁻ 0.31
3/2⁻ 0.38
7/2⁻ 0.0
7/2⁻ 0.0
Calc.
Exp.
Negative parity
MeV Jπ Jπ MeV
1.30 3/2⁺
0.97 7/2⁺
0.94 1/2⁺
1/2⁺ 1.13
7/2⁺ 1.03
3/2⁺ 1.02
5/2⁻ 0.83
0.54 5/2⁺
0.01 3/2⁺
0.01 3/2⁺
Exp.
Calc.
Positive parity

Chapter 5

Experimental Results and Comparison with Microscopic Calculations

In order to test the microscopic formalism described in chapter 2 and the wave functions of Kutschera[25] the (p,α) reaction has been studied on the Ti isotopes 46, 48 and 50. The following sections A, B and C will give descriptions and results of the investigations.

Section A: The $^{46}Ti(p,\alpha)^{43}Sc$ Reaction

A.1 α-spectrum:

The (p,α) reaction of ^{46}Ti isotope was studied at a proton energy of E_p = 40.35 Mev. The emerging α-particles were detected using 6 silicon surface barrier detectors, as discussed in chapter 3. Target details are also given in chapter 3.

Fig. (5.1) shows a typical spectrum for ^{43}Sc obtained at θ_{lab} = 45°. An overall energy resolution of 70 Mev FWHM was obtained, resulting from beam energy spread, beam divergence, energy straggling in the target and electronic circuitry resolution.

States in ^{43}Sc with excitation energies up to 6.22 kev were observed in the present work. These levels are summarized in table (5.1). Details of calculations and uncertainties in excitation energies are given in chapter 3.

The spectrum observed here resembles qualitatively the 30 Mev spectrum of Nolen[63] obtained from the same reaction. However, they did not report any quantitative results.

Among the salient features of the spectrum shown in Fig. (5.1) is

Fig. (5.1) The $^{46}Ti(p,\alpha)^{43}Sc$ spectrum

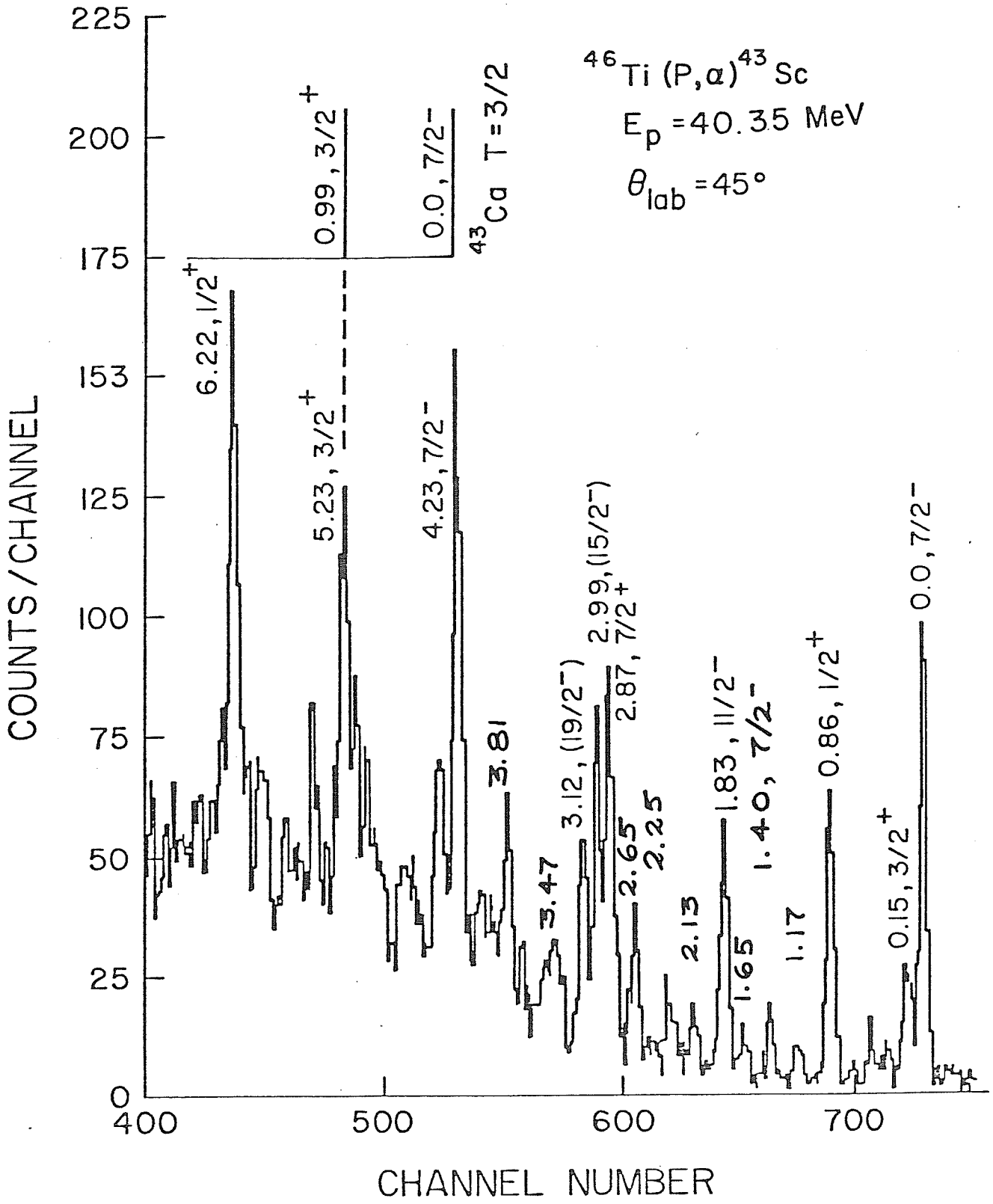
^{46}Ti (P,α)^{43}Sc
E_p =40.35 MeV
θ_{lab} =45°
^{43}Ca T=3/2
0.99, 3/2+
0.0, 7/2−
6.22, 1/2+
5.23, 3/2+
4.23, 7/2−
3.81
3.47
3.12, (19/2−)
2.99, (15/2−)
2.87, 7/2+
2.65
2.25
2.13
1.83, 11/2−
1.65
1.40, 7/2−
1.17
0.86, 1/2+
0.15, 3/2+
0.0, 7/2−
COUNTS/CHANNEL
CHANNEL NUMBER
225
200
175
153
125
100
75
50
25
0
400
500
600
700

the excitation of positive parity states at low excitation energies as predicted by the collective model discussed in chapter 4. For example, the $3/2^+$ state at 0.15 Mev and the $1/2^+$ at 0.86 Mev state. The same feature is observed as well in both ^{45}Sc and ^{47}Sc spectra.

A second important feature of the spectrum shown in Fig. (5.1) is the excitation of high spin states. The levels at 2.99 and 3.12 Mev have been assigned to the values $J^\pi = 15/2^-$ and $19/2^-$ on the basis of angular distributions obtained in the present work. Such assignments agree with previous assignments[64] from (α,p) reactions. Selection rules inhibit the population of these high spin seniority three states in one nucleon transfer reactions. Thus the study of the (p,α) reaction is of demonstrated advantage in such cases.

It may be added that the ability of the (p,α) reaction to excite states with both $T_>$ and $T_<$ is demonstrated through the excitation of the level at 4.23 Mev with $J^\pi = 7/2^-$ and $T = 3/2$. This level is the isobaric analog (IA) of the ^{43}Ca ground state. This is in agreement with M.B.Z. model prediction[56] of 4.17 Mev. A simple calculation of Coulomb displacement energy[75] predicts such a state to have an excitation energy of 4.28 Mev. Similarly, the state at 5.23 Mev, $3/2^+$ is believed to be the $T = 3/2$ IA of the ^{43}Ca 0.99 Mev, $3/2^+$ state. Again, this assignment is supported by the observed excitation energy and the angular distribution shape, as will discussed in the following subsection.

One notices from table (5.1) that among the states excited in the (p,α) reaction there are some states that are not (or only very weakly) excited by the (α,p)[65],[66] and (^6Li,τ)[67] reactions. These states are of positive parity: e.g. 0.15 Mev, $3/2^+$; 0.86 Mev, $1/2^+$; 2.87 Mev, $7/2^+$; 5.23 Mev, $3/2^+$

Table (5.1) Data Summary for ^{43}Sc

Excitation Energies (Mev)				
$(p,\alpha)^a$	$(\alpha,p)^{(65)}$	$(^6Li,\tau)^{(67)}$	J^π	Adopted value[64], (b)
0.0	0.0	0.0	$7/2^-$	0.0, $7/2^-$
0.15	very weakly excited		$3/2^+$	0.151, $3/2^+$
	0.85		$5/2^-$	0.845, $5/2^-$
0.86			$1/2^+$	0.855, $1/2^+$
1.17			$3/2^+$	
	1.18	1.18	$3/2^-$	1.179, $3/2^-$
1.40	1.41		$7/2^-$	1.407, $7/2^-$
1.65			$(5/2)^+$	1.651, $5/2^+$
	1.81	1.81	$1/2^-, 3/2^-$	1.810, $3/2^-$
1.83	1.83	1.83	$11/2^-$	1.829 $(7/2^-, 11/2^-)$
2.13				2.141 $(3/2, 5/2)^+$
2.25				2.244 $(3/2, 7/2)^-$
	2.28	2.29	$3/2^-$	2.289, $5/2^-$
2.65	2.62	2.63	$9/2^-, 11/2^-$	2.634 $(5/2-11/2)^-$
2.87			$7/2^+$	2.875
2.99	2.98	2.99	$15/2^-$	2.987 $(7/2-15/2)^-$
3.12	3.12	3.12	$19/2^-$	3.123 $(5/2-19/2)^-$
3.47				
3.81				3.806, $7/2^+$
4.23			$7/2^-$	4.235, $7/2^-$
5.23			$3/2^+$	5.236 $(3/2-17/2)^+$
6.22			$1/2^+$	6.222, $1/2^+$

(a) Present work

(b) Listed only are states with interest to present work.

and 6.22 Mev, $1\frac{1}{2}^{+}$. The disappearance of these states from the stripping reactions spectra confirms that these states are mainly proton hole states. However, these positive parity states have been excited in the reaction $^{42}Ca(^{3}He,d)^{43}Sc$[68] through the relatively large two-hole components in the ^{42}Ca ground state[69],[70],[71].

On the other hand there are states observed in both the (α,p) and $(^{6}Li,\tau)$ reactions that are not observed in the present (p,α) work. Examples are 1.18 Mev, $3\frac{1}{2}^{-}$; 1.81 Mev, $3\frac{1}{2}^{-}$ and 2.29 Mev, $3\frac{1}{2}^{-}$. The observation of these states in stripping reactions but not in a pickup reaction indicates that these states are mainly particle states with the main configuration $(fp)^3$. In order to observe these states in a (p,α) reaction the target should contain an appreciable amount of configuration mixing in the $1f_{5/2}$ and $2p_{3/2}$ shells, which apparently is not the case for ^{46}Ti. Finally states like 0.0 Mev, $7\frac{1}{2}^{-}$; 1.83 Mev, $11\frac{1}{2}^{-}$ and 2.99 Mev, $15\frac{1}{2}^{-}$ are observed here and in the stripping reactions (α,p) and $(^{6}Li,\tau)$. This is an indication that the main configuration of these states is $(f_{7/2})^3$. This is supported by the prediction of the M.B.Z. model for these states.

A.2 Angular Distributions - DWBA cluster Calculations:

Angular distributions obtained for states (or group of states) in ^{43}Sc are shown in Figs. (5.2) through (5.6) inclusive. The errors shown are the quadratic sum of the statistical and fitting errors, which are given by the code Autofit[50]. The solid lines are the results of zero-range DWBA calculations using a cluster form factor. The triton cluster was bound by its experimental separation energy while the dimensions of the Woods-Saxon well were chosen to reproduce the experimental angular

Fig. (5.2) Angular distributions for the negative parity states 0.0, $\frac{7}{2}^-$; 1.40 Mev, $\frac{7}{2}^-$ and 1.83 Mev, $1\frac{1}{2}^-$. The solid lines are the results of cluster zero-range DWBA calculations.

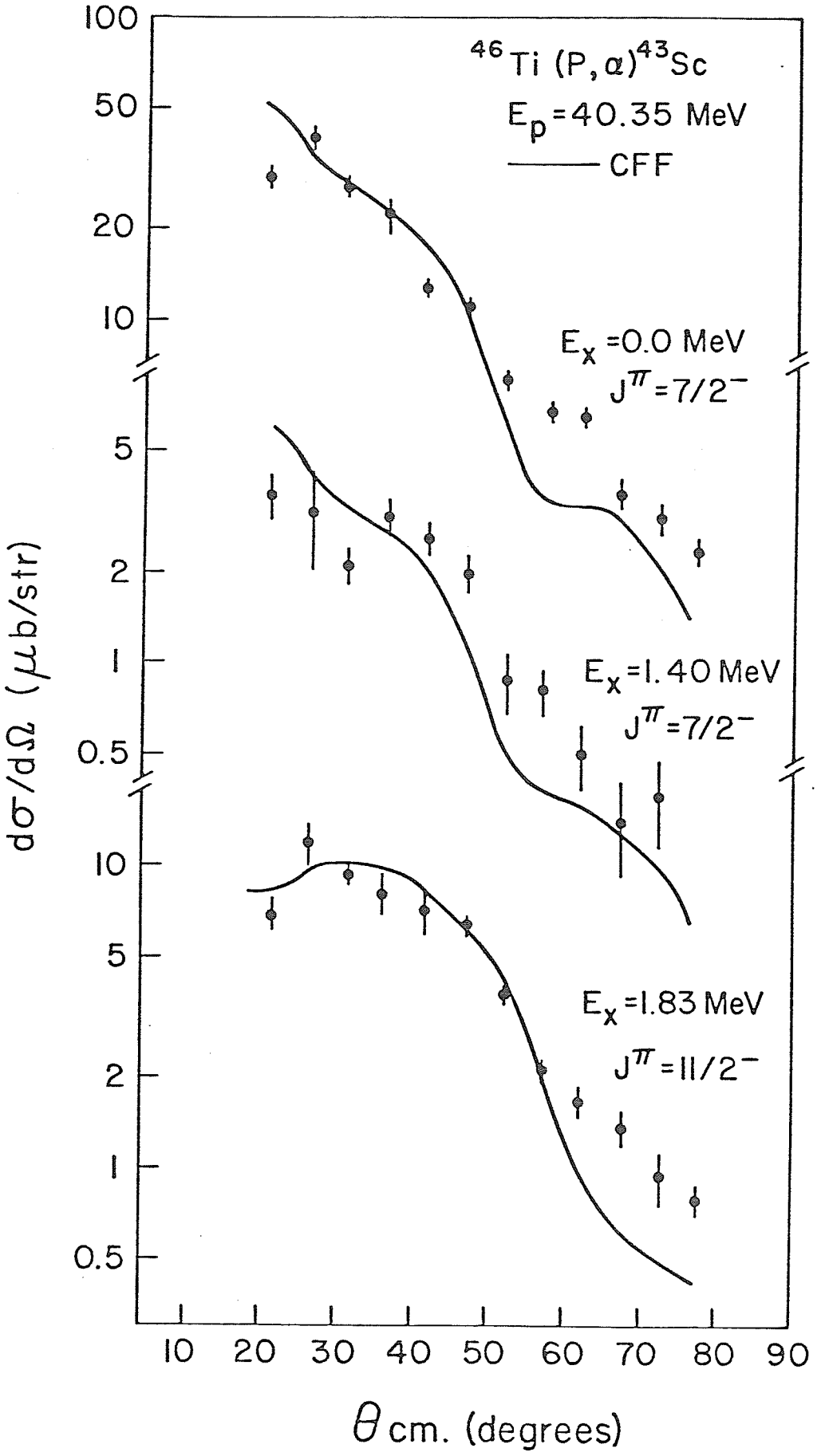
^{46}Ti (P, α)^{43}Sc
E_p = 40.35 MeV
CFF
E_x = 0.0 MeV
J^π = 7/2$^-$
E_x = 1.40 MeV
J^π = 7/2$^-$
E_x = 1.83 MeV
J^π = 11/2$^-$
dσ/dΩ (μb/str)
θ cm. (degrees)
100
50
20
10
5
2
1
0.5
10
5
2
1
0.5
10 20 30 40 50 60 70 80 90

Fig. (5.3) Angular distributions for the positive parity states 0.15 Mev, $3/2^+$; 0.86 Mev, $1/2^+$ and 2.87 Mev, $7/2^+$. The solid lines are the results of cluster zero-range DWBA calculations.

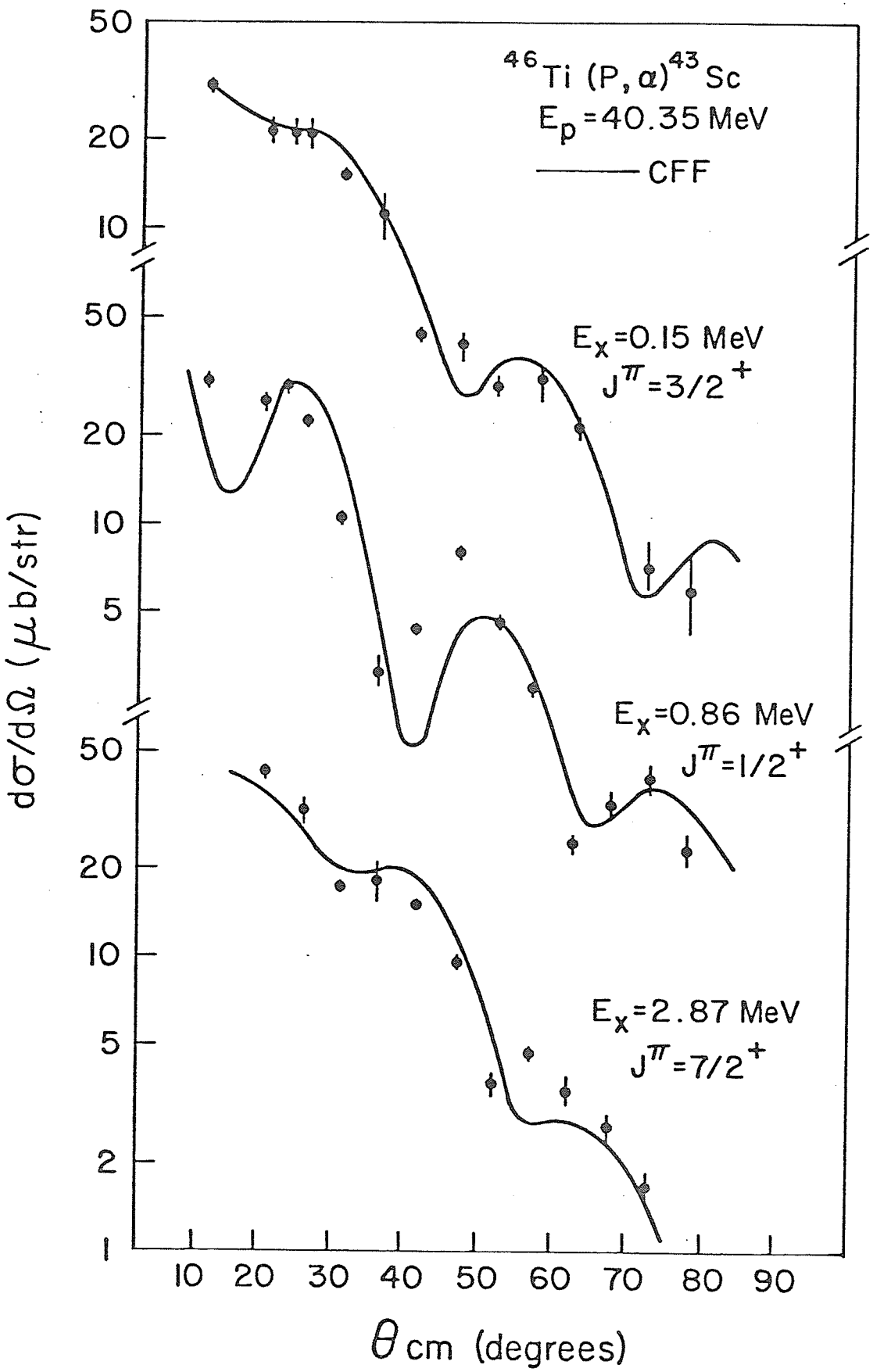
^{46}Ti (P, α)^{43}Sc
E_p = 40.35 MeV
CFF
E_x = 0.15 MeV
$J^\pi = 3/2^+$
E_x = 0.86 MeV
$J^\pi = 1/2^+$
E_x = 2.87 MeV
$J^\pi = 7/2^+$
dσ/dΩ (μb/str)
θ cm (degrees)
50
20
10
5
2
1
10 20 30 40 50 60 70 80 90

Fig. (5.4) Angular distributions for the high spin states 2.99 Mev, $15/2^-$ and 3.12 Mev, $19/2^-$. The solid lines are the results of zero-range cluster DWBA calculations.

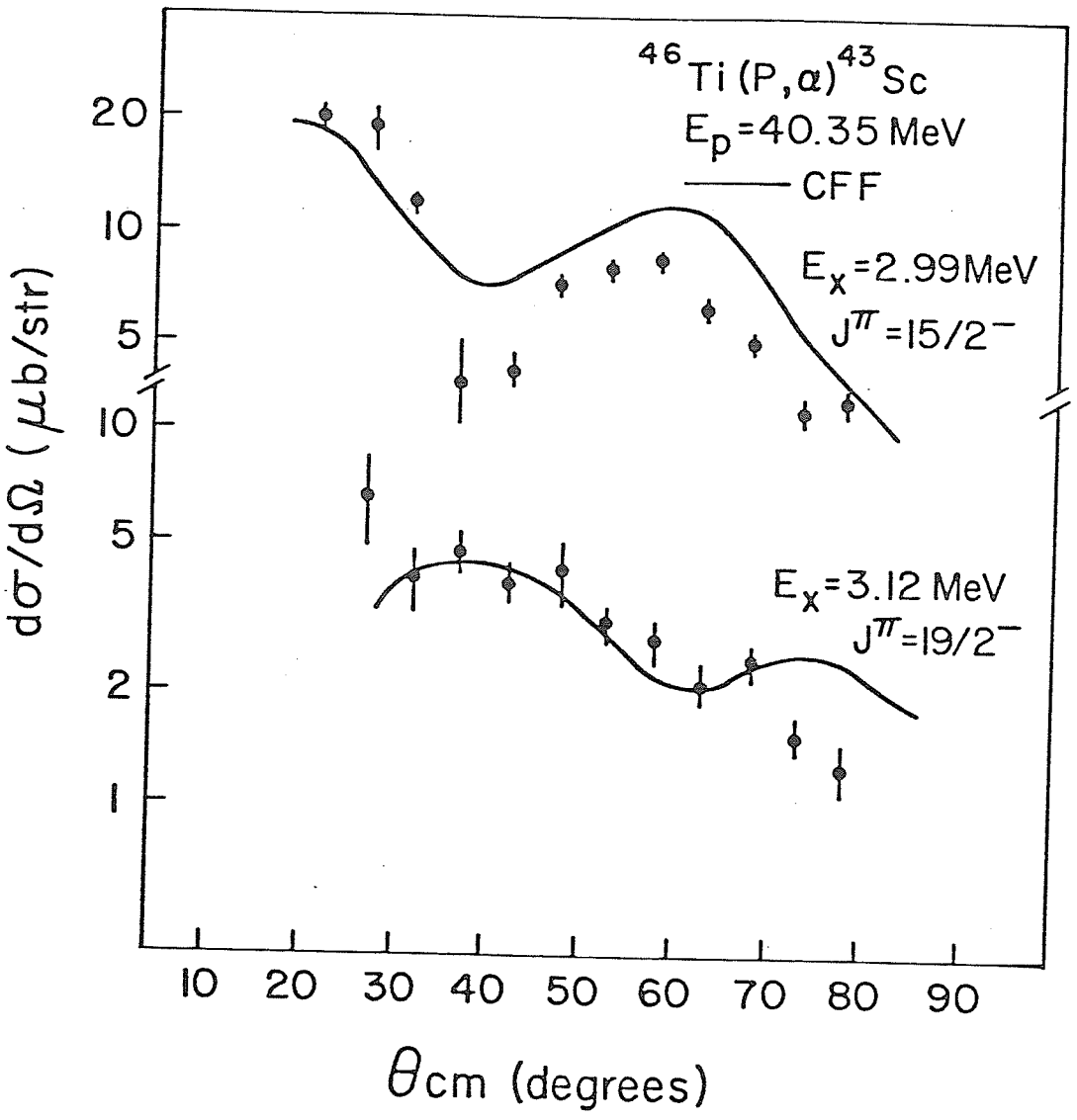
^{46}Ti (P,α)^{43}Sc
E_p=40.35 MeV
CFF
E_x=2.99MeV
J^π=15/2$^-$
E_x=3.12 MeV
J^π=19/2$^-$
dσ/dΩ (μb/str)
θcm (degrees)
20
10
5
10
5
2
1
10
20
30
40
50
60
70
80
90

Fig. (5.5) Angular distributions for the IAS to $^{43}Ca(T=\frac{3}{2})$: 4.23 Mev, $\frac{7}{2}^-$; 5.23 Mev, $\frac{3}{2}^+$ and 6.22 Mev, $\frac{1}{2}^+$. The solid lines are the results of zero-range cluster DWBA calculations.

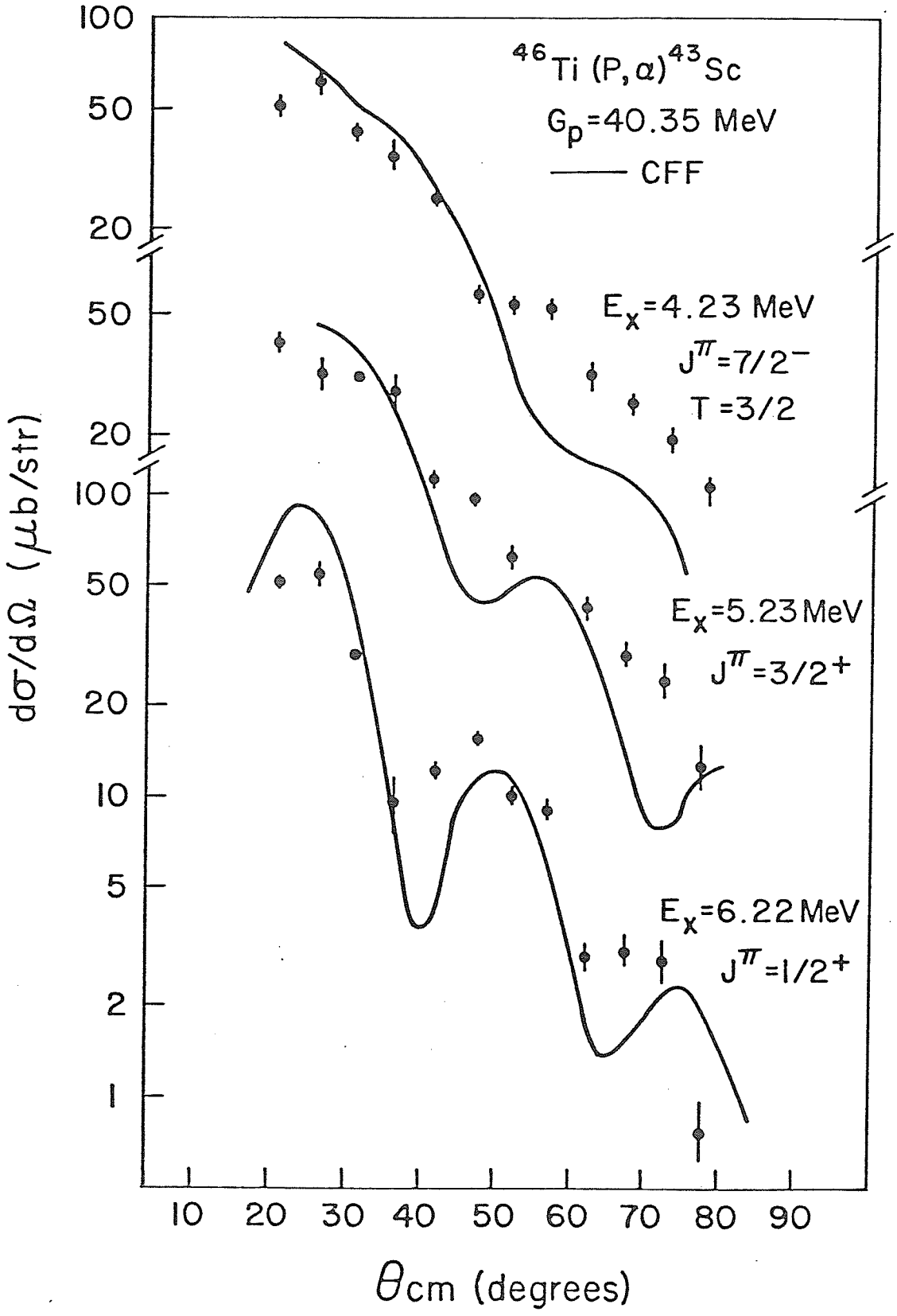
^{46}Ti (P, α)^{43}Sc
G_p=40.35 MeV
—— CFF
E_x=4.23 MeV
J^π=7/2$^-$
T=3/2
E_x=5.23 MeV
J^π=3/2$^+$
E_x=6.22 MeV
J^π=1/2$^+$
dσ/dΩ (μb/str)
θcm (degrees)
100
50
20
10
5
2
1
10 20 30 40 50 60 70 80 90

Fig. (5.6) Angular distributions for the states 1.65 Mev and 3.81 Mev. No definite J^{π} assignment has been made

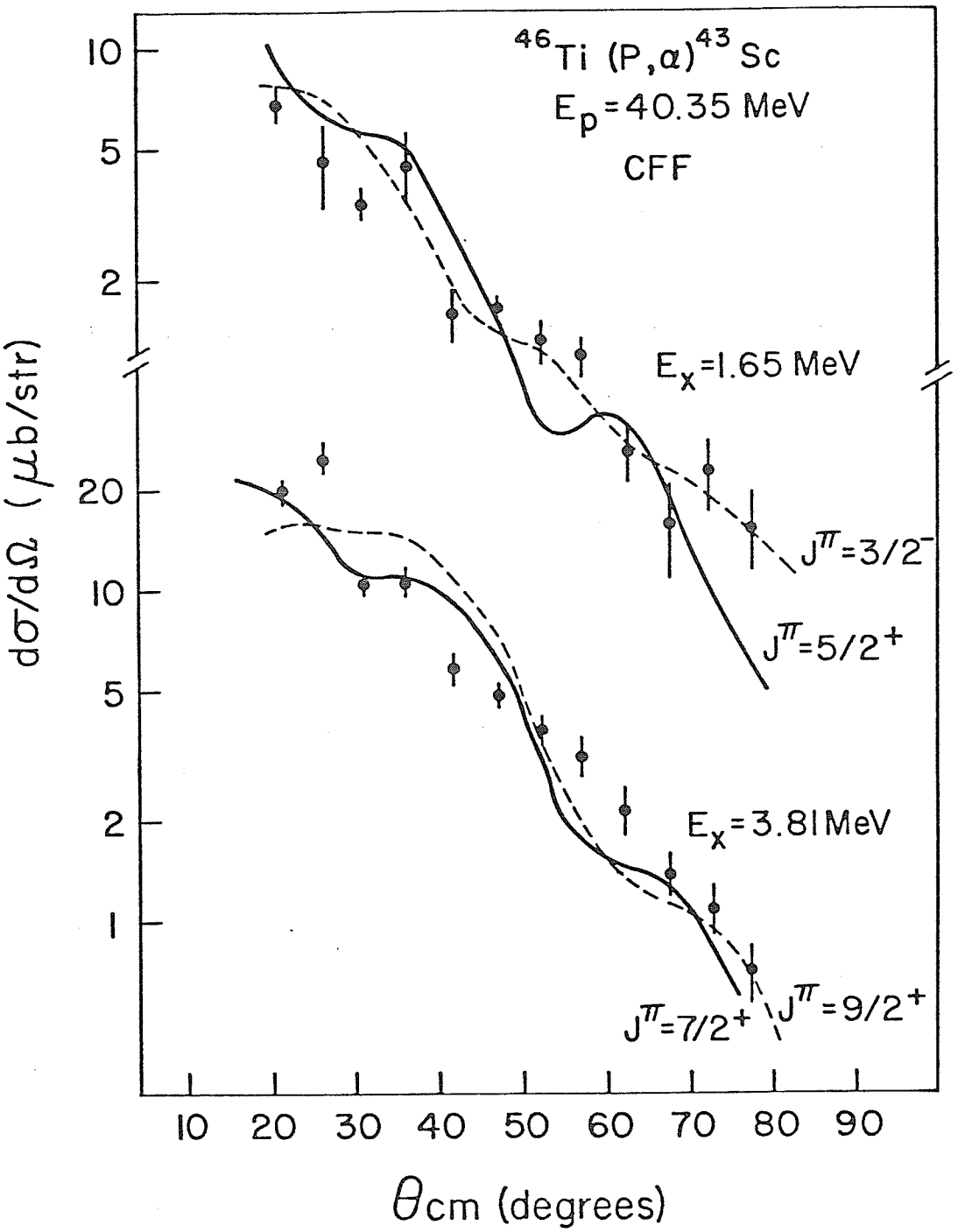
^{46}Ti (P,α)^{43}Sc
E_p=40.35 MeV
CFF
E_x=1.65 MeV
J^π=3/2$^-$
J^π=5/2$^+$
E_x=3.81MeV
J^π=7/2$^+$
J^π=9/2$^+$
dσ/dΩ (μb/str)
θcm (degrees)
10
5
2
20
10
5
2
1
10 20 30 40 50 60 70 80 90

distributions as discussed in chapter 3. The optical model parameters are shown in table (3.3). The calculated angular distributions have been normalized by eye to the experimental distributions. The calculated angular distributions confirmed the known and previously determined J^{π} values for the states 0.0 Mev, $7/2^-$; 0.15 Mev, $3/2^+$; 0.86 Mev, $1/2^+$ and 1.83 Mev, $11/2^-$. On the other hand, the calculated distribution for the state 2.99 Mev was used to make a unique J^{π} assignment of $15/2^-$. This level was given the assignment $(7/2 - 15/2)^-$ from γ-ray work[64] but all other J^{π} values gave an inferior fit to that of $J^{\pi} = 15/2^-$. For some other states it was difficult to make spin assignments due to the similarities in the angular distributions for different J transfer, or to poor statistics, or to the possibility of overlapping states within one peak. An example of this is the state 1.65 Mev $(5/2)^+$ which could be fitted by more than one J value, though both of them do not actually reproduce the data well. A similar case is the state 3.81 Mev. Both these states are shown in Fig. (5.6) and will not be considered for quantitative analysis.

A.3 DWBA Calculations - Microscopic Form Factor:

The microscopic form factor formalism introduced and implemented as described in chapter 2 was used in order to get quantitative information. Such calculations need detailed wave functions together with spectroscopic amplitudes as discussed earlier in chapter 2 and appendix B. However, as a zeroth order calculation simple configurations for the transferred nucleons were assumed in order to test to what extent such configurations would be able to explain the observed features in the (p,α) reaction.

It was assumed that ^{46}Ti can be represented by a doubly closed ^{40}Ca with two extra-core $1f_{7/2}$ protons and four extra-core $1f_{7/2}$ neutrons. Both protons and neutrons have seniority zero. The negative parity states are then populated by picking up a $1f_{7/2}$ proton and two $1f_{7/2}$ neutrons coupled to an angular momentum $J' \geq 0$, dependent on the J^{π} value of the final state. The positive parity states are populated by picking up a (2s-1d) shell proton and two $1f_{7/2}$ neutrons. Fig. (5.7) shows a diagramatic representation of these wave functions. The overlap integral I_{AB} was calculated as prescribed in chapter 2. MFF corresponding to these configurations were calculated and CFF tails attached as previously described.

The zero range DWBA calculations using these MFF are shown in Figs. (5.8) to (5.11) inclusive. Also shown are the cluster transfer fits for comparison purposes. The MFF fits are better than the CFF fits for some states while worse for others.

Table (5.2) shows the results of this zeroth order calculation. Column 6 shows the ratio $\sigma_{exp}/\sigma_{theory}$ for states in ^{43}Sc where $\sigma_{theory}(\sigma_{th}) = N.\ \sigma_{DWBA}$, N is an overall normalization factor including unspecified factors in the form factor program and factors in DWUCK 2. σ_{DWBA} is the DWBA cross section calculated by the code DWUCK 2 using the MFF described previously. The constancy of this ratio is an indication of agreement between experiment and theory. As shown in table (5.2) the ratios σ_{exp}/σ_{th} are in agreement with one another for most of the states - within a factor of 2.5. Exceptions are the states 1.40 Mev, $7/2^-$ and 2.87 Mev, $7/2^+$. This is an indication that for these, in particular, the simple wave functions assumed are inadequate and more detailed wave

Fig.(5.7) Simple wave functions for $^{46}Ti(p,\alpha)^{43}Sc$.

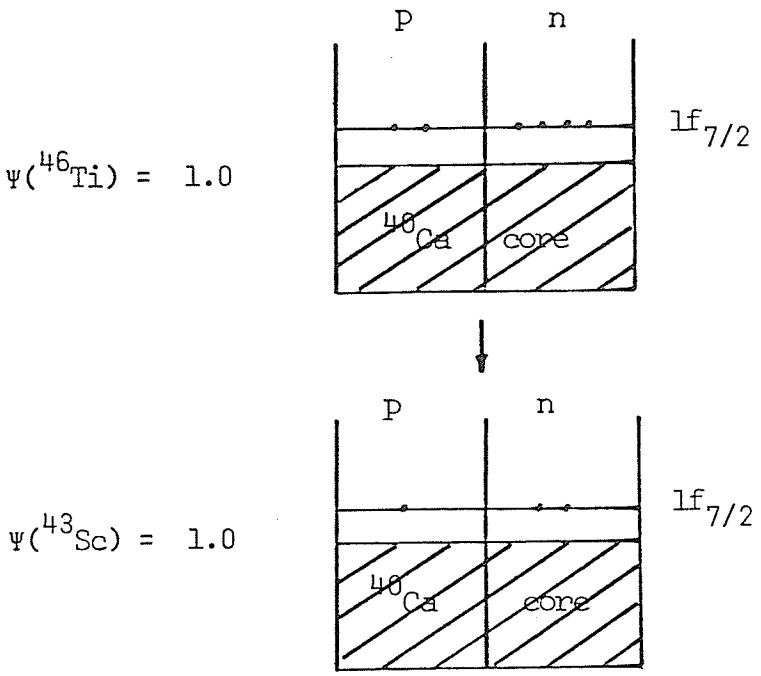

(a) negative parity state transition

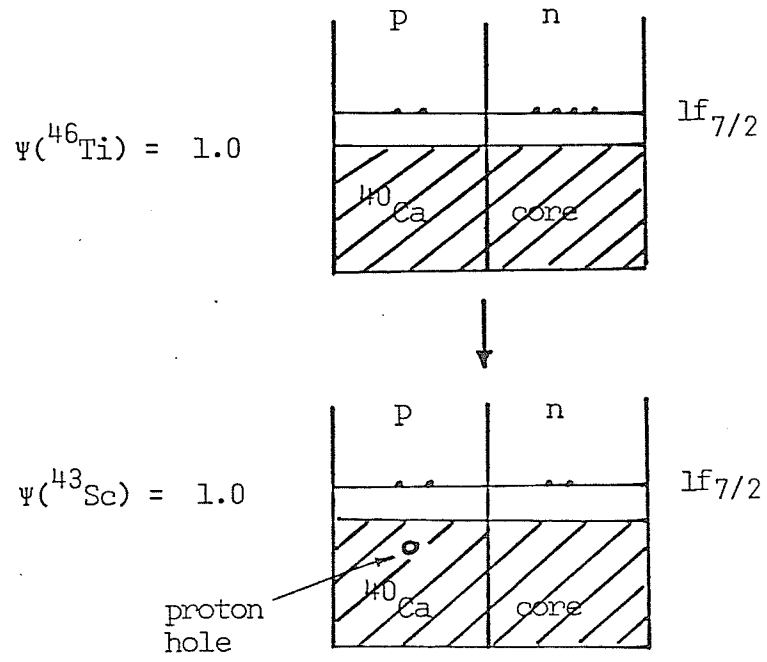

(b) positive parity state transition

Fig. (5.8) Angular distributions for the states 0.0, $7/2^-$; 1.40 Mev, $7/2^-$ and 1.83 Mev, $11/2^-$. The solid lines are the results of zero-range MFF DWBA calculations. The dashed lines are the CFF fits.

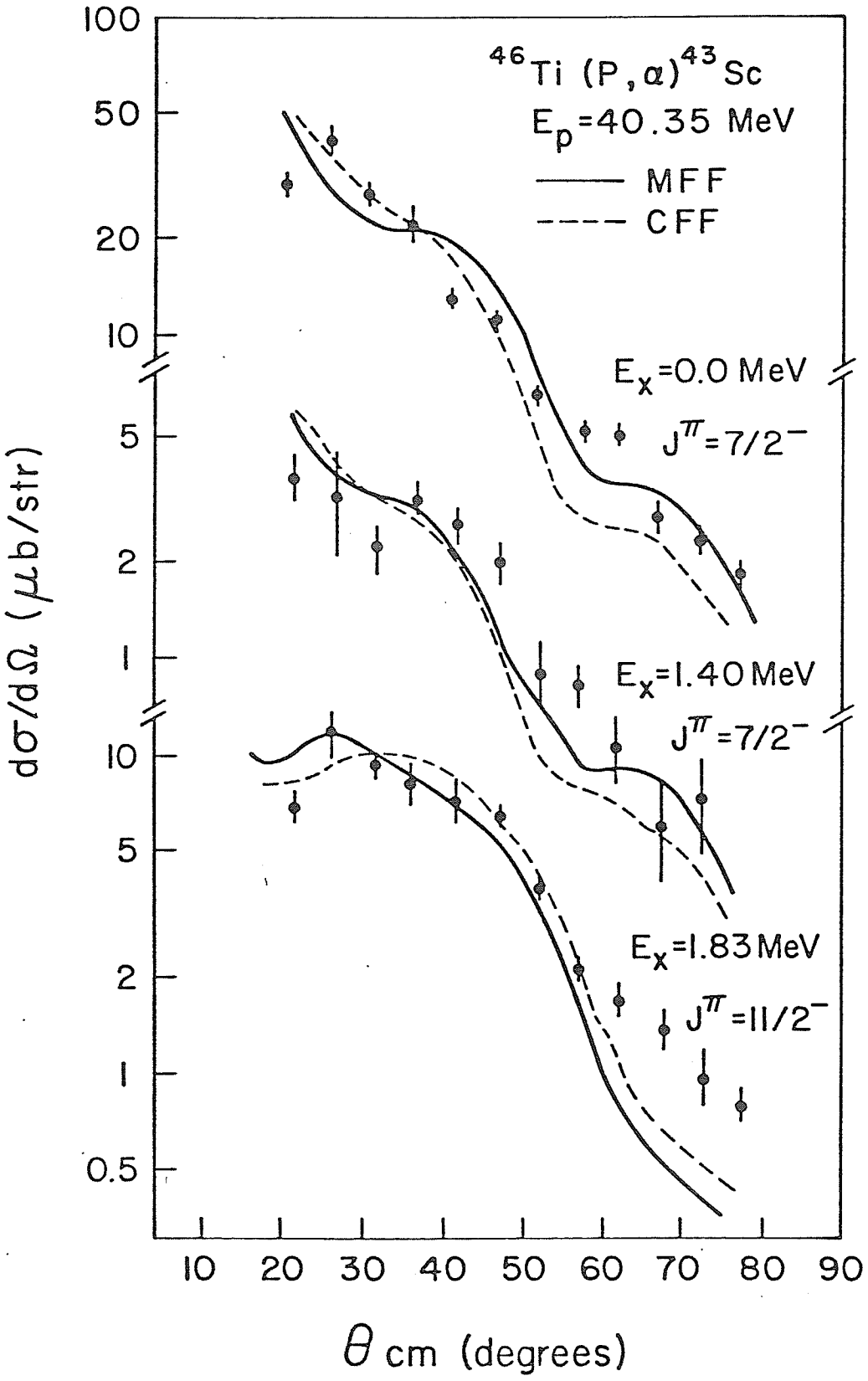
^{46}Ti (P, α)^{43}Sc
E_p=40.35 MeV
MFF
CFF
E_x=0.0 MeV
J^π=7/2$^-$
E_x=1.40 MeV
J^π=7/2$^-$
E_x=1.83 MeV
J^π=11/2$^-$
dσ/dΩ (μb/str)
θ cm (degrees)
100
50
20
10
5
2
1
10
5
2
1
0.5
10 20 30 40 50 60 70 80 90

Fig. (5.9) Angular distributions for the positive parity states 0.15 Mev, $\frac{3}{2}^+$; 0.86 Mev, $\frac{1}{2}^+$ and 2.87 Mev, $\frac{7}{2}^+$. The solid lines are the results of zero-range microscopic DWBA calculations. The dashed lines are the results of cluster calculations.

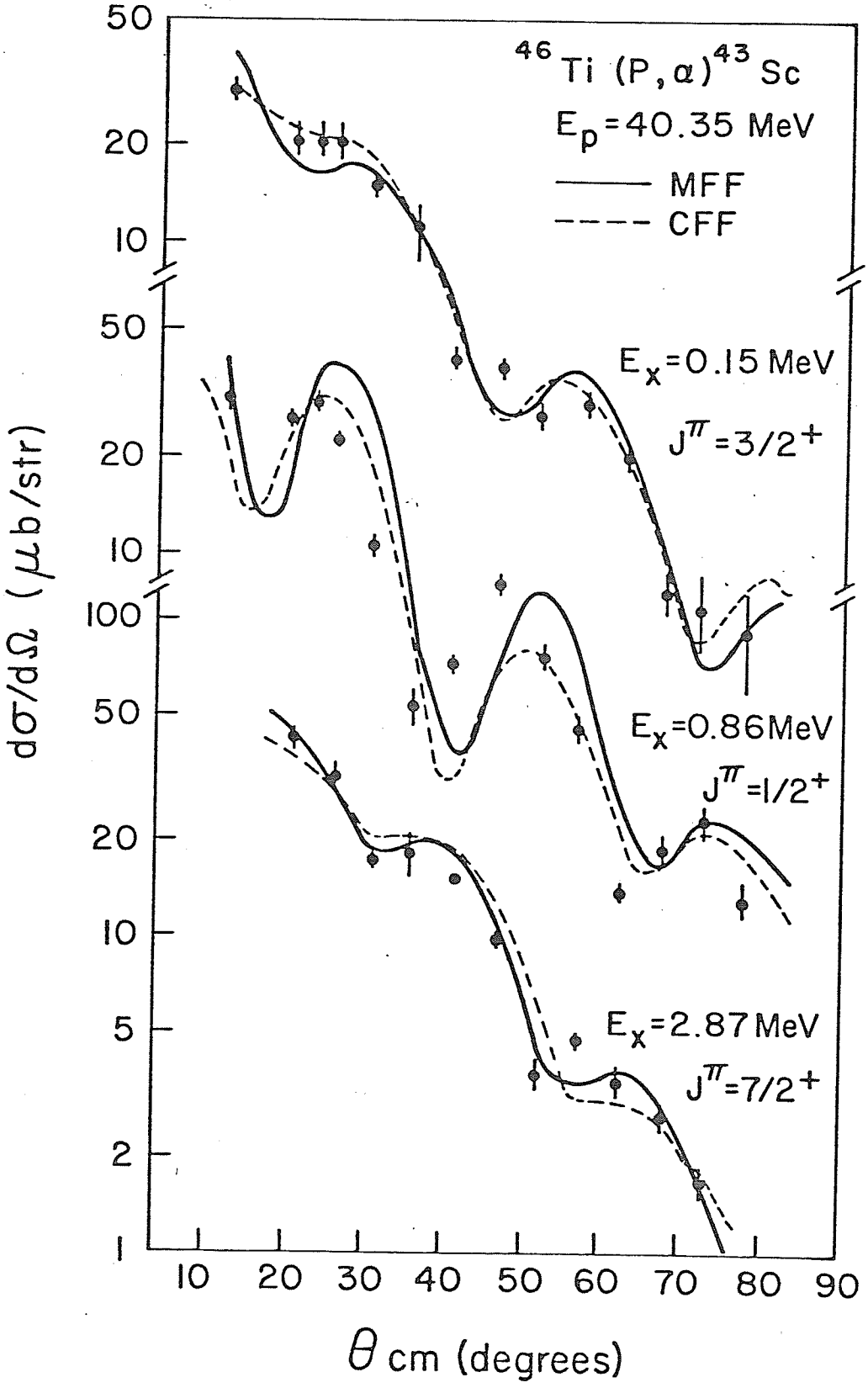
^{46}Ti (P, α)^{43}Sc
E_p=40.35 MeV
MFF
CFF
E_x=0.15 MeV
J^π=3/2$^+$
E_x=0.86MeV
J^π=1/2$^+$
E_x=2.87 MeV
J^π=7/2$^+$
dσ/dΩ (μb/str)
θ cm (degrees)
50
20
10
50
20
10
100
50
20
10
5
2
1
10 20 30 40 50 60 70 80 90

Fig. (5.10) Angular distributions for the high spin states 2.99 Mev, $^{15}/_{2}^{-}$ and 3.12 Mev, $^{19}/_{2}^{-}$. The solid lines are the results of zero-range microscopic DWBA calculations. The dashed lines are the cluster fits.

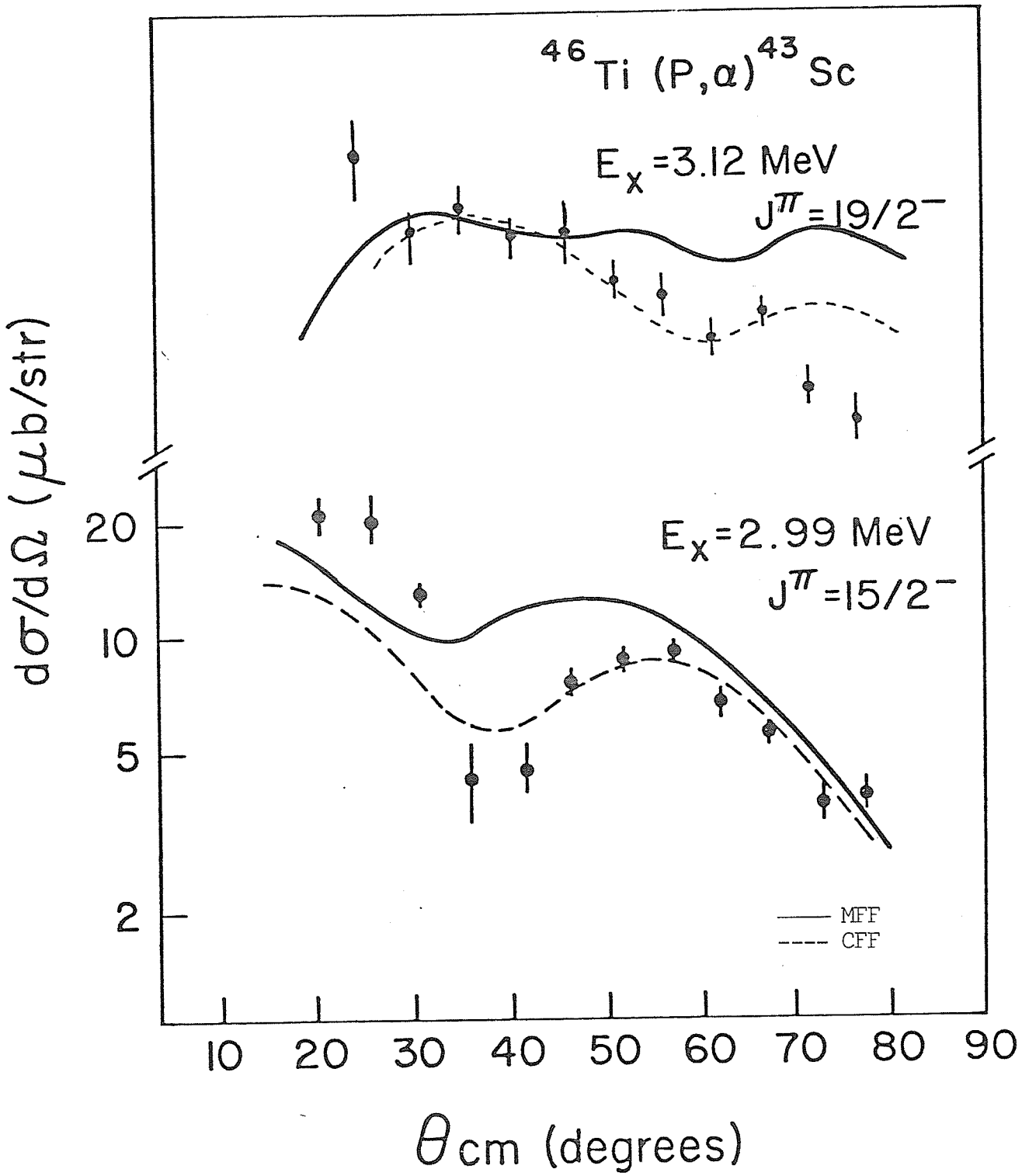
^{46}Ti (P,α)^{43}Sc
E_x=3.12 MeV
J^π=19/2$^-$
E_x=2.99 MeV
J^π=15/2$^-$
MFF
CFF
dσ/dΩ (μb/str)
20
10
5
2
10 20 30 40 50 60 70 80 90
θcm (degrees)

Fig. (5.11) Angular distributions for the isobaric analogs of the low-lying states of ^{43}Ca, the $T=\frac{3}{2}$: 4.23 Mev, $\frac{7}{2}^-$; 5.23 Mev, $\frac{3}{2}^+$ and 6.22 Mev, $\frac{1}{2}^+$ states. The solid lines are the results of zero-range MFF DWBA calculations. The dashed lines are the result of CFF fits.

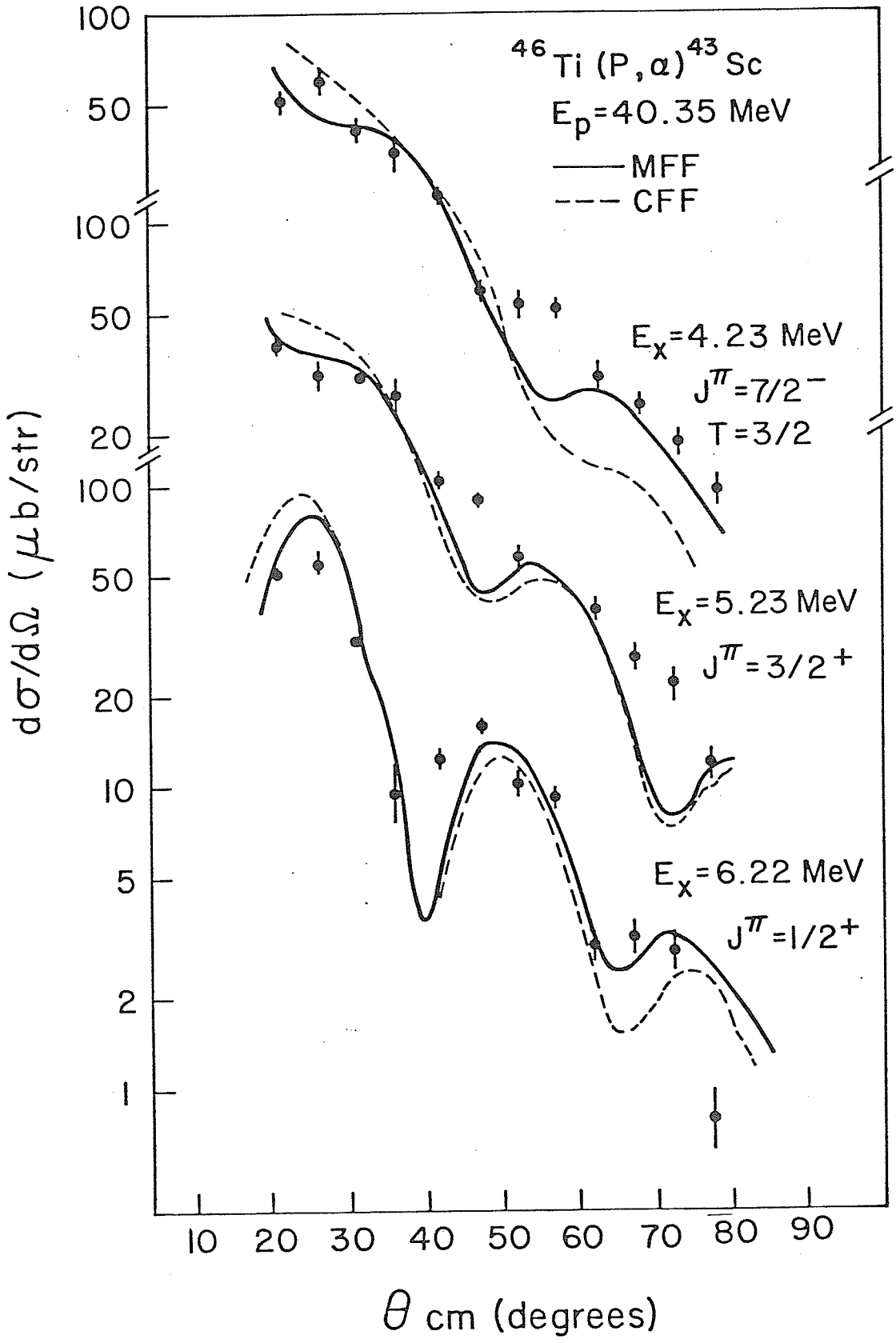
^{46}Ti (P, α)^{43}Sc
E_p=40.35 MeV
MFF
CFF
E_x=4.23 MeV
J^π=7/2$^-$
T=3/2
E_x=5.23 MeV
J^π=3/2$^+$
E_x=6.22 MeV
J^π=1/2$^+$
dσ/dΩ (μb/str)
θ cm (degrees)
100
50
20
10
5
2
1
10 20 30 40 50 60 70 80 90

Table (5.2) Comparisons of σ_{exp}/σ_{th} for states in ^{43}Sc from the $^{46}Ti(p,\alpha)^{43}Sc$ reaction

state, J^π	$\lvert^{46}Ti>$	$\lvert^{43}Sc>$	configurations of transferred nucleons	No of nodes N	σ_{exp}/σ_{th} (*)
0.0, $7/2^-$	(a)	(b)	$\pi lf_{7/2}(1\ 7/2) \otimes \nu lf^2_{7/2}(0\ 0)$	3	$\equiv 1.0$
0.15, $3/2^+$	(a)	(c)	$\pi ld_{3/2}(1\ 3/2) \otimes \nu lf^2_{7/2}(0\ 0)$	3	0.75
0.86, $1/2^+$	(a)	(c)	$\pi 2s_{1/2}(1\ 1/2) \otimes \nu lf^2_{7/2}(0\ 0)$	4	2.5
1.40, $7/2^-$	(a)	(b)	$\pi lf_{7/2}(1\ 7/2) \otimes \nu lf^2_{7/2}(0\ 0)$	3	0.1
1.83, $11/2^-$	(a)	(d)	$\pi lf_{7/2}(1\ 7/2) \otimes \nu lf^2_{7/2}(2\ 2)$	2	1.8
2.87, $7/2^+$	(a)	(c)	$\pi ld_{3/2}(1\ 3/2) \otimes \nu lf^2_{7/2}(2\ 2)$	2	5.5
2.99, $15/2^-$	(a)	(d)	$\pi lf_{7/2}(1\ 7/2) \otimes \nu lf^2_{7/2}(2\ 6)$	1	1.2
3.12, $19/2^-$	(a)	(d)	$\pi lf_{7/2}(1\ 7/2) \otimes \nu lf^2_{7/2}(2\ 6)$	0	0.5
4.23, $7/2^-$	(a)	(b)	$\pi lf_{7/2}(1\ 7/2) \otimes \nu lf^2_{7/2}(0\ 0)$	3	1.1

(*) An overall normalization N of 46.3×10^6 was used for the ground state. See text for definition of N.

(a) $\lvert^{46}Ti> = \lvert^{40}Ca$ doubly closed shell $> \lvert\ \pi lf^2_{7/2}(0\ 0) \otimes \nu lf^4_{7/2}(0\ 0)\ >$

(b) $\lvert^{43}Sc> = \lvert^{40}Ca$ doubly closed shell $> \lvert\ \pi lf_{7/2}(1\ 7/2) \otimes \nu lf^2_{7/2}(0\ 0)\ >$

(c) $\lvert^{43}Sc> = \lvert^{40}Ca$ doubly closed shell $> \lvert\ \pi j^{-1}\ \pi lf^2_{7/2}(0\ 0) \times \nu lf^2_{7/2}(0\ 0)\ >$

(d) $\lvert^{43}Sc> = \lvert^{40}Ca$ doubly closed shell $> \lvert\ \pi lf_{7/2}(1\ 7/2) \otimes \nu lf^2_{7/2}(\nu\ j)\ >$

functions are needed to predict the observed strengths. Also, it should be pointed out that for the 2.99 Mev, $15/2^-$ state it was assumed that the two neutrons transferred are coupled to J' = 6 and not to 4 for example. The explanation for this is that the value of the product of the form factor and the overlap integral for J' = 4 is much smaller than that for J' = 6 resulting in a larger σ_{exp}/σ_{th} ratio.

In regards to the 1.40 Mev, $7/2^-$ state Johnstone and Payne[72] pointed out that this state cannot be understood in terms of an $(1f_{7/2})^3$ configuration and an unexcited core. They showed that the major component of this state should be 5p-2h. This picture is not very different from Seth's[73] weak-coupling core-excitation picture for the same state where he suggested that the dominant component of the wave function is the one in which the ^{42}Ca core is excited to its 0_2^+ 1.88 state, the $1f_{7/2}$ proton is weakly coupled to it. The 0_2^+ state in ^{42}Ca is known to have more than 75% 4p-2h component with the hole component predominantly in the $1d_{3/2}$ shell. Taking such a component into consideration will reduce σ_{theory} considerably since the number of nodes will be one less than the number shown in table (5.2). This will bring the ratio σ_{exp}/σ_{th} ratio into line with other states.

As for the 2.87 Mev, $7/2^+$ state it is clear that the pure hole state picture with the two neutrons coupled to angular momentum J' = 2 is inadequate to reproduce the experimentally observed strength. This suggests a more complicated structure for this state. Unfortunately no other information is available about this state in the literature.

For the $\frac{1}{2}^+$ state one expects that the ratio σ_{exp}/σ_{th} will be higher by a factor of ~ 2.3 because of the reason discussed in the text p.35.

A more realistic calculation should use shell model wave functions. As discussed in chapter 4 there are only two complete sets of shell model wave functions available for both Ti and Sc isotopes, one is the M.B.Z. model[56] and the other is the calculation of Kutschera[25]. In the present work the Kutschera wave functions will be used since they employ a more recent set of two-body matrix element. Furthermore, they have the advantage of using the same sign convention adopted in the microscopic formalism discussed in chapter 2. Kutschera provided a tabulation of the cfp's, so the same values can be used in the calculations of the overlap integral I_{AB} as were used in the shell model calculations.

Table (5.3) shows the ratios σ_{exp}/σ_{th} for the negative parity states using the Kutschera wave functions. The overlap integral was calculated for each possible configuration as prescribed in Appendix B. One notices immediately the improvement in the ratios σ_{exp}/σ_{th} over those in table (5.2).

Moreover, by introducing the 5p-2h component in the wave function of the 1.40 Mev, $\frac{7}{2}^-$ state as discussed previously, the ratio σ_{exp}/σ_{th} increased from 0.1 to 0.7. It should be mentioned that the wave function of this state (given by wave function "f" in table (5.3)) has a sign ambiguity. The signs shown gave a reasonable value for the ratio σ_{exp}/σ_{th}. The other sign choice gave a much worse value.

For the 1.83 Mev, $1\frac{1}{2}^-$ state, the strength was predicted correctly indicating that this state is mainly of 3p-0h structure. A similar conclusion has been reached by Zamick[74]. The excitation of this state

Table (5.3) Comparisons of σ_{exp}/σ_{th} for states in ^{43}Sc from the $^{46}Ti(p,\alpha)^{43}Sc$ reaction using shell model wave functions

state, J^π	$\lvert^{46}Ti>$	$\lvert^{43}Sc>$	configurations of transferred nucleons	σ_{exp}/σ_{th} (h)
0.0, $7/2^-$	(a)	(b)	All possible configurations	$\equiv 1.0$
1.40, $7/2^-$	(a)	(f)	All possible configurations	0.7
1.83, $11/2^-$	(a)	(c)	All possible configurations	1.0
2.99, $15/2^-$	(a)	(d)	All possible configurations	0.7
3.12, $19/2^-$	(a)	(g)	$\pi lf_{7/2}(1\ 7/2) \otimes \nu lf_{7/2}^2(2\ 6)$	0.8

(a) $0.855\ |\pi lf_{7/2}^2(0\ 0) \otimes \nu lf_{7/2}^4(0\ 0);\ 0^+> + 0.496\ |\pi lf_{7/2}^2(2\ 2) \otimes \nu lf_{7/2}^4(2\ 2);\ 0^+> + .096\ |\pi lf_{7/2}^2(2\ 4) \otimes \nu lf_{7/2}^4(2\ 4);\ 0^+>$

(b) $0.788\ |\pi lf_{7/2}(1\ 7/2) \otimes \nu lf_{7/2}^2(0\ 0);\ 7/2^-> + 0.562\ |\pi lf_{7/2}(1\ 7/2) \otimes \nu lf_{7/2}^2(2\ 2);\ 7/2^-> + 0.22\ |\pi lf_{7/2}(1\ 7/2) \otimes \nu lf_{7/2}^2(2\ 4);\ 7/2^->$

(c) $0.815\ |\pi lf_{7/2}(1\ 7/2) \otimes \nu lf_{7/2}^2(2\ 2);\ 11/2^-> + 0.505\ |\pi lf_{7/2}(1\ 7/2) \otimes \nu lf_{7/2}^2(2\ 4);\ 11/2^->$

(d) $0.879\ |\pi lf_{7/2}(1\ 7/2) \otimes \nu lf_{7/2}^2(2\ 4);\ 15/2^-> + 0.477\ |\pi lf_{7/2}(1\ 7/2) \otimes \nu lf_{7/2}^2(2\ 6);\ 15/2^->$

(e) $1.0\ |\pi lf_{7/2}^2(0\ 0) \otimes \nu lf_{7/2}^4(0\ 0);\ 0^+>$

(f) $\sqrt{.25}\ |\pi lf_{7/2}(1\ 7/2) \otimes \nu lf_{7/2}^2(0\ 0);\ 7/2^-> + \sqrt{.75}\ |\pi lf_{7/2}(1\ 7/2) \otimes \nu f_{7/2}^4(0\ 0)\ \nu d_{3/2}^{-2}(0\ 0)>$

(g) $1.0\ |\pi lf_{7/2}(1\ 7/2) \otimes \nu lf_{7/2}^2(2\ 6);\ 19/2^->$

(h) The overall normalization N is 47.2×10^6. It was adjusted to yield a value of 1.0 for the ground state.

in both (^{6}Li,τ) and (α,p) reactions as mentioned earlier lends further support for this conclusion.

Although the $(1f_{7/2})^n$ model calculations gave satisfactory results, it is important to include the $1f_{7/2} - 2p_{3/2}$ mixing[58]. This is so because the energy difference is so small that the $2p_{3/2}$ and $1f_{7/2}$ configurations are mixed. Another reason for the need to include the configuration mixing from $2p_{3/2} - 1f_{5/2}$ shells is that the ^{43}Sc spectrum calculated by Flowers[60], by allowing the three extra-core nucleons to occupy the complete 1f2p shell, agrees better with the experimental one. However, in order to use such wave functions one needs a similar calculation for the target nucleus. Such calculations are not currently available to us.

The uncertainty of the ratio σ_{exp}/σ_{th} shown in tables (5.2) and (5.3) depends on the quality of the fit and the size of the error bars. A typical value of uncertainty is about 15% for most of the states. This increases up to about 45% for the 0.86 Mev, $\frac{1}{2}^+$ state. It should be noted that the uncertainties mentioned above are due only to the normalization procedure. Other uncertainties due to approximations in the calculation of the MFF have been discussed earlier in chapter 2.

Section B: The ^{48}Ti(p,α)^{45}Sc Reaction

B.1 α-spectrum:

The ^{48}Ti(p,α)^{45}Sc reaction was studied at a proton energy of 40.35 Mev. The emerging α-particles were detected using the same detection system used for the ^{46}Ti(p,α) reaction described previously in chapter 3. All experimental details and target information are in chapter 3.

Fig.(5.12) shows a typical spectrum of ^{45}Sc at $\theta_{lab} = 25°$. The overall energy resolution was about 80 kev FWHM resulting from the same

Fig. (5.12) The $^{48}Ti(p,\alpha)^{45}Sc$ spectrum

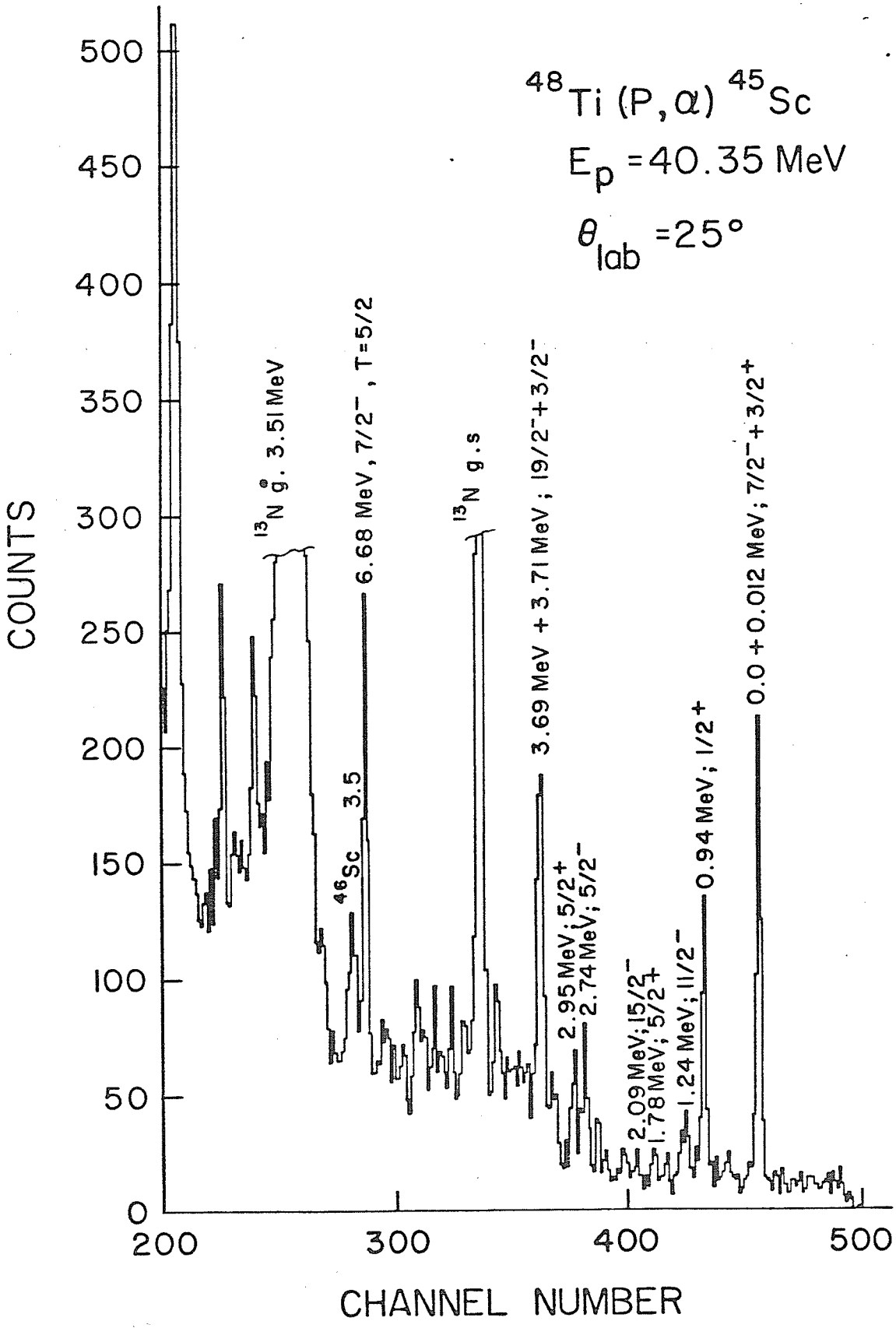
^{48}Ti (P, α) ^{45}Sc
E_p = 40.35 MeV
θ_{lab} = 25°
COUNTS
CHANNEL NUMBER
0
50
100
150
200
250
300
350
400
450
500
200
300
400
500
^{13}N g. 3.51 MeV
^{46}Sc 3.5
6.68 MeV, 7/2⁻, T=5/2
^{13}N g.s
3.69 MeV + 3.71 MeV; 19/2⁻+3/2⁻
2.95 MeV; 5/2⁺
2.74 MeV; 5/2⁻
2.09 MeV; 15/2⁻
1.78 MeV; 5/2⁺
1.24 MeV; 11/2⁻
0.94 MeV; 1/2⁺
0.0 + 0.012 MeV; 7/2⁻+3/2⁺

factors discussed in section A.

States in ^{45}Sc with excitation energies up to $\sim$ 7 Mev were observed and they are summarized in table (5.4). The excitation energies given there were calculated as prescribed in chapter 3.

One may notice from table (5.4) that the number of states excited strongly enough to extract angular distributions in the present (p,α) study is much less than the number of states observed in single-particle pickup[31], for example. This feature is also observed in the study of the $^{48}Ti(\bar{p},\alpha)^{45}Sc$ reaction at 80 Mev[28]. This behaviour might be due to the coherence property of the (p,α) reaction where cancellation of amplitudes can occur.

Otherwise, the main features of the ^{43}Sc spectrum discussed in section A were observed again in ^{45}Sc including the excitation of the 6.68 Mev, $\frac{7}{2}^-$ state which is the IA of the ^{45}Ca g.s. T = $\frac{5}{2}$. Simple calculations predict this state to have an excitation energy of 6.75 Mev, while the M.B.Z. model prediction is 6.48 Mev. Both are in reasonable agreement with experiment.

One notices from Fig. (5.12) and table (5.4) that the (p,α) reaction can excite states with spins $11\frac{1}{2}^-$, $15\frac{1}{2}^-$ and $19\frac{1}{2}^-$. Such high spin states cannot be observed in the (d,^{3}He) reaction. This represents one of the advantages of studying the (p,α) reaction, in spite of the considerable difficulty in extracting quantitative information from the low cross sections to these states. These high spin states can be seen in the (p,p') reaction. Positive parity states appear at energies as low as 12 Kev. The explanation of this very low excitation energy is given in chapter 4.

Table (5.4) Data Summary for ^{45}Sc

Ex, J^{π}		
$(p,\alpha)^{(a)}$	$(p,\alpha)^{(76)}$	$(d,^3He)^{(31)}$
0.0, $7/2^-$ }	0.0, $7/2^-$	0.0, $7/2^-$
0.012, $3/2^+$ }		0.012, $3/2^+$
		0.377, $3/2^-$
		0.543, $5/2^+$
		0.72, $5/2^-$
0.94, $1/2^+$	0.94, $1/2^+$	0.94, $1/2^+$
		1.067, $3/2^-$
1.24, $11/2^-$	1.24, $11/2^-$	
		1.3 $(3/2,5/2)^+$
		1.557, $1/2^-$
1.78, $5/2^+$		1.8, $3/2^+$ $5/2^+$
2.09, $15/2^-$	2.11, $15/2^-$	
		2.29, $3/2^-$
2.74, $5/2^-$	2.76, $5/2^-$	
2.95, $5/2^+$	2.98,	2.91, $5/2^+$
		3.48, $5/2^+$
	3.57, $17/2^-$	
3.69, $19/2^-$	3.69, $19/2^-$	
3.71, $3/2^-$		3.73, $5/2^+$
6.68, $7/2^-$, T = $5/2$		

(a) present work.

B.2 Angular Distributions - Cluster DWBA Cluster Calculations:

Figs. (5.13), (5.14) and (5.15) show the angular distributions obtained for states (or groups of states) in ^{45}Sc. The error bars represent the quadratic sum of the statistical and fitting errors. The solid lines are the result of zero-range DWBA calculations using the code DWUCK 2[36] and cluster form factors as discussed previously.

The J^{π} assignments for the states 0.94 Mev, 1.24 Mev, 1.78 Mev, 2.09 Mev, 2.74 Mev and 2.95 Mev were taken from the literature[77]. The J^{π} values are $1/2^+$, $11/2^-$, $5/2^+$, $15/2^-$, $5/2^-$ and $5/2^+$, respectively. The DWBA calculations are in agreement with these assignments.

As mentioned earlier, the first excited state ($J^{\pi} = 3/2^+$) lies only 12 Kev above the ground state[31],[77] (see also chapter 4) which makes it impossible to resolve these two states. In an attempt to analyze this doublet a linear combination of $7/2^-$ and $3/2^+$ angular distributions were used to fit the experimental distribution. It was found that the linear combination:

$$1.0\ (\text{g.s.},\ 7/2^-) + (0.6 \pm 0.1)\ (0.012,\ 3/2^+)$$

gave a reasonable fit to the data. This relative strength ratio between the $3/2^+$ and $7/2^-$ states is close to the ratio between the 0.0, $7/2^-$ and 0.15 Mev, $3/2^+$ states in ^{43}Sc.

A similar situation has been encountered for the states at 3.69 Mev where no single J^{π} angular distribution can fit the data. Careful analysis of the peak width showed that this is actually a doublet consisting of the states 3.69 Mev, $19/2^-$ and 3.71 Mev, $3/2^-$. This is supported by the fit shown in Fig. (5.15) where the linear combination:

Fig. (5.13) Angular distributions for the states 0.0, $7/2^-$ and 0.012, $3/2^+$, 1.24, $11/2^-$ and 2.74, $5/2^-$. The solid lines are the result of cluster zero-range DWBA calculations.

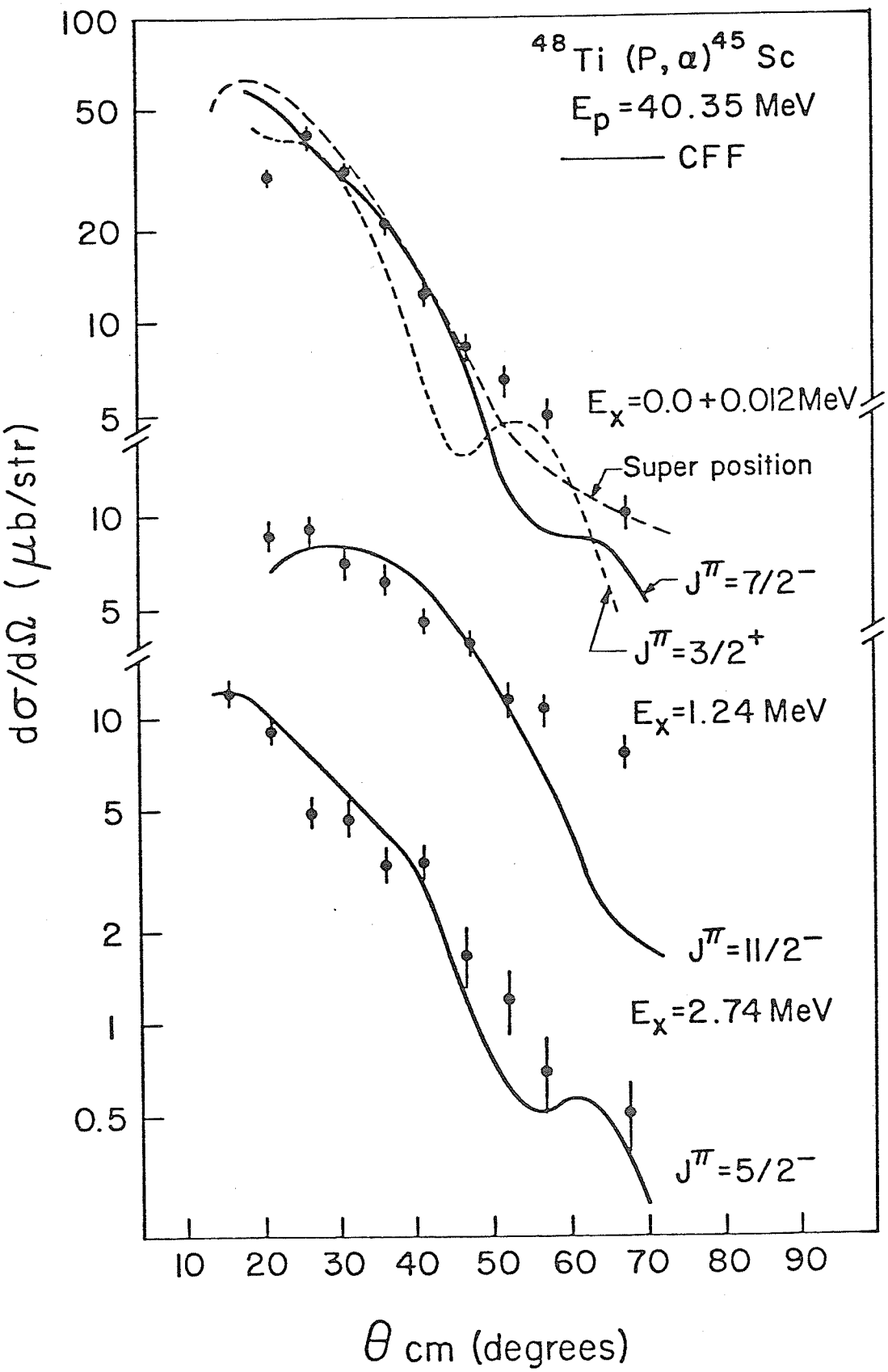
^{48}Ti (P, α)^{45}Sc
E_p = 40.35 MeV
CFF
E_x = 0.0 + 0.012 MeV
Super position
$J^\pi = 7/2^-$
$J^\pi = 3/2^+$
E_x = 1.24 MeV
$J^\pi = 11/2^-$
E_x = 2.74 MeV
$J^\pi = 5/2^-$
dσ/dΩ (μb/str)
θ cm (degrees)
100
50
20
10
5
10
5
10
5
2
1
0.5
10
20
30
40
50
60
70
80
90

Fig. (5.14) Angular distributions for the states 0.94, $\frac{1}{2}^+$ 1.78, $\frac{5}{2}^+$ and 2.95, $\frac{5}{2}^+$. The solid lines are the result of zero-range DWBA cluster calculations.

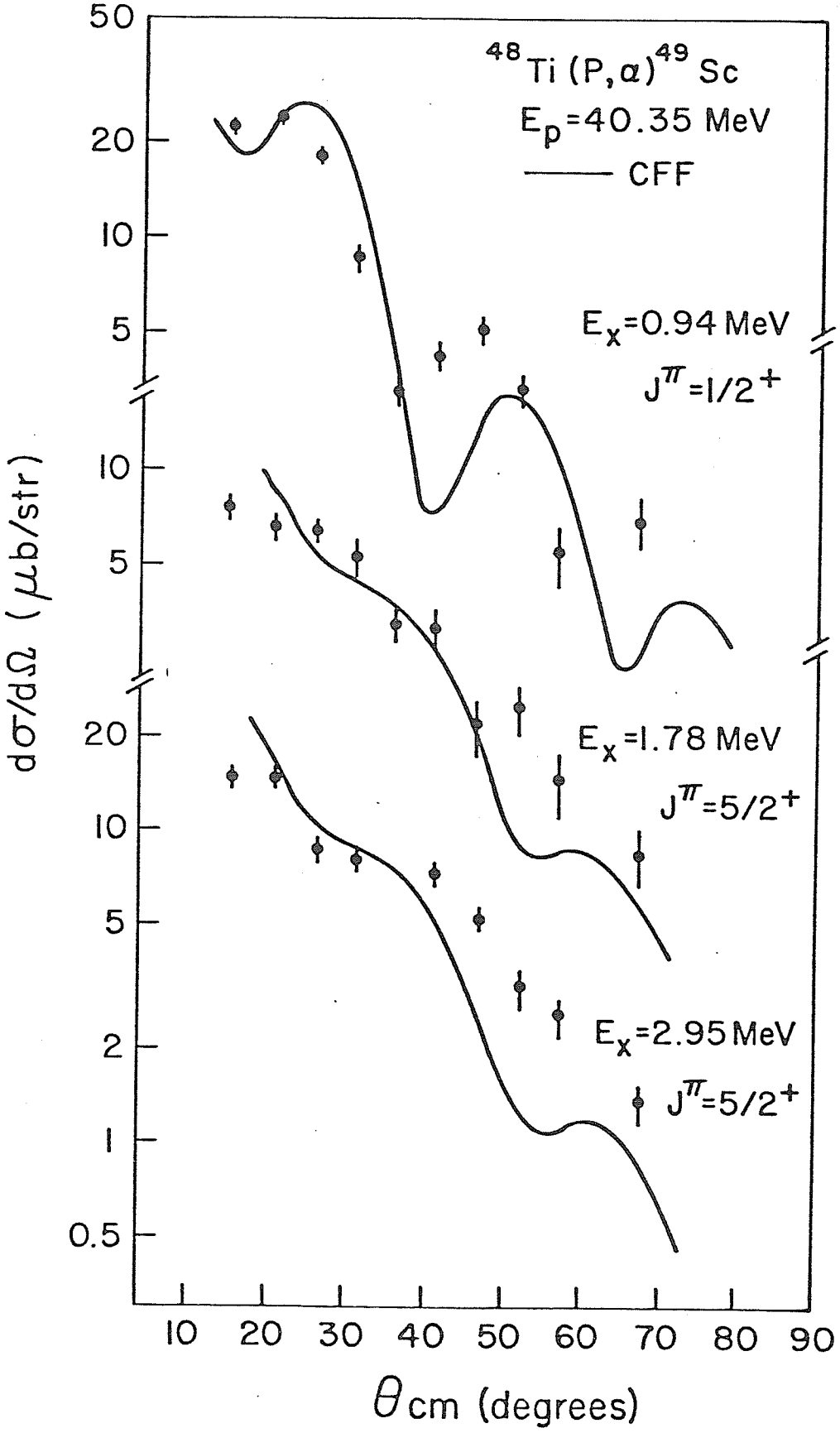
^{48}Ti (P,α)^{49}Sc
E_p=40.35 MeV
CFF
E_x=0.94 MeV
J^π=1/2$^+$
E_x=1.78 MeV
J^π=5/2$^+$
E_x=2.95 MeV
J^π=5/2$^+$
dσ/dΩ (μb/str)
θcm (degrees)
50
20
10
5
10
5
20
10
5
2
1
0.5
10 20 30 40 50 60 70 80 90

Fig. (5.15) Angular distributions for the states 2.09, $^{15}/_{2}^{-}$; 3.69, $^{19}/_{2}^{-}$; 3.71, $^{3}/_{2}^{-}$ and 6.68 Mev, $^{7}/_{2}^{-}$. The solid lines are the results of DWBA cluster zero-range calculations.

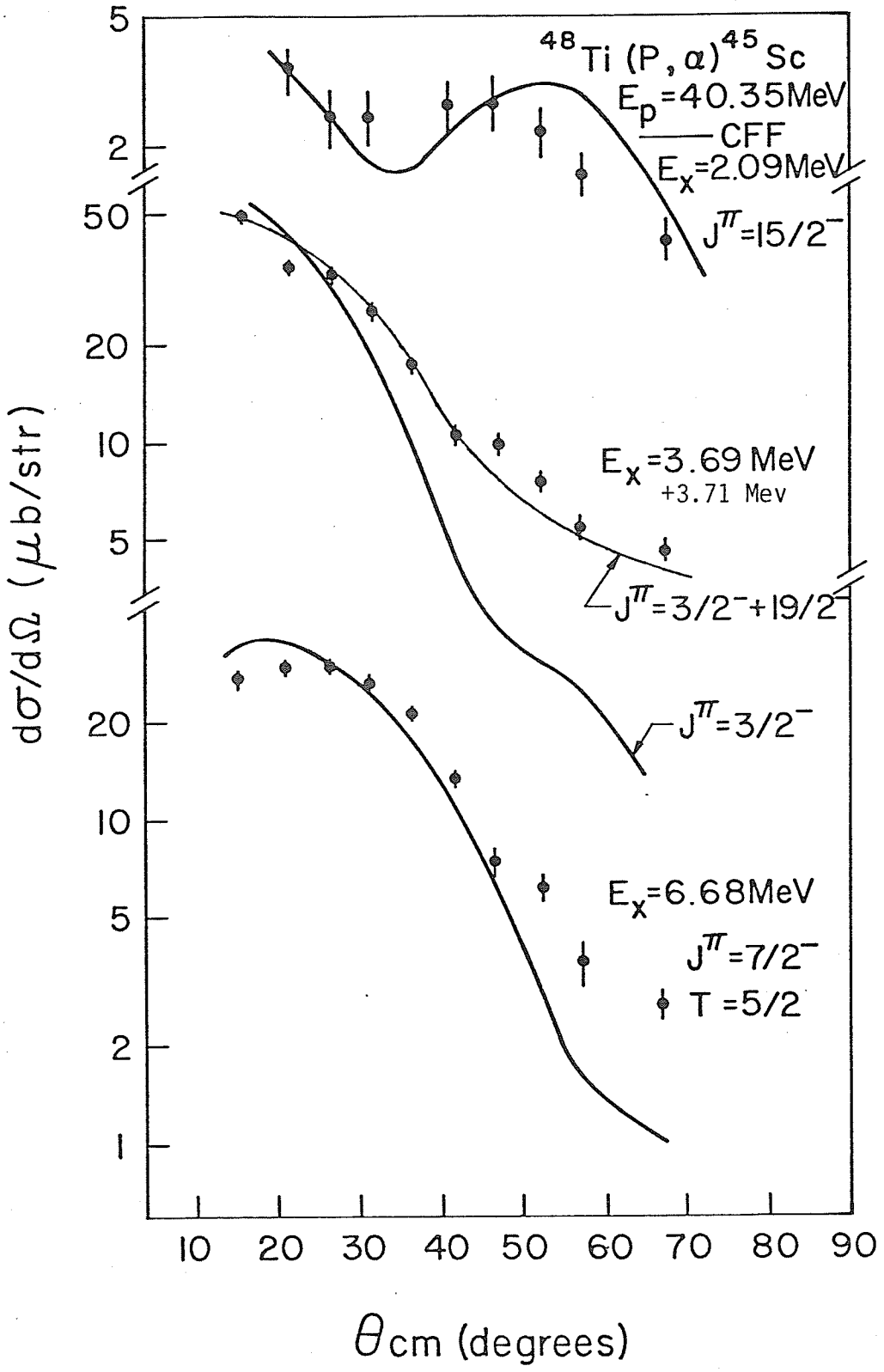
^{48}Ti (P, α)^{45}Sc
E_p=40.35MeV
CFF
E_x=2.09MeV
J^π=15/2$^-$
E_x=3.69 MeV
+3.71 Mev
J^π=3/2$^-$+19/2$^-$
J^π=3/2$^-$
E_x=6.68MeV
J^π=7/2$^-$
T =5/2
dσ/dΩ (μb/str)
θcm (degrees)

$$1.0\ (3.69\ \text{Mev},\ 19\tfrac{-}{2}) + (1.0 \pm .1)(3.71\ \text{Mev},\ \tfrac{3}{2}^-)$$

fits the data well.

The 1.78 Mev state has been assigned to the value $J^\pi = \frac{5}{2}^+$ on the basis of the angular distribution. The value $J^\pi = (\frac{3}{2}, \frac{5}{2})^+$ had been assigned to this level from the reaction $^{46}Ti(d,^3He)^{45}Sc$[29]. However from life time measurements[78] and the $(\alpha,p\gamma)$ reaction a unique assignment $J^\pi = \frac{5}{2}^+$ has been obtained. This is in agreement with our assignment.

B.3 DWBA Calculations - Microscopic Form Factor:

A procedure similar to that described in section A.3 was followed in analyzing the $^{48}Ti(p,\alpha)^{45}Sc$ reaction using the MFF. Zero order calculations where only simple configurations for the transferred nucleons are assumed will be considered first. In these calculations the ^{48}Ti nucleus was assumed to be a doubly closed ^{40}Ca core with two extra-core $1f_{7/2}$ protons and six extra-core $1f_{7/2}$ neutrons. Again, the negative parity states are then populated by picking up a $1f_{7/2}$ proton and two $1f_{7/2}$ neutrons with the proper angular momentum coupling. The positive parity states are populated by picking up a (s-d) shell proton and two $1f_{7/2}$ neutrons. Figs. (5.16) and (5.17) show the results of zero-range DWBA calculations using the microscopic form factor. We notice the quality of the fit is comparable to or somewhat better than that of the cluster form factor fits.

In all the above calculations the microscopic form factor tail was replaced by the CFF tail. The overlap integral I_{AB} was calculated as described in Appendix B, and by the aid of the recursion relations of

Fig. (5.16) Angular distributions for the states 0.0, $\frac{7}{2}^-$ + 0.012, $\frac{3}{2}^+$; 1.24 Mev, $\frac{11}{2}^-$ and 2.09, $\frac{15}{2}^-$. The solid lines are the result of zero-range microscopic DWBA calculations. The dashed lines are the cluster fits.

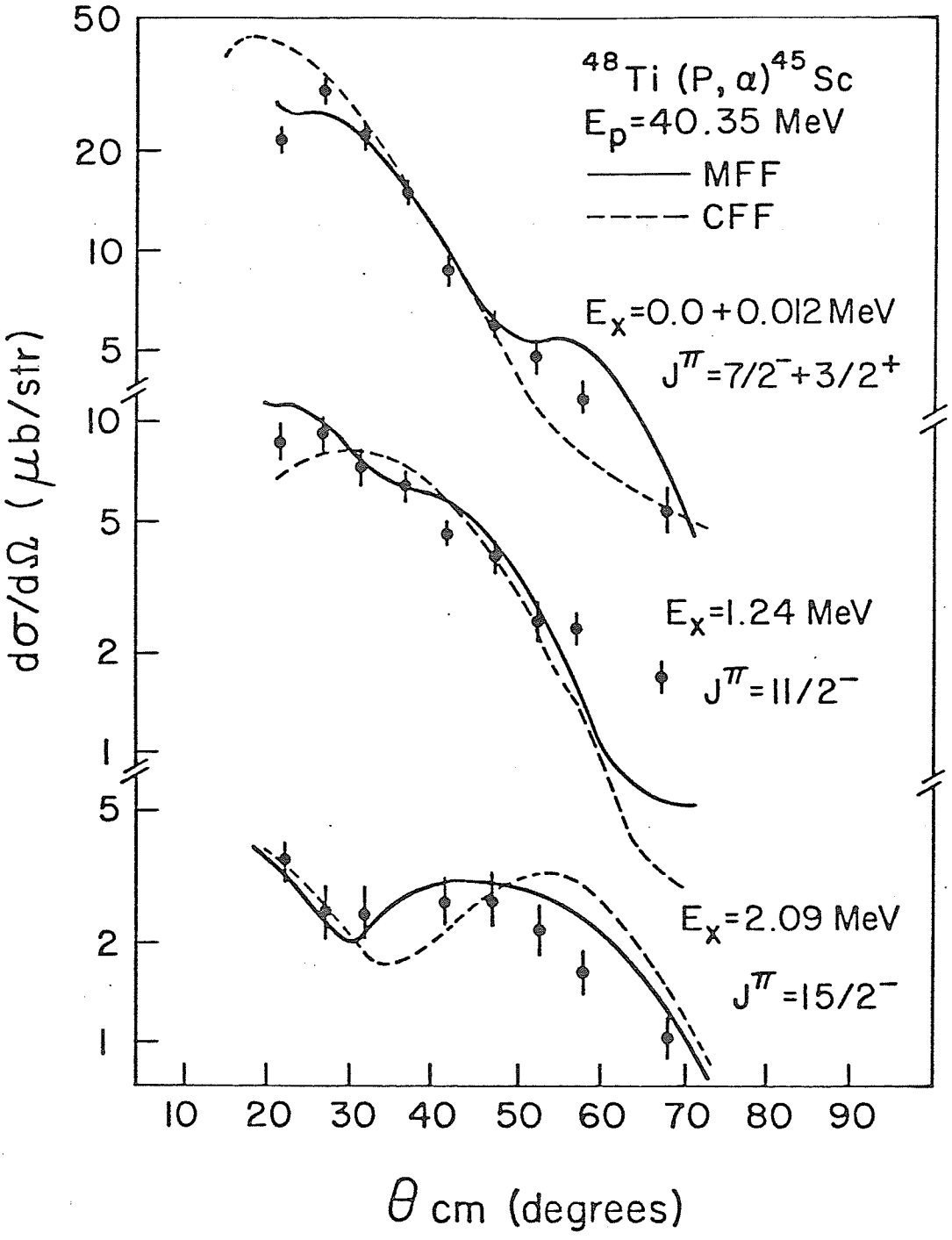
^{48}Ti (P, α)^{45}Sc
E_p=40.35 MeV
MFF
CFF
E_x=0.0 + 0.012 MeV
J^π=7/2$^-$+3/2$^+$
E_x=1.24 MeV
J^π=11/2$^-$
E_x=2.09 MeV
J^π=15/2$^-$
dσ/dΩ (μb/str)
θ cm (degrees)
50
20
10
5
2
1
10 20 30 40 50 60 70 80 90

Fig. (5.17) Angular distributions for the states 0.94, $\frac{1}{2}^+$; 2.74, $\frac{5}{2}^-$, 2.95, $\frac{5}{2}^-$ and 6.68, $\frac{7}{2}^-$. The solid lines are the result of zero-range microscopic DWBA calculations. The dashed lines are the cluster fits.

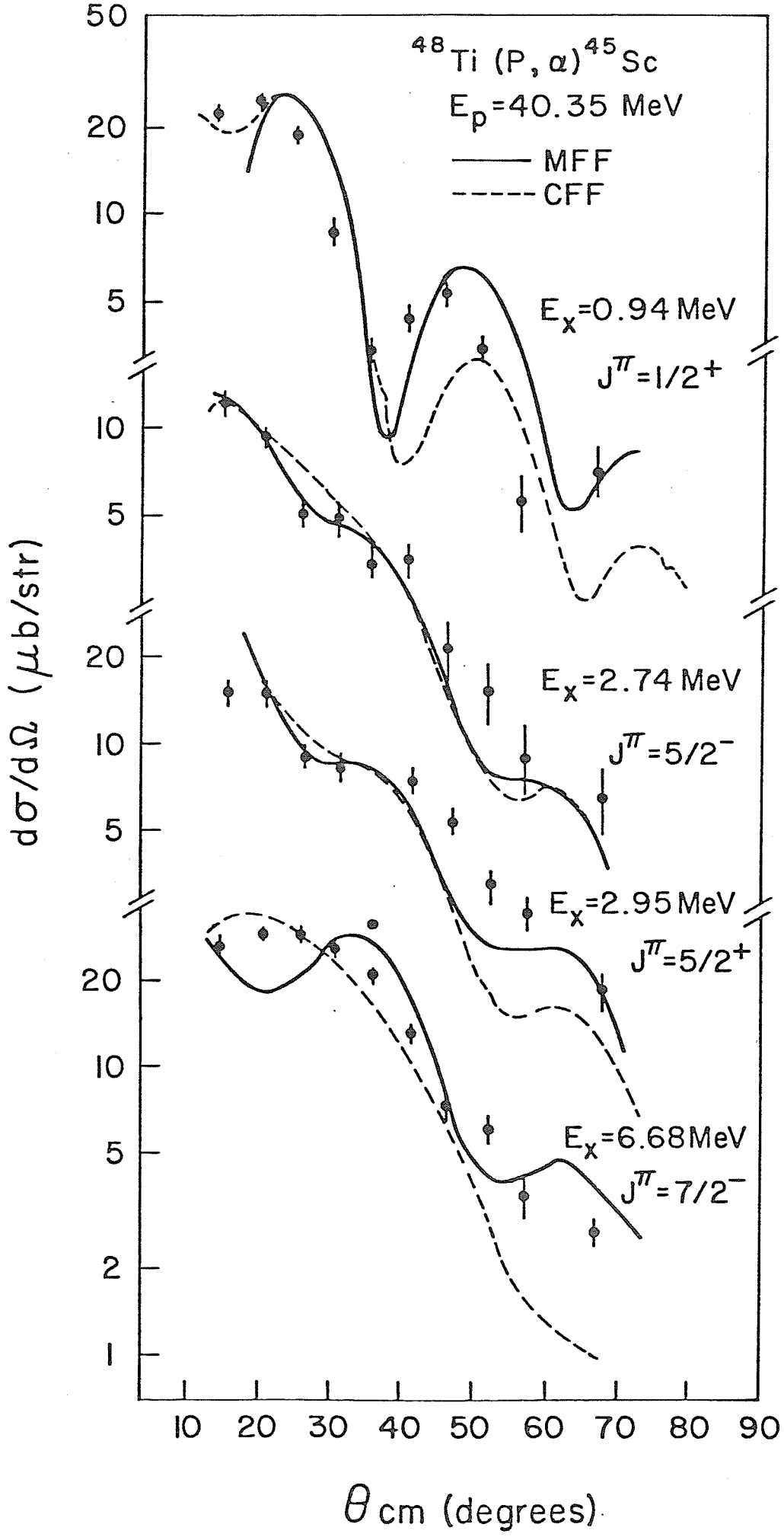
^{48}Ti (P, α)^{45}Sc
E_p=40.35 MeV
MFF
CFF
E_x=0.94 MeV
J^π=1/2$^+$
E_x=2.74 MeV
J^π=5/2$^-$
E_x=2.95 MeV
J^π=5/2$^+$
E_x=6.68 MeV
J^π=7/2$^-$
dσ/dΩ (μb/str)
θ cm (degrees)

Ref. (38).

Table (5.5) shows the ratios σ_{exp}/σ_{th} for states in ^{45}Sc calculated according to the simple picture described above. With the exception of the 3.71 Mev, $3/2^-$ all the ratios σ_{exp}/σ_{th} are in agreement with one another within a factor of 3. Another exception is the 2.74 Mev, $5/2^-$ state. The ratio σ_{exp}/σ_{th} for this state is two order of magnitudes higher than other ratios. This is a direct result of the low value of the structure factor:

$$I_{AB}(\gamma,J',J) \cdot \begin{bmatrix} \ell_1 & \ell_2 & J' \\ 1/2 & 1/2 & 0 \\ j_1 & j_2 & J' \end{bmatrix} \cdot \begin{bmatrix} J' & \ell_3 & L \\ 0 & 1/2 & 1/2 \\ J' & j & J \end{bmatrix}$$

for these states. Table (5.6) shows the structure factors for the 2.74 Mev, $5/2^-$ and 3.71 Mev, $3/2^-$ states compared to the ground state. It is clear that for these states the $(1f_{7/2})^n$ picture is inadequate.

Pohl[79] has suggested that the ^{48}Ti ground state contains a neutron component of the form $[1f_{7/2}^5(3\ 5/2) \otimes 1f_{5/2}(1\ 5/2)]_{J=0}$ which is as high as 20%. Furthermore, the $^{48}Ti(p,d)^{47}Ti$ reaction[80] provides evidence for the presence of 2p-shell neutron components in the ground state wave function through the ℓ=1 transitions. Also the excitation of $3/2^-$ states in the $^{48}Ti(d,^3He)^{47}Sc$ reaction[30],[31] is evidence that there is a 2p-shell proton component in the ^{48}Ti ground state wave function. Thus, a shell model calculation in the $1f_{7/2}$ - $2p_{3/2}$ - $1f_{5/2}$ basis is required to describe the observed strength properly.

The states 0.0 Mev, $7/2^-$; 1.24 Mev, $11/2^-$; 3.69 Mev, $19/2^-$ and 6.68 Mev,

Table (5.5) Comparison of σ_{exp}/σ_{th} for states in ^{45}Sc from the $^{48}Ti(p,\alpha)$ Reaction - Zero order calculations

state, J^π	$\|^{48}Ti>$	$\|^{45}Sc>$	configurations of transferred nucleons	No of nodes N	σ_{exp}/σ_{th} (*)
0.0, $7/2^-$	(a)	(b)	$\pi 1f_{7/2}(1\ 7/2)\otimes\nu 1f^2_{7/2}(0\ 0)$	3	≡ 1.0
0.012, $3/2^+$	(a)	(c)	$\pi 1d_{3/2}(1\ 3/2)\otimes\nu 1f^2_{7/2}(0\ 0)$	3	0.7
0.94, $1/2^+$	(a)	(c)	$\pi 2S_{1/2}(1\ 1/2)\otimes\nu 1f^2_{7/2}(0\ 0)$	4	1.9
1.24, $11/2^-$	(a)	(b)	$\pi 1f_{7/2}(1\ 7/2)\otimes\nu 1f^2_{7/2}(2\ 2)$	2	1.6
1.78, $5/2^+$	(a)	(c)	$\pi 1d_{5/2}(1\ 5/2)\otimes\nu 1f^2_{7/2}(0\ 0)$	3	0.3
2.09, $15/2^-$	(a)	(b)	$\pi 1f_{7/2}(1\ 7/2)\otimes\nu 1f^2_{7/2}(2\ 6)$	1	0.4
2.74, $5/2^-$	(a)	(b)	$\pi 1f_{7/2}(1\ 7/2)\otimes\nu 1f^2_{7/2}(2\ 2)$	3	(102)
2.95, $5/2^+$	(a)	(c)	$\pi 1d_{5/2}(1\ 5/2)\otimes\nu 1f^2_{7/2}(0\ 0)$	3	0.33
3.69, $19/2^-$	(a)	(b)	$\pi 1f_{7/2}(1\ 7/2)\otimes\nu 1f^2_{7/2}(2\ 6)$	0	1.1
3.71, $3/2^-$	(a)	(b)	$\pi 1f_{7/2}(1\ 7/2)\otimes\nu 1f^2_{7/2}(2\ 2)$	4	5.5
6.68, $7/2^-$	(a)	(b)	$\pi 1f_{7/2}(1\ 7/2)\otimes\nu 1f^2_{7/2}(0\ 0)$	3	1.4

(a) $|^{48}Ti> = |^{40}Ca$ doubly closed shell $> |\pi 1f^2_{7/2}(o\ o)\otimes\nu 1f^6_{7/2}(o\ o)>$

(b) $|^{45}Sc> = |^{40}Ca$ doubly closed shell $> |(\pi 1f_{7/2})(1\ 7/2)\otimes\nu 1f^4_{7/2}(\nu\ J)>$

(c) $|^{45}Sc> = |^{40}Ca$ doubly closed shell $> |(\pi 1f^2_{7/2})(o\ o)(\pi j)^{-1}_j\otimes\nu 1f^4_{7/2}(o\ o)>$

(*) An overall normalization N of 24.6×10^6 was used for the ground state. See text for definition of N.

Table (5.6) Structure factors for few states in ^{45}Sc

state, J^{π}	configuration of transferred nucleons	structure factor
0.0 Mev, $7/2^-$	$\pi lf_{7/2}(1\ 7/2) \otimes \nu lf_{7/2}(o\ o)$	0.490
2.74 Mev, $5/2^-$	$\pi lf_{7/2}(1\ 7/2) \otimes \nu lf_{7/2}(2\ 2)$	0.006
3.71 Mev, $3/2^-$	$\pi lf_{7/2}(1\ 7/2) \otimes \nu lf_{7/2}(2\ 2)$	0.034

$^{7}/_{2}^{-}$ are all described well by the $(1f_{7/2})^5$ picture. On the other hand the cross section predicted for the state 2.09 Mev, $^{1}5/_{2}^{-}$ is high. Other possible values of the neutron coupling angular momentum J' yield even higher cross sections, resulting in a lower σ_{exp}/σ_{th} ratio. A detailed wave function is needed where combination of different neutron couplings are included.

The 0.94 Mev, $1/_{2}^{+}$ state is known to be mainly a proton hole state. It is excited in the $^{46}Ti(d,^{3}He)^{45}Sc$ reaction[31] with a spectroscopic factor of 1.55. This gives a validity to the simple picture assumed for this state. However, the $5/_{2}^{+}$ states excited in the (p,α) reaction do not appear to be a pure $d_{5/2}$ hole and the structure of these states is likely more complicated in nature. The spectroscopic factors extracted from the (d,^{3}He) reaction[31] indicate that the $d_{5/2}$ hole strength is fragmented over at least 14 different states.

The next degree of sophistication is to use the shell model wave functions of Kutschera[25]. The results of such calculations are shown in table (5.7). The ratios σ_{exp}/σ_{th} are consistent with each other. As for the 2.74 Mev, $5/_{2}^{-}$ state, the theoretical cross section was calculated using the empirical wave function suggested by Pohl[79] for the ^{48}Ti ground state as mentioned earlier. The consideration of such configuration mixing brought the ratio σ_{exp}/σ_{th} for this state from 102 to 6.2 for the choice of signs shown in table (5.7). It is reasonable to expect that the ratio σ_{exp}/σ_{th} for the $3/_{2}^{-}$ and $5/_{2}^{-}$ states can be brought in line with other ratios if $2p_{3/2}$ and $1f_{5/2}$ proton components are included in the wave functions.

Table (5.7) Comparison of σ_{exp}/σ_{th} for states in ^{45}Sc from the $^{48}Ti(p,\alpha)^{45}Sc$ Reaction using shell model wave functions

state, J^π	$\lvert^{48}Ti>$	$\lvert^{45}Sc>$	configurations of transferred nucleons	σ_{exp}/σ_{th} (*)
0.0, $7/2^-$	(a)	(b)	All possible configurations	1.0
1.24, $11/2^-$	(a)	(c)	All possible configurations	0.3
2.09, $15/2^-$	(a)	(d)	All possible configurations	0.6
2.74, $5/2^-$	(f)	(g)	All possible configurations	6.2
3.69, $19/2^-$	(a)	(e)	All possible configurations	0.7
3.71, $3/2^-$	(a)	(h)	$\pi lf_{7/2}(1\ 7/2) \otimes \nu lf_{7/2}^{-2}(2\ 2)$	2.1

(a) $\equiv \lvert^{48}Ti,\ 0^+> =$ $.929\ \lvert\pi lf_{7/2}^2(o\ o) \otimes \nu lf_{7/2}^6(o\ o)>$

$-.37\ \lvert\pi lf_{7/2}^2(2\ 2) \otimes \nu lf_{7/2}^6(2\ 2)>$

$-.025\ \lvert\pi lf_{7/2}^2(2\ 4) \otimes \nu lf_{7/2}^6(2\ 4)>$

$-.007\ \lvert\pi lf_{7/2}^2(2\ 6) \otimes \nu lf_{7/2}^6(2\ 6)>$

(b) $\equiv \lvert^{45}Sc, J = 7/2> =$ $0.855\ \lvert\pi lf_{7/2}(1\ 7/2) \otimes \nu lf_{7/2}^4(o\ o)>$

$+0.496\ \lvert\pi lf_{7/2}(1\ 7/2) \otimes \nu lf_{7/2}^4(2\ 2)>$

$+0.96\ \lvert\pi lf_{7/2}(1\ 7/2) \otimes \nu lf_{7/2}^4(2\ 4)>$

(c) $\equiv \lvert^{45}Sc, J = 11/2^-> =$ $.738\ \lvert\pi lf_{7/2}(1\ 7/2) \otimes \nu lf_{7/2}^4(2\ 2)>$

$-.219\ \lvert\pi lf_{7/2}(1\ 7/2) \otimes \nu lf_{7/2}^4(2\ 4)>$

$-.237\ \lvert\pi lf_{7/2}(1\ 7/2) \otimes \nu lf_{7/2}^4(2\ 6)>$

(d) $\equiv \lvert^{45}Sc, J = 15/2^-> =$ $.517\ \lvert\pi lf_{7/2}(1\ f7/2) \otimes \nu lf_{7/2}^4(2\ 4)>$

$-.418\ \lvert\pi lf_{7/2}(1\ 7/2) \otimes \nu lf_{7/2}^4(2\ 6)>$

$-.608\ \lvert\pi lf_{7/2}(1\ 7/2) \otimes \nu lf_{7/2}^4(4\ 4)>$

$$(e) \equiv |^{45}Sc, J = 19/2^- > = .987\ |\pi lf_{7/2}(1\ 7/2) \otimes \nu lf^4_{7/2}(2\ 6) >$$

$$(f) \equiv |^{48}Ti,\ 0^+ > = \sqrt{0.2}\ |\pi lf^2_{7/2}(o\ o) \otimes [\nu lf^5_{7/2}(3\ 5/2) \otimes \nu lf_{5/2}(1\ 5/2)]_{J'=0} >$$

$$+ \sqrt{0.8}\ |\pi lf^2_{7/2}(o\ o) \otimes \nu lf^6_{7/2}(o\ o) >$$

$$(g) \equiv |^{45}Sc,\ 5/2^- > = 1.0\ |[\pi lf_{7/2}(1\ 7/2) \otimes \nu lf^4_{7/2}(2\ 2)]_{J=5/2^-} >$$

$$(h) \equiv |^{45}Sc,\ 3/2^- > = 1.0\ |[\pi lf_{7/2}(1\ 7/2) \otimes \nu lf^4_{7/2}(2\ 2)]_{J=3/2^-} >$$

(*) An overall normalization N of 41.3×10^6 was used for the ground state.

Section C: The $^{50}Ti(p,\alpha)^{47}Sc$ Reaction

C.1 α-spectrum:

This reaction was studied at the same proton energy used for the ^{46}Ti and ^{48}Ti isotopes. The emerging α-particles were detected using the same setup described in previous sections. Fig. (5.18) shows a typical spectrum of ^{47}Sc obtained at $\theta_{lab} = 25°$. Similar to the studies for the other two isotopes the energy resolution was about 80 kev. States in ^{47}Sc with excitation energies up to 8.4 Mev were excited. However, the ^{47}Sc spectrum is complicated by the presence of about 18% ^{48}Ti isotopes in the target.

Table (5.8) summarizes the ^{47}Sc data obtained. Also shown in table (5.7) are levels in ^{47}Sc excited through $(d,^3He)$[31] and (t,α)[81] reactions. Similar to the discussion in sections A and B there are some states excited in the (p,α) reaction but not in the other single-particle reaction; among those is the level at 3.09 Mev with $J^\pi = 15/2^-$. This level cannot be reached by single-nucleon pickup. As in ^{45}Sc, the strength of the $1d_{5/2}$ hole is fragmented over several states as observed in the studies of the $(d,^3He)$ and (t,α) reactions. However in the (p,α) reaction only one level with $J^\pi = 5/2^+$ (2.38 Mev) was identified. On the other hand, the strengths of the $1d_{3/2}$ and $2s_{1/2}$ holes are concentrated mainly in one state for each[81] at .77 Mev and 1.37 Mev, respectively. This is deduced from the measured spectroscopic factor[82] of 3.47 and 1.71. Only one level with $J^\pi = 1/2^+$ and one level with $J^\pi = 3/2^+$ were identified in the present work.

Fig. (5.18) The $^{50}Ti(p,\alpha)^{47}Sc$ spectrum

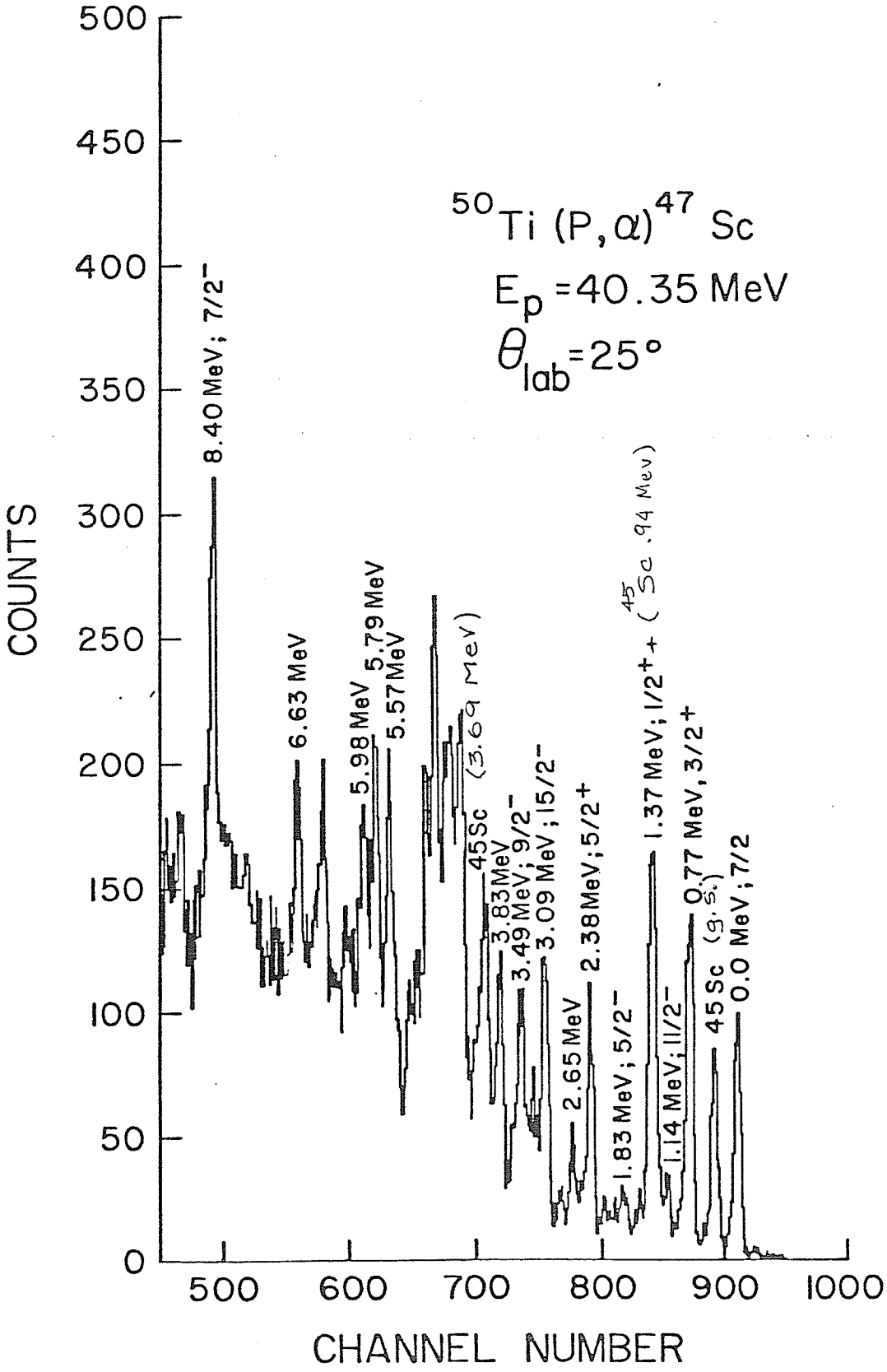
^{50}Ti (P, α)^{47} Sc
E_p = 40.35 MeV
θ_{lab} = 25°
8.40 MeV; 7/2⁻
6.63 MeV
5.98 MeV
5.79 MeV
5.57 MeV
45Sc (3.09 MeV)
3.83 MeV
3.49 MeV; 9/2⁻
3.09 MeV; 15/2⁻
2.65 MeV
2.38 MeV; 5/2⁺
1.83 MeV; 5/2⁻
1.37 MeV; 1/2⁺ + (45Sc .94 MeV)
1.14 MeV; 11/2⁻
0.77 MeV, 3/2⁺
45Sc (g.s.)
0.0 MeV; 7/2
COUNTS
CHANNEL NUMBER
0
50
100
150
200
250
300
350
400
450
500
500
600
700
800
900
1000

Table (5.8) Data Summary for ^{47}Sc

Ex (Mev), J^{π}		
$(p,\alpha)^{(a)}$	$(d,^{3}He)^{(31)(b)}$	$(t,\alpha)^{(81)(b)}$
0.0, $7/2^-$	0.0	0.0, $\ell=3$
0.77, $3/2^+$	.78	.767, $\ell=2$
1.14, $11/2^-$		1.145
1.37, $1/2^+$	1.39	1.39, $\ell=0$
1.83, $5/2^-$		
2.38, $5/2^+$	2.39	2.377, $\ell=2$
2.65, $5/2^-$		
3.09, $15/2^-$		
3.49, $9/2^-$		
3.83		3.804, $\ell=2$
5.57, $(3/2^-)$		5.571, $\ell=1$
5.79	5.75	5.76, $\ell=2$
5.98		5.987
6.63		6.62
8.40, $7/2^-$		

(a) present work

(b) only levels of interest are shown

C.2 Angular Distributions - DWBA Cluster Calculations:

In Figs. (5.19) - (5.22) the angular distributions obtained for states or group of states in ^{47}Sc are shown. The errors shown are the quadratic sum of the statistical and fitting errors. The solid lines are the result of zero-range DWBA calculations using the code DWUCK 2[36] and a cluster form factor as previously described. The spin assignments for the states 0.0 Mev, 0.77 Mev, 1.37 Mev, 2.38 Mev were taken from existing literature[31],[81],[82]. The DWBA calculations are in agreement with these assignments.

On the basis of the observed angular distributions, levels at 1.14 Mev, 3.09 Mev, 2.65 Mev and 3.49 Mev could be assigned to $J^{\pi} = 11/2^-$, $15/2^-$, $5/2^-$ and $9/2^-$, respectively. The $11/2^-$ and $15/2^-$ states cannot be excited in single proton pickup reactions as mentioned earlier. The $\ell = 1$ level identified in the (t,α) experiment[81] at 5.571 Mev probably corresponds to the level at 5.57 Mev observed in the present experiment. However, assuming that this level is of 7p-0h with respect to ^{40}Ca core, the DWBA cluster calculation cannot reproduce the observed distribution with a form factor having 4 nodes, as shown in Fig. (5.22).

The level at 8.40 Mev was assigned to $J^{\pi} = 7/2^-$. This level is probably the $T = 7/2$ isobaric analog of ^{47}Ca ground state. This is in close agreement with M.B.Z. model prediction of 8.404 Mev and Bardin[83] assignment. A simple calculation similar to that performed for ^{46}Ti and ^{48}Ti predicts this level to have an excitation energy of 8.48 Mev. DWBA calculation with $J^{\pi} = 7/2$ reproduces the experimental angular distribution fairly well.

Fig. (5.19) Angular distributions for the negative parity states 0.0, $\frac{7}{2}^-$; 1.14 Mev, $1\frac{1}{2}^-$ and 1.83 Mev, $\frac{5}{2}^-$. The solid lines represent the results of cluster zero-range DWBA calculations.

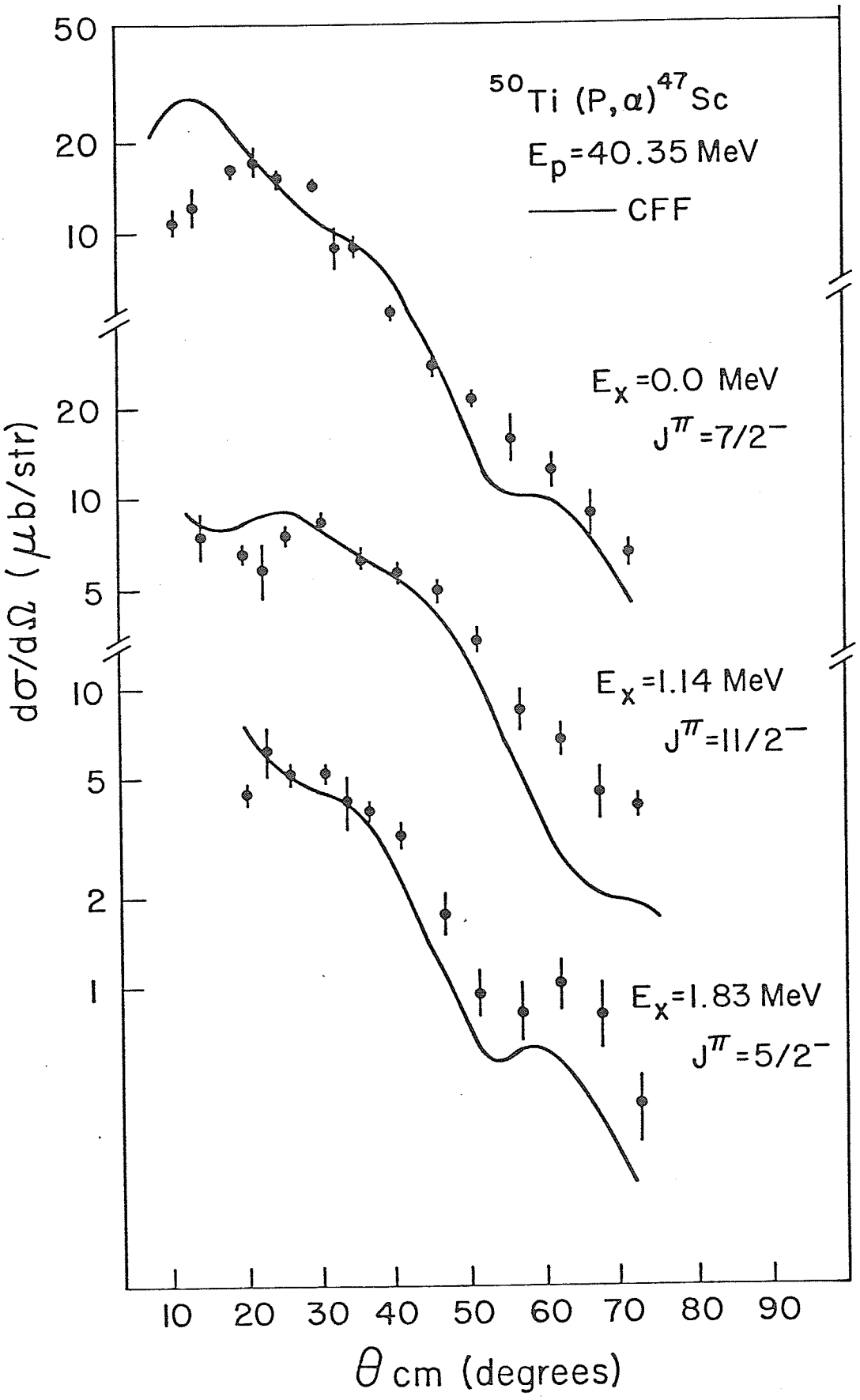
^{50}Ti (P,α)^{47}Sc
E_p=40.35 MeV
CFF
E_x=0.0 MeV
J^π=7/2$^-$
E_x=1.14 MeV
J^π=11/2$^-$
E_x=1.83 MeV
J^π=5/2$^-$
dσ/dΩ (μb/str)
θ cm (degrees)
50
20
10
5
2
1
10 20 30 40 50 60 70 80 90

Fig. (5.20) Angular distributions for the positive parity states .77 Mev, $3/2^+$; 1.37 Mev, $1/2^+$; and 2.38 Mev, $5/2^+$. The solid lines are the results of cluster zero-range DWBA calculations.

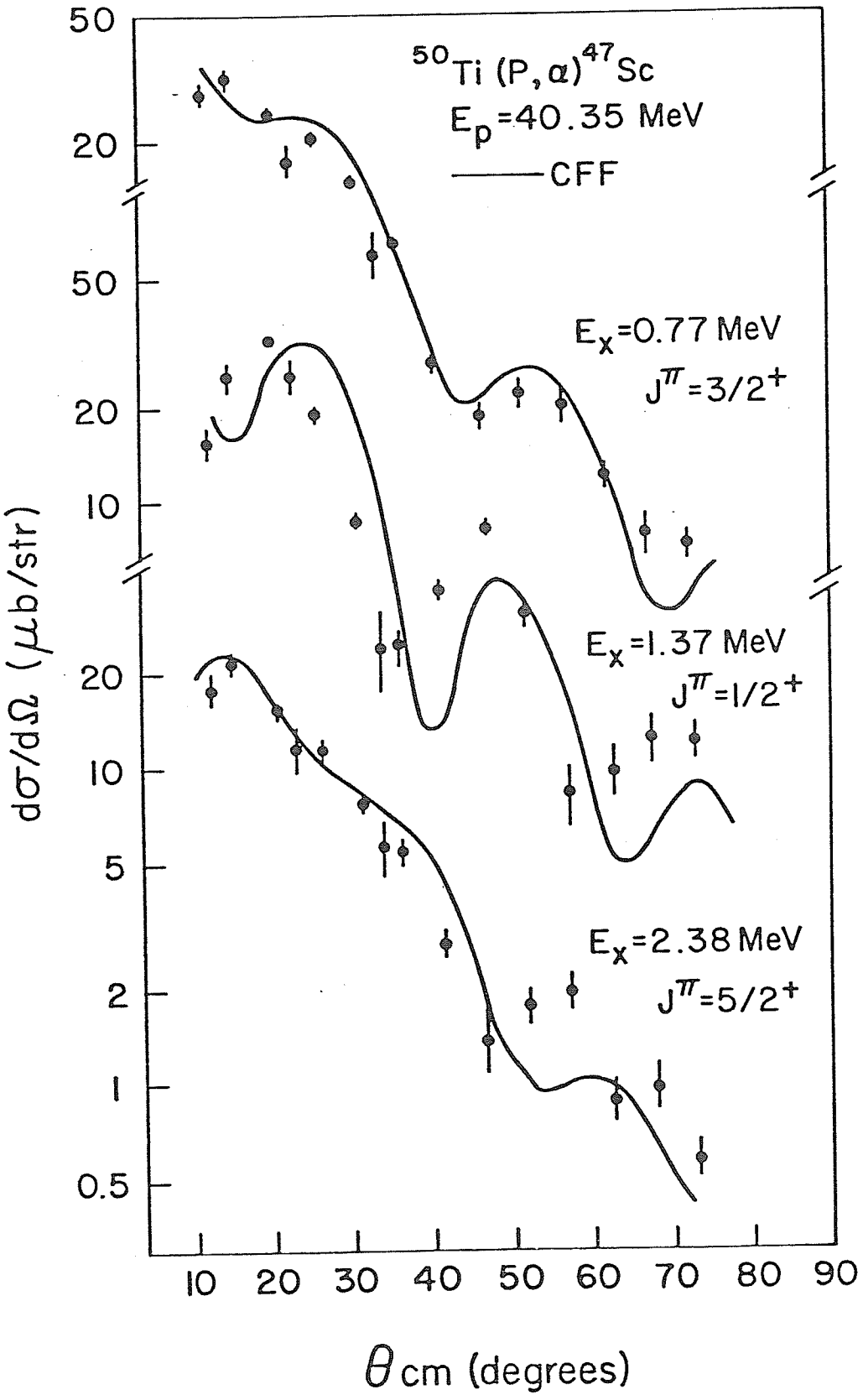
^{50}Ti (P, α)^{47}Sc
E_p=40.35 MeV
CFF
E_x=0.77 MeV
J^π=3/2$^+$
E_x=1.37 MeV
J^π=1/2$^+$
E_x=2.38 MeV
J^π=5/2$^+$
dσ/dΩ (μb/str)
θcm (degrees)
50
20
50
20
10
20
10
5
2
1
0.5
10 20 30 40 50 60 70 80 90

Fig. (5.21) Angular distributions for the states 2.65 Mev, $5/2^-$; 3.09 Mev, $15/2^-$ and 3.49 Mev, $9/2^-$. The solid lines represent the results of cluster zero-range DWBA calculations.

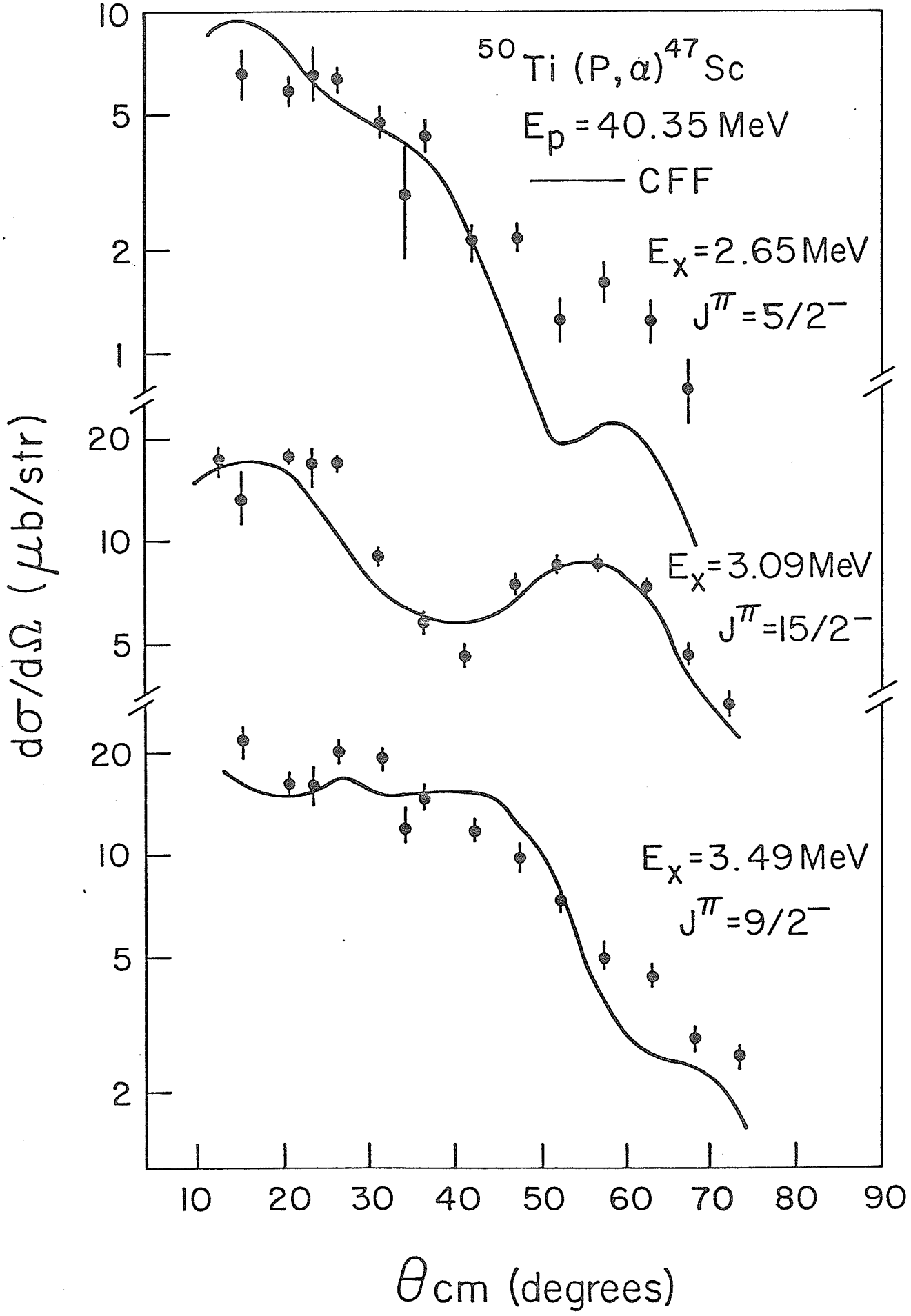
^{50}Ti (P, α)^{47}Sc
E_p = 40.35 MeV
CFF
E_x = 2.65 MeV
J^π = 5/2$^-$
E_x = 3.09 MeV
J^π = 15/2$^-$
E_x = 3.49 MeV
J^π = 9/2$^-$
dσ/dΩ (μb/str)
θcm (degrees)
10
5
2
1
20
10
5
20
10
5
2
10 20 30 40 50 60 70 80 90

Fig. (5.22) Angular distributions for the states 5.57 Mev, $\frac{3}{2}^-$ and 8.40 Mev, $\frac{7}{2}^-(t=\frac{7}{2})$. The solid lines represent the results of cluster zero-range DWBA calculations.

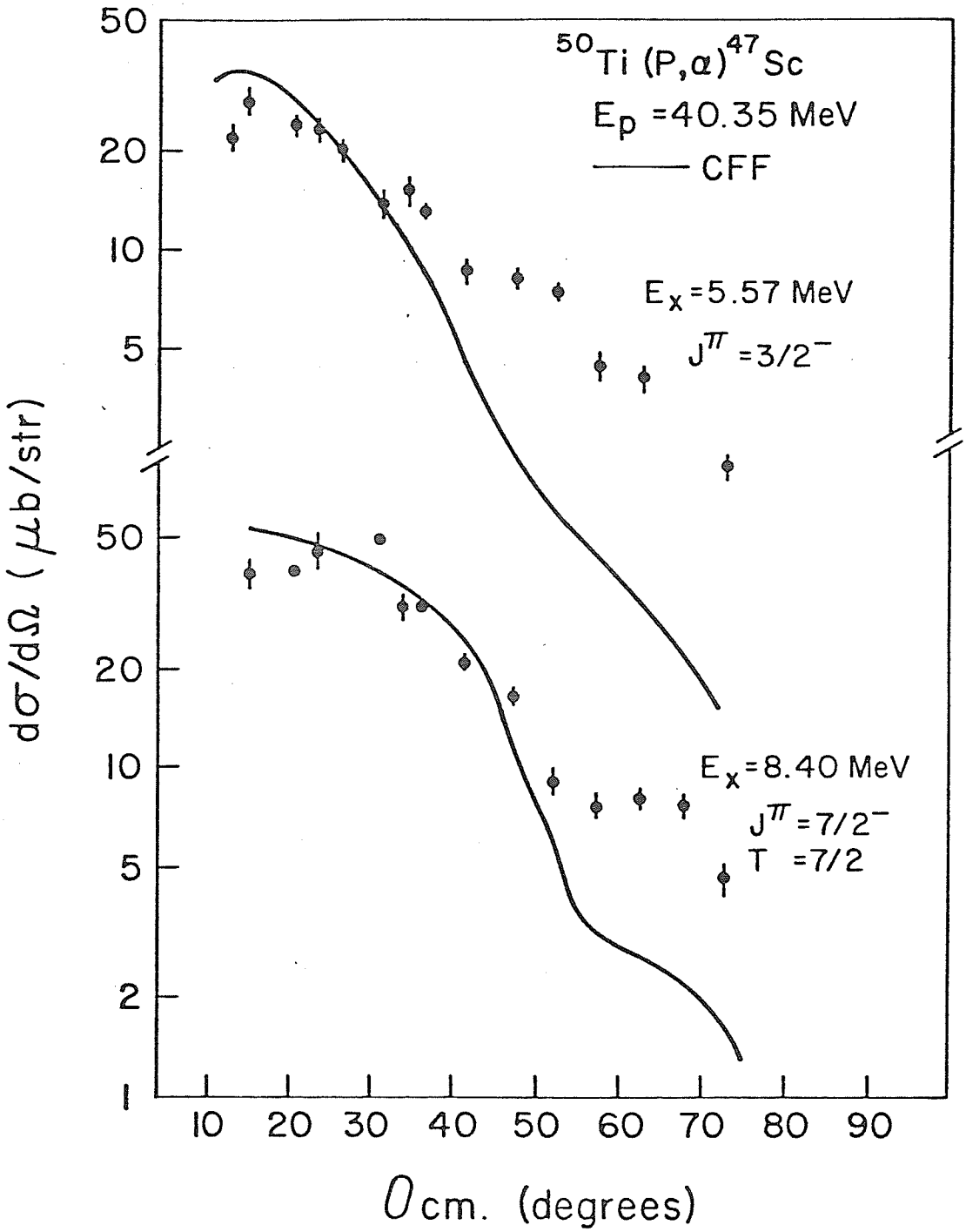
^{50}Ti (P,α)^{47}Sc
E_p =40.35 MeV
CFF
E_x=5.57 MeV
J^π =3/2$^-$
E_x=8.40 MeV
J^π =7/2$^-$
T =7/2
dσ/dΩ (μb/str)
θcm. (degrees)
50
20
10
5
2
1
10 20 30 40 50 60 70 80 90

Fig. (5.23) shows the angular distributions for levels at 3.83 Mev, 5.7 Mev., 5.98 Mev and 6.63 Mev. These levels could not be fitted by a single curve and most probably they represent groups of states. Information available in the literature is not sufficient to investigate these states any further.

C.3 DWBA Calculations - Microscopic Form Factors:

The microscopic form factors were calculated as described previously in chapter 2. Figs. (5.24), (5.25) and (5.26) show angular distribution levels in ^{47}Sc and the results of zero-range DWBA calculations using microscopic form factors. The quality of the fits is comparable to that obtained with cluster form factors.

Similar to the discussion of ^{43}Sc and ^{45}Sc we begin the ^{47}Sc discussion with the zeroth order calculations. The transferred nucleon configurations were assumed to be the simplest possible ones. Positive and negative parity states were assumed to be populated in the same manner described in sections B.3 and C.3.

Table (5.9) shows the results of these calculations. The ratios σ_{exp}/σ_{th} are in agreement with one another within a factor of $\sim$ 3 for most of the states. The error in σ_{exp}/σ_{th} due to the normalization procedure is of the same order of magnitude as that for the cases of ^{46}Ti and ^{48}Ti.

In striking disagreement are the levels 1.83 Mev, $\frac{5}{2}^-$ and 5.57 Mev, $\frac{3}{2}^-$. The high σ_{exp}/σ_{th} ratios indicate that this simple picture is inadequate to describe these two states. Similar behaviour has been noticed during the discussion of ^{45}Sc. Configuration mixing might be the reason for the high ratio as will be discussed at a later stage.

Fig. (5.23) Angular distributions for the levels (or groups of levels) at 3.83 Mev, 5.98 Mev and 6.63 Mev.

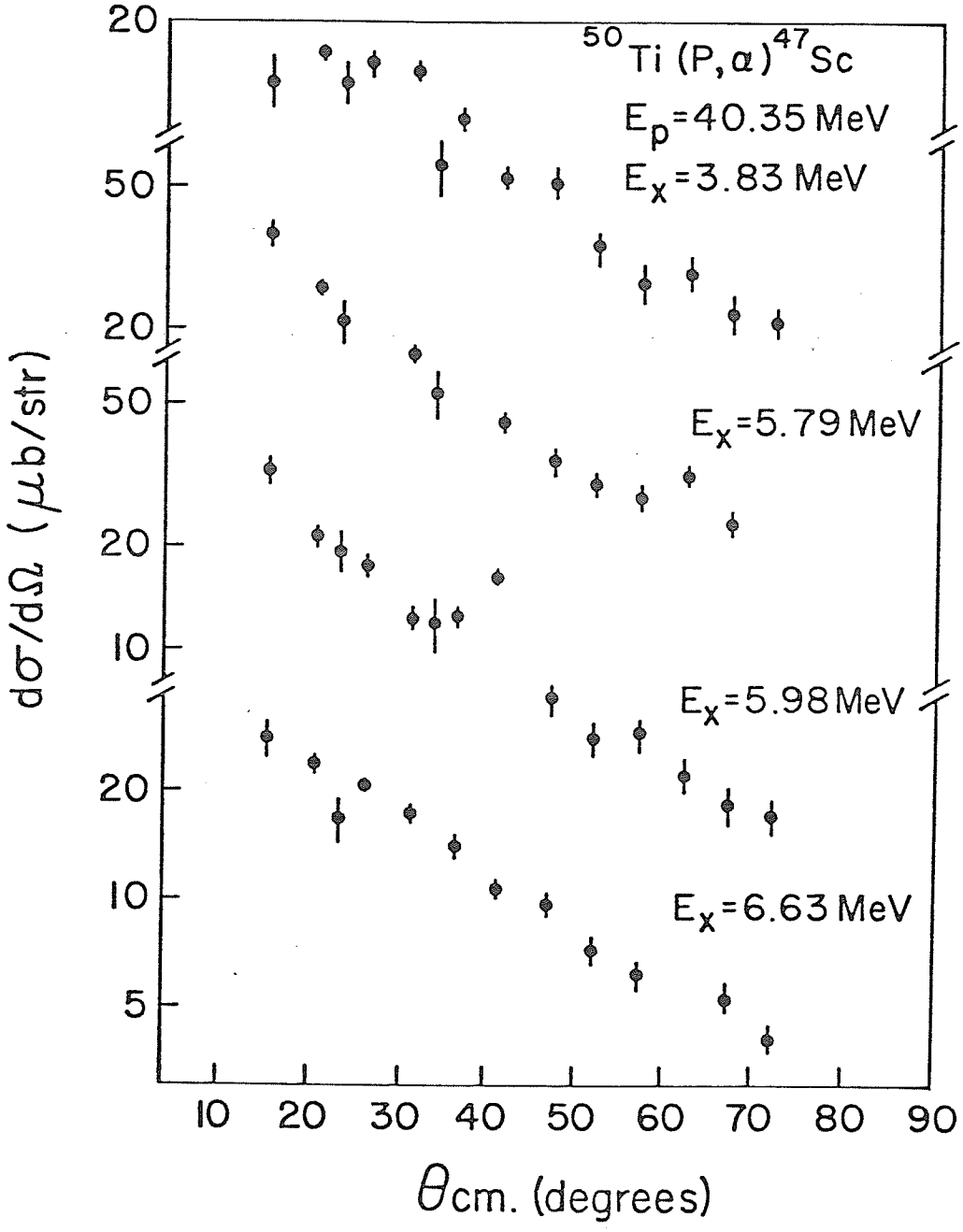
^{50}Ti (P,α)^{47}Sc
E_p=40.35 MeV
E_x=3.83 MeV
E_x=5.79 MeV
E_x=5.98 MeV
E_x=6.63 MeV
dσ/dΩ (μb/str)
θcm. (degrees)
20
50
20
50
20
10
20
10
5
10 20 30 40 50 60 70 80 90

Fig. (5.24) Angular distributions for the states 0.0, $7/2^-$; 1.14 Mev, $1\,1/2^-$ and 1.83 Mev, $5/2^-$. The solid lines are the result of zero-range DWBA calculations using microscopic form factor. The dashed lines are the result of cluster calculations.

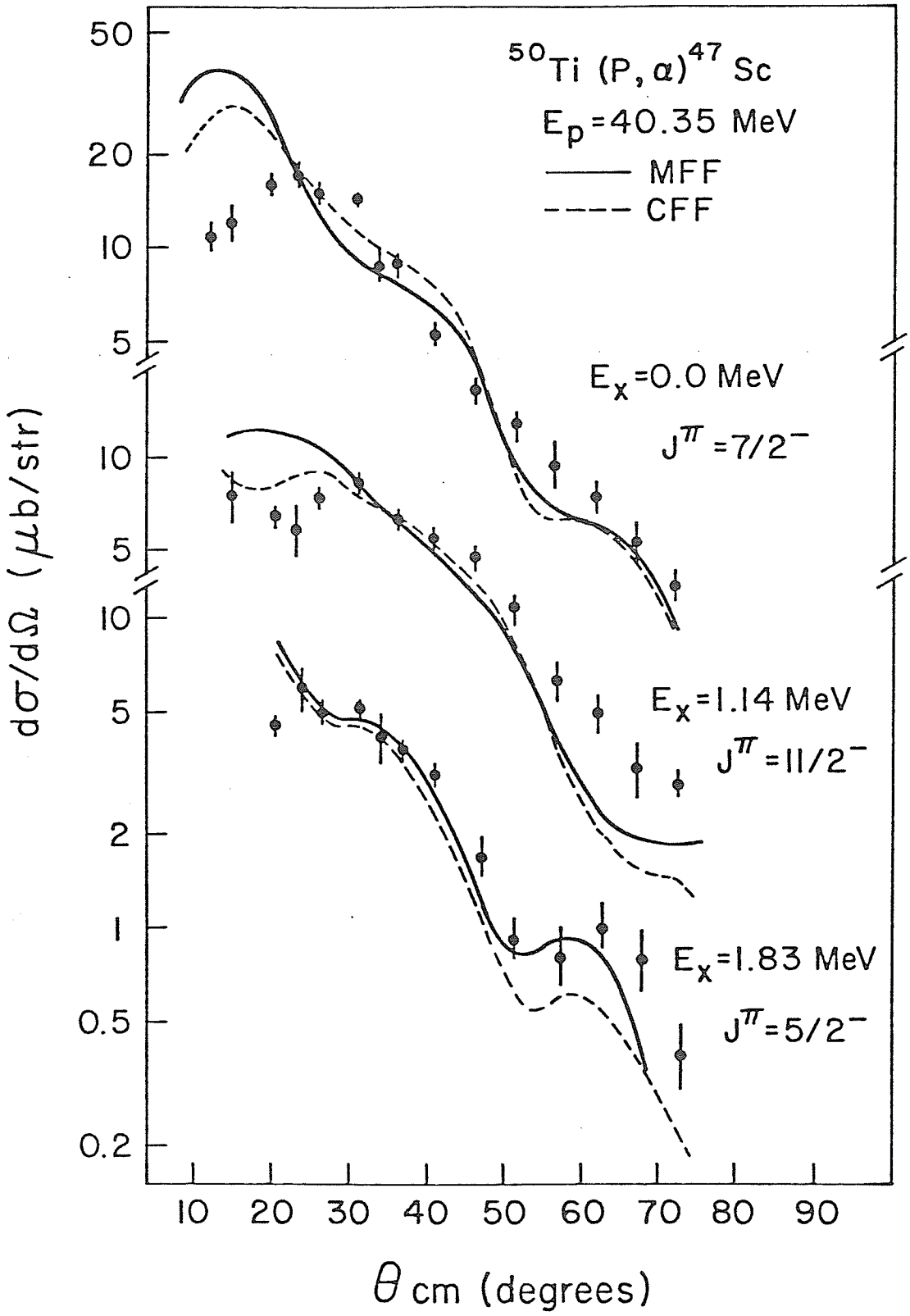
^{50}Ti (P, α)^{47} Sc
E_p=40.35 MeV
MFF
CFF
E_x=0.0 MeV
J^π=7/2$^-$
E_x=1.14 MeV
J^π=11/2$^-$
E_x=1.83 MeV
J^π=5/2$^-$
dσ/dΩ (μb/str)
θ cm (degrees)
50
20
10
5
10
5
10
5
2
1
0.5
0.2
10
20
30
40
50
60
70
80
90

Fig. (5.25) Angular distributions for the states 0.77 Mev, $3/2^+$; 1.37 Mev, $1/2^+$ and 2.38 Mev, $5/2^+$. The solid lines represent the results of zero-range DWBA calculations using microscopic form factor. The dashed lines are the result of cluster calculations.

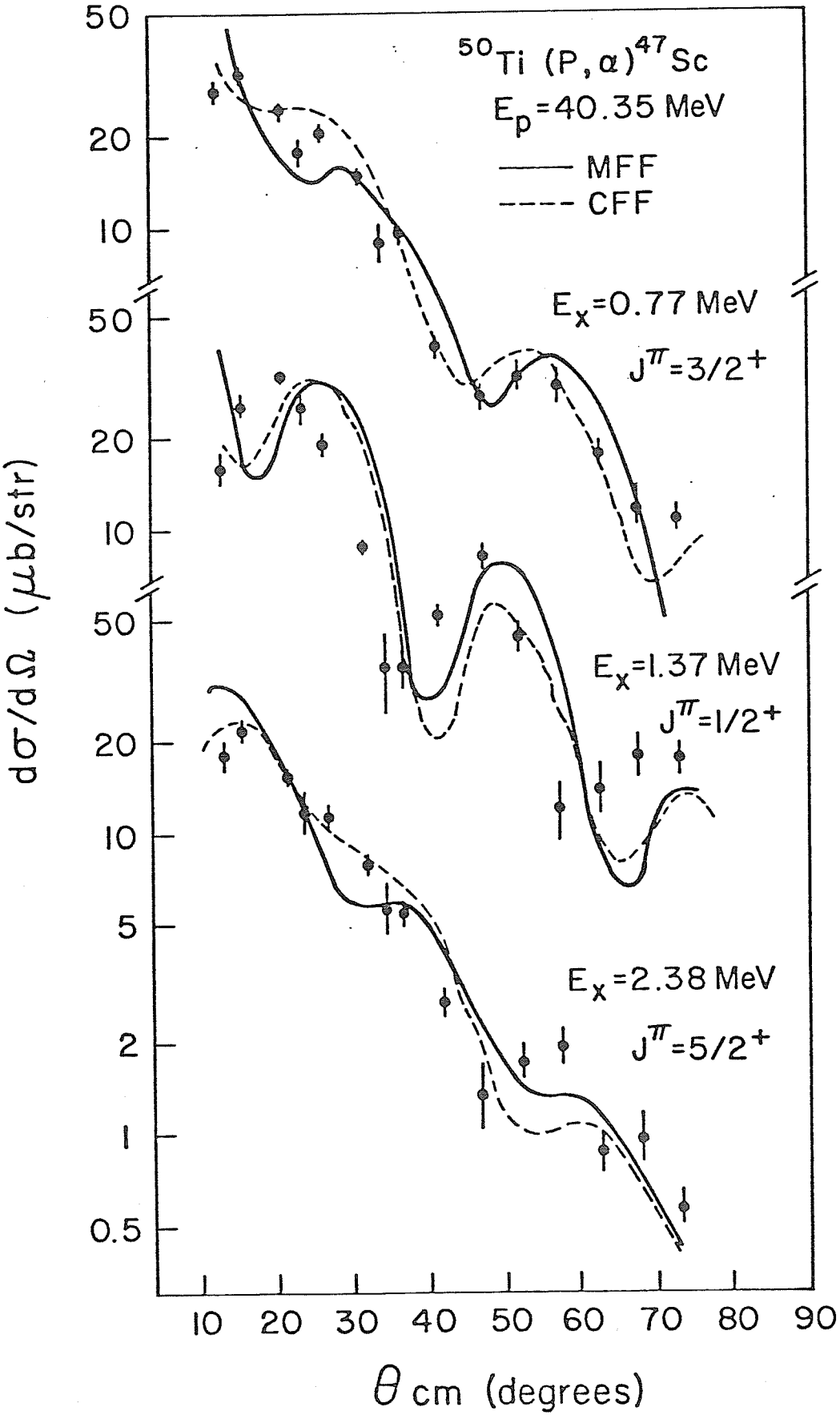
^{50}Ti (P, α)^{47}Sc
E_p=40.35 MeV
MFF
CFF
E_x=0.77 MeV
J^π=3/2$^+$
E_x=1.37 MeV
J^π=1/2$^+$
E_x=2.38 MeV
J^π=5/2$^+$
dσ/dΩ (μb/str)
θ cm (degrees)
50
20
10
5
2
1
0.5
10 20 30 40 50 60 70 80 90

Fig. (5.26) Angular distributions for the states 3.09 Mev, $1\frac{5}{2}^-$; 3.49 Mev, $\frac{9}{2}^-$; 5.57 Mev, $\frac{3}{2}^-$ and 8.40 Mev, $\frac{7}{2}^-$. The solid lines represent the result of zero-range DWBA calculations using microscopic form factor. The dashed lines are the result of cluster calculations.

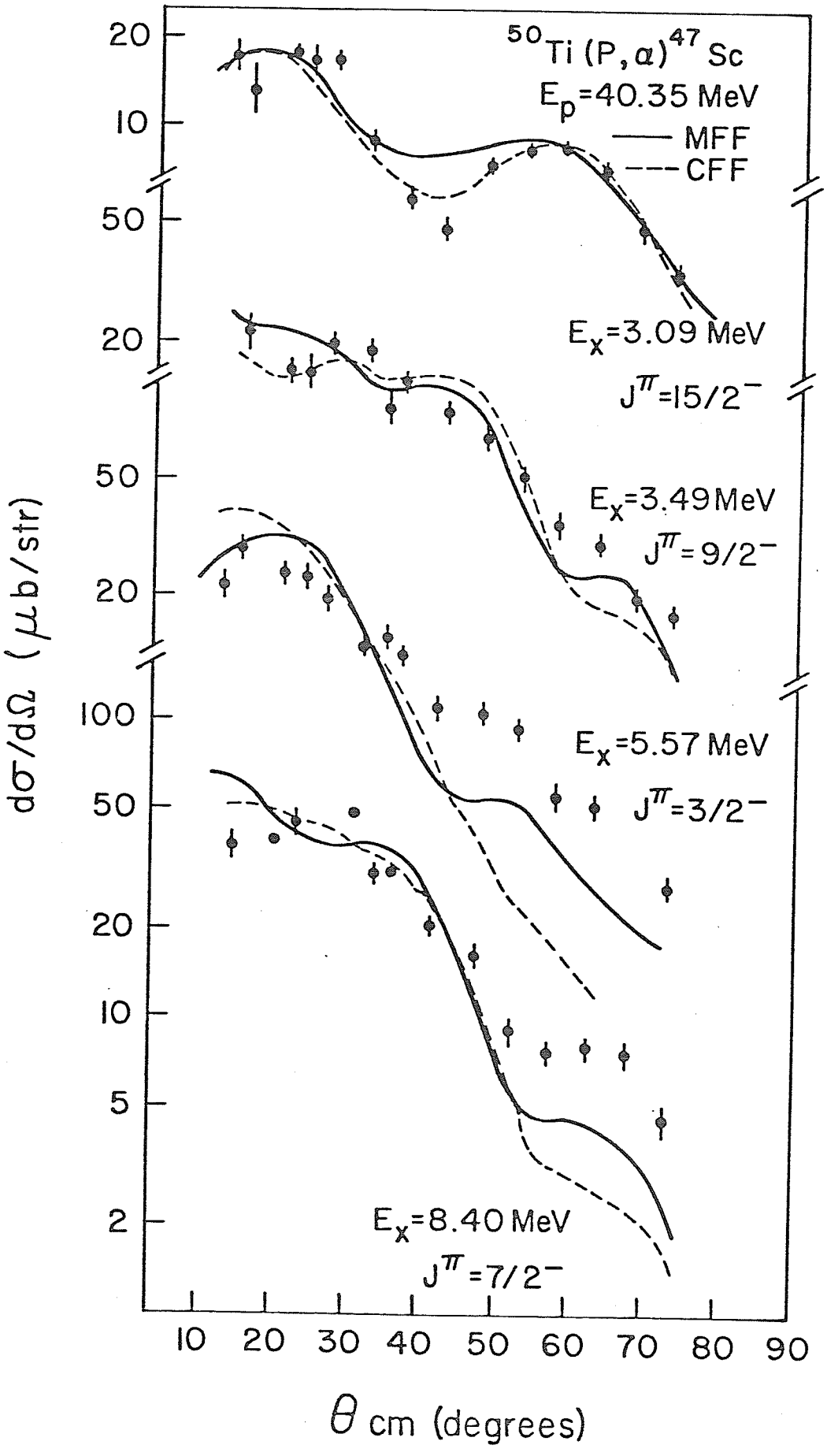
^{50}Ti (P, α)^{47} Sc
E_p=40.35 MeV
MFF
CFF
E_x=3.09 MeV
J^π=15/2$^-$
E_x=3.49MeV
J^π=9/2$^-$
E_x=5.57 MeV
J^π=3/2$^-$
E_x=8.40 MeV
J^π=7/2$^-$
dσ/dΩ (μb/str)
θ cm (degrees)
20
10
50
20
50
20
100
50
20
10
5
2
10 20 30 40 50 60 70 80 90

As for the rest of the states it is not surprising that the zeroth order calculations were able to reproduce reasonably the observed transition strength. This is mainly because the shell model calculations of Kutschera[25] predicted a simple wave function for the ^{50}Ti ground state. The levels 0.77 Mev, $3/2^+$ and 1.37 Mev, $1/2^+$ were observed in the (d,^{3}He) reaction[31] with spectroscopic factors 3.54 and 1.71, respectively; i.e. over 85% of the shell model sum rule. Thus assuming that these states are pure proton hole states is a reasonable first approximation. The theoretical cross section predicted for the 1.14 Mev, $1/2^-$ state is about two times larger than the experimental one. A more complicated structure may be needed to describe this level properly.

Proton pickup reactions indicate[31],[81] that the strength of the $1d_{5/2}$ hole is fragmented over at least 10 states with the state 2.38 Mev, $5/2^+$ having only 10% of the $1d_{5/2}$ hole strength. This means that the assumption of a pure hole state in calculating the ratio σ_{exp}/σ_{th} for this table is incorrect and the agreement with the values in table (5.9) is fortuitous. Assuming a different configuration for the transferred nucleons for this state such as $[\pi 1d_{3/2}(1\ 3/2) \otimes \nu\ 1f_{7/2}(2\ 2)]_{5/2}$ predicted a ratio σ_{exp}/σ_{th} which is an order of magnitude higher. This disagreement with the (d,^{3}He) reaction result should be interpreted as this state having a more complicated structure and its components inferfering in such way that the outcome resembles a pure $1d_{5/2}$ effect.

The study of the reaction ^{50}Ti(p,d)^{49}Ti by Kashy[80] provides evidence of $2p_{3/2}$ neutron admixtures in the ground level of ^{50}Ti through the observation of $\ell = 1$ transition. In a mixed-configuration shell-model calculation for nuclei with N = 28 and $20 < Z \leq 28$, Lips[61] calculated

Table (5.9) Comparison of σ_{exp}/σ_{th} for states in ^{47}Sc from the $^{50}Ti(p,\alpha)$ Reaction

state, J^π	$\lvert^{50}Ti>$	$\lvert^{47}Sc>$	configurations of transferred nucleons	No of nodes	σ_{exp}/σ_{th}(d)
0.0, $7/2^-$	(a)	(b)	$\pi 1f_{7/2}(1\ 7/2) \otimes \nu 1f^2_{7/2}(o\ o)$	3	≡ 1.0
0.77 Mev, $3/2^+$	(a)	(c)	$\pi 1d_{3/2}(1\ 3/2) \otimes \nu 1f^2_{7/2}(o\ o)$	3	2.1
1.14 Mev, $11/2^-$	(a)	(b)	$\pi 1f_{7/2}(1\ 7/2) \otimes \nu 1f^2_{7/2}(2\ 2)$	2	0.4
1.37 Mev, $1/2^+$	(a)	(c)	$\pi 2s_{1/2}(1\ 1/2) \otimes \nu 1f^2_{7/2}(o\ o)$	4	2.8
1.83 Mev, $5/2^-$	(a)	(b)	$\pi 1f_{7/2}(1\ 7/2) \otimes \nu 1f^2_{7/2}(2\ 2)$	3	16.5
2.38 Mev, $5/2^+$	(a)	(c)	$\pi 1d_{5/2}(1\ 5/2) \otimes \nu 1f^2_{7/2}(o\ o)$	3	0.9
3.09 Mev, $15/2^-$	(a)	(b)	$\pi 1f_{7/2}(1\ 7/2) \otimes \nu 1f^2_{7/2}(2\ 6)$	1	1.6
5.57 Mev, $3/2^-$	(a)	(b)	$\pi 1f_{7/2}(1\ 7/2) \otimes \nu 1f^2_{7/2}(2\ 2)$	4	16.0
8.40 Mev, $7/2^-$	(a)	(b)	$\pi 1f_{7/2}(1\ 7/2) \otimes \nu 1f^2_{7/2}(o\ o)$	3	2.9

(a) $\lvert^{50}Ti> = \lvert^{40}Ca$ doubly closed shell $> \lvert \pi 1f^2_{7/2}(o\ o) \otimes \nu 1f^8_{7/2}(o\ o)>$

(b) $\lvert^{47}Sc> = \lvert^{40}Ca$ doubly closed shell $> \lvert \pi 1f_{7/2}(1\ 7/2) \otimes \nu 1f^6_{7/2}(\alpha\ J)>$

where α is the seniority of the 6 neutrons coupled to angular momentum J.

(c) $\lvert^{47}Sc> = \lvert^{40}Ca$ doubly closed shell $> \lvert \pi 1f^2_{7/2}(o\ o)j^{-1}(1\ j) \otimes \nu 1f^6_{7/2}(o\ o)>$

(d) An overall normalization N of 33.0×10^6 was used for the ground state. See text for definition of N.

the wave functions of ^{50}Ti as a mixture of the proton configurations $(1f_{7/2})^2$ and $(1f_{7/2}^1 2p_{3/2}^1)$. The ^{48}Ca was assumed to be a good closed core[87]. They found that the ground level of ^{50}Ti is about 85% pure $(1f_{7/2})^n$. An empirical wave function was constructed of the form:

$$|^{50}Ti \text{ g.s.} > = |^{48}Ca \text{ doubly closed core} > .$$

$$\{0.92\ |\pi 1f_{7/2}^2 (o\ o) > + 0.39\ |\pi 2P_{3/2}^2 (o\ o) >\}.$$

The wave function for the residual nucleus was assumed to be pure $(1f_{7/2})^n$. Repeating the calculations for the 5.57 Mev, $3/2^-$ state, the ratio σ_{exp}/σ_{th} decreased to 1.5 from 16.0. The sign choice was made on empirical basis. The other sign choice gave a larger value. This again illustrates the importance of configuration mixing in the microscopic treatment of the (p,α) reaction.

Table (5.10) shows the ratios σ_{exp}/σ_{th} for a few negative parity states in ^{43}Sc using the Kutschera[25] shell model wave functions. This realistic calculation could not be extended to include all observed states, like the 1.83 Mev, 5.57 Mev and 8.40 Mev states, for example, because of lack of wave functions. Wave functions given in Ref. (25) are only for the lowest two lines of each spin.

Nevertheless, one notices that for the 1.14 Mev, $11/2^-$ state the ratio σ_{exp}/σ_{th} has improved, while for the 3.09 Mev, $15/2^-$ state the ratio has decreased from 1.6 to 0.6.

A shell model calculation that includes $1f_{7/2}$ - $2p_{3/2}$ - $1f_{5/2}$ proton components is needed in order to extract more quantitative information for this reaction.

Table (5.10) Comparison of σ_{exp}/σ_{th} for states in ^{47}Sc from $^{50}Ti(p,\alpha)$ Reaction using the Kutschera shell model wave functions

state, J^{π}	$\|^{50}Ti>$	$\|^{47}Sc>$	configuration of transferred nucleons	σ_{exp}/σ_{th} (*)
0.0, $7/2^-$	(a)	(b)	All possible configurations	$\equiv 1.0$
1.14, $11/2^-$	(a)	(c)	All possible configurations	0.9
3.09, $15/2^-$	(a)	(d)	All possible configurations	0.6

(*) An overall normalization factor N of 25.7×10^6 was used for the ground state.

(a) $|^{50}Ti, 0^+> = 1.0\ |\pi lf_{7/2}^2(0\ 0) \otimes \nu lf_{7/2}^8(0\ 0)>$

(b) $|^{47}Sc, 7/2^-> = .928\ |\pi lf_{7/2}(1\ 7/2) \otimes \nu lf_{7/2}^6(0\ 0)>$

$-.370\ |\pi lf_{7/2}(1\ 7/2) \otimes \nu lf_{7/2}^6(2\ 2)>$

$-.025\ |\pi lf_{7/2}(1\ 7/2) \otimes \nu lf_{7/2}^6(2\ 4)>$

(c) $|^{47}Sc, 11/2^-> = .926\ |\pi lf_{7/2}(1\ 7/2) \otimes \nu lf_{7/2}^6(2\ 2)>$

$-.376\ |\pi lf_{7/2}(1\ 7/2) \otimes \nu lf_{7/2}^6(2\ 4)>$

$-.035\ |\pi lf_{7/2}(1\ 7/2) \otimes \nu lf_{7/2}^6(2\ 6)>$

(d) $|^{47}Sc, 15/2^-> = -.639\ |\pi lf_{7/2}(1\ 7/2) \otimes \nu lf_{7/2}^6(2\ 4)>$

$+.769\ |\pi lf_{7/2}(1\ 7/2) \otimes \nu lf_{7/2}^6(2\ 6)>$

Chapter 6

Summary and Conclusions

The $^{46,48,50}Ti(p,\alpha)^{43,45,47}Sc$ reactions were studied at a proton energy of 40.35 Mev. The choice of the bombarding energy was such that compound nucleus effects are negligible. The overall energy resolution was about 80 Kev FWHM.

States with excitation energies up to about 7 Mev in both ^{43}Sc and ^{45}Sc and up to about 8 Mev in ^{47}Sc were excited. The excitation energies for all observed states agreed well with the values given in the literature. The error in the excitation energies was about 10-15 Kev. Due to the high density of states in the Sc isotopes, only states whose calculated excitation energies did not vary by more than 15 Kev from angle to angle were considered for analysis. Angular distributions for the emerging α-particles were extracted over the angular range for 15° - 75°. The spin assignments J^{π} for most of the states were taken from the existing literature. For those states where more than one value of J was given, the angular distributions shape could frequently be used in making a definitive assignment. Thus the 2.99 Mev, 3.12 Mev and 5.23 Mev states of ^{43}Sc were assigned to $1\frac{5}{2}^-$, $1\frac{9}{2}^-$ and $\frac{3}{2}^+$, respectively. The 1.78 Mev state of ^{45}Sc was assigned to $\frac{5}{2}^+$. Similarly, the 1.14 Mev, 3.09 Mev and 2.65 Mev in ^{47}Sc were assigned to $1\frac{1}{2}^-$, $1\frac{5}{2}^-$ and $\frac{5}{2}^-$, respectively.

Both positive and negative parity states were excited. The positive parity states are excited by picking up two (fp) shell neutrons and one (sd) shell proton, while the negative parity states are excited

by picking up three (fp) shell nucleons. One of the interesting features of the spectra of the odd Sc isotopes is the appearance of positive parity states at very low excitation energies. This behaviour can be qualitatively understood from the Nilsson diagram. Similar behaviour has been observed in the ^{19}F spectrum.

Isobaric analogs of the low-lying states of the Ca isotopes were observed in the Sc spectra. The excitation energies of all states agreed well with the theoretical predictions.

In order to extract spectroscopic information, the microscopic form factor for the (p,α) reaction formulated by Falk[24] was used. This form factor was calculated using single-particle states calculated in a Woods-Saxon potential and then expanded in a harmonic oscillator basis. Due to the complexity of this kind of calculation that involves large numbers of terms in the expansion, only the dominant term in the expansion was considered, i.e. the single-particle states were taken to be harmonic oscillator functions. This truncation simplifies the calculations considerably. The main effect of this truncation is to cause the form factor to fall rapidly in the exterior region. No significant difference is introduced in the interior region. To correct for this difference and to be able to reproduce the angular distributions correctly the MFF tail was replaced by a CFF tail.

Expressions for calculating shell model spectroscopic amplitudes needed in applying the shell model wave functions to this reaction study were derived.

As a first order calculation the formalism was tested assuming the simplest possible configurations for the transferred nucleons. The target

nuclei were assumed to be represented by a simple $(1f_{7/2})^n$ picture.. The agreement with the experiment was within a factor of 3 for most cases. For some of the states the disagreement was as high as two orders of magnitudes as discussed in further detail below. The $1/2^+$ and $3/2^+$ states in ^{45}Sc and ^{47}Sc were found to be mainly proton hole states. This is in agreement with the results available from the $(d,^3He)$ reactions on ^{46}Ti and ^{48}Ti. The 2.37 Mev, $5/2^+$ state in ^{47}Sc is not a pure $1d_{5/2}$ state[31]. However, the MFF predicted the observed strength correctly assuming it to be a pure $1d_{5/2}$ hole state. This agreement with experiment must be considered fortuitous; a more complicated structure for this state is indicated.

More realistic calculations were performed using the $(1f_{7/2})^n$ shell model wave functions of Kutschera[25]. Although the agreement with experiments was better than that of the first order calculations, some disagreement remained for some states. It was found that the $(1f_{7/2})^n$ wave functions are incapable of describing the $3/2^-$ and $5/2^-$ states. The structure amplitudes for the $3/2^-$ and $5/2^-$ states from pickup of three $1f_{7/2}$ nucleons are very small and mixing from the $2p_{3/2}$ and $1f_{5/2}$ subshells must be considered. This suggestion is supported by the spectroscopic factors measured for some states excited in single-nucleon transfer reactions. These states should not be excited unless certain configuration mixing exists in wave functions. On the other hand, the Kutschera wave functions described well the high spin states ($J^\pi = {}^{11}/_2^-$, ${}^{15}/_2^-$ and ${}^{19}/_2^-$) indicating that the configuration mixing is less significant for these states.

An interesting feature of the (p,α) reaction is the excitation of states with $T = T_>$ as well as the $T_<$ states. It would be interesting to compare the strengths of both transitions. However, this requires

the calculation of spectroscopic factors in the JT representation for each state. This procedure was found to be complicated and difficult to calculate for the case of the (p,α) reaction since it involves 3 particle cfp's.

The uncertainty in the calculated cross sections have two different sources. The first, due to truncation in the harmonic oscillator expansion will be discussed shortly. The second is due to the choice of the optical model parameters. It was found that slightly different optical model parameters, yielding essentially a fit of comparable quality, could change the calculated cross sections by 15% on the average. The last factor could be considerably reduced if polarization data were available. Simultaneous fits for both cross section and analyzing power should help to select a unique set of optical model parameters.

The sensitivity of the analyzing power to nuclear structure details was investigated using the microscopic formalism. Figs. (6.1) and (6.2) show the analyzing powers for the $\frac{3}{2}^-$ and $\frac{7}{2}^-$ states using the MFF and different configurations for the transferred nucleons. Also shown are the analyzing powers calculated using the CFF. For the $\frac{3}{2}^-$ state the results shown in Fig. (6.1) indicate that there is no marked dependence of the analyzing power on the configurations used in the MFF calculation. Neither are the MFF predictions very different from the CFF predictions. For the $\frac{7}{2}^-$ state, although configurations with different numbers of nodes (N) gave slightly different analyzing powers, these nevertheless are not different from the respective cluster predictions. Thus, we conclude that no significant microscopic structure information can be obtained from the analysis of the analyzing power. Hence, the main

Fig. (6.1) The calculated analysing powers for the $^{50}Ti(p,\alpha)^{47}Sc$, $J^{\pi}=3/2^{-}$ state at 40.35 Mev using different configurations for the transferred nucleons.

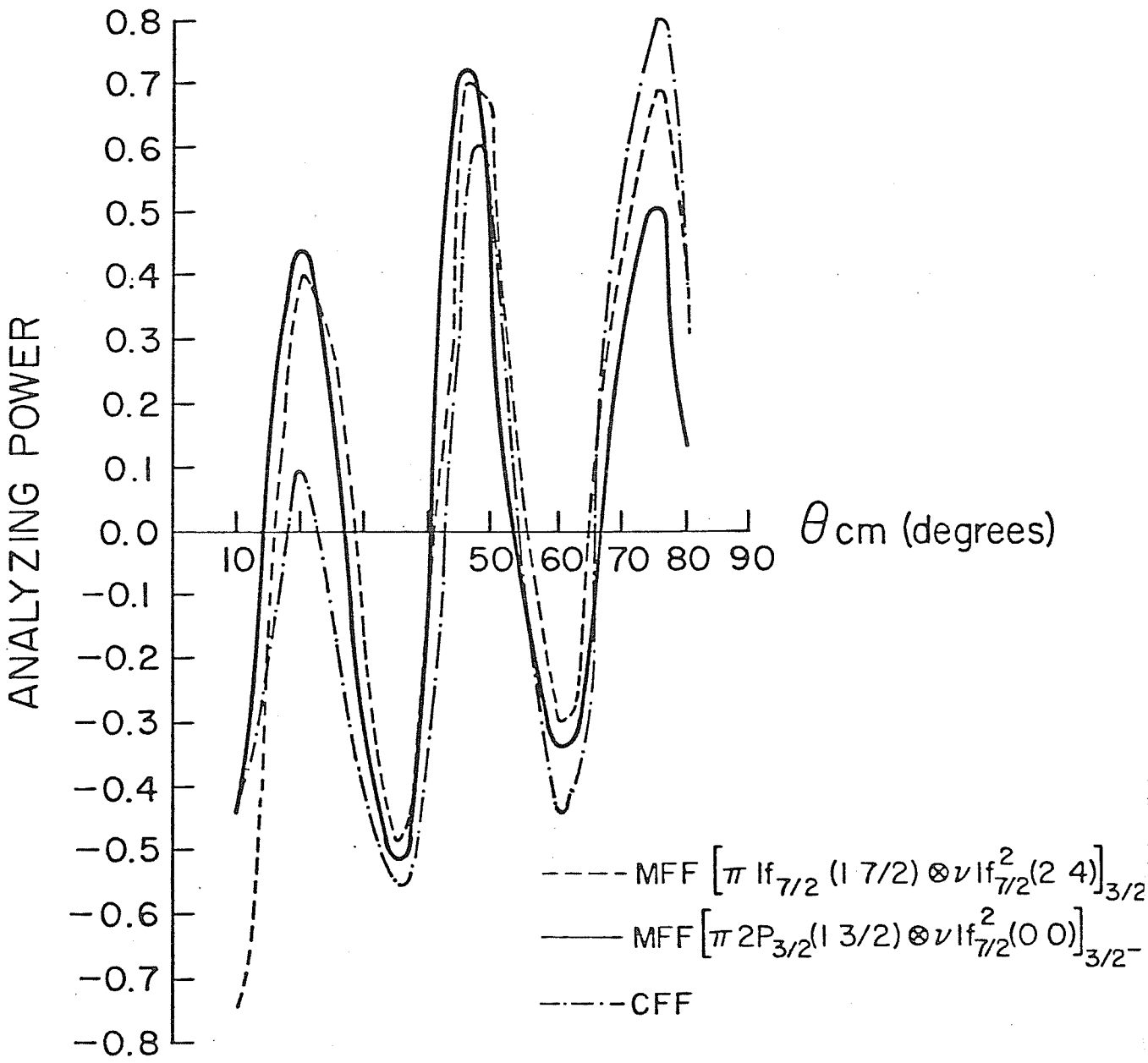
ANALYZING POWER
0.8
0.7
0.6
0.5
0.4
0.3
0.2
0.1
0.0
−0.1
−0.2
−0.3
−0.4
−0.5
−0.6
−0.7
−0.8
10
50
60
70
80
90
θcm (degrees)
---- MFF [π 1f7/2 (1 7/2) ⊗ν 1f7/2² (2 4)]3/2
—— MFF [π 2P3/2 (1 3/2) ⊗ν 1f7/2² (0 0)]3/2−
-·-·- CFF

Fig. (6.2) The calculated analysing power for the $7/2^-$ state in ^{47}Sc .

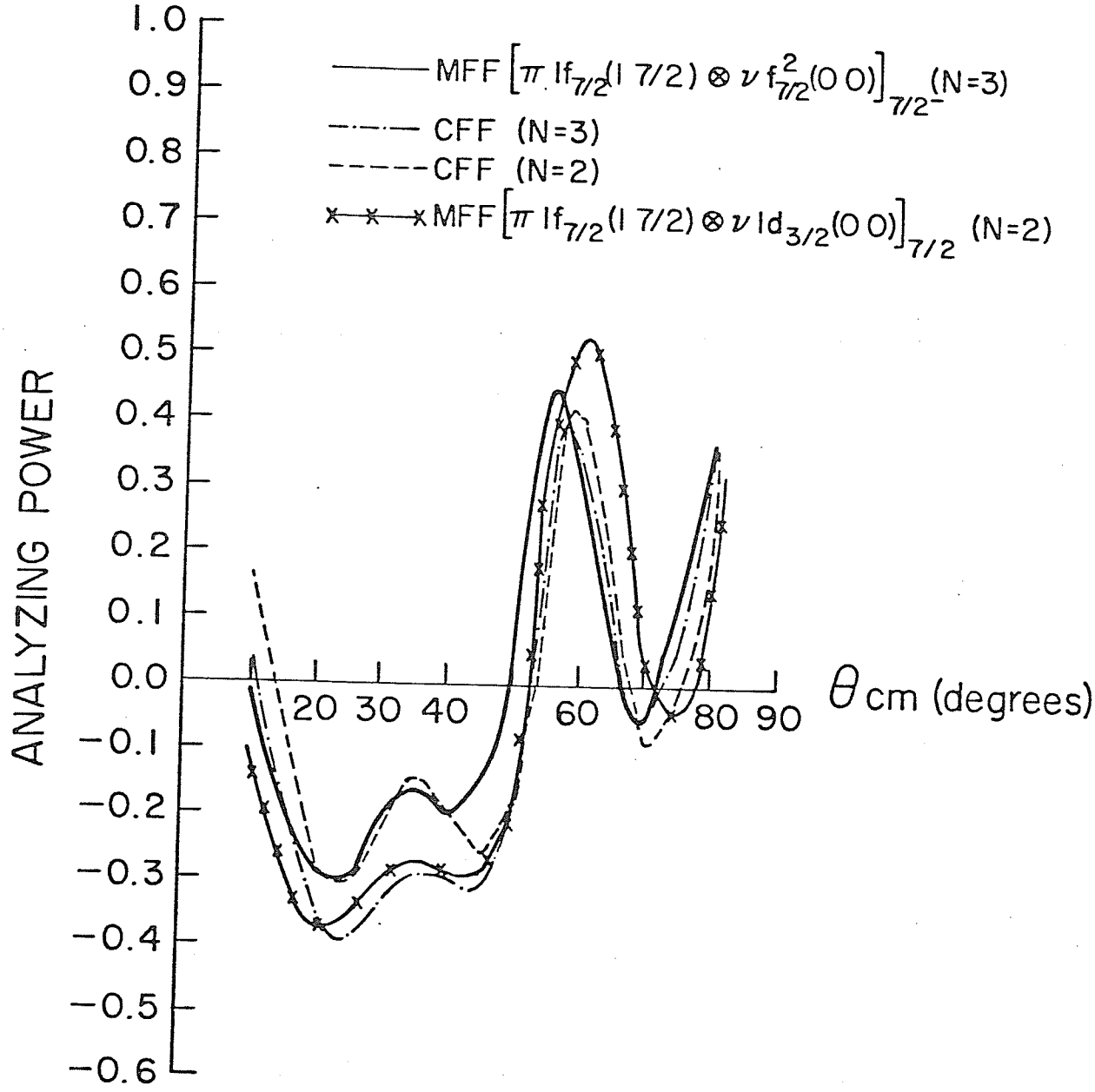
MFF $\left[\pi\, 1f_{7/2}(1\ 7/2) \otimes \nu\, f^2_{7/2}(0\ 0)\right]_{7/2}$ (N=3)
CFF (N=3)
CFF (N=2)
MFF $\left[\pi\, 1f_{7/2}(1\ 7/2) \otimes \nu\, 1d_{3/2}(0\ 0)\right]_{7/2}$ (N=2)
ANALYZING POWER
1.0
0.9
0.8
0.7
0.6
0.5
0.4
0.3
0.2
0.1
0.0
−0.1
−0.2
−0.3
−0.4
−0.5
−0.6
20 30 40 60 80 90
θ cm (degrees)

manifestation of structure details are manifested in the strength of transitions. Of course, analyzing power measurements are still useful for distinguishing between $j=\ell\pm\frac{1}{2}$.

A normalization between the experimental cross sections measured in the present work and the zero range DWBA calculations using the MFF is obtained by writing:

$$\sigma_{th}\ (\mu b/str) = N \cdot \sigma_{DWBA} = \sigma_{exp}$$

where N is a normalization factor defined in chapter 2. Table (6.1) shows the results obtained for the reactions $^{46,48,50}Ti(p,\alpha)^{43,45,47}Sc$ at 40.35 Mev. The difference in the values of N is due to different structures and variations in the optical model parameters and it is difficult to isolate the part due to optical model parameters.

The relative measured cross sections for the ground state transitions for the $^{46,48,50}Ti$ targets were found to be 1 : 0.8 : 0.5, respectively. Assuming a simple picture for these transitions (i.e. $\pi lf_{7/2}(l_{7/2}) \otimes \nu lf^2_{7/2}(o\ o)$), the calculated spectroscopic factors are $1 : 1 : \frac{2}{3}$ which is a reasonable agreement.

For a more careful comparison of the ground state transitions, we compare the square of the magnitudes of the form factors at the outer maxima. This way the effect of different optical model parameters is eliminated. Using Kutschera wave functions, the predicted relative transition strengths were found to be 1 : 0.8 : 0.9 for Ti 46, 48 and 50, respectively.

The uncertainty in the ratio σ_{exp}/σ_{th}, due to the truncation of the H.O. expansion, for each isotope separately was found to be about 24% for all J^π values studied with the exception $J^\pi = \frac{1}{2}^+$ where the

Table (6.1) Normalization factors between experiment and theory

Isotope	N for zero-order calculations	N for calculations using Kutschera wave functions
^{46}Ti	46.3×10^6	47.2×10^6
^{48}Ti	24.6×10^6	41.3×10^6
^{50}Ti	33.0×10^6	25.7×10^6

uncertainty is as high as a factor of ~ 2. There is no explanation at the present time.

In conclusion, we can say that the microscopic formalism used here together with the simplifications introduced provides a powerful tool in extracting quantitative information from the (p,α) reactions. However, there is a need for complete shell model wave functions for both target and residual nuclei in the 2s-1d-1f-2p basis in order to make use of the formalism fully.

APPENDIX A

2.G

Nuclear Physics A334 (1980) 445–469; © *North-Holland Publishing Co., Amsterdam*

INVESTIGATION OF MICROSCOPIC FORM FACTORS FOR THE (p, α) REACTION †

W. R. FALK, R. ABEGG †† and S. K. DATTA

Cyclotron Laboratory, Department of Physics, University of Manitoba, Winnipeg, Canada

Received 27 March 1979
(Revised 2 July 1979)

Abstract: Microscopic form factors for the three-nucleon transfer (p, α) reaction are described, with special emphasis on their comparison with conventional cluster form factors. Considerable differences in shape of these form factors is found, especially in the surface region. An extension of the earlier zero-range descriptions of the microscopic form factor to include finite-range effects, is formulated and tested. Center of mass corrections, the α-particle size parameter, and non-local corrections in the single-particle states, all have a strong influence on the shape of the microscopic form factor. The implications of these observations for the extraction of nuclear structure information is discussed, especially as this affects the commonly used procedure of replacing the microscopic form factor with a cluster form factor, in the actual DWBA calculation.

1. Introduction

The distorted wave Born approximation (DWBA) analyses of multinucleon transfer reactions (e.g. (p, α), (d, ^{6}Li) etc.) have generally employed cluster form factor descriptions of the transferred nucleons. This procedure is simple to implement and, using the radius and diffuseness parameters of the bound state as empirical quantities, acceptable fits to the shapes of experimental angular distributions can usually be obtained [1–6]). Interest in extracting nuclear structure information from these reactions has led to various microscopic approaches in describing the form factor [1–3, 7–9]). Although a number of (p, α) analyses have been performed using microscopic form factors, some with considerable success [8, 10]), other investigators have found that much inferior fits to the angular distributions were obtained [11]). Our recent investigations have shown that microscopic form factors differ considerably in shape from the corresponding cluster form factors that give acceptable fits. This difference in shape accounts for the featureless shape and rapid drop with increasing angle of the calculated angular distributions frequently observed.

Despite these deficiencies one still hopes to obtain relative cross-section predictions in order to interpret direct reaction data in terms of the nuclear structure of the participating nuclei. It is with this in mind that we present the following discussion of microscopic three-nucleon form factors, including an extension of the earlier

† Supported in part by the Natural Sciences and Engineering Research Council of Canada.
†† Present address: TRIUMF, University of British Columbia, Vancouver, Canada.

zero-range (ZR) theory to include finite-range effects [12]). An understanding of the sensitivity of the details of the microscopic form factors to various parameters that enter the calculation is essential to assess the reliability of the extracted nuclear structure information.

Numerous arguments can be advanced as possible causes for the differences and/or deficiencies in the microscopic form factors noted above. These are briefly summarized below.

(i) *Alpha-particle size.* Arima [13]) has suggested that the α-particle changes its size as it approaches a nucleus. It is shown in the discussion to follow that the α-particle size is a sensitive parameter in the calculated form factor shapes.

(ii) *Configuration space.* Numerous papers dealing with one- and two-nucleon transfer [14-16]) emphasize the importance of a sufficiently large configuration space in calculating transfer form factors. Direct reactions, with their sensitivity to nuclear surface effects demand use of an adequate configuration space. Vallieres *et al.* [15]) give examples of extended basis shell-model (EBSM) calculations in which the resulting form factors for (t, p) reactions increase in the asymptotic region by as much as 50%, and the outer maximum shifts to larger radius. Pinkston [16]) emphasizes the importance of core-excited components in the ground states of nuclei (e.g. ^{16}O) particularly for pickup reactions. His EBSM calculations based on a surface delta interaction predict constructive interference of higher-order configurations and hence an enhancement and extension of the form factor in the nuclear surface region.

(iii) *Antisymmetrization between picked-up nucleons and the core.* In the standard DWBA treatment of α-transfer Chant *et al.* [17]) have noted the seemingly unacceptably large radii required in the phenomenological Woods-Saxon potential used to generate the α-core relative wave function. This relative wave function, generated in a potential constructed from a folding model, does not take account of antisymmetrization between the nucleons in the α-particle and those of the core. Jackson [18]) has shown that explicit inclusion of antisymmetrization effects in such calculations results in a large increase of the rms radius of the relative wave function. The importance of these effects in α-decay have also been treated by several authors [19,20]).

(iv) *Finite-range (FR) effects.* Conventional finite-range calculations using cluster form factors have been investigated previously [2]). In this paper finite-range microscopic form factors are developed and investigated to see to what extent they overcome the deficiencies noted for the ZR microscopic form factors.

(v) *Non-local effects in the single-particle states.* The damping of the interior portion of the wave function that results when corrections are applied for the non-local nature of the nucleon-nucleus interaction [21,22]) is much more pronounced when applied to three-nucleon transfer than for single-nucleon transfer. Results of calculations to be presented show that the form factor is shifted to larger radius (by approximately 0.1 fm in ^{40}Ca) when non-local corrections are applied.

(p, α)

2. Microscopic finite-range three-nucleon form factors

The expression for the nuclear matrix element in the DWBA, for a reaction A(p, α)B is given by [22, 23])

$$\langle B\alpha|V|Ap\rangle = \binom{2}{1}^{\frac{1}{2}}\binom{N}{2}^{\frac{1}{2}}\binom{Z}{1}^{\frac{1}{2}}\int \psi_B^*\psi_\alpha^* V\psi_A\psi_p \mathrm{d}\xi, \tag{2.1}$$

where the integration $\mathrm{d}\xi$ is over all coordinates excluding the coordinates of relative motion in the incident and outgoing channel. We now proceed to express more explicitly the terms appearing in the above integral. Fig. 1 displays the relevant

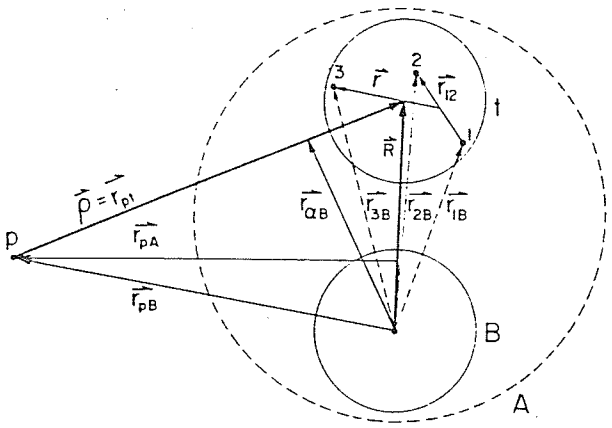

Fig. 1. Coordinates for the pickup reaction A(p, α)B. Particles 1 and 2 refer to the two neutrons and particle 3 to the proton; collectively these three nucleons are represented by the symbol t (triton). The relationships $\boldsymbol{u} = \frac{1}{2}\boldsymbol{r}_{12}$ and $\boldsymbol{v} = \frac{1}{3}\boldsymbol{r}$ are used in the text.

coordinates, where the additional relationships $\boldsymbol{u} = \frac{1}{2}\boldsymbol{r}_{12}$ and $\boldsymbol{v} = \frac{1}{3}\boldsymbol{r}$ will be employed. Separate treatment of neutrons and protons is assumed throughout.

2.1. THE INTERACTION, V

For analytical simplicity, a spin-independent Gaussian interaction between the incoming proton and each of the picked-up nucleons is assumed:

$$V \approx V_{pA} - \bar{U}_{pA} = \sum_{i=1}^{3} V_{pi} = \sum_{i=1}^{3} V_0 \exp(-\beta^2 r_{pi}^2), \tag{2.2}$$

where the range of the interaction is $1/\beta$. The subsequent use of the expression (2.2) in the integration over the internal coordinates causes great difficulty because of the complexity of the angular momentum coupling. Thus the expression for the

interaction was further simplified by writing

$$V \approx V_0\{e^{-\beta^2(s^2+u^2)}[e^{2\beta^2\rho\cdot u}+e^{-2\beta^2\rho\cdot u}]+e^{-\beta^2 w^2}\}, \tag{2.3}$$

with $s^2 = \rho^2+v^2-2\rho\cdot v$ and $w^2 = \rho^2+4v^2+4\rho\cdot v$. Eq. (2.3) differs from the full expression (2.2) in that two terms $\pm 2\beta^2\, v\cdot u$ appearing in r_{p1}^2 and r_{p2}^2 have been neglected. After averaging over the angular part of these terms, it is reasonable that only a small overall contribution should remain. To facilitate the integration over du, a series expansion of the exponential terms involving $\rho\cdot u$ was made, where the angular part was re-expressed using the addition theorem for the spherical harmonics. The terms involving $\rho\cdot v$ were handled similarly. Similar approaches in the finite-range treatment of two-nucleon transfer have been discussed by several authors [24].

2.2. ALPHA-PARTICLE WAVE FUNCTION

The outgoing α-particle is composed of the incident proton and the three picked-up nucleons. A simple Gaussian form was assumed for the spatial part of the α-particle wave function:

$$\psi_a = N_a \exp(-\eta^2 \sum_{i<j=1}^{4} r_{ij}^2) = N_a \exp(-\eta^2(3\rho^2+24v^2+8u^2)). \tag{2.4}$$

The α-particle size parameter η has a value of approximately 0.233 fm^{-1} [ref. [25]] and is related to the equivalent oscillator parameter ν_a for the α-particle through the relations $\eta^2 = \frac{1}{8}\nu_a$.

2.3. FINAL NUCLEUS WAVE FUNCTION, ψ_B

The coordinates of the nucleons comprising nucleus B are referred to the fixed center of the shell-model potential, as shown in fig. 2. Then, the wave function of

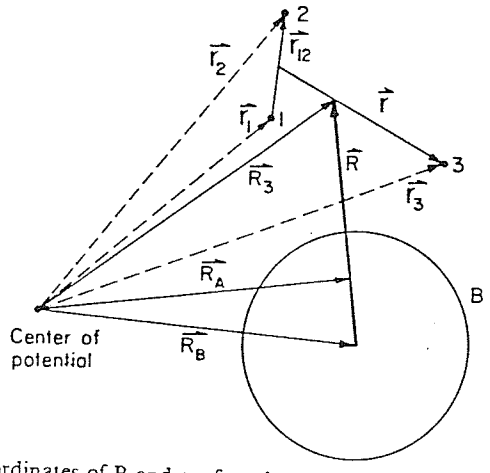

Fig. 2. Nucleon coordinates of B and t referred to the center of the shell-model potential.

B, ψ_B, can be written as [26])

$$\psi_{BM_B}^{J_B} = \phi_{M_B}^{J_B}(\xi_B) R_{00}(B\nu R_B^2) Y_0^0(\hat{R}_B), \tag{2.5}$$

where $\phi(\xi_B)$ is the wave function of the internal coordinates of B, and R_{00} a harmonic oscillator function in its lowest quantum state, $n = l = 0$, with oscillator parameter B times the nucleon oscillator parameter, ν. (In this and subsequent expressions, A and B are also used to designate the mass numbers of nuclei A and B respectively.) The distance between the c.m. of B and the center of the potential is given by R_B. The result (2.5) follows from a series of successive Moshinsky transformations which convert the single-particle motion into internal (relative) and c.m. motion.

2.4. TARGET NUCLEUS WAVE FUNCTION, ψ_A

With reference to the coordinates displayed in fig. 2 the target wave function is now expanded as follows:

$$\psi_{AM_A}^{J_A}(R_B, \xi_B, r_1, r_2, r_3) = \sum_{M_B}^{\gamma J_B J' J} \mathcal{S}_{AB}(\gamma, J'J) \times (J_B' M_B' JM | J_A M_A)[\phi_{M_B}^{J_B}(\xi_B) R_{00}(B\nu R_B^2) Y_0^0(\hat{R}_B) \psi_M^{\gamma J' J}(r_1, r_2, r_3), \tag{2.6}$$

where $\mathcal{S}_{AB}(\gamma, J'J)$ is an expansion coefficient for transfer of three nucleons with the configuration $\gamma \equiv [(n_1 l_1 j_1), (n_2 l_2 j_2), (n_3 l_3 j_3)]$. These expansion coefficients $\mathcal{S}_{AB}$ are proportional to the corresponding spectroscopic amplitudes for the given transition,

$$S_{AB}^{\frac{1}{2}}(\gamma, J'J) = \binom{Z}{1}^{\frac{1}{2}} \binom{N}{2}^{\frac{1}{2}} \mathcal{S}_{AB}(\gamma, J'J). \tag{2.7}$$

The three-nucleon wave functions, $\psi(r_1, r_2, r_3)$, with quantum numbers $(J'JM)$, and nucleon coordinates, again referred to the center of the shell model potential, is further described in the following section.

2.5. WAVE FUNCTION OF THE THREE TRANSFERRED NUCLEONS

The normalized and antisymmetrized wave function in j-j coupling of the three transferred nucleons is given by [27])

$$\psi_M^{\gamma J' J}(r_1, r_2, r_3) = \sum_{m_{12} m_3} (J' m_{12} j_3 m_3 | JM) \left\{ \frac{1}{[2(1+\delta_{\gamma_1 \gamma_2})]^{\frac{1}{2}}} \times \sum_{m_1 m_2} (j_1 m_1 j_2 m_2 | J' m_{12})[\psi_{m_1}^{n_1 l_1 j_1}(r_1) \psi_{m_2}^{n_2 l_2 j_2}(r_2) - \psi_{m_1}^{n_1 l_1 j_1}(r_2) \psi_{m_2}^{n_2 l_2 j_2}(r_1)] \right\} \psi_{m_3}^{n_3 l_3 j_3}(r_3), \tag{2.8}$$

where $\gamma_1 \equiv (n_1 l_1 j_1)$ and $\gamma_2 \equiv (n_2 l_2 j_2)$. For the subsequent transformation to internal and center of mass coordinates eqn. (2.8) must first be expressed in L-S coupling. This

result, for one of the above terms is

$$\psi^{\gamma J' J}_{M}(r_1, r_2, r_3) = \sum^{L'S'LS}_{\lambda\mu_1} (L\lambda S\mu_1|JM) \begin{bmatrix} l_1 & l_2 & L' \\ \frac{1}{2} & \frac{1}{2} & S' \\ j_1 & j_2 & J' \end{bmatrix} \begin{bmatrix} L' & l_3 & L \\ S' & \frac{1}{2} & S \\ J' & j_3 & J \end{bmatrix}$$
$$\times \{ \sum_{\mu' \mu_3} (S' \mu' \tfrac{1}{2} \mu_3 | S \mu_1) \chi^{\frac{1}{2}}_{\mu_3}(3) (\sum_{\mu_1 \mu_2} (\tfrac{1}{2}\mu_1 \tfrac{1}{2}\mu_2 | S' \mu') \chi^{\frac{1}{2}}_{\mu_1}(1) \chi^{\frac{1}{2}}_{\mu_2}(2)) \}$$
$$\times \{ \sum_{\lambda' \lambda_3} (L' \lambda' l_3 \lambda_3 | L \lambda) \psi^{n_3 l_3 j_3}_{\lambda_3}(r_3) (\sum_{\lambda_1 \lambda_2} (l_1 \lambda_1 l_2 \lambda_2 | L' \lambda') \psi^{n_1 l_1 j_1}_{\lambda_1}(r_1) \psi^{n_2 l_2 j_2}_{\lambda_2}(r_2)) \}. \tag{2.9}$$

Here neutrons 1 and 2 have been coupled to a total angular momentum J', which in turn is coupled to the third particle, the proton, to yield a total angular momentum J. The intrinsic spin of the two neutrons, S', is zero. The square brackets [ ] are normalized 9-j symbols expressing the transformation from j-j to L-S coupling.

The spatial part of this three-nucleon wave function is now conveniently transformed to internal and c.m. motion using two successive Moshinsky transformations. A further restriction is imposed that only internal orbital angular momenta $l' = l = 0$ are retained. (l' is the orbital angular momentum of the two neutrons about their common center of mass, and l the orbital angular momentum of the proton and dineutron about their center of mass.) Without this simplification enormous complications follow in the allowed angular momentum couplings and the evaluation of the radial integrations. Details of the above transformation have been given before [7, 8]); the result is that eq. (2.9) can now be written as

$$\psi^{\gamma J' J}_{M}(r_1, r_2, r_3) = \sum^{LS}_{\lambda\mu_1} (L\lambda S\mu_1|JM) \begin{bmatrix} l_1 & l_2 & J' \\ \frac{1}{2} & \frac{1}{2} & 0 \\ j_1 & j_2 & J' \end{bmatrix} \begin{bmatrix} J' & l_3 & L \\ 0 & \frac{1}{2} & S \\ J' & j_3 & J \end{bmatrix}$$
$$\times \{ \sum_{\mu_3} (00 \tfrac{1}{2} \mu_3 | S \mu_1) \chi^{\frac{1}{2}}_{\mu_3}(3) [\sum_{\mu_1 \mu_2} (\tfrac{1}{2}\mu_1 \tfrac{1}{2}\mu_2 | 00) \chi^{\frac{1}{2}}_{\mu_1}(1) \chi^{\frac{1}{2}}_{\mu_2}(2)] \}$$
$$\times \sum_{p_1 p_2 p_3} a'_{p_1} a'_{p_2} a'_{p_3} \sum_{N'n'Nn} \langle p_1 l_1 p_2 l_2, J' | \mu, \mu | N' J' n' 0, J' \rangle$$
$$\times \langle N' J' p_3 l_3, L | 2\mu, \mu | N L n 0, L \rangle \times R_{n'0}(2\nu u^2) Y^0_0(\hat{u}) \times R_{n0}(6\nu v^2) Y^0_0(\hat{v})$$
$$\times R_{NL}(3\nu R_3^2) Y^{\lambda}_{L}(\hat{R}_3). \tag{2.10}$$

The symbol μ in the Moshinsky brackets represents the nucleon mass. The a'_{p_i} are the coefficients in the harmonic oscillator expansion of the single-particle states generated in the fixed center shell-model potential; that is

$$\psi^{n_i l_i j_i}_{\lambda_i}(r_i) = \sum_{p_i} a'_{p_i} R_{p_i l_i}(\nu r_i^2) Y^{\lambda_i}_{l_i}(\hat{r}_i) \tag{2.11}$$

(p, α)

2.6. CENTER-OF-MASS CORRECTIONS

Combining the result of eq. (2.10) with that of eq. (2.6) one further Moshinsky transformation can be performed as follows:

$$[R_{00}(B\nu R_B^2)Y_0^0(\hat{R}_B)][R_{NL}(3\nu R_3^2)Y_L^\lambda(\hat{R}_3)]$$
$$= \sum_{n^*l^*\lambda^*N^\dagger L^\dagger\lambda^\dagger} (l^*\lambda^* L^\dagger\lambda^\dagger|L\lambda)\langle 00NL, L|B\mu, 3\mu|n^*l^*N^\dagger L^\dagger, L\rangle [R_{n^*l^*}(A\nu R_A^2)Y_{l^*}^{\lambda^*}(\hat{R}_A)]$$
$$\times \left[R_{N^\dagger L^\dagger}\left(\frac{3B}{A}\nu R^2\right)Y_{L^\dagger}^{\lambda^\dagger}(\hat{R})\right]. \tag{2.12}$$

If the c.m. motion of the A nucleons is in its lowest quantum state with $n^* = l^* = 0$, it follows that $N^\dagger = N$ and $L^\dagger = L$. The Moshinsky bracket is then [28])

$$\langle 00NL, L|B\mu, 3\mu|00NL, L\rangle = \left(\frac{B\mu}{B\mu+3\mu}\right)^{N+L/2} = \left(\frac{A-3}{A}\right)^{N+L/2} \tag{2.13}$$

This term is referred to as a c.m. correction term [2, 26, 29]). It is to be noted from eq. (2.12) that the motion of the c.m. of the three-nucleon cluster with respect to the residual nucleus B involves the oscillator parameter $(3B/A)\nu$.

Another c.m. correction occurs if the single-particle states are calculated in a potential referred to the c.m. of the residual nucleus B. This wave function of relative motion, expanded in a harmonic oscillator series, would be

$$\phi_\lambda^{nlj}(\boldsymbol{r}_B) = \sum_p a_p R_{pl}(\nu_{s.p.} r_B^2) Y_l^\lambda(\hat{\boldsymbol{r}}_B). \tag{2.14}$$

However, following arguments similar to the ones used above to obtain the motion of the three nucleon cluster relative to the nucleus B, it can be shown that the motion of a nucleon relative to the $A-1$ nucleons as given by the fixed center shell-model potential is (cf. eq. (2.11))

$$\phi_\lambda^{nlj}(\boldsymbol{r}_B) = \sum_p a_p' \left(\frac{A-1}{A}\right)^{p+l/2} R_{pl}\left[\left(\frac{A-1}{A}\right)\nu r_B^2\right] Y_l^\lambda(\hat{\boldsymbol{r}}_B). \tag{2.15}$$

Thus, comparing (2.14) and (2.15), one obtains

$$a_p' = \left(\frac{A}{A-1}\right)^{p+l/2} a_p, \tag{2.16}$$

$$\nu_{s.p.} = \left(\frac{A-1}{A}\right)\nu. \tag{2.17}$$

The shell-model nucleon oscillator parameter ν is thus greater than the single-particle oscillator parameter $\nu_{s.p.}$ used in the actual expansion of the bound-state wave functions, by a factor of $A/(A-1)$.

2.7. NUCLEAR MATRIX ELEMENT

Collecting all the various terms given in the previous sections into the nuclear matrix element, the integrations over the internal coordinates du and dv, while tedious and lengthy (because of the power series expansion of the integrand in terms of u and v), can be performed. The result is

$$\langle \mathrm{B}\alpha|V|\mathrm{Ap}\rangle \propto \sum_{LJM_BM\lambda\mu_t} (J_BM_BJM|J_AM_A)(L\lambda\tfrac{1}{2}\mu_t|JM)(\tfrac{1}{2}\mu_t\tfrac{1}{2}\mu_p|00)$$

$$\times \sum_{\gamma J'} \mathcal{I}_{AB}(\gamma, J'J) \begin{bmatrix} l_1 & l_2 & J' \\ \frac{1}{2} & \frac{1}{2} & 0 \\ j_1 & j_2 & J' \end{bmatrix} \begin{bmatrix} J' & l_3 & L \\ 0 & \frac{1}{2} & \frac{1}{2} \\ J' & j_3 & J \end{bmatrix} F^{\gamma}_{J'L}(\rho, R) Y^{\lambda}_{L}(\hat{R}). \tag{2.18}$$

The function $F^{\gamma}_{J'L}(\rho, R)$, which we call the form factor for transfer of the configuration $(\gamma, J'J)$, depends on the radial coordinates ρ and R, and is given by

$$F^{\gamma}_{J'L}(\rho, R) = g(\gamma) \sum_{p_1p_2p_3} \sum_{N'n'Nn} a_{p_1}a_{p_2}a_{p_3} \left(\frac{A}{A-1}\right)^{p_1+p_2+p_3+(l_1+l_2+l_3)/2}$$

$$\times \langle p_1l_1p_2l_2, J'|\mu, \mu|N'J'n'0, J'\rangle\langle N'J'p_3l_3, L|2\mu, \mu|NLn0, L\rangle$$

$$\times \left(\frac{A-3}{A}\right)^{N+L/2} I_{nn'}(\nu, \nu_\alpha, \beta, \rho) R_{NL}\left[\frac{3(A-3)}{A}\nu R^2\right]. \tag{2.19}$$

Results of all the internal integrations are now contained in the overlap integral $I_{nn'}$ which, in this finite range form factor, depends on β and ρ, in addition to ν and ν_α. The factor $g(\gamma)$ results from the antisymmetrization of the two neutrons, introduced in eq. (2.8), and has the value $g = 1$, if $\gamma_1 = \gamma_2$, and $g = \sqrt{2}$, if $\gamma_1 \neq \gamma_2$ [ref. [23]].

3. Characteristics of the zero-range microscopic form factor (ZRMFF)

In the zero range approximation the overlap integral $I_{nn'}$ depends only on the ratio of the oscillator parameters, $\varepsilon = \nu_\alpha/\nu$. The result is [7])

$$I_{nn'}(\varepsilon) = \frac{[(2n'+1)!]^{\frac{1}{2}}}{2^{n'}n!} \frac{[(2n+1)!]^{\frac{1}{2}}}{2^{n}n!} \frac{1}{3^{\frac{1}{2}}(\frac{3}{4})^{\frac{1}{2}}} \frac{\varepsilon^{\frac{3}{2}}}{(1+\varepsilon)^3} \left(\frac{\varepsilon-1}{\varepsilon+1}\right)^{n+n'}. \tag{3.1}$$

Calculations of the ZRMFF, $F^{\gamma}_{J'L}(R)$, have been performed for ^{40}Ca(p, α)^{37}K and are shown in figs. 3 and 4. The sensitivity of the shape of the form factor to the assumed value of the α-particle oscillator parameter, ν_α, arises through the dependence of $I_{nn'}(\varepsilon)$ on ν_α, and is shown in fig. 3. Details of the Woods-Saxon parameters and binding energies used in the calculation of the single-particle states were similar to those used for ^{42}Ca [ref. [7])], and are given in table 1. The shell model oscillator parameter had a value $\nu = 0.256$ fm^{-2}, corresponding to $\nu_{s.p.} = 0.250$ fm^{-2}. It is observed that as ν_α is decreased, or equivalently, the α-particle size is increased, the form factor tends to peak at a larger radius in the nuclear surface region. Considerable

(p, α)

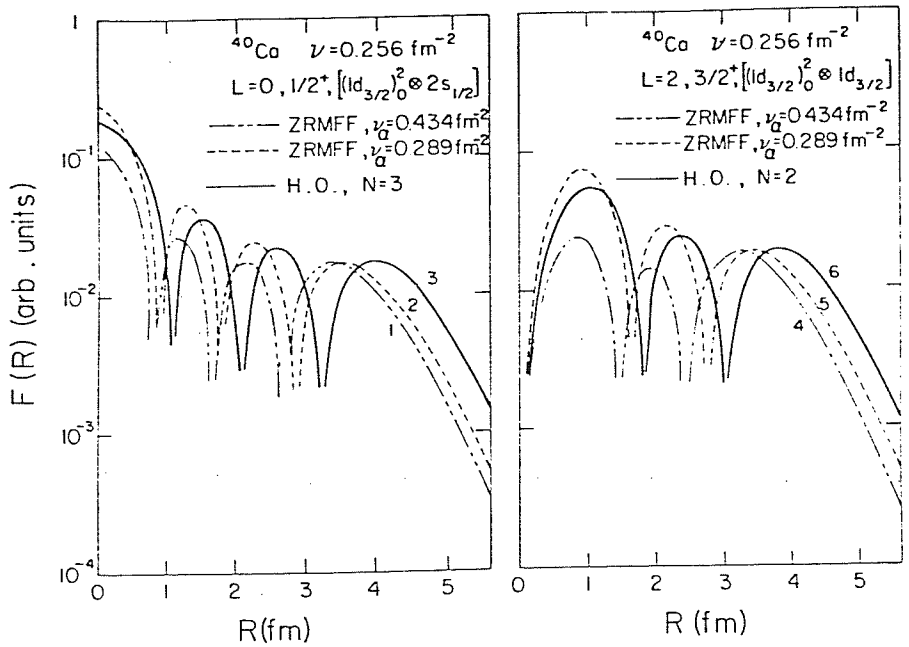

Fig. 3. ZRMFF for ^{40}Ca, $L = 0$ and $L = 2$ transfer, as a function of ν_α. The two $1d_{3/2}$ neutrons are coupled to total angular momentum zero. Parameters used in the calculation of these (numbered) curves are specified in table 1. The harmonic oscillator function (H.O.) was calculated with the oscillator parameter 0.712 fm^{-2}.

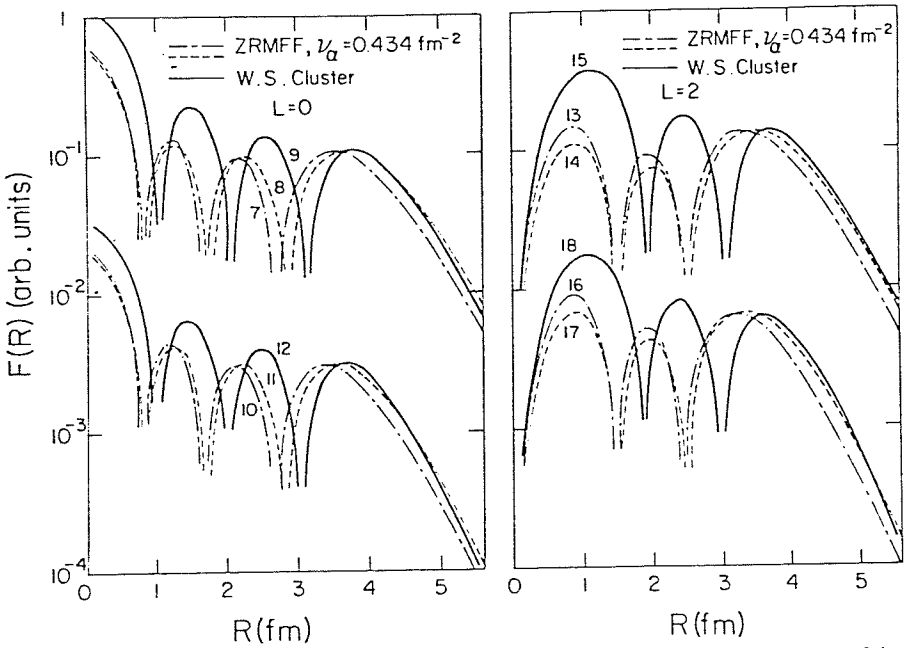

Fig. 4. Dependence of the ZRMFF for ^{40}Ca, $L = 0$ and $L = 2$ transfers, on the parameters of the single-particle states. Details for these (numbered) curve are given in table 1. Mass-three cluster form factors are shown for comparison.

TABLE 1

Parameters for ^{40}Ca(p, α) three-nucleon transfer form factors

	ν_a	$\varepsilon = (\nu_a/\nu)$ [a]	Three transferred nucleons [b]				Nucleon bound state parameters [e] ($\nu_{s.p.} = 0.250$ fm^{-2})				Comments
			L	J	N [c]	total binding energy (MeV) [d]	r_0 (fm)	a_0 (fm)	binding energies (MeV) [f] neutrons	proton	
1 ZRMFF	0.434	1.694	0	½	3	42.02	1.17	0.692	16.07	9.88	
2 ZRMFF	0.289	1.126	0	½	3	42.02	1.17	0.692	16.07	9.88	
3 HO cluster			0		3						
4 ZRMFF	0.434	1.694	2	½	2	40.23	1.17	0.692	16.07	8.09	
5 ZRMFF	0.289	1.126	2	½	2	40.23	1.17	0.692	16.07	8.09	
6 HO cluster			2		2						
7 ZRMFF	0.434	1.694	0	½	3	24.00	1.152	0.692	8.00	8.00	
8 ZRMFF	0.434	1.694	0	½	3	24.00	1.25	0.65	8.00	8.00	
9 WS cluster [g]			0	½	3	26.34					
10 ZRMFF	0.434	1.694	0	½	3	40.14	1.152	0.692	16.07	8.00	
11 ZRMFF	0.434	1.694	0	½	3	40.14	1.25	0.65	16.07	8.00	
12 WS cluster [g]			0	½	3	42.02					
13 ZRMFF	0.434	1.694	2	½	2	24.00	1.152	0.692	8.00	8.00	
14 ZRMFF	0.434	1.694	2	½	2	24.00	1.25	0.65	8.00	8.00	
15 WS cluster [g]			2	½	2	24.97					
16 ZRMFF	0.434	1.694	2	½	2	40.14	1.152	0.692	16.07	8.00	
17 ZRMFF	0.434	1.694	2	½	2	40.14	1.25	0.65	16.07	8.00	
18 WS cluster [g]			2	½	2	40.23					
19 ZRMFF	0.289	1.126	2	½	2	40.23	1.17	0.692	16.07	8.09	non-locality correction of 0.85 fm
20 ZRMFF	0.434	1.694	2	½	2	40.23	1.17	0.692	16.07	8.09	non-locality correction of 0.85 fm
21 ZRMFF	0.434	1.694	2	½	2	40.23	1.17	0.692	16.07	8.09	
22 ZRMFF	0.434	1.694	2	½	2	40.23	1.17	0.692	16.07	8.09	no c.m. corrections
23 FRMFF	0.434	1.694	2	½	2	24.00	1.25	0.65	8.00	8.00	$1/\beta = 1.47$ fm
24 FRMFF	0.434	1.694	0	½	3	24.00	1.25	0.65	8.00	8.00	$1/\beta = 1.47$ fm

[a]) Shell model oscillator parameter $\nu = 0.250\ (40/39) = 0.256$ fm^{-2}.

[b]) Mass-three oscillator parameter $\nu_{c.m.} = 3(37/40)\nu = 0.712$ fm^{-2}. The nucleon configurations for the $L = 0$ and $L = 2$ transfers were $[(1d_{3/2})^2_0 \otimes 2s_{1/2}]$ and $[(1d_{3/2})^2_0 \otimes 1d_{3/2}]$ respectively.

[c]) Calculated from eq. (3.2).

[d]) Either the sum of the nucleon binding energies as given in columns 10 and 11, or the separation energy of the triton in the Woods-Saxon well.

[e]) Spin-orbit parameters $V_{s.o.} = 5.90$ MeV, $r_{s.o.} = 1.014$ fm, $a_{s.o.} = 0.526$ fm were used in the calculations, and a Coulomb radius parameter $r_c = 1.32$ fm.

[f]) Essentially two series of calculations are represented; the first where the neutrons and protons were given the single-particle binding energies discussed in ref. [7]), and secondly where their binding energy was fixed at 8 MeV. In the latter case the total three-nucleon separation energy of 24 MeV is very close to the experimental triton separation energies of 24.97 and 26.34 MeV to the g.s. and first excited states of ^{37}K respectively. In the former case the sum of the single-particle binding energies considerably exceeds the experimental triton separation energy and also the three-nucleon separation energy of 33.45 MeV.

[g]) Woods-Saxon cluster wave function calculated with parameters $r_0 = 1.20$ fm and $a_0 = 0.50$ fm.

variations in the interior region are also observed as ν_x is varied. For values of ν_x greater than 0.434 and for values less than 0.289, the calculated form factors differ little from the ones calculated for these two values respectively. Also shown in fig. 3 for further comparison are harmonic oscillator functions for $L = 0$ and 2 representing the motion of the mass-three cluster, calculated with an oscillator parameter of 0.712 fm^{-2} ($= 3\nu(A-3)/A$).

Nucleon bound state parameters in the previous calculations were selected in accordance with accepted optical-model parameters and single-particle separation energies [7]). The dependence of the ZRMFF on these parameters is investigated in fig. 4 for $L = 0$ and $L = 2$ transfers. Curves 7 and 8 of fig. 4 were calculated with identical parameters except for the radius and diffuseness parameters of the nucleon Woods-Saxon well which were 1.152 and 0.692, and 1.25 and 0.65 fm respectively as given in table 1. (The latter combination of 1.25 and 0.65 fm is the one most frequently used in the literature in DWBA analysis of single-nucleon transfer reactions!) The form factors resulting from these calculations exhibit differences in the position of the outer maximum of about $\frac{1}{4}$ fm, and decreasing differences in the nuclear interior. For comparison, a mass-three cluster form factor (curve 9) calculated as a bound state in a Woods-Saxon well with $r_0 = 1.20$ and $a_0 = 0.50$ fm is also shown in fig. 4. The curve differs markedly from the ZRMFF in the nuclear interior, and approximates curve 8 reasonably well for $R \geqq 4$ fm. Changing the nucleon binding energies as for curves 10 and 11 of fig. 4 moves the outer maximum to smaller radius as expected, in close accord with the shift in the cluster form factor of approximately the same total binding energy. The foregoing remarks apply generally to the $L = 2$ form factors shown in the right hand portion of fig. 4 as well, with perhaps a more marked discrepancy between the cluster and ZRMFF in the nuclear interior.

Our experience with the use of these ZRMFF in DWBA calculations has shown that they systematically yield angular distribution shapes which are less satisfactory than those obtained from the cluster form factors, particularly when the smaller radius parameter of $r_0 = 1.17$ fm is employed. Other investigators have made similar observations [30]).

In every instance, the number of nodes obtained in the ZRMFF is equal to that deduced from the relationship

$$2N + L = \sum_{i=1}^{3} 2n_i + l_i, \tag{3.2}$$

where n_i, l_i are the single-particle shell-model state quantum numbers. However, energy conservation restrictions permit a range of N-values given by

$$2N + L + 2(n' + n) = (2p_1 + l_1) + (2p_2 + l_2) + (2p_3 + l_3). \tag{3.3}$$

The large deviation of the shape of the ZRMFF from that of an oscillator function with oscillator parameter $\nu = 0.712$ fm^{-2} (curves 3 and 6 in fig. 3) would thus seem to arise through the contributions from N-values other than that given by eq. (3.2).

It is instructive to examine the behavior of the overlap integral $I_{nn'}(\varepsilon)$ given by eq. (3.1). This is done in fig. 5 where the ratios I_{10}/I_{00} and I_{20}/I_{00} are plotted as a function of ε. Clearly, for values of ε considerably larger than unity, contributions from terms n', $n \neq 0$ – or equivalently, from a range of N values – are significant. (It should be

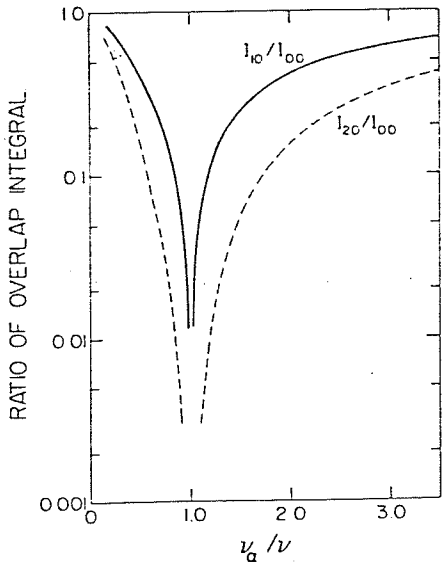

Fig. 5. Behavior of the overlap integral $I_{nn'}$ as a function of $\varepsilon = \nu_\alpha/\nu$.

noted that if the single-particle states are represented by single harmonic oscillator functions, in place of an expansion, the resulting ZRMFF should become identical to the oscillator functions shown in fig. 3, in the limit $\nu_\alpha/\nu = 1$.) Presenting this in further detail, fig. 6 shows the contributions to $L = 0$ and $L = 2$ form factors for several values of N, and the resultant form factors summing over all contributions from $N = 0$ to $N = 7$. For the $L = 0$ ZRMFF the term in $N = 2$ contributes to the form factor with the same sign in the surface region as the (dominant) $N = 3$ term, whereas the $N = 4$ term contributes with the opposite sign. The consequence is that the form factor is strongly enhanced in the region between 3–4 fm and decreased for $r \geqq 4$ fm. Similar observations are made regarding the $L = 2$ form factor. As noted earlier, these ZRMFF with their broad outer maximum peaking well inside the nuclear radius, fail to produce acceptable angular distributions when used in DWBA calculations. Other parameters used in calculating the curves of fig. 6 were identical to those given for curves 1 and 4 of table 1.

In order to complete the discussion the ZRMFF we show in fig. 7 the result of neglecting c.m. effects, and the role of non-local [21,22]) corrections applied to the single-particle states. Comparing curves 21 and 22 in this figure we see that c.m. effects are large in the nuclear surface region and beyond. To a lesser extent, yet still important, is the further enhancement of the form factor in the surface region when

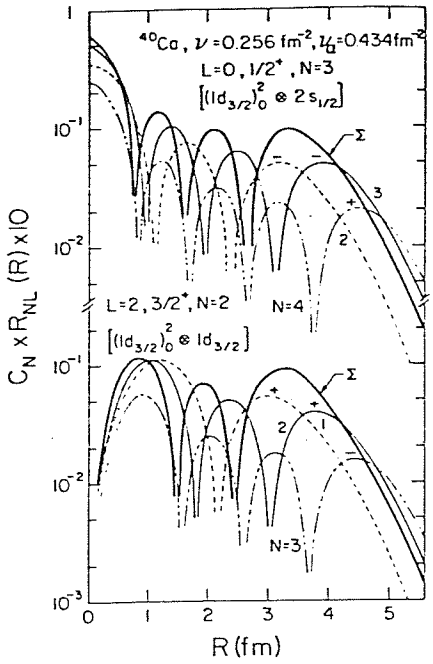

Fig. 6. Contributions to the $L = 0$ ZRMFF from the dominant oscillator terms $N = 2, 3$ and 4, and the dominant terms $N = 1$, 2 and 3 for the $L = 2$ ZRMFF. The composite form factors are indicated by Σ, and include terms $N = 0$ to $N = 7$. C_N is the coefficient of the harmonic oscillator function R_{NL} determined from eq. (2.19).

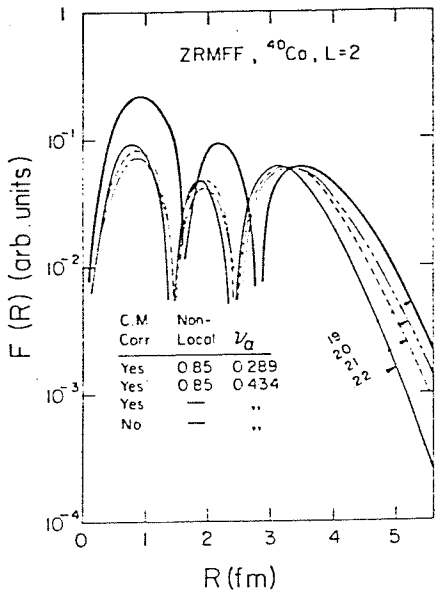

Fig. 7. Dependence of the $L = 2$ ZRMFF for ^{40}Ca on center of mass (c.m.) corrections, non-local effects, and on ν_α. Other details of these (numbered) curves are given in table 1.

a non-locality correction of 0.85 fm is applied to each of the three single-particle bound states. The effect of changing the α-particle oscillator parameter from 0.434 fm^{-2} to 0.289 fm^{-2} is seen to be comparable to these other effects.

4. Characteristics of the finite-range microscopic form factor (FRMFF)

A computer code has been written which performs the full calculation of the finite-range microscopic form factor (FRMFF) as given by eq. (2.19). One example of such a form factor (for ^{40}Ca) for an $L = 2$ transfer is shown in fig. 8. The ρ-dependence of this two-dimensional form factor is indicated by the series of curves drawn for different values of ρ. An interaction range $1/\beta = 1.47$ fm was used. The curve for $\rho = 0$ is rather similar to the corresponding curve (curve 14) of the ZRMFF of fig. 4, with the latter exhibiting less damping in the interior region and peaking at somewhat greater radius. Curves for $\rho \neq 0$ in fig. 8 exhibit an approximate Gaussian dependence on ρ, and a shift of the maxima to larger R as ρ increases. Nevertheless, even for $\rho \lesssim 2$ fm, the outer maximum occurs at a radius of only $\approx 3\frac{1}{2}$ fm. Qualitatively

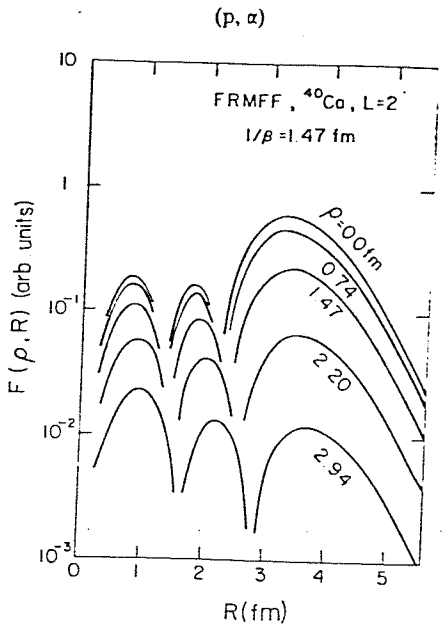

Fig. 8. $L = 2$ FRMFF for ^{40}Ca with an interaction range, $1/\beta = 1.47$ fm. Other details are given under curve 23 of table 1.

similar results were obtained for other L-transfers, which exhibited a dependence on v_a and non-locality corrections similar to that of the ZRMFF.

The exact finite range DWBA code LOLA [31]) was modified to allow the kernels to be calculated from the FRMFF $F(\rho, R)$. This modification is necessary since the form factor can no longer be simply factored into a product of two functions, one of which depends on ρ only, and the other on R only. Sample DWBA calculations for $L = 0$ and $L = 2$ transfer for ^{40}Ca(p, α)^{37}K are presented in fig. 9. Also shown for comparison are three other calculations representing a conventional zero-range cluster transfer (ZR cluster), a conventional finite-range calculation (FR cluster), and a zero-range microscopic form factor calculation (ZRMFF). The proton and α-particle optical-model parameters were kept fixed for all these calculations and are shown in table 2, with the exception that the FR calculations contained no spin-orbit term in the proton channel. (The code LOLA [31]) does not make provision for spin-orbit terms in the optical-model potentials.) These parameters are the same as those used in ref. [7]). The p + t bound-state parameters for the FR cluster calculation were taken from the n + t optical-model analysis of Sherif and Podmore [32]). The data shown in this figure will be the subject of a forthcoming publication.

Neglect of spin-orbit effects in the FR calculations will affect the shape of the DWBA angular distributions because of the j-dependence of the (p, α) reaction. However, it is known [2, 7]) that these effects are not very pronounced for $L = 2$ transfer in the $A = 40$ region. Calculations were subsequently performed in ZR in which the spin-orbit potential was set to zero. The differences in the angular distributions with and without the spin-orbit potential were not substantial. For $L = 0$

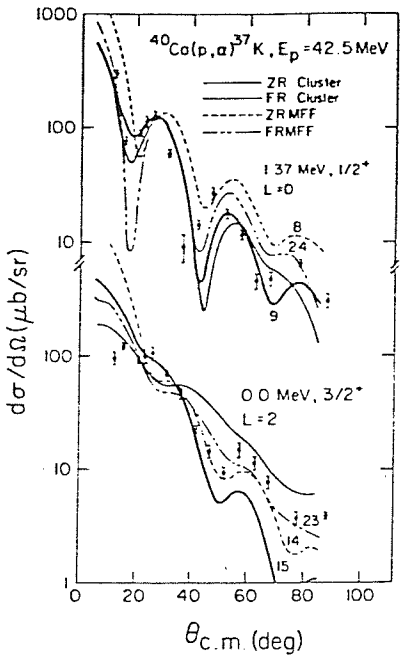

Fig. 9. $L = 0$ and $L = 2$ transfer DWBA calculations for ^{40}Ca using zero-range cluster (ZR cluster), finite-range cluster (FR cluster), zero-range microscopic (ZRMFF), and finite-range microscopic (FRMFF) form factors. The optical-model and bound-state parameters are given in table 2, with further details (on the corresponding numbered curves) presented in table 1. The FR calculations contain no spin-orbit term in the proton channel.

TABLE 2

Optical-model parameters used in the DWBA calculations for the distorted waves and the bound states

	V	r	a	W'	$r_{W'}$	$a_{W'}$	W'_D [a])	$V_{s.o.}$	$r_{s.o.}$	$a_{s.o.}$	r_C
p+^{40}Ca	44.85	1.152	0.692	4.49	1.309	0.549	3.92	4.32	1.014	0.526	1.32
α+^{37}K	210.0	1.41	0.59	20.2	1.66	0.35					1.30
t+^{37}K	[b])	1.20	0.50								1.25
p+t	52.3 [c])	1.488	0.144								1.30

[a]) The radius and diffuseness parameters for the surface term were the same as for the imaginary volume term.

[b]) Selected to yield the experimental separation energy.

[c]) Selected to yield the experimental separation energy of 19.814 MeV.

transfer, the spin-orbit term has the effect of reducing the minima in the neighborhood of 20° and 44°. Hence, inclusion of the spin-orbit term in the FR calculations would likely bring them more closely in line with the corresponding ZR calculations in the angular distributions of fig. 9. Without the spin-orbit term the $L = 2$ transfer angular distributions are modified mainly in the neighborhood of 60°, with the small maximum largely disappearing in these calculations. Thus, here also, inclusion of the spin-orbit

term in the FR calculations would likely bring these angular distributions into closer correspondence with the ZR ones.

While none of the DWBA calculations of fig. 9 represent high quality fits to the experimental data, they may all be considered acceptable for the poorly L-matched (p, α) reaction, keeping in mind the previous comments on the neglect of the spin-orbit term in the FR calculations. Microscopic form factors for both the ZRMFF and FRMFF calculations employed nucleon bound-state parameters $r_0 = 1.25$ fm and $a_0 = 0.65$ fm. Totally unacceptable fits were obtained if the radius parameter $r_0 = 1.17$ fm was used in the form factor calculations. Thus we conclude that an empirically adjusted radius parameter for the nucleon bound state parameter, to the somewhat large value of 1.25 fm, yields form factors, and subsequently angular distributions, which fit the data about as well as conventional cluster transfer calculations.

5. Nuclear structure information and microscopic form factors

The previous sections have shown that microscopic form factors for three-nucleon transfer, calculated according to the given prescription, have a broad outer maximum, and require a large nucleon radius parameter to produce acceptable angular distributions when used in DWBA codes. An immediate question which then follows is how, and in what manner, this microscopic information can be used in analysing (p, α) reactions in the extraction of nuclear structure information. A related question is that of the implementation of this rather complicated and lengthy procedure which is not generally available as an experimenter's tool in analysing data.

Both questions have been dealt with through various approximations made to the ZR equivalent of the expression for the form factor, eq. (2.19). Smits [1,2]) and Pellegrini *et al.* [33]) restrict the summations in eq. (2.19) by assuming oscillator functions for the single particle states and including only those terms for which $n = n' = 0$. The latter approximation is a good one when $\nu_\alpha/\nu \approx 1$, that is, for light nuclei, but for heavier nuclei (assuming $\nu \approx A^{-\frac{1}{3}}$)[†] the ratios of the overlap integrals I_{10}/I_{00}, I_{20}/I_{00} etc. are not small as can be seen in fig. 5. On the other hand, non-zero values of n and n' imply smaller values of N, because of the energy conservation restriction, and hence oscillator functions of relative motion R_{NL} with fewer nodes. These functions will clearly have their outer maximum at a smaller radius and hence contribute less to the surface region of the nucleus. To the extent that the DWBA cross section is sensitive to the surface region only, the largest N-value alone will be important. Their procedure, subsequently, was to replace the single-oscillator function R_{NL}, representing the motion of the three-nucleon cluster relative to the residual nucleus B, with a cluster wave function of the same N and L calculated in a Woods-Saxon potential. Since this can be carried out in standard DWBA codes and the angular

[†] The oscillator parameter ν for various nuclei was calculated from the formula given by Bertsch [34]), $\nu = 0.02411\,(45/A^{1/3} - 25/A^{2/3})$.

distribution calculated with this form factor, a considerable simplification is introduced. The nuclear structure information is then contained in all the remaining terms of eqs. (2.18) and (2.19) as normalization factors.

Another approach described below also calculates the angular distribution assuming a cluster transfer, but treats the nuclear structure information, as a normalization factor to the DWBA calculation, as follows [35]). The normalization of the form factor, calculated according to eq. (2.19) (in ZR),

$$\text{FF normalization} = \int_0^\infty [F^J_{J,L}(R)]^2 R^2 \mathrm{d}R, \tag{5.1}$$

is computed, and this result together with the remaining terms of eq. (2.18), considered as the structure-containing quantity.

The following figures (10–12) contain numerous plots of the form factor normalization as a function of ν_α/ν for various nucleon configurations, and for a range of nuclei. Since the dominant term in the ZRMFF occurs for $n = n' = 0$, for which the overlap integral $I_{nn'}$ is proportional to $q^{-1} = [\sqrt{\varepsilon}/(1+\varepsilon)]^3$, all the form factor normalizations have been multiplied by the reciprocal of this factor to facilitate the comparison. For all the results shown, with the exception of the ^{40}Ca results in fig. 10, the single-particle states were taken to be harmonic oscillator states calculated with the shell-model oscillator parameter indicated in each figure. A full harmonic oscillator expansion of the Woods-Saxon single-particle states for ^{40}Ca was used for a few selected cases only.

Fig. 10 shows the results for ^{16}O in which p-shell nucleons only were considered. Examination of these curves indicates that the relative normalization of the form factors changes only little as ν_α is varied since the curves are very similar in shape.

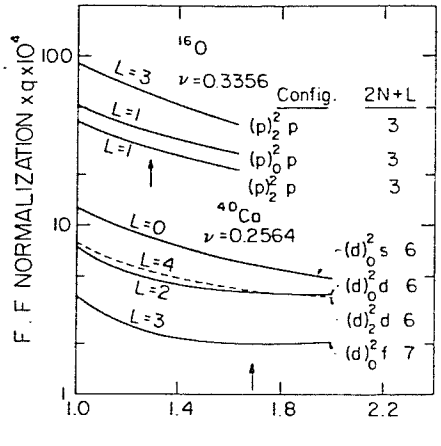

Fig. 10. Form factor normalizations as given by eq. (5.1) for ^{16}O and ^{40}Ca. The 1p subshell only is considered for ^{16}O, and the $1d_{3/2}$, $2s_{1/2}$ and $1f_{7/2}$ subshells for ^{40}Ca. Harmonic oscillator single-particle states have been used for ^{16}O, and Woods-Saxon single-particle states for ^{40}Ca as given for curves 1 and 4 in table 1.

An important factor in the case of such a light nucleus is the small value of the overlap integral $I_{nn'}$ for $n, n' \neq 0$. The results for ^{40}Ca in the lower portion of fig. 10 are for form factors in which the single particle states were calculated in a Woods-Saxon potential with the same parameters as used in fig. 3. These curves should be compared with the corresponding ones of fig. 11 which represent calculations with harmonic oscillator single-particle states. Indeed, the similarities between the corresponding curves for these different calculations is remarkable, except possibly for the smallest values of ε. The vertical arrow in this and succeeding figures indicates the value of ε for whcih $r_a = 0.434$, its accepted value.

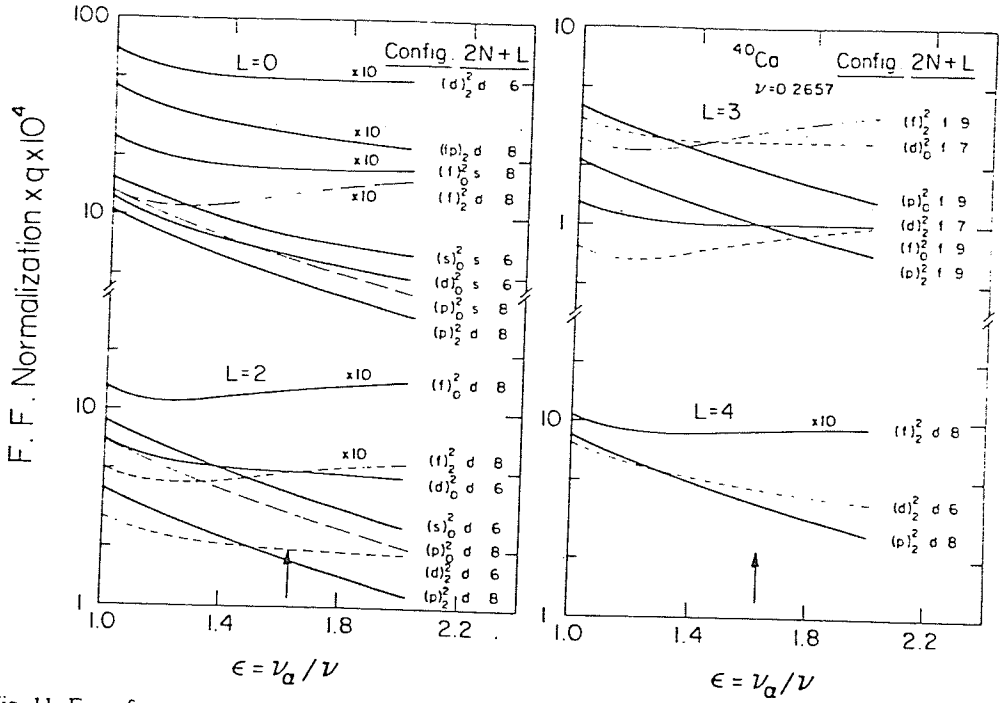

Fig. 11. Form factor normalizations as given by eq. (5.1) for ^{40}Ca using harmonic oscillator single-particle states. Results are shown for configurations from the 1d, 2s, 2p and 1f subshells.

Numerous curves in fig. 11 for L-transfers $L = 0$ to $L = 4$ show similar behavior, the normalization decreasing by a factor of about three as ε varies from 1 to 2. Generally, these curves comprise configurations where the single particle states have lower orbital angular momenta. A rather different behavior as a function of ε is observed for those curves representing configurations involving the higher orbital angular momenta of the single-particle states. These curves may be relatively independent of ε or, indeed, show an increase with increasing ε, after an initial decrease. It is abundantly clear from these results that the value of ε used in extracting the nuclear structure information from the DWBA analysis is an important and sensitive parameter if many configurations are involved. Indeed, in crossing a major shell as

in Ca, where both sd and pf nucleons need be considered in the target and residual nucleus wave functions, large uncertainties may be present in the extracted nuclear structure information. By the same token, it is observed that for certain configurations, spanning all L-values, relative insensitivity to ε would result. The implications for one of the simplifying approaches that considers only terms in the form factor for which $n = n' = 0$, or equivalently, $\nu_a/\nu = 1$, must thus be clearly borne in mind.

More striking yet are the variations in the normalizations for form factors involving the ^{130}Te(p, α)^{127}Sb reaction, as shown in fig. 12. The neutron orbits considered are the

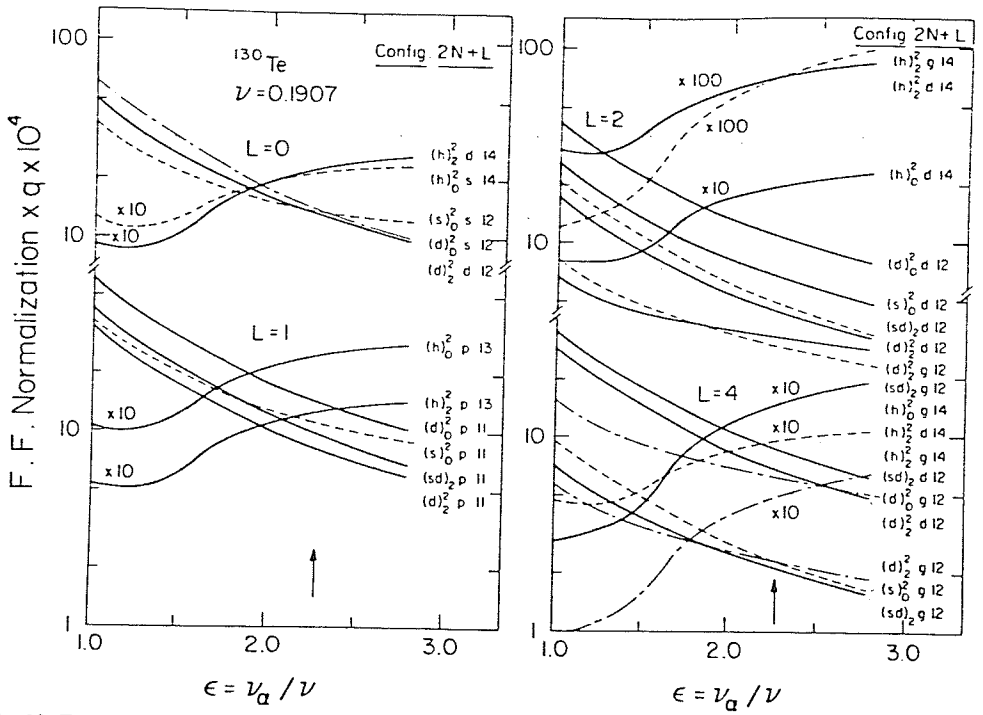

Fig. 12. Form factor normalizations as given by eq. (5.1) for ^{130}Te using harmonic oscillator single-particle states. Results are shown for configurations from the $3s_{1/2}$, $2d_{3/2}$ and $1h_{11/2}$ neutron subshells and the 2p, $1f_{5/2}$, 1g, 2d and $3s_{1/2}$ proton subshells.

$3s_{\frac{1}{2}}$, $2d_{\frac{3}{2}}$ and $1h_{\frac{11}{2}}$ subshells, and the proton orbits the 2p, $1f_{\frac{5}{2}}$, 1g, 2d and $3s_{\frac{1}{2}}$ subshells. Two major groupings of the curves are observed: those whose normalization increases with increasing ε, as represented by all the configurations involving $(h_{\frac{11}{2}})^2$ neutrons, and the remaining curves which show a monotonic decrease of the normalization factor with increasing ε. This qualitatively different behavior of the two groupings of curves is not understood at present. However, from classical considerations, one expects that form factors comprised of nucleons with large orbital angular momenta to be largely surface localized, and hence exhibit quite a different normalization dependence on ε. This is illustrated in figs. 13 and 14 where $L = 0$ and $L = 4$ form factors respectively are shown for different configurations. The ones involving two

(p, α)

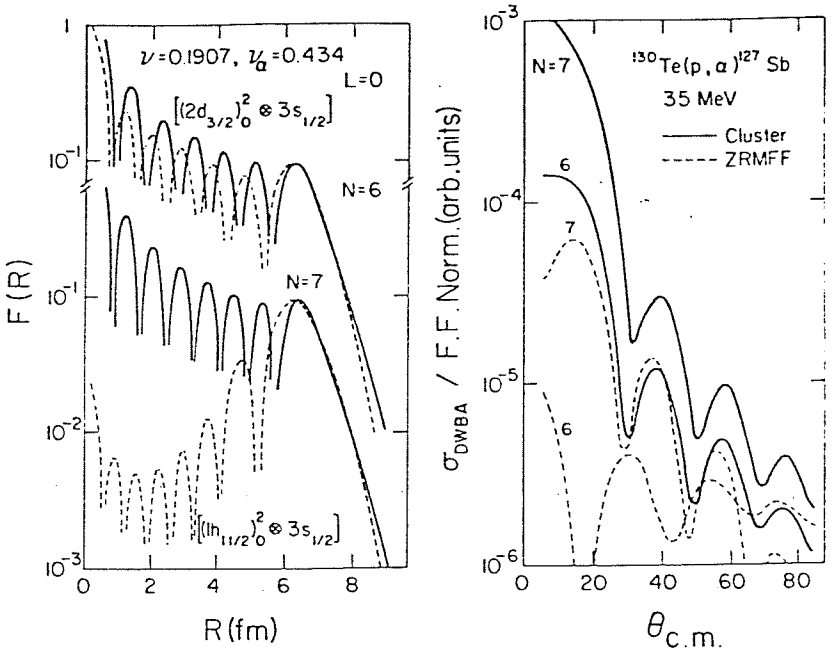

Fig. 13. Cluster and microscopic form factors for $^{130}Te(p, \alpha)^{127}Sb$, and the corresponding DWBA angular distributions. The ZRMFF's have been normalized to the cluster form factors at the outer maximum. The incorrect asymptotic behavior of the ZRMFF's was modified by replacement with the cluster form factor in the asymptotic region, prior to calculating the angular distributions. Cluster form factor binding energy is 16.70 MeV.

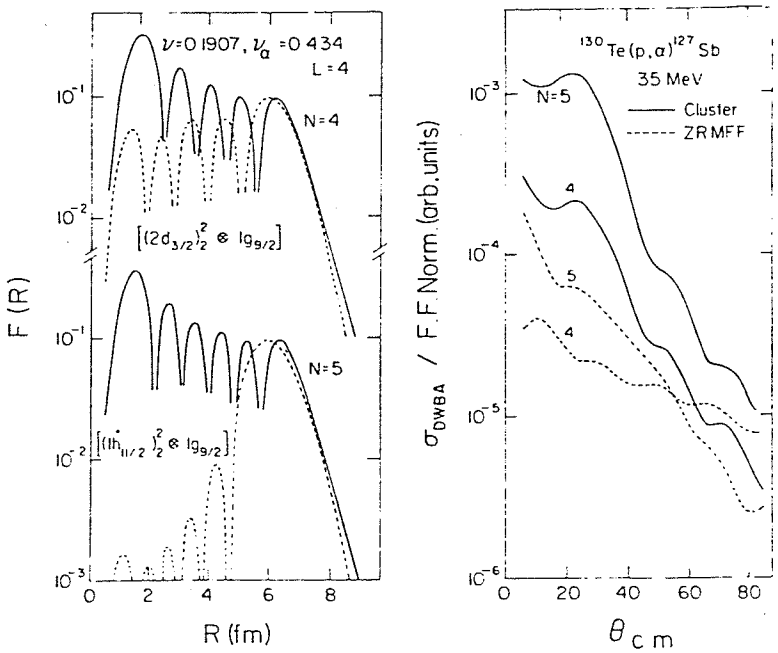

Fig. 14. Caption as for fig. 13. Cluster form factor binding energy is 17.85 MeV.

$h_{\frac{1}{2}}$ nucleons are very strongly damped in the nuclear interior. In contrast, the cluster form factors exhibit quite a marked rise in the amplitude of the oscillations with decreasing radius. Similar behavior was displayed for ZRMFF of all L-values. Since DWBA calculations using an inner radial cutoff have indicated sizable contributions from the nuclear interior in the generally poorly L-matched (p, α) reaction [8-10], one might well expect sensitivity to the interior details of the form factor and hence to the configurations involved in this reaction. DWBA calculations performed with an inner radial cutoff did, indeed, show a marked sensitivity to the radial cutoff, especially when this cutoff occurred within the broad outer maximum of the ZRMFF.

Furthermore, the relationships between the form factor normalizations and the corresponding magnitudes and shapes of the DWBA angular distributions turn out to be complicated ones. This is shown in the right hand portions of figs. 13 and 14 where, for each of the form factors, σ_{DWBA} divided by the form factor normalization, is plotted. For the same L and N, the magnitudes differ widely, and the shapes also show strong variations. Optical-model parameters for the distorted waves and the bound states were taken from the analysis of Sn(p, α)In reactions by Smits and Siemssen [1]. The microscopic form factors, calculated using single-oscillator functions for the single-particle states, were modified in the asymptotic region by attaching the cluster form factor tail before the angular distributions were calculated.

A quantitative summery of these results is presented in table 3 where σ_{DWBA} for the cluster form factor is compared with σ_{DWBA}/(FF normalization) for the ZRMFF. (The cluster form factors are normalized to unity.) The results for ^{40}Ca are from the angular distributions shown in fig. 9 and the information given therein. For this reaction, relative differences between $L = 0$ and $L = 2$ transfers for the above quantities appear to be about 20 %, in addition to the overall factor of about

TABLE 3

Comparisons of σ_{DWBA} calculated for various form factors

Reaction	L	N	Microscopic form factor			Cluster form factor
			config.	$(\sigma/\mathrm{Norm}) \times 10^5$ [a]	$(\sigma/c) \times 10^5$ [b]	$\sigma \times 10^5$
^{40}Ca(p, α)^{37}K	0	3	$(1d_{3/2})^2_0 \otimes 2s_{1/2}$	6.52	4.85	4.09 [c]
	2	2	$(1d_{3/2})^2_0 \otimes 1d_{3/2}$	4.49	2.74	3.32 [d]
^{130}Te(p, α)^{127}Sb	0	6	$(2d_{3/2})^2_0 \otimes 3s_{1/2}$	0.40	0.31	1.26 [e]
	0	7	$(1h_{11/2})^2_0 \otimes 3s_{1/2}$	1.32	0.64	3.00 [e]
	4	4	$(2d_{3/2})^2_2 \otimes 1g_{9/2}$	2.27	1.18	22.2 [f]
	4	5	$(1h_{11/2})^2_2 \otimes 1g_{9/2}$	6.02	2.88	135 [f]

[a]) Norm is the form factor normalization as defined by eq. (5.1).
[b]) c = [outer peak maximum (MFF)/outer peak maximum (cluster)]^2.
[c]) Cross section comparisons made at the peak in the neighborhood of 26°.
[d]) Cross section comparisons made at 36°.
[e]) Cross section comparisons made at the peak in the neighborhood of 38°.
[f]) Cross section comparisons made at 24°.

1.4 between the cluster and microscopic results. On the other hand, the Te(p, α) results show overall factors of 2 to 20 between the cluster and microscopic results and relative differences of 3 to 10 between $L = 0$ and $L = 4$ transfers. An alternative means of comparing the cluster and microscopic results is shown in the second last column of table 3 where the magnitudes of the form factors at their outer maxima are used as the basis of comparison. The conclusions reached above are little altered by this change. Thus, representing the ZRMFF by the equivalent cluster form factor in DWBA calculations, leads to large uncertainties in the extraction of the relative strengths of different L-transfers for a reaction like Te(p, α)Sb, for the example given. Furthermore, the approximation equivalent to setting $\varepsilon = 1$, must seriously misinterpret the relative strengths of the various contributions.

6. Discussion and summary

Microscopic form factors (MFF) for the (p, α) reaction have been formulated and investigated in the zero-range and finite-range approximation. The single-nucleon states of the transferred nucleons require use of a Woods-Saxon radius parameter of at least 1.25 fm (together with $a_0 \approx 0.65$), in their calculation, in order that the MFF exhibit approximately the same radial size as a cluster wave function calculated with parameters $r_0 = 1.20$ fm and $a_0 = 0.50$ fm. (The latter cluster wave function, when used as the form factor in DWBA calculations, yields angular distributions generally in acceptable agreement with the experimental data.) Other factors affecting the radial size of the MFF include c.m. effects, non-local corrections in the single particle wave functions, and the α-particle size parameter. An increase in the rms radius of the α-particle from 1.61 fm to 1.97 fm ($\nu_\alpha = 0.434 \rightarrow \nu_\alpha = 0.289$) shifts the outer maximum of the MFF to larger radius by about 0.15 fm for ^{40}Ca. Center of mass corrections to the MFF enter through the modification of the oscillator parameter for the mass-three cluster (i.e. $3\nu(A-3)/A$) and are increasingly important as the mass of the target nucleus decreases. For ^{40}Ca, inclusion of the c.m. correction shifts the outer maximum to larger radius by about 0.2 fm. A non-locality correction of 0.85 in each of the three single-particle wave functions produces a qualitatively similar, but somewhat smaller effect, as the c.m. correction.

The MFF, in all cases, has a much broader outer maximum than the corresponding cluster form factor, and also differs considerably from the cluster in the nuclear interior. Angular distributions calculated for the MFF and cluster form factor consequently showed differences which in some cases (e.g. ^{130}Te) were very large. In other cases, as for ^{40}Ca, much better agreement was obtained.

All the previous remarks apply equally to the FRMFF as well as the ZRMFF. In particular, much superior fits to the angular distributions were obtained with a radius parameter of 1.25 fm, rather than with 1.17 fm, in calculating the single-particle states. Thus, inclusion of finite range effects fails to compensate for a form factor where the outer maximum occurs at too small a radius.

Differences in the cluster and MFF are also clearly manifest in the relative magnitudes of the calculated cross sections (for form factors of the same normalization). This has a most direct bearing on procedures where the DWBA angular distributions are calculated assuming cluster form factors which have been normalized in some manner to the MFF. The procedure described in the present work of using the normalization of the fully calculated MFF was shown to lead to consistent results for the two configurations investigated for ^{40}Ca(p, α). On the other hand, for the ^{130}Te(p, α) reaction, for the configurations and L-transfers investigated, the predicted strength of the $L = 0$ transfer to that of the $L = 4$ transfer can be too small by an order of magnitude. This may explain in part the recent [35]) finding that the 1.11 MeV, $\frac{1}{2}^+$ state in ^{127}Sb is observed with a strength approximately seven times greater than predicted.

The procedure adopted by Smits [1,2]) in which the summations in eq. (2.19) are restricted to only those terms for which $n = n' = 0$ must also lead to large uncertainties in the extracted nuclear structure information in certain cases, depending upon the nucleon configurations involved in the transfer. Figs. 10–12 emphasize this point showing the dependence of the MFF normalization on the ratio v_a/v.

Relative magnitudes of the cross sections predicted using the FRMFF could not be adequately investigated because of the very long computation times involved.

Finally, in making an overall assessment, the importance of the differences in the shapes of the cluster and MFF cannot be minimized. If the MFF describes the physical situation inadequately, some of the effects mentioned in the introduction need to be incorporated in an extension of the theory. The cluster form factor, calculated with the empirically selected radius and diffuseness parameters, continues to yield the better dynamical description of the (p, α) and (α, p) reactions at the present time.

The authors are grateful to Dr. B. Bayman who performed a number of form factor calculations to serve as an independent check of our procedure. Good agreement was observed between these two methods of calculating the ZRMFF.

References

1) J. W. Smits and R. H. Siemssen, Nucl. Phys. A261 (1976) 385
2) J. W. Smits, Ph.D. Thesis, Groningen 1977, unpublished
3) P. A. Smith, J. A. Nolen, Jr., R. G. Markham and M. A. M. Shahabuddin, Phys. Rev. C18 (1978) 2065
4) R. J. Peterson and H. Rudolph, Nucl. Phys. A241 (1975) 253
5) F. L. Milder, J. Jänecke and F. D. Becchetti, Nucl. Phys. A276 (1977) 72
6) N. Anantaraman, H. E. Gove, J. P. Trentleman, J. P. Draayer and F. C. Jundt, Nucl. Phys. A276 (1977) 119
7) W. R. Falk, Phys. Rev. C8 (1973) 1757
8) W. R. Falk, A. Djaloeis and D. Ingham, Nucl. Phys. A252 (1975) 452
9) W. R. Falk, Proc. Int. Conf. on clustering aspects of nuclear structure and nuclear reactions, Winnipeg 1978, ed. W. T. H. van Oers, J. P. Svenne, J. S. C. McKee and W. R. Falk (AIP Conf. Proc. No. 47, New York 1978) p. 292

10) H. Guyer, V. Meyer, H. H. Müller, W. Reichart, H. Jasicek, H. Oberhummer, P. Riehs, R. Wagner and W. Pfeifer, Phys. Rev. C18 (1978) 1626
11) K. van der Borg, R. J. de Meijer and A. van der Woude, Nucl. Phys. A273 (1976) 172
12) R. Abegg, W. R. Falk and S. K. Datta, Proc. Int. Conf. on clustering aspects of nuclear structure and nuclear reactions, Winnipeg 1978, ed. W. T. H. van Oers, J. P. Svenne, J. S. C. McKee and W. R. Falk (AIP Conf. Proc. No. 47, New York 1978) p. 692
13) A. Arima, Proc. Int. Conf. on clustering aspects of nuclear structure and nuclear reactions, Winnipeg 1978, ed. W. T. H. van Oers, J. P. Svenne, J. S. C. McKee and W. R. Falk (AIP Conf. Proc. No. 47, New York 1978) p. 1
14) G. M. McAllen, W. T. Pinkston and G. R. Satchler, Particles and Nuclei 1 (1971) 412;
A. Prakash and N. Austern, Ann. of Phys. 51 (1969) 418;
R. J. Jaffe and W. J. Gerace, Nucl. Phys. A125 (1969) 1;
P. J. Iano and W. T. Pinkston, Nucl. Phys. A237 (1975) 189
15) M. Vallieres, Da Hsuan Feng and R. H. Ibarra, Nucl. Phys. A256 (1976) 21
16) W. T. Pinkston, Nucl. Phys. A295 (1978) 345
17) N. S. Chant, P. G. Roos and C. W. Wang, Phys. Rev. C17 (1978) 8
18) D. F. Jackson, J. of Phys. G4 (1978) 1287
19) D. F. Jackson and M. Rhoades-Brown, J. of Phys. G4 (1978) 1441
20) T. Fliessbach and H. J. Mang, J. of Phys. G4 (1978) 1451
21) F. G. Perey, Proc. Conf. on direct interactions and nuclear reaction mechanisms, Padua, 1962, ed. E. Clementel and C. Villi (Gordon and Breach, New York, 1963) p. 125
22) N. Austern, in Direct nuclear reaction theories (Wiley, New York, 1970) p. 99
23) I. S. Towner ad J. C. Hardy, Adv. in Phys. 18 (1969) 401
24) J. Joseph, C. Fayard, E. El-Baz and J. Lafoucrière, Nucl. Phys. A142 (1970) 217;
N. S. Chant, Nucl. Phys. A211 (1973) 269;
J. Dobeš, Nucl. Phys. A215 (1973) 581
25) N. K. Glendenning, Phys. Rev. 137 (1965) B102
26) M. Ichimura, A. Arima, E. C. Halbert and T. Terasawa, Nucl. Phys. A204 (1973) 225
27) A. de-Shalit and I. Talmi, in Nuclear shell theory (Academic Press, NY, 1963) p. 183
28) Yu. F. Smirnov, Nucl. Phys. 27 (1961) 177
29) I. Rotter, Nucl. Phys. A135 (1969) 378;
W. T. Pinkston, Nucl. Phys. A291 (1977) 342
30) P. A. Smith, private communication
31) R. M. DeVries, University of Rochester Report, 1974, unpublished
32) H. S. Sherif and B. S. Podmore, Proc. Int. Conf. on few particle problems in the nuclear interaction, Los Angeles, 1972, ed. I. Slaus, S. A. Moszkowski, R. P. Haddock and W. T. H. van Oers (North-Holland, Amsterdam, 1972) p. 691
33) F. Pellegrini, G. Calvelli, P. Guazzoni and S. Micheletti, Phys. Rev. C18 (1978) 613
34) G. F. Bertsch, in The practitioner's shell model (North-Holland, Amsterdam, 1972) p. 33
35) P. Debenham, W. R. Falk, O. Abou-Zeid and N. E. Davison, J. Phys. G5 (1979) 981

APPENDIX B

Sample Calculation for the Spectroscopic Amplitudes

Consider the reaction $^{46}Ti(p,\alpha)^{43}Sc_{g.s.}$. For the purpose of illustration we consider only the component of the wave functions of both target and residual nuclei shown below:

$$|^{46}Ti,\ 0^+> = |^{40}Ca \text{ doubly closed core} > |\pi lf_{7/2}^2(2\ 2) \otimes \nu lf_{7/2}^4(2\ 2)>_0 + \ldots.$$

$$|^{43}Sc,\ 7/2^-> = |^{40}Ca \text{ doubly closed core} > |\pi lf_{7/2}^1(1\ 7/2) \otimes \nu lf_{7/2}^2(2\ 2)>_{7/2} + \ldots.$$

In the above expressions the symbols ν and π represent neutrons and protons respectively. The notation $\pi lf_{7/2}^2(2\ 2)$ represents two $lf_{7/2}$ protons coupled to seniority 2 and angular momentum 2, represented by the first and second numbers within the brackets, respectively.

One possibility of the transferred nucleon configuration is picking up one $lf_{7/2}$ proton and two $lf_{7/2}$ neutrons coupled to angular momentum $J' = 0$.

From Equ. (2.11) the spectroscopic amplitude for the above transition is given by:

$$S^{1/2}(7/2^1\ 7/2^2\ 0\ 7/2) = (\tfrac{2}{1})^{1/2}(\tfrac{4}{2})^{1/2} < 7/2^2(2\ 2)\{|7/2^1(1\ 7/2);\ 7/2> < 7/2^4(2\ 2)\{|7/2^2(2\ 2);\ 7/2^2(0)> \begin{bmatrix} 7/2 & 2 & 7/2 \\ 7/2 & 0 & 7/2 \\ 2 & 2 & 0 \end{bmatrix} \qquad (B.1)$$

The 9-j symbol and the one-particle cfp are equal to 1. We concentrate

now on evaluating the two-particle cfp.

The relation between two-particle cfp and one-particle cfp is given by:(38)

$$< j^n (\alpha J)|\} j^{n-2}(\alpha_2 J_2); J^2(J') > = \sum_{\alpha_1 J_1} < j^{n-1}(\alpha_1 J_1)|\} j^{n-2}(\alpha_2 J_2); j > \cdot < j^n(\alpha J)\{| j^{n-1}(\alpha_1 J_1); j > \cdot (-1)^{J_2+J+2j} \sqrt{(2J_1+1)(2J'+1)} \begin{Bmatrix} J_2 & j & J_1 \\ j & J & J' \end{Bmatrix} \tag{B.2}$$

where { } is the 6-j symbol.

For the case in hand we have n=4. α_1 could take the values 1 or 3.

For $\alpha_1 = 3$ $\quad J_1 = 7/2$

For $\alpha_1 = 3$ $\quad J_1$ $3/2, 5/2, 9/2, 11/2$

I. <u>For $\alpha_1 = 1$, $J_1 = 7/2$</u>: The contribution to Equ. (B.2) is given by:

$$< 7/2^3(1\ 7/2)\ \{| 7/2^2(2\ 2); 7/2 > < 7/2^4(2\ 2)\ \{| 7/2^3(1\ 7/2); 7/2 > \cdot (-1)^{2+2+7} \sqrt{8x1} \begin{Bmatrix} 2 & 7/2 & 7/2 \\ 7/2 & 2 & 0 \end{Bmatrix} \tag{B.3}$$

Tables in Appendix C were used for the one-particle cfp. It is worth mentioning that this table is the same one used by Kutschera(24) in calculating his shell-model wave functions. Equ. (B.3) will reduce to:

$$(-.32678)\ (.57735)\ (-1)\ \frac{(\sqrt{8})\ (-1)}{\sqrt{8x5}} = -.09623 \tag{B.4}$$

II. Similarly:

(i) For $\alpha_1 = 3, \quad J_1 = 3/2$

$$< 7/2^3(3\ 3/2)|\}\ 7/2^2(2\ 2);\ 7/2 > \cdot < 7/2^4(2\ 2)\{|\ 7/2^3(3\ 3/2);\ 7/2 > \cdot (-1)^{2+2+7}\sqrt{4}$$

$$\begin{Bmatrix} 2 & 7/2 & 3/2 \\ 7/2 & 2 & 0 \end{Bmatrix} = .03712 \qquad \text{(B.5)}$$

(ii) For $\alpha_1 = 3, \quad J_1 = 5/2$

$$< 7/2^3(3\ 5/2)\{|\ 7/2^2(2\ 2);\ 7/2 > < 7/2^4(2\ 2)\{|\ 7/2^3(3\ 5/2);\ 7/2 > (-1)^{2+2+7}\sqrt{6}$$

$$\begin{Bmatrix} 2 & 7/2 & 5/2 \\ 7/2 & 2 & 0 \end{Bmatrix} = 0.52658 \qquad \text{(B.6)}$$

(iii) For $\alpha_1 = 3, \ J_1 = 9/2$

$$< 7/2^3(3\ 9/2)\{|\ 7/2^2(2\ 2);\ 7/2 > < 7/2^4(4\ 4)\{|\ 7/2^3(3\ 9/2);\ 7/2 > \cdot (-1)^{2+2+7}\sqrt{10}$$

$$\begin{Bmatrix} 2 & 7/2 & 9/2 \\ 7/2 & 2 & 0 \end{Bmatrix} = .04467 \qquad \text{(B.7)}$$

(iv) For $\alpha_1 = 3, \quad J_1 = 11/2$

$$< 7/2^3(3\ 11/2)\{|\ 7/2^2(2\ 2);\ 7/2 > < 7/2^4(2\ 2)\{|\ 7/2^3(3\ 11/2);\ 7/2 > \cdot (-1)^{2+2+7}\sqrt{12}$$

$$\begin{Bmatrix} 2 & 7/2 & 11/2 \\ 7/2 & 2 & 0 \end{Bmatrix} = 0.1443 \qquad \text{(B.8)}$$

substituting (B.3) to (B.8) inclusive into (B.2) we get:

$$< \mathcal{Z}_2^4(2\ 2)\{|\ \mathcal{Z}_2^2(2\ 2);\ \mathcal{Z}_2^2(o) > = .09623 + .03712 + .52628 + .04467 + .1443$$

$$= 0.65644 \qquad \text{(B.9)}$$

substituting (B.9) into (B.1) we get:

$$S^{1/2}\ (\mathcal{Z}_2^1\ \mathcal{Z}_2^2 \circ \mathcal{Z}_2) = \underline{\underline{2.27398}}$$

OR

$$I_{AB} = \frac{S^{1/2}}{\binom{2}{1}^{1/2}\binom{4}{2}^{1/2}} = \underline{\underline{.65644}}$$

The above procedure has to be repeated for all possible configurations of the transferred nucleons that connect initial and final states.

APPENDIX C

Coefficients of Fractional Parentage (cfp) Tabulation

$$\langle j^{n-1}(\alpha_1 J_1)\, j \,|\, j^n(\nu J)\rangle \; ; \; j = 7/2$$

(Reference 25)

n = 1

ν	J	$\alpha_1 J_1$ = o o
1	$7/2$	1.00

n = 2

ν	J	$\alpha_1 J_1$ = 1 $7/2$
o	o	1.00
2	2	1.00
	4	1.00
	6	1.00

n = 3

ν	J	$\alpha_1 J_1$ = o o	2 2	2 4	2 6
1	$7/2$	0.50	-.372678	-.50	- .600925
3	$3/2$		-.46291	.886405	
	$5/2$		-.781736	-.246183	0.57296
	$9/2$		-.321208	-.805823	0.497418
	$11/2$		-.527046	.443813	0.724743
	$15/2$			-.476731	.879049

n = 4

ν	J	$\alpha_1 J_1 = 1\ 7/2$	$3\ 3/2$	$3\ 5/2$	$3\ 9/2$	$3\ 11/2$	$3\ 15/2$
o	o	1.00					
2	2	.577350	-.253546	.524404	-.278174	-.500	
	4	.577350	.361873	.123092	.520137	.313823	-.389249
	6	.577350		-.238366	-.267183	.426401	.597196
4	2		-.560612	-.158114	.754854	-.301511	
	4		-.175933	-.658281	.128388	.645497	.320256
	5		.387298	-.333712	.553912	-.439390	.469871
	8				-.373979	-.483494	.798438

APPENDIX D

Energy levels of ^{43}Sc, ^{45}Sc and ^{47}Sc

(From Ref. 64 and 77)

E_x(keV)	J^π; T	τ or Γ
0	$7/2^-$	$\tau_{1/2}$ = 3.891 ± 0.012 h
152.0 ± 0.2	$3/2^+$	τ_m = 632 ± 8 us
472.3 ± 0.3	$3/2^-$	226 ± 15 ps
845.0 ± 0.4	$5/2^-$	330 ± 110 fs
855.3 ± 0.3	$1/2^+$	32 ± 4 ps
880.4 ± 0.2	$5/2^+$	6.4 ± 0.9 ps
1 158.5 ± 0.3	$3/2^+$	6.4 ± 1.5 ps
1 179.2 ± 0.3	$3/2^-$	700 ± 200 fs
1 336.8 ± 0.2	$7/2^+$	1.2 ± 0.5 ps
1 407.5 ± 0.8	$7/2^-$	290 ± 70 fs
1 651.1 ± 0.4	$5/2^+$	250 ± 40 fs
1 810.7 ± 0.5	$3/2^-$	22 ± 7 fs
1 829.9 ± 0.2	$(7/2, 11/2)^-$	320 ± 40 fs
1 883.8 ± 0.6	$(5/2, 9/2)^-$	80 ± 30 fs
1 931.7 ± 0.4	$9/2^+$	3.4 ± 0.8 ps
1 962.5 ± 0.4	$5/2^-$	100 ± 20 fs
2 094.3 ± 0.3	$3/2^-$	440 ± 100 fs
2 106.3 ± 0.5	$(1/2^+ - 7/2^+)$	400 ± 80 fs
2 114.3 ± 0.9		
2 141.9 ± 0.9	$(3/2, 5/2^+)$	300 ± 60 fs
2 244 ± 2	$(3/2 - 7/2)^-$	
2 289.1 ± 0.6	$5/2^-$	<30 fs
2 336.0 ± 0.7	$(5/2, 9/2)^-$	<60 fs
2 382.8 ± 0.5	$(3/2, 7/2)$	
2 459.0 ± 1.2	$(5/2, 9/2)^-$	<60 fs
2 552.8 ± 0.3	$(7/2, 11/2)^+$	740 ± 100 fs
2 580.3 ± 0.6	$(1/2^+ - 7/2^+)$	150 ± 50 fs
2 634.8 ± 1.4	$(5/2 - 11/2)^-$	300 ± 100 fs
2 657 ± 10	$1/2^+$	
2 670.3 ± 0.5	$(3/2 - 7/2)^-$	
2 760.5 ± 1.5	$(5/2, 9/2)^-$	<70 fs
2 796 ± 2		
2 810.8 ± 0.7	$(5/2 - 9/2)^-$	<120 fs
2 840.0 ± 1.2	$(3/2 - 17/2)^+$	
2 846.2 ± 1.5		
2 859.7 ± 1.6	$(1/2 - 13/2)^+$	
2 875 ± 2		
2 985.3 ± 1.2	$(3/2, 5/2)$	82 ± 18 fs
2 987.4 ± 0.3	$(7/2 - 15/2^-)$	8.1 ± 1.1 ps
3 123.2 ± 0.3	$(5/2 - 19/2)^-$	679 ± 11 ns
3 141.3 ± 0.7	$(7/2 - 13/2)^+$	
3 160 ± 2		
3 205 ± 10		
3 261 ± 2		
3 290.4 ± 1.4	$(3/2 - 11/2)^-$	
3 327.2 ± 1.2		
3 331.4 ± 1.7		
3 374 ± 2	$(3/2 - 11/2)^-$	
3 451.7 ± 0.9	$(5/2, 7/2)^+$	<10 fs
3 463 ± 2	$(1/2 - 13/2)^+$	

E_x(keV)	J^π; T	τ_m or Γ
3 503 ± 2	$7/2^-$	
3 615 ± 8		
3 645.4 ± 1.8		
3 677.3 ± 1.5	$(1/2 - 13/2)^+$	
3 700 ± 10	$(5/2 - 19/2)^-$	
3 733.8 ± 1.8		
3 755.0 ± 0.8		
3 757 ± 2		
3 806.6 ± 0.7	$7/2^+$	
3 843 ± 2	$(3/2 - 17/2)^+$	
3 860 ± 2		
3 899 ± 6		
3 937 ± 7	$(1/2 - 13/2)^+$	
3 955 ± 6		
4 007 ± 2	$(3/2 - 17/2)^+$	
4 038 ± 2	$(7/2 - 15/2)^-$	
4 138 ± 10	$(3/2 - 17/2)^+$	
4 157 ± 2	$(1/2 - 15/2)^-$	
4 211 ± 10	$(1/2 - 13/2)^+$	
4 235 ± 4	$7/2^-$; 3/2	
4 276 ± 8		
4 351 ± 10	$(5/2, 7/2)^-$	
4 371 ± 2	$7/2^-$	
4 430 ± 2		
4 461 ± 4	$(5/2, 9/2)$	τ_m < 5 fs
4 511 ± 8		
4 555 ± 10		
4 584 ± 10		
4 665 ± 4	$(1/2, 3/2)^-$	
4 720 ± 5	$(1/2, 3/2)^-$; $(3/2)$	
4 766 ± 5	$(1/2, 3/2)^-$	
4 817 ± 6	$(1/2, 3/2)^-$	
4 875 ± 8		
4 895 ± 5	$(1/2, 3/2)^-$	
4 942 ± 15		
5 022 ± 5	$(1/2, 3/2)^-$	
5 195 ± 12		
5 236 ± 10	$(3/2 - 17/2)^+$	
5 262 ± 7	$(1/2, 3/2)^-$	
5 327 ± 16		
5 461 ± 15		
5 502 ± 6	$(1/2, 3/2)^-$	
5 540 ± 15	$(1/2, 3/2)^-$	
5 641 ± 5		
5.70 - 8.04 MeV, many levels among which		
6 143 ± 2	$3/2^-$; 3/2	Γ = 125 ± 15 eV
6 222 ± 10	$1/2^+$; 3/2	50 ± 10 eV
6 685 ± 2	$1/2^-$; 1/2 + 3/2	125 ± 10 eV
6 696 ± 2	$1/2^-$; 1/2 + 3/2	70 ± 20 eV
6 710 ± 2	$1/2^-$; 1/2 + 3/2	1 300 ± 100 eV

^{43}Sc Energy Levels

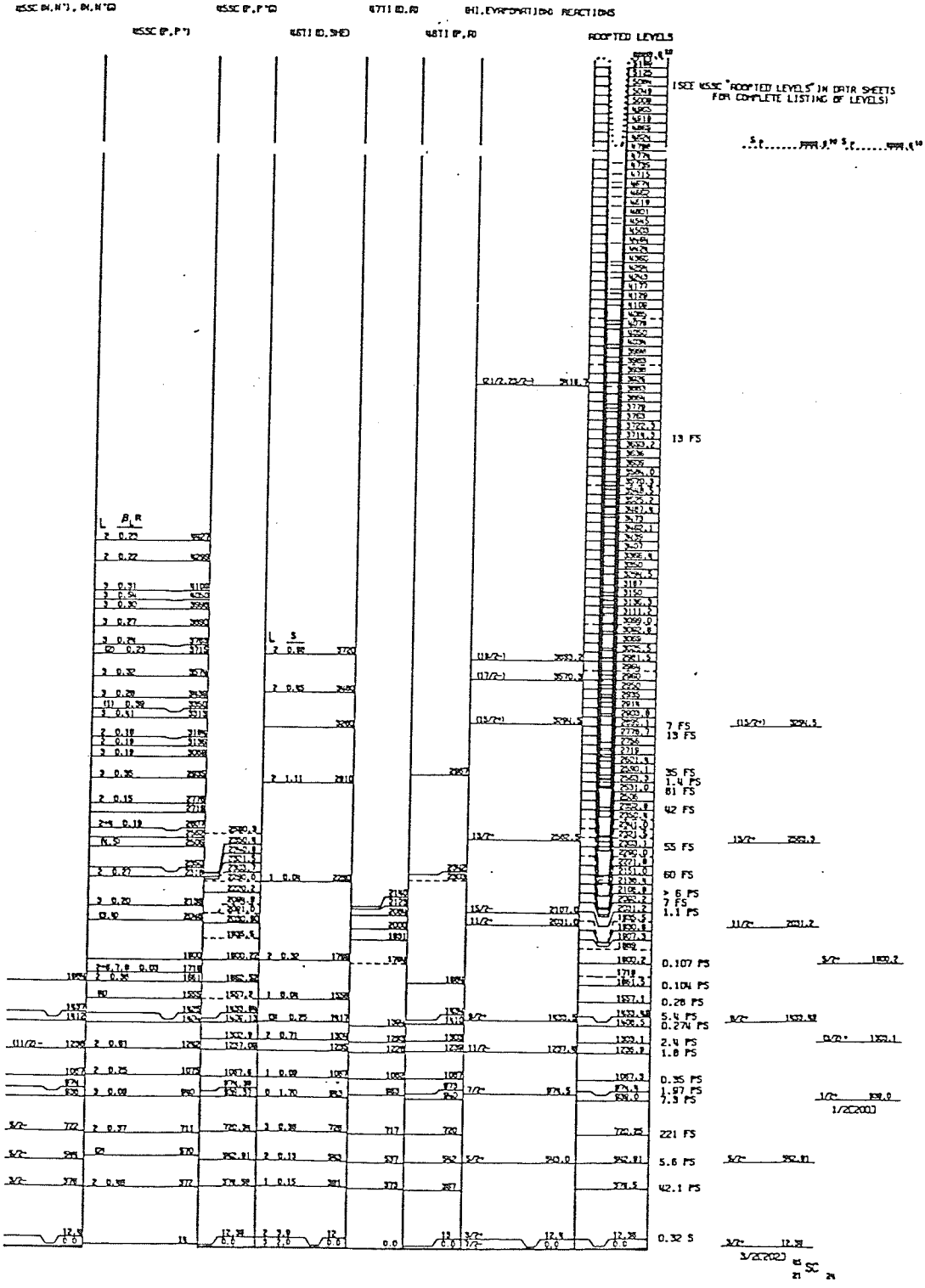

^{45}Sc Energy Levels

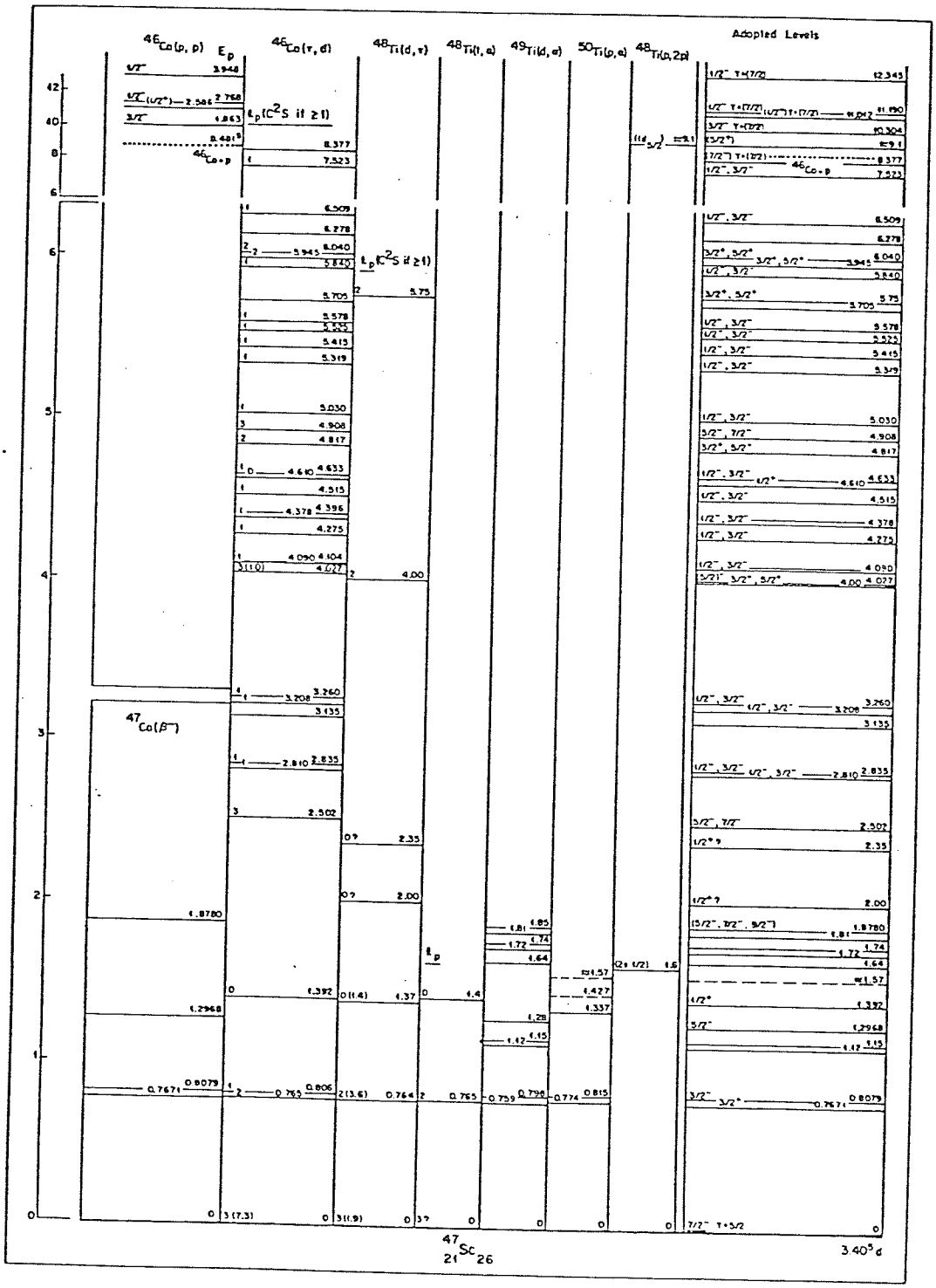

^{47}Sc Energy Levels

References

1. B.F. Bayman, Argonne National Laboratory Report ANL 6878 (1964) 335.

2. M.H. Macfarlane, Argonne National Laboratory Report ANL 6878 (1964) 249.

3. W.R. Falk, Phys. Rev. C8 (1973) 1757.

4. J.W. Smits, Ph.D. Thesis, Groningen 1976, unpublished.
J.W. Smits, R.H. Siemssen, S.Y. van der Werf and R. van der Woude, Nucl. Phys. A319 (1979) 29.

5. K.A. Aniol, Ph.D. Thesis, Australian National University, 1977, unpublished.

6. J.E. Glenn, C.D. Zafiratos and C.S. Zaidins, Phys. Rev. Lett. 26, (1971) 328.

7. L.S. August, P. Shapiro and L.R. Cooper, Phys. Rev. Lett. 23, (1969) 537.

8. D. Bucurescu, M. Ivascu, G. Semenescu and M. Titirici, Nucl. Phys. A189 (1972) 577.

9. Y. Togishi, S. Seki, T. Aoki, M. Sesagasa, M. Sato, K. Katorp, T. Mikumo and J. Sanada, Proceedings of the International Conference on Nuclear Structure, Tokyo (1977) 564.

10. W.R. Falk, A. Djaloeis and D. Ingham, Nucl. Phys. A252 (1975) 452.

11. R.O. Ginaven, A.M. Bernstein, R.M. Drisko and J.B. McGrory, Phys. Lett. 25B (1967) 206.

12. I.S. Towner and J.C. Hardy, Adv. in Phys. 18 (1969) 401.

13. N.K. Glendenning, Phys. Rev. 137 (1965) B102.

14. C.B. Fulmer and B.L. Cohen, Phys. Rev. 112 (1958) 1672.

15. R. Sherr, Conf. on Direct Interactions and Nuclear Reaction Mechanisms, Gordon and Brench, New York (1963) 1025.

16. J.D. McCullen, B.F. Bayman and L. Zamick, Phys. Rev. 134 (1964) B515.

17. J.A. Nolen, Ph.D. Thesis, Princeton 1965, unpublished.

18. P. Debenham, W.R. Falk, O. Abouzeid and N.E. Davison, J. Phys. G: Nuclear Physics, vol. 5, no. 7 (1979) 981.

19. L. Ph. Roesch, O. Abouzeid and W.R. Falk, Nucl. Phys. A333 (1980) 157.

20. P.A. Smith, Ph.D. Thesis, Michigan State University, 1976, unpublished.

21. B.F. Bayman and A. Kallio, Phys. Rev. 156 (1967) 1121.

22. F. Pellegrini, G. Calvelli, P. Guazzoni and S. Micheletti, Phys. Rev. C15 (1977) 573.

23. K. Preisinger, H. Jasicek, H. Oberhummer, P. Riehs, H. Müller and P. Schober, Nucl. Phys. A332 (1979) 278.

24. W.R. Falk, R. Abegg and S.K. Datta, Nucl. Phys. A334 (1980) 445.

25. W. Kutschera, B.A. Brown and K. Ogawa, Rivista Dell Nuovo Cimento, vol. 1, no. 12 (1978) 1.

26. J.J. Buitendage, W.J. Nande, R. Sayman, N.A.J. Rust and J.W. Koen, Zeit. Phys. A295, no. 2 (1980) 107.

27. H.S. Plendl, L.J. Defelice and R.K. Sheline, Nucl. Phys. 73 (1965) 131.

28. R.N. Boyd, S.L. Blatt, T.R. Donoghue and H.J. Hausman, Van de Graaff Accelerator Laboratory Report VDG-013, November 1979, P. 111.

29. H. Ohnuma, Phys. Rev. C3 (1971) 1192.

30. G. Mairle and G.J. Wagner, Z. Physik 251 (1972) 404.

31. P. Doll, G. Mairle, H. Breuer, K. Knöpfle, T. Tohei and G.J. Wagner, J. Phys. G, Vol. 5, no. 16 (1979) 1421.

32. T. Yamazaki, M. Kondo and S. Yamake, J. Phys. Soc. Japan 18 (1963) 620.

33. G.R. Satchler, Nucl. Phys. 55 (1964) 1.

34. W. Tobocman, Theory of Direct Nuclear Reactions, 1961, Oxford University Press.

35. A. Messiah, Quantum Mechanics, 1961, North-Holland Publishing Company.

36. P.D. Kunz, DWUCK 2, a DWBA Code, unpublished.

37. M.H. Macfarlane and J.B. French, Rev. Mod. Phys. 32 (1960) 567.

38. I. Talmi and A. deShalit, Nuclear Shell Theory, 1963, Academic Press, New York.

39. R.M. Drisko and G.R. Satchler, Phys. Lett. 9 (1964) 342.

40. R. de Vries, LOLA, a computer code, University of Rochester report, 1974, unpublished.

41. W.R. Falk, Private communication.

42. J.M. Nelson and B.E. Macefield, DWBA, a computer code.

43. G.F. Bertsch, "The practitioner's shell model", North Holland, Amsterdam (1972) 33.

44. C.M. Perey and F.G. Perey, Atomic Data and Nucl. Data. Tables 17 (1976) 1.

45. J.J. Burgerjen, Nucl. Inst. Meth. 43 (1966) 381.

46. R.A. Batten, J. Bruckshaw, I. Gusdal, G. Knote, A. McIlwain, J.S.C. McKee and S. Oh, Nucl. Inst. Meth. 136 (1976) 6.

47. J.J. Livingood, The Optics of Dipole Magnets (Academic Press, New York), 1969.

48. P. Debenham and W.R. Falk, University of Manitoba Cyclotron Progress Report, 1972 and to be published.

49. W.R. Falk, O. Abou-Zeid and L. Ph. Roesch, Nucl. Instr. 137 (1976) 261.

50. J.R. Comfort, Autofit, a computer code, ANL Report PHY-1970B.

51. F.D. Becchetti and G.W. Greenlees, Phys. Rev. 182 (1969) 1190.

52. K.R. Greider and L.R. Dodd, Phys. Rev. 146 (1966) 671.

53. R.M. DelVechio and W.W. Daehnick, Phys. Rev. C6 (1972) 2095.

54. Joseph Priest and J.S. Vincent, Phys. Rev. 182 (1969) 1121.

55. M.A. Melkanoff, Seek, A computer program for Automatic searches in elastic scattering analysis with nuclear optical model, UCLA Report No. 66-10-1966.

56. J.D. McCullen, B.F. Bayman and L. Zamick, Princeton University Technical Report NYO-9891, June 1964.

57. I.P. Johnstone, Nucl. Phys. 110A (1968) 429.

58. G. Ripka and L. Zamick, Phys. Lett. 23 (1966) 250.

59. B.H. Flowers and I.P. Johnstone, Phys. Lett. 23 (1966) 23.

60. I.P. Johnstone and B.H. Flowers, Proc. Phys. Soc. 91 (1967) 310.

61. K. Lips and M.T. McEllistrem, Phys. Rev. C1 (1970) 1009.

62. J.D. Prentice, Phys. Lett. 3 (1963) 201.

63. Jerry Nolen and Paul Zemany, Michigan State University Cyclotron Laboratory Annual Report (1971) P. 30.

64. P.M. Endt and C. van der Leun, Nucl. Phys. A310 (1978) no. 1,2.

65. I. Fischman, C.E. Thorn and A.M. Bernstein, Phys. Lett. 41B (1972) 298.

66. W.R. Phillips, R. De la Pena and T.A. Critchley, Nulc. Phys. A90 (1967) 379.

67. R.A. Lindgren, Phys. Lett., Vol. 48B, no. 3 (1974) 204.

68. W.P. Alford et al., Phys. Rev. 149 (1966) 820.

69. W.J. Gerace and A.M. Green, Nucl. Phys. A93 (1967) 110.

70. B.H. Flowers and L.D. Skouras, Nucl. Phys. A116 (1968) 529.

71. P. Federman and S. Pittel, Phys. Rev. 186 (1969) 1106.

72. I.P. Johnstone and G.L. Payne, Nucl. Phys. A124 (1969) 217.

73. Kamal K. Seth, H. Ohnuma, T. Seuhiro, S. Yamada and S. Takeda, Phys. Rev. Lett. 30 (1973) 132.

74. L. Zamick, Topical conference on the structure of $1f_{7/2}$ nuclei, Padova, 1971, p. 9.

75. W.J. Courtney and J.D. Fox, Atomic Data and Nuclear Data Tables, 15 (1975) 142.

76. Fay Ajzenberg-Selove, Nuclear Spectroscopy, Academic Press, 1960, p. 1009.

77. Nuclear Data sheets, Vol. 22, no. 1 (1977).

78. R.L. Schulte, J.D. King and H.W. Taylor, Can. J. Phys. 52 (1974) 131.

79. H. Pohl. R. Souto and G.J. Wagner, Z. Physik 245 (1971) 216.

80. E. Kashy and T.W. Conlon, Phys. Rev. 135 (1964) B389.

81. Y. Bandinet-Robinet, J.M. Delbrouk-Habaru, J. Vervier, Nucl. Phys. A171 (1971) 253.

82. M.L. Halbert, Nuclear data sheets, 22 (1977) 59.

83. B. Bardin, Ph.D. Thesis, University of Colorado, 1964, unpublished.

84. M. Toulemonde, L. Deschenes, A. Jamshidi, N. Schulz, Nucl. Phys. A227 (1974) 309.

85. J.M. Delbrouck, Y. Bandinet-Robinet, J. Vervier, Nucl. Phys. A227 (1974) 257.

86. V.V. Tokarevskii and V.N. Scherbin, Sov. J. Nucl. Phys. 25 (1977) 8.

87. T.W. Conlon, B.F. Bayman and E. Kashy, Phys. Rev. 144 (1966) 940.

88. A.P. Zuker, Proceedings of the topical conference on the structure of $1f_{7/2}$ nuclei, Padova (1971). R.A. Ricci, Editor.

89. Manuel Rotenberg, R. Bivins, N. Metropolis and J. Wooten, The 3-j and 6-j symbols, The Technology Press, M.I.T., 1959.